Universidade de Aveiro Departamento de Engenharia Mecânica
2015

Helena Sofia Marques Pinto Soares

Electrólitos para Células de Combustível de Óxidos Cerâmicos

Universidade de Aveiro Departamento de Engenharia Mecânica
2015

Helena Sofia Marques Pinto Soares

Electrolytes for Ceramic Oxide Fuel Cells

Dissertação apresentada à Universidade de Aveiro para cumprimento dos requisitos necessários à obtenção do grau de Doutor em Nanociências e Nanotecnologia, realizada sob a orientação científica do Doutor Duncan Fagg, Equiparado a Investigador Auxiliar do Departamento de Engenharia Mecânica da Universidade de Aveiro

Dedico este trabalho aos meus pais pelo incansável apoio e estímulo durante esta etapa da minha vida, assim como pela dedicação e esforço durante toda a minha formação.

o júri

presidente

Prof. Doutor José Carlos da Silva Neves
professor catedrático do Departamento de Eletrónica, Telecomunicações e Informática

Prof. Doutor César Augusto Correia de Sequeira
professor associado do Instituto Superior Técnico da Universidade de Lisboa

Doutor Glenn Christopher Mather
investigador principal do Instituto de Cerámica y Vidrio (CSIC), Madrid – Espanha

Doutor Filipe Miguel Henriques Lebre Ramos Figueiredo
equiparado a investigador principal do laboratório CICECO – Centro de Investigação em Materiais Cerâmicos e Compósitos da Universidade de Aveiro

Doutor Duncan Paul Fagg
equiparado a investigador auxiliar da Universidade de Aveiro

Prof. Doutora Maria Manuela Silva Pires Silva
professora auxiliar da Escola de Ciências da Universidade do Minho

agradecimentos

O presente trabalho de investigação só foi possível graças ao apoio e ao envolvimento de um significativo número de pessoas e instituições.

Desta forma, em primeiro lugar, gostaria de agradecer ao meu orientador, Doutor Duncan Fagg, o apoio, orientação e supervisão durante todo o processo do meu doutoramento.

Ao Professor Doutor José Grácio, pelo constante incentivo, preocupação e confiança dada durante toda a minha pós-graduação. Foi e, pela sua memória, será alguém a quem muito devo. Nunca me esquecerei de si!

Aos meus colegas e amigos dos departamentos de Engenharia de Materiais e Cerâmica e de Engenharia Mecânica um muito obrigada pela constante boa disposição e bom ambiente proporcionados diariamente. Um agradecimento especial à Ana, à Isabel e ao Yang não só pela vossa amizade, mas também por todo o apoio, ajuda e disponibilidade nas diferentes fases deste período da minha vida.

Ao Professor Doutor Paulo Ferreira (University of Texas at Austin, Austin – Estados Unidos da América) um agradecimento sincero pela amizade, disponibilidade e pela fantástica forma como me recebeu na sua instituição. Uma inspiração profunda.
Ao Doutor Marc Willinger (Fritz Haber Institute - Max-Planck-Gesellschaft, Berlim - Alemanha) eternamente agradecida pela possibilidade de me acolher na sua instituição para a realização de trabalho essencial à investigação agora apresentada.

Gostaria, ainda, de agradecer à Universidade de Aveiro, em especial ao Centro de Tecnologia Mecânica e Automação da Universidade de Aveiro (TEMA), centro em que me encontro associada enquanto aluna de doutoramento, e ao Departamento de Engenharia de Materiais e Cerâmica, pela disponibilização de todos os meios físicos disponíveis para a realização do trabalho de investigação.

À INNOVNANO, um agradecimento sincero e sentido por acreditarem e confiarem em mim, e, ainda, por me darem a oportunidade de fazer parte desta equipa. Aos meus colegas e amigos da INNOVNANO por diariamente me apoiarem e me fazerem crescer. Ao Nuno, um especial obrigada por todos os debates e discussões de ideias e dúvidas, e pela motivação diária para que esta etapa da minha vida fosse ultrapassada.

Aos meus amigos, um especial obrigada pela vossa amizade, presença, paciência, atenção e constante incentivo principalmente nos momentos mais difíceis e de maior nervosismo tão característicos desta pós-graduação.
Vera, Carolina, Andreia, Duarte, Hugo, Tiago, Mariana Botto, Ju e Mi, a vocês, muito obrigada por acreditarem e me fazerem acreditar, dia após dia, que era possível!

Finalmente, um agradecimento muito especial à minha família por estarem sempre presentes e me fazerem crescer.
Isabel e Alexandre não tenho palavras para descrever o quão agradecida estou do vosso apoio, ajuda e amizade. Muito obrigada por tudo!

Ao meu irmão Duarte, sem ti não seria o que sou hoje!

Por último, por serem tão importantes e por ser a eles que dedico o meu doutoramento, queria agradecer aos meus pais. Obrigada pelas incríveis pessoas que são e por todo o esforço e dedicação que mostraram durante a minha formação. Muito obrigada por terem estado sempre do meu lado. Sem vocês, não seria possível!

palavras-chave

Células de combustível, electrólitos, óxidos cerâmicos, aditivos de sinterização condutividade protónica, condutividade iónica, densificação, microestrutura.

resumo

O principal objetivo deste trabalho é o desenvolvimento e processamento de novos materiais cerâmicos protónicos e iónicos para utilizar como eletrólito das células de combustível de óxidos sólidos (PCFCs e SOFCs, respetivamente). Com este estudo pretende-se, então, desenvolver novas formas de processamento e/ou materiais que apresentem características eletroquímicas atrativas, à base de óxidos cerâmicos nanométricos de pós preparados por processos mecanoquímicos.

Existem alguns requisitos que devem ser tidos em conta de forma a garantir a máxima eficiência das PCFCs, destacando-se a elevada condutividade protónica do eletrólito aquando da operação numa gama de temperaturas intermédias, 500-700ºC. Os materiais do tipo “perovskite” foram apresentados como potenciais candidatos a incorporar o eletrólito das PCFCs, sendo o $BaZrO_3$ dopado com 15 mol% de ítrio (BZY) o material base escolhido neste trabalho. Apesar da sua conhecida elevada condutividade protónica, estes materiais apresentam algumas limitações, tais como a fraca sinterabilidade e crescimento de grão. De forma a ultrapassar esta dificuldade, foram adicionadas pequenas quantidades de óxidos de zinco, fósforo e boro que foram estudados como possíveis aditivos de sinterização. A adição de ZnO mostrou melhorias significativas na densificação quando comparado com o material não modificado (BZY), permitindo ainda reduzir a temperatura de sinterização de 1600ºC para 1300ºC. Neste trabalho estudou-se, também, qual o melhor mecanismo de solução sólida para a adição deste aditivo, tendo-se obtido a máxima condutividade protónica nos materiais em que o Zn é intencionalmente introduzido na composição de base de “perovskite”. O P_2O_5 mostrou ser menos efetivo como aditivo de sinterização. A sua presença foi bastante prejudicial no crescimento de grão, apesar dos elevados níveis de densificação obtidos quando adicionado em quantidades entre 4 e 8 mol%. Porém, a utilização de fósforo mostrou também ser dramática no transporte elétrico, diminuindo a condutividade não só no interior do grão (“bulk”) como nas suas fronteiras. Já a adição de H_3BO_3 ao $BaZrO_3$ (BZO) mostrou-se muito efetiva para a sinterização deste componente. Contudo, quando adicionado ao sistema dopado com ítria ($BaZr_{0.85}Y_{0.15}O_{3-\delta}$, BZY), o comportamento é diferente, produzindo níveis deficientes de densificação quando comparado com o BZY puro. Este fenómeno ocorre devido à formação de fases secundárias de borato de bário, cujas temperaturas de fusão são bastante elevadas.

Na última parte deste trabalho foi estudado um novo material com condutividade iónica de iões óxido, o $(Ba,Sr)GeO_3$ dopado com K. Neste estudo pretendia-se, não só avaliar a possibilidade de preparar estes pós com recurso a processos mecanoquímicos, como também estudar o papel da variação do raio iónico do catião metálico alcalino-terroso no transporte iónico, homogeneidade composicional e estrutura cristalina. Verificou-se que este material apresenta uma alteração significativa na condutividade iónica com o aumento da temperatura de operação em ambas as composições (Ba e Sr).

keywords

Fuel cells, electrolytes, ceramic oxides, sintering additives, proton conductivity, ionic conductivity, densification, microstructure.

abstract

The main objective of this dissertation is the development and processing of novel ionic conducting ceramic materials for use as electrolytes in proton or oxide-ion conducting solid oxide fuel cells. The research aims to develop new processing routes and/or materials offering superior electrochemical behavior, based on nanometric ceramic oxide powders prepared by mechanochemical processes.

Protonic ceramic fuel cells (PCFCs) require electrolyte materials with high proton conductivity at intermediate temperatures, 500-700ºC, such as reported for perovskite zirconate oxides containing alkaline earth metal cations. In the current work, $BaZrO_3$ containing 15 mol% of Y (BZY) was chosen as the base material for further study. Despite offering high bulk proton conductivity the widespread application of this material is limited by its poor sinterability and grain growth. Thus, minor additions of oxides of zinc, phosphorous and boron were studied as possible sintering additives. The introduction of ZnO can produce substantially enhanced densification, compared to the un-doped material, lowering the sintering temperature from 1600ºC to 1300ºC. Thus, the current work discusses the best solid solution mechanism to accommodate this sintering additive. Maximum proton conductivity was shown to be obtained in materials where the Zn additive is intentionally adopted into the base perovskite composition. P_2O_5 additions were shown to be less effective as a sintering additive. The presence of P_2O_5 was shown to impair grain growth, despite improving densification of BZY for intermediate concentrations in the range 4 – 8 mol%. Interreaction of BZY with P was also shown to have a highly detrimental effect on its electrical transport properties, decreasing both bulk and grain boundary conductivities. The densification behavior of H_3BO_3 added $BaZrO_3$ (BZO) shows boron to be a very effective sintering aid. Nonetheless, in the yttrium containing analogue, $BaZr_{0.85}Y_{0.15}O_{3-\delta}$ (BZY) the densification behavior with boron additives was shown to be less successful, yielding impaired levels of densification compared to the plain BZY. This phenomenon was shown to be related to the undesirable formation of barium borate compositions of high melting temperatures.

In the last section of the work, the emerging oxide-ion conducting materials, $(Ba,Sr)GeO_3$ doped with K, were studied. Work assessed if these materials could be formed by mechanochemical process and the role of the ionic radius of the alkaline earth metal cation on the crystallographic structure, compositional homogeneity and ionic transport. An abrupt jump in oxide-ion conductivity was shown on increasing operation temperature in both the Sr and Ba analogues.

LIST OF FIGURES

LIST OF TABLES

LIST OF ABBREVIATIONS

AFC	Alkaline Fuel Cell
BZO	Barium Zirconate ($BaZrO_3$)
BZY	15mol% Yttrium-doped Barium Zirconate ($BaZr_{0.85}Y_{0.15}O_{3-\delta}$)
CGO	Gadolinium-doped ceria
CSO	Samarium-doped ceria
DMFC	Direct Methanol Fuel Cell
DSC	Differential Scanning Calorimetry
EDS	Energy Dispersive Spectroscopy
FT-IR	Fourier Transform Infrared Spectroscopy
HTPC	High-temperature Proton Conductor
HTXRD	High Temperature X-ray Diffraction
IT-SOFC	Intermediate Temperature-solid Oxide Fuel Cell
JCPDS	Joint Committee on Powder Diffraction Standards
LSGM	Lanthanum Gallate doped with Strontium and Magnesium
MCFC	Molten Carbonate Fuel Cell
PAFC	Phosphoric Acid Fuel Cell
PCFC	Proton Ceramic Fuel Cell
PEM	Proton Exchange Membrane
PEMFC	Proton Exchange Membrane Fuel Cell
PTC	Positive Temperature Coefficient
SEM	Scanning Electron Microscopy
SOFC	Solid Oxide Fuel Cell
STEM	Scanning Transmission Electron Microscopy
STEM-XEDS	Scanning Transmission Electron Microscopy coupled with X-ray Energy Dispersive Spectroscopy
TEM	Transmission Electron Microscopy
TGA	Thermogravimetric Analysis
TVF	Thermal Vibration Factor
XEDS	X-ray Energy Dispersive Spectroscopy
XRD	X-ray Diffraction
YSZ	Yttria-stabilised Zirconia

LIST OF SYMBOLS

β	Full Width at Half Maximum
β^*	Intregral Breath
δ	Average Grain Boundary Thickness
ε	Average Apparent Diameter (Crystallite Size)
η	Mean Lattice Strain
2θ	X-ray Angle
λ	X-ray Wavelength
ρ	Resistivity
ρ_r	Relative Density
ρ_i	Initial Density
ρ_t	Theoretical Density
σ	Conductivity
σ_{bulk}	Bulk conductivity
σ_{gb}	Uncorrected Grain Boundary Conductivity
σ_{gb}^*	Normalized Grain Boundary Conductivity
$\sigma_{OH_O^{\bullet}}^*$	Protonic Conductivity at $pH_2O = 1$ atm
σ_p^*	Hole Conductivity at $pO_2 = 1$ atm and $pH_2O = 0$ atm
$\sigma_{V_O^{\bullet\bullet}}^*$	Oxide Ion Conductivity when $pH_2O = 0$ atm
σ_{total}	Total conductivity
ΔG	Gibbs Energy
a,b,c	Lattice Parameters
d*	Interplanar Distance
e^-	Electron
$h^{\bullet}$	Electron holes
i	Current
k	Shape Factor
p	Holes
pH_2O	Water Vapour Partial Pressure
pO_2	Oxygen Partial Pressure
r_A	Ionic Radii of the Species of Perovskite at the A-site
r_B	Ionic Radii of the Species of Perovskite at the B-site
r_O	Ionic Radii of Oxygen
t	Goldschmidt Tolerance Factor
v	Voltage
A	Sample Cross Sectional Area
A_0	Pre-exponential Factor
C	Capacitance

C_{gb}	Grain Boundary Capacitance
C_{bulk}	Bulk Capacitance
D	Mean Grain Size
$D\sigma$	Proton Mobility
Ea	Activation Energies
K_h	Equilibrium Constant for the exchange of Oxygen
K_H	Equilibrium Constant for the Exchange of Water (Hydration)
L	Sample Length
M(III)	Trivalent Dopant
$M_B^{/}$	Concentration of a Singly Charged Acceptor Dopant
O_O^x	Lattice Oxygen
$OH_O^{\bullet}$	Positively Charged Protonic Defects
PLC_s	Percentage Linear Change of the Sample in the Axial Direction
PLC_p	Percentage Linear Change of a Pre-densified Sample in the Axial Direction
Q	Pseudo-capacitance
R	Resistance
R_{gb}	Grain Boundary Resistance
T	Temperature
V	Volume
V_M	Molar Volume
$V_O^{\bullet\bullet}$	Oxide Ion Vacancies
W_0	Characteristic Frequency
Y (III)	Trivalent Cation
Z’, Z’’	Impedance Frequencies

TABLE OF CONTENTS

CHAPTER 5. EMERGING MATERIALS: (Ba,Sr)GeO$_3$-BASED ION CONDUCTORS…………… p. 141

CHAPTER 1. INTRODUCTION

Global warming is worsened by the fact that power usage is continuously increasing throughout the world and its generation continues to be heavily dominated by the use of fossil fuels. Energy issues must, therefore, be one of the main topics of discussion in sustainable development. Some potential solutions have been developed in order to get a cleaner energy infrastructure: i) energy conservation through improved energy efficiency, ii) reduction in fossil fuel dependence. These solutions have lead to an increasing role of environmentally friendly energies sources such as water, sun, wind, biomass, geothermal, hydrogen, in the energy mix and the development of more efficient technologies for energy conversion, such as fuel cells [1].

1.1 FUEL CELLS

Fuel cells are one of the key enabling technologies for a future hydrogen economy and a promising substitute for traditional electricity production methods. It is only in the last 20 years that their performance has been confirmed by successful operation in both stationary and mobile electrical power generation systems, combustion engines, portable extension and micro power, despite the fact that the technology was first discovered almost two centuries ago. Although there has been some controversy concerning the authorship in the invention of the fuel cell, several literature sources point to the conclusion that it was Sir William Robert Grove (1839), who introduced the concept of the hydrogen fuel cell. Grove discovered that by immersing two platinum electrodes with one end in a solution of sulphuric acid and the other two ends separately sealed in containers of oxygen and hydrogen, a constant current was found to be flowing between the electrodes. He also noted that sealed containers contained water together with the respective gases and that the water level rose in both tubes as the current flowed. The next step was to realize that by combining pairs of electrodes connected in series a higher voltage could be produced, thus creating what he called a gas battery, i.e. the first fuel cell [1-3].

In 1900, scientists and engineers predicted that fuel cells would be common for producing electricity and motive power within a few years. Nonetheless, their progression to the market has been slow, mainly due to the previous abundance of cheap fossil fuel energy.

Nowadays fuel cells are starting to become an important component in the energy cycle, due to their high conversion efficiencies and the possibility of pollution free electrical power generation. Now that oil is scarce, expensive and subject to political vicissitudes, and the Earth is subjected to potentially severe environmental damage, fuel cells are becoming a serious and credible option to substitute other technologies for the production of electricity [1-3].

There are now many manufacturers working on fuel cell applications of very different nature. For example, there are many uses of fuel cells with direct application in the automotive sector as aircrafts, ships, trains, buses, cars, motorcycles, trucks and forklifts. There are also vending machines, vacuum cleaners machines and traffic signals that operate by fuel cells. At a smaller scale, there is also a growing market for fuel cells for mobile phones, laptops and portable electric devices. While, at larger scale, there are hospitals, police stations and banks that have stationary fuel cell systems for generating electrical power at their facilities. Water treatment plants and waste dumps are beginning to use fuel cells to carry out the process of converting the methane gas produced for electricity generation. As we can see, the number of different applications of fuel cells is very extensive [3].

1.1.1 ADVANTAGES AND LIMITATIONS OF FUEL CELLS

An important number of benefits can be associated with these devices, including environmental advantages and operating costs. Fuel cells have clean emissions (table 1.1), high efficiency (between two or three times more than basic fuel burning generators), high power reliability, multi-fuel capability (allows fuel selection, hydrogen may be extracted from natural gas, propane, butane, methanol and diesel fuel, or these fuels may be reformed internally at the anode), constant power production, high durability and ease of maintenance. As they have a simple design with no moving parts fuel cells can also reduce noise (table 1.2). Their waste heat can be recycled and used to provide hot water or space heating for a home or office and they offer higher power densities than batteries as well as being smaller and lighter and having much longer lifetimes. They also show high energy security (due to a reduced dependence on oil) while their high efficiency can reduce the energy cost, as shown on table 1.3. Overall, it is expected that fuel cells will play an essential role in any future hydrogen fuel economy [1-7].

Table 1.1 –Fuel cell air emissions benefits from one year of operation [1].

Air emissions [a]	**SO_x**	**NO_x**	**CO**	**Particles**	**Organic compounds**	**CO_2**
Fossil fuelled plant	28 000	41 427	28 125	500	468	4 044 000
Fuel cell	0	0	72	0	0	1 860 000

[a] Pounds of emissions per 1 650 MWh from one year full operation

Table 1.2 – Fuel cell's sound operation benefits [1].

Means	Gas-electric	Microturbine	Diesel-electric	Fuel cell	Social conversation
Sound level	high	moderate	high	low	low [a]
Sound proofing	required	required	required	not required	not required

[a] Similar to fuel cell sound level

Table 1.3 – Comparison of fuel cell with other power generating systems: capacity range, efficiency and operating costs [6].

	Reciprocating engine diesel	Turbine generator	Photovoltaic	Wind turbine	Fuel cells
Capacity range	500 kW - 50 MW	500 kW - 5 MW	1 kW - 1 MW	10 kW - 1 MW	200 kW - 2 MW
Efficiency	35%	29-42%	6-19%	25%	40-85%
Capital cost ($/kW)	200-350	450-870	6600	1000	1500 - 3000
Operation & Maintenance cost ($/kW)	0.005 - 0.015	0.005 - 0.0065	0.001 - 0.004	0.01	0.0019 - 0.0153

Despite these advantages, there are some limitations for the progression of fuel cells into the market. In their simplest form they use oxygen and hydrogen as the power supply. Thus, one main limitation comes from the need to source this hydrogen, to store it and to distribute it safely. Although a very large effort is being made to resolve these problems, this work remains in its infancy. It should also be noted that hydrogen is currently, mainly produced by the steam reforming of methane, a fossil fuel, which defeats the environmental benefits and objectives of fuel cell usage. Alternative routes to produce hydrogen, such as electrolysis of water using renewable electricity, solar photolysis or biological dissociation are, therefore, under parallel study. Some fuel cells also have problems with electrolyte management, such as corrosive liquid electrolytes, or high costs due to use expensive catalysts or high hydration requirements of their electrolytes, or suffer from high degradation issues due to high operating temperatures [1]. The life span of fuel cells can be shortened by pulsed demand, impurities in the gas stream, while low power density per volume, poor accessibility and durability are other challenges for fuel cell technology development. Though, great breakthrough is still required, positive progress has been witnessed throughout the recent years [6].

1.1.2 WORKING PRINCIPLE OF FUEL CELLS

A fuel cell is an energy conversion device that generates electricity and heat by an electrochemically reaction that is spontaneous. It occurs between a gaseous fuel (hydrogen) and an oxidant gas (oxygen from the air) through an ion conducting electrolyte (eq. 1.1). During this process, water and heat are formed at the exhaust. Fuel cells are often compared to batteries as both have the same work purpose, i.e., both convert the energy produced by a chemical reaction into usable electric power. Nonetheless, in a battery this chemical reaction is internally provided and cycled, while in a fuel cell the reaction will continue to generate power, as long as an external fuel is supplied. In other words, it does not run down or require any recharging [1-8].

$$H_{2\,(g)} + \frac{1}{2}O_{2\,(g)} \rightarrow H_2O + energy \qquad (1.1)$$

Its ability to convert chemical energy directly to electrical energy gives much higher conversion efficiency than that obtainable by a conventional thermo-mechanical system due to the fact that a fuel cell is not subject to the Carnot limitation, allowing more electricity to be extracted from the same amount of fuel. [1,2,5].

A fuel cell has four main parts: two electrodes (the anode and the cathode), the catalysts, and an electrolyte. The two electrodes are sandwiched around the electrolyte. A combustible fuel such as hydrogen is fed over the anode, while oxygen, normally in the form of air, passes over the cathode. For an oxide-ion conducting fuel cell, oxygen atoms are reduced on the porous cathode surface by electrons. The formed oxide ions diffuse through the electrolyte to the fuel rich and porous anode, where they react with the fuel (hydrogen) and return the electrons to an external circuit. Pure water and a large amount of heat are produced by the electrochemical reaction [1,2,5,6].

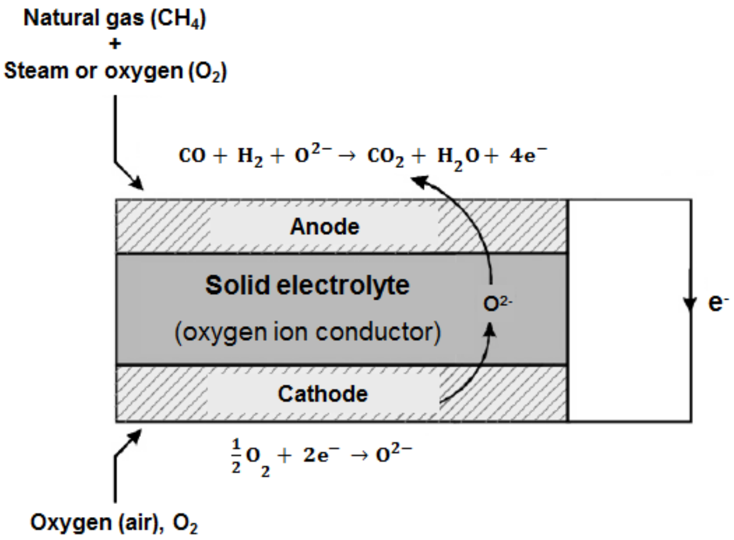

Fig. 1.1 – Schematic configuration of a fuel cell (adapted from [2]).

The electrodes are required to bring about the necessary charge transfer reactions, cycling the electronic charge and delivering or removing the charge carrying ionic species to or from the electrolyte without themselves being consumed or corroded. For the progression of these charge transfer reactions three phases must be brought into contact: the gaseous phase, the liquid/solid electrolyte and the electronically conducting phase (the electrode itself). The anode disperses the hydrogen gas equally over the whole surface of the catalyst and conducts the electrons to be used as a useful power in an external circuit (eq. 1.2). The cathode distributes the oxygen fed to it onto the surface of the catalyst and conducts the electrons back from the external circuit where they can recombine to form oxide-ions, pass across the electrolyte, and further combine with hydrogen to form water (eq. 1.3). The electrolyte works as a barrier to gas diffusion, but permits ions to migrate across it. The catalysts are used to facilitate these charge transfer reactions and their type is dependent of the type of fuel cell and the operating temperature. [1,2,6,7].

For the oxide-ion conducting fuel cell described the fuel cell reactions can be summarized as:

$$Anode:\ H_2 + O^{2-} \rightarrow H_2O + 2e^- \tag{1.2}$$

$$Cathode:\ \frac{1}{2}O_2 + 2e^- \rightarrow O^{2-} \tag{1.3}$$

1.1.3 TYPES OF FUEL CELLS

Fuel cells are a family of technologies. There is a range of designs available for fuel cells; however, they all operate with the same basic principles. The main difference in various fuel cell designs is the chemical characteristics of the electrolyte, which may be either liquid or solid, and the type of mobile ionic species. Because ion conduction is a thermally activated process and its magnitude varies dramatically from one material to the next, the nature of the electrolyte determines the operating temperature of the fuel cell. Table 1.4 shows the most important types of fuel cells and their operating characteristics [1,2,6-8].

Table 1.4 – Technical characteristics of different fuel cells [1].

Fuel Cell Types	**Electrolyte**	**Operating Temperature (ºC)**	**Fuel**
Alkaline (AFC)	Potassium hydroxide (KOH)	50-200	Pure hydrogen, or hydrazine
Phosphoric Acid (PAFC)	Phosphoric acid	160-210	Hydrogen from hydrocarbons and alcohol
Solid Oxide (SOFC)	Stabilised zirconia and Doped perovskite	600-1000	Natural gas or propane
Molten Carbonate (MCFC)	Molten salt (nitrates, sulphates, carbonates, …)	630-650	Hydrogen, carbon monoxide, natural gas, propane, marine diesel
Proton-exchange Membrane (PEMFC)	Polymer, proton Exchange membrane	50-80	Less pure hydrogen from hydrocarbons or methanol
Direct Methanol (DMFC)	Polymer	60-200	Liquid methanol

The most obvious differences between the fuel cells is in their specific operating temperatures. Molten Carbonate (MCFC) and Solid Oxide Fuel Cells (SOFCs) have higher operating temperatures (650ºC and 600-1000ºC, respectively), compared to the much lower operating temperature of around 100ºC and 200ºC for Alkaline (AFC) and PEM Fuel Cells and phosphoric acid fuel cells (PAFC), respectively [1,2]. Such higher temperatures open the possibility of alternative fuel usage in these fuel cell types.

Fig. 1.2 compares the maximum operating temperature of fuel cells *vs* output power. For reasons of electrode activity (which can be described into higher efficiency and greater fuel flexibility), higher temperature of operation is preferred (higher output power can be achieved at higher operating temperature due to lower internal resistances). But for portable (intermittent) power applications, lower temperature operation is typically favoured as it enables rapid start-up as well as minimizes stresses due to thermal cycling [6,7].

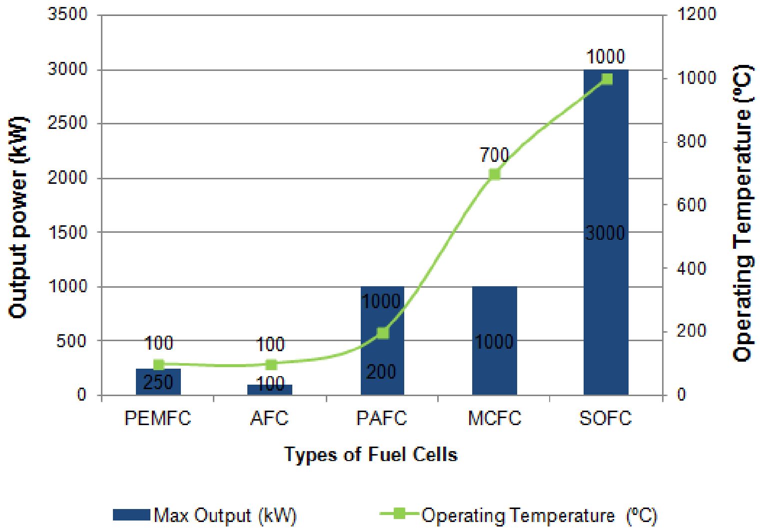

Fig. 1.2 – Comparison of maximum operating temperature of fuel cell vs. output power [6].

Fig. 1.3 demonstrates the electric efficiencies and combined heat and power (CHP) efficiencies of various fuel cells [6].

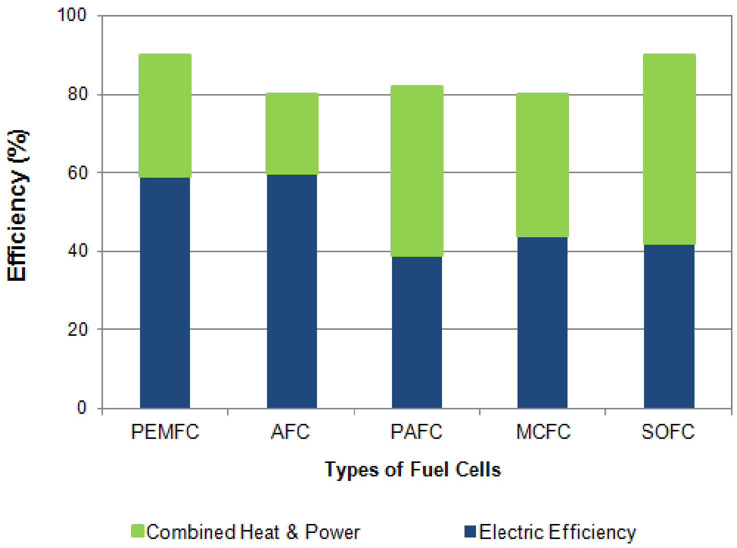

Fig. 1.3 – Efficiency of different fuel cell types [6].

Alkaline is the most electrically efficient (60%) fuel cell type, followed by polymer electrolyte membrane (58%) and molten carbonate (47%). While AFCs are the most efficient, the PEMFC is ideal for transportation applications like automotives and buses due to its lower operation temperature. PAFC is economically efficient; however, they suffer from low electrical efficiency. Due to their higher temperatures of operation, molten carbonate (MCFC) and solid oxide fuel cells

(SOFC) offer high combined heat and power efficiency and have their greatest applicability in stationary power generation [6,7].

The number of different applications of fuel cells is very extensive and should be adapted according to fuel cell type [1-6]. With various types of fuel cell technologies available, it is necessary to clarify which technology is best suited to a specific application. Fuel cells can produce a wide range of power from 1 to 10 MW; hence they can be employed in almost any application that needs power from small range power devices as mobile phones or laptops, to the large range power applications for generating electrical power at hospitals or banks [3,6].

1.2 CERAMIC OXIDE FUEL CELLS

The ceramic fuel cell differs from the other type of fuel cells in the type of the electrolyte. It is an all solid-state energy conversion device that produces electricity by electrochemically combining the fuel and the oxidant across an ionic conducting ceramic which can be an oxide-ion conductor or a proton conductor. However, their operation temperature requirements are at the upper end of the temperature scale, normally over 600ºC [9].

This choice of the type of electrolyte leads to two classifications: hydrogen-ion (proton) conducting fuel cell (designated as Protonic Ceramic Fuel Cell) or oxide-ion conducting fuel cells (traditionally referred to as Solid Oxide Fuel Cells). Despite the fact that the electrolyte in a PCFC is also often formed from a solid oxide material, such as the perovskite materials, this separation in nomenclature between PCFC and SOFC is now widely established based on their different conducting ionic species. The major operational difference between the two types of fuel cell is the side in which water is produced, the oxidant side in PCFCs and the fuel side in SOFCs. Furthermore, certain gases (e.g., carbon monoxide) can be used as fuel in oxide-ion conducting fuel cells but cannot be electrochemically oxidised in proton conducting fuel cells [9].

1.2.1 PROTONIC CERAMIC FUEL CELLS (PCFC)

The Protonic Ceramic Fuel Cell (PCFC) has the highest theoretical efficiency among the fuel cells, when using hydrogen as fuel, due to the possibility of operation close to 100% fuel utilization (fig. 1.5). It is based on a proton (hydrogen ion) conductor, especially perovskite oxides that have been found to exhibit appreciably high proton conduction in hydrogen-containing atmospheres (*i.e.*, H_2 or water vapour atmospheres) at elevated temperatures (600ºC to 800ºC). The most common high-temperature proton conductors are acceptor doped Ba and Sr based perovskites, such as Y, Yb, Gd-doped $BaCeO_3$, $SrCeO_3$ or $BaZrO_3$ [9,10].

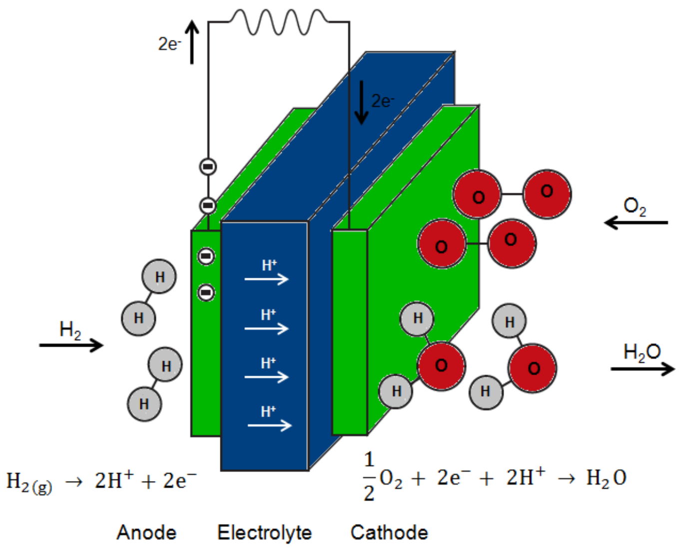

Fig. 1.4 – Typical schematic configuration of the operating principles of a Proton Ceramic Fuel Cell – PCFC (adapted from [11]).

The main benefit of a PCFC (equations 1.4 and 1.5) as opposed to an oxide-ion conducting fuel cell (SOFC) (equations 1.2, 1.3) is that they form product water at the cathode where it does not dilute the fuel; thus allowing for more complete fuel utilization [7,9,10].

$$Anode: \quad H_{2(g)} \rightarrow 2H^+ + 2e^- \tag{1.4}$$

$$Cathode: \quad \frac{1}{2}O_{2(g)} + 2H^+ + 2e^- \rightarrow H_2O \tag{1.5}$$

Although this limitation of fuel utilization is a serious drawback for the maximum efficiency of a SOFC, the SOFC offers advantages towards direct internal steam reforming when hydrocarbons are used as the fuel, due to the ability to oxidise the formed carbon monoxide by-product. In contrast, if a PCFC operates with hydrocarbon fuels, reforming either needs to be accomplished before reaching the anode side, with separation of formed hydrogen, or, alternatively, water or another oxidant must be added to the natural gas fuel to enable complete fuel oxidation [7,9,10].

Nonetheless, a further option for direct hydrocarbon fuel utilization in PCFCs is that of dehydrogenation reactions. For example, methane dehydrogenation in dry conditions can allow the production of hydrogen and valuable high-molecular hydrocarbons without H_2O, CO and CO_2 generation (equation 1.6 and 1.7) [7,9,10].

$$2CH_4 \rightarrow C_2H_4 + 2H_2 \tag{1.6}$$

$$2CH_4 \rightarrow C_2H_6 + H_2 \tag{1.7}$$

However, work on PCFCs remains in its infancy, with many studies still being performed in order to clarify the basic conduction mechanisms and to optimize the electrolyte materials. Nonetheless, small laboratory-scale single cells have now been produced and show promising behaviour in the intermediate temperature range (600-800ºC) [12].

1.2.2 SOLID OXIDE FUEL CELLS (SOFC)

A more mature alternative to PCFC is that of fuel cells containing an oxide-ion conducting electrolyte (fig. 1.5). In this case, the category is called Solid Oxide Fuel Cells (SOFCs) which traditionally have been operated at high temperatures (800 – 1000ºC). These fuel cells have shown tremendous reliability when operated continuously, with good fuel flexibility allowing a variety of hydrocarbon fuels to be utilized. Nonetheless, they have been shown to be costly for widespread commercialization, with poor stability under intermittent operation and necessitating expensive materials for their fabrication in order to survive their high temperature of operation (e.g., high temperatures preclude the use of metals as interconnect materials, which typically have lower fabrication costs compared to ceramics) [1,2,5-8,13,14].

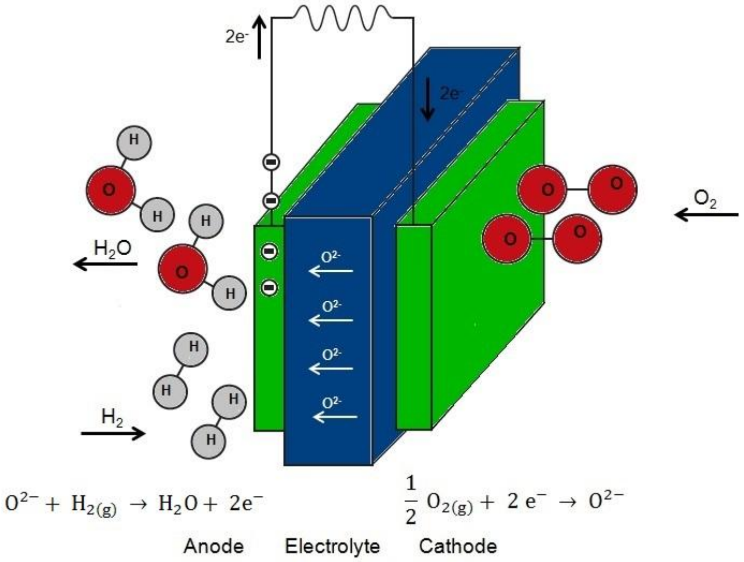

Fig. 1.5 – Typical schematic configuration of the operating principles of a Solid Oxide Fuel Cell – SOFC (adapted from [11]).

When the solid ceramic electrolyte is an oxide-ion conductor, SOFCs can use a fuel mixture of hydrogen and carbon monoxide (formed by internally reforming hydrocarbon fuel) that is fully electrochemically combusted with air as the oxidant. SOFCs operate traditionally above 800ºC where oxygen reduction and dissociation occurs at the cathode, while fuel oxidation happens at the anode. The oxide-ions migrate through the electrolyte to the anode and react with hydrogen to form water (equations 1.2 and 1.3). The anode should be porous to conduct fuel in the gaseous phase and to transport the gaseous products of fuel oxidation away from the electrolyte and fuel electrode interfaces [6,7].

The electrolyte has a large impact on the fuel cell performance and, plays a key role in determining the operating conditions as it is responsible for the solid state transport of the oxide-ion from cathode to anode. In order to get an optimum fuel cell performance, the electrolyte material must have a fully dense structure to prevent reactant cross-over and offer a high ionic conductivity (typically, larger than 10^{-2} S/cm) at the required operating temperature with negligible electronic conductivity.

The most widespread oxide-ion conducting SOFC systems have employed an yttria-stabilised zirconia (YSZ) electrolyte. This material not only show good oxide-ion conductivity but also exhibits desirable stability in both oxidising and reducing atmospheres. They offer good stability towards other components used in the cell and are abundant. However, their high operating temperatures (above 800ºC) to achieve sufficient oxide-ion conductivity will increase not only the cost, but also the instability issues in terms of mechanical and chemical compatibilities between the SOFC constituents. These elevated temperatures gives a strong motivation to identify an oxide-ion conducting electrolyte that can operate at intermediate temperatures in the range 600ºC – 800ºC, with a ionic conductivity, σ_o, ~ 10^{-2} $S.cm^{-1}$ [2,7,9,10], which will be discussed in the later section 1.3.

Two possible design configurations for SOFCs have emerged, which can also be adopted for PCFCs: a planar design (fig. 1.6(a)) and tubular design. (fig. 1.6(b)). The planar design has the components assembled in flat stacks, where the air and fuel flow through channels built into interconnects separating the cathode and the anode of neighbouring cells. On the other hand, in the tubular design the components are assembled in the form of a hollow tube, with the cell constructed in layers around a tubular cathode. In this configuration, air flows through the inside of the tube and fuel flows around the exterior [9,15,16].

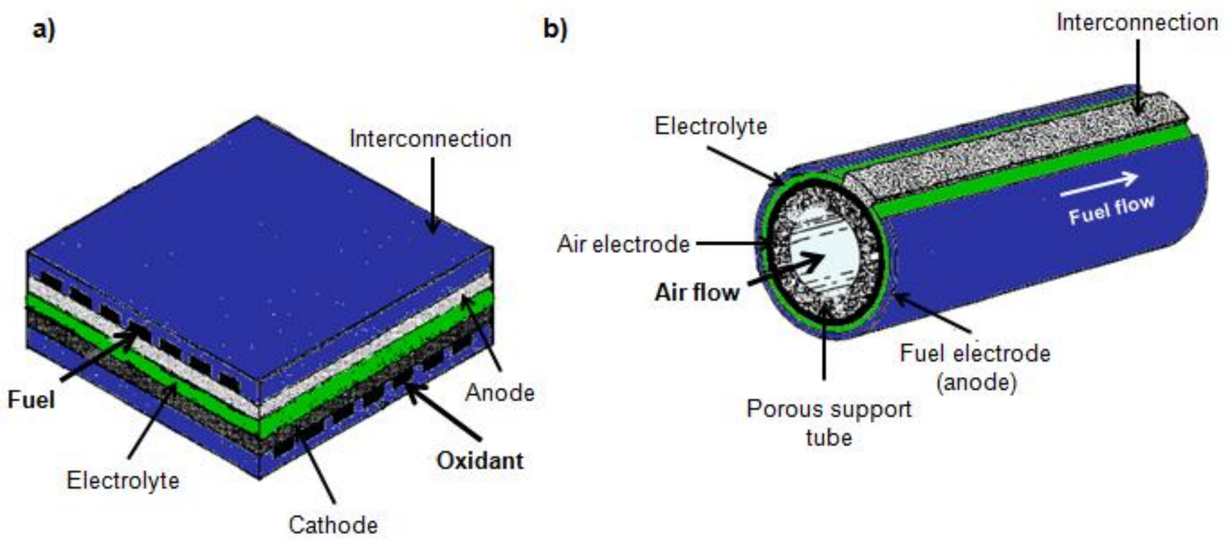

Fig. 1.6 – Design configuration of solid oxide fuel cells: a) flat plate – planar design and b) tubular design of SOFC (adapted from [9]).

The planar-type design is widely chosen because it has low fabrication costs and high power density. Its performance is a crucial point once it offers a greater contact area for the current-collectors. Nonetheless, the tubular design offers a greater mechanical stability [17].

Each component in the fuel cell has more than one function and, thus, must follow strict requirements. All components (cathode, anode, electrolytes and interconnects) must be chemical and physically stable in their appropriate chemical environments as well as resisting chemical interactions between cell components and being morphologically stable, i.e., the chemical expansion and degradation of components in their working environments should be controlled and each component must have similar thermal expansion behaviour in order to minimize thermal stresses that may causes cracking or delamination during fabrication and operation [2,4,10,13,15].

Multiple cells are connected in series to produce larger quantities of power by interconnects, which are usually electronically conducting ceramic or metallic materials depending on operating temperature [2,4,13-15].

1.2.3 ADVANTAGES AND LIMITATIONS OF CERAMIC OXIDE FUEL CELLS

Ceramic fuel cells can be simpler and more efficient than many other technologies with several advantages offered over competing fuel cell types: the use of non-precious catalyst materials, no liquids involved in the fuel cell and an invariant electrolyte. The use of a solid electrolyte reduces the problems associated with material corrosion and electrolyte management issues. Additionally, as all the components are solid, ceramic fuel cells can be fabricated in very thin layers and cell components can be configured into unique shapes that are unachievable in fuel cell systems having a liquid electrolyte. This feature allows various cell designs that can be tailored to distinct applications [9].

The high operating temperatures (above 600ºC) that SOFCs and/or PCFCs typically require allows internal reforming and promotes reaction kinetics, offering distinct financial savings due to the ability to operate without precious metal catalysts. Such fuel cells also produce high quality by-product heat for cogeneration or for use in a bottoming cycle. The formed heat can be used to drive a turbine to produce more electricity and increase the system efficiency to significantly higher values than can be accomplished by any conventional electricity generation method or low temperature fuel cell. The tolerance of anode catalysts to impurities in the fuel such as carbon monoxide and variations in the fuel composition are further potential advantages of SOFCs over the other types of fuel cells [1,2,5,6,8,9,13,14].

Nonetheless, their elevated operation temperatures have also some negative consequences. They are responsible for an increase in costs, particularly those related to interconnects, manifolding and sealing materials and can also adversely impact fuel cell lifetimes due to temperature related materials degradation issues [2]. Thus, various approaches for the reduction of the operation temperature have been proposed to overcome these difficulties. Systems that can operate at temperatures below 800ºC have been studied where low ohmic losses are maintained by the adoption of thin film electrolytes or the adoption of alternative electrolyte materials offering higher ionic conductivities at these temperatures, such as doped cerias, $LaGaO_3$ based phases or protonic conducting phases [11,16,18,19], which will be discussed in the later section 1.3.

Despite the apparent simplicity of the electrode processes, proper electrode performance is still one of the main hurdles for SOFC, especially at reduced operation temperatures. Although, high temperature is advantageous when it comes to the kinetics of electrode processes, such temperatures place high demands on the mechanical and chemical stability of the materials in the fuel cell assembly. Although many of these stability issues may be resolved by cell operation at intermediate temperatures, the resultant slower electrode kinetics at these lower temperatures leads to impaired electrical efficiencies due to an increase in electrode polarization losses. Thus, to combat this performance decrease, extensive research effort has been focused in the pursuit of alternative electrode materials that maintain low polarization resistances at intermediate temperatures [20,21].

The advantageous possibility to use metallic interconnects at intermediate temperatures, to reduce costs, is still dependent on the ability to offer good corrosion resistance, both tolerating oxidizing and reducing conditions without substantial degradation. This factor limits the potential choice of alloys to those that combine formation of slow growing electrical conducting oxide scales with slow creep rates [10].

For PCFCs with alkaline earth containing perovskite electrolytes the main degradation issues have been those related to the basic nature of the electrolyte material and subsequent reaction with CO_2

and high water vapour partial pressures. Several of these materials are thermodynamically unstable at intermediate temperatures even at the low partial pressures of carbon dioxide present in air. In addition, large grain boundary resistances are shown to be an obstacle, especially for $BaZrO_3$ based electrolytes. On the other hand, for alternative non-perovskite oxides the challenge has been their much lower ionic conductivity. This limitation could be solved by thinner electrolytes, nonetheless, such thicknesses may be vulnerable to mechanical stresses [10,22-25].

1.3 CERAMIC OXIDE SOLID ELECTROLYTES

The most important property of a candidate electrolyte material is the level of ionic conductivity which should ideally be greater than 10^{-2} Scm^{-1}, at the working temperature. An ideal electrolyte is the conductor of a single mobile ionic species and an electronic insulator. Electrolytes can have different natures: liquid, polymer, glass, or ceramic, and the choice between them depend on the nature of the reactants. Moreover, the type of conduction of the fuel cell will be dependent on the type of the electrolyte selected. Where the ionic conduction is protonic in nature, for example, in fuel cells such as PEM or PCFCs, these fuel cells offer the benefits of generating the by-product H_2O at the cathode, where the fuel does not become diluted as a function of utilization. For PEM fuel cells protonic conduction is provided by a hydronium ion conducting electrolyte that requires careful water management to maintain the high water vapour partial pressures required for the existence of this species. In comparison, water management is simplified in PCFC due to the necessity of a significantly lower level of pH_2O for full hydration of the protonic ceramic electrolyte. Ceramic solid electrolytes are used in electrochemical cells having gaseous or liquid reactants which can operate in an operate-circuit mode such as the oxygen sensors, or in a power application as in an oxygen pump or a SOFC [26]. Such solid electrolytes are typically ionically conducting oxides in the form of membranes that should be dense enough to be impermeable to gases while being thin enough to minimize ohmic losses. A demanding set of properties are, therefore, required for potential electrolyte materials that include: the level of conductivity as well as chemical stability under redox conditions, chemical inertness with anode and cathode materials; and stable microstructures and mechanical properties. Because the electrolyte is a solid in a ceramic fuel cell, the cells do not have to be constructed in the plate-like configuration typical of other fuel cell types [7,26-28].

In the case of PCFCs, the main open challenge is to develop a proton-conducting electrolyte material that currently satisfies two of the essential requirements: high proton conductivity and good chemical stability. In order to achieve these needs, perovskite-type oxides, such as acceptor doped Ba and Sr-based perovskites have been presented as the main materials [23]. The state of the art concerning these materials is discussed in detail in the following section 1.3.1.

In contrast, the classic oxide-ion conductors have an oxygen-deficient fluorite (Sc and Y-stabilized zirconia or Sm- and Gd-doped ceria) or perovskite (Sr- and Mg-doped $LaGaO_3$) structure with oxygen transport via oxygen vacancies. Additionally, oxide-ion transport in apatites, scheelite, Ruddlesden-Popper, and mayenite structures have also been suggested, for use as electrolytes in SOFC. However, these alternative electrolyte structures typically show promising performance only at elevated temperatures (≥ 800ºC). Thus,suitable solutions are still highly desired to find other ceramic materials that can show high oxygen ionic conductivity under lower temperatures (<800ºC) [7,29,30]. Recently, a new family of superior solid oxide-ion conductors have been identified exhibiting acceptable oxide-ion conductivity due to the presence of either a terminal oxygen vacancy or an interstitial oxide-ion. These materials consist of a 2D layered structure with generic formula $Sr_{3-x}A_xM_3O_{9-0.5x}$, where A = Na or K and M = Si or Ge and have been identified as a promising electrolyte for intermediate temperature-solid oxide fuel cells (IT-SOFC) [30-33]. The status of these novel oxide-ion electrolytes is discussed in further detail in the following section 1.3.2.

1.3.1 PEROVSKITE-TYPE PROTON CONDUCTORS

Perovskite-type proton conductors have been studied as electrolyte materials for PCFCs due to their lower activation energy for proton migration that enables higher levels of ionic conductivity to be obtained at lower temperatures than in typical oxide-ion conductors [19,34].

Perovskite was the name used to describe the rare mineral calcium titanium oxide with the composition $CaTiO_3$. From this origin, the term perovskite is now commonly employed to name a wide range of materials of the same structure type. It has a general stoichiometry ABO_3, which “A” and “B” are cations. It can be synthesized with a wide variety of combinations of chemical elements, on the general basis that cations of large ionic radii will assume an A-site location while smaller cations will be accommodated on the B-site. In addition the structure is highly tolerant to vacancy formation [18,34].

It can accommodate most of the metallic ions in the periodic table with a significant number of different anions: The A-site can be filled either by cations A^{+} (Na, K), A^{2+} (Ca, Sr, Ba) or A^{3+} (Fe, La, Gd); and the B-site can be occupied either by B^{5+} (Nb, W), B^{4+} (Ce, Zr, Ti) or B^{3+} (Mn, Fe, Co, Ga). This flexibility of the structure to accommodate a wide range of cations results in a number of properties, ranging from insulating, semiconducting, superconducting and the most important one and the motivation of the present work, ionically conducting. Due to their diverse physical/chemical properties over wide temperature ranges. Perovskite ceramics can offer ferroelectric and/or piezoelectric properties, such as $BaTiO_3$ and $Pb(ZrTi)O_3$ which play a dominant role in the electroceramics industry. Further industries have shown special interest in r perovskites, like $(SrCaLa)MnO_3$ as colossal magnetoresistance, $BaTiO_3$ as PTC thermistor, or $Li_{0.5-x}La_xTiO_2$ as battery materials. Table 1.5 lists the properties and applications of some commonly studied perovskites [11,27,34].

Table 1.5 – Properties and applications of perovskites [11].

Property	**Application**	**Material**
Proton conductivity	SOFC electrolyte Hydrogen sensor H_2 production / extraction	$BaCeO_3$, $SrCeO_3$, $BaZrO_3$
Ionic conductivity	Solid electrolyte	$(La,Sr)(Ga,Mg)O_{3-\delta}$
Mixed conductivity	SOFC electrode	$La(Sr,Ca)MnO_{3-\delta}$, $LaCoO_3$, $(La,Sr)(Co,Fe)O_{3-\delta}$
Ferroelectric / Piezoelectric	Piezoelectric transducer Thermistor actuator	$BaTiO_3$, $Pb(Zr,Ti)O_3$, $Pb(Mg,Nb)O_3$
Catalytic	Catalyst	$LaFeO_3$, $La(Ce,Co)O_3$
Electrical / Dielectric	Multilayer capacitor Dielectric ressonator Thin film resistor	$BaTiO_3$, $BaZrO_3$
Magnetic	Magnetic memory Ferromagnetism	$GdFeO_3$, $LaMnO_3$
Optical	Electrooptical modulator	$(Pb,La)(Zr,Ti)O_3$
	Laser	$YAlO_3$, $KNbO_3$
Superconductivity	Superconductor	$Ba(Pb,Bi)O_3$, $BaKBiO_3$

The structure of an ideal cubic perovskite is illustrated in fig. 1.7, where the A-site is occupied by a cation that generally has a larger ionic radius than the B-cation and presents a +2 valence. The A-site cation is located in the corners of the unit cell (0, 0, 0), while the B-site cation is usually a transition metal or a rare earth which has a +4 valence and forms a six-coordinated octahedron with its neighbouring oxygen ions, being itself located in the center (½, ½, ½). Finally, the oxygen atoms are located at the center of each face of the unit cell (0, ½, ½). The cubic perovskite has the Pm-3m (221) space group. However, this structure is seldom attained at ambient conditions of temperature and pressure due to differences among the A, B and O ionic radii [11,35].

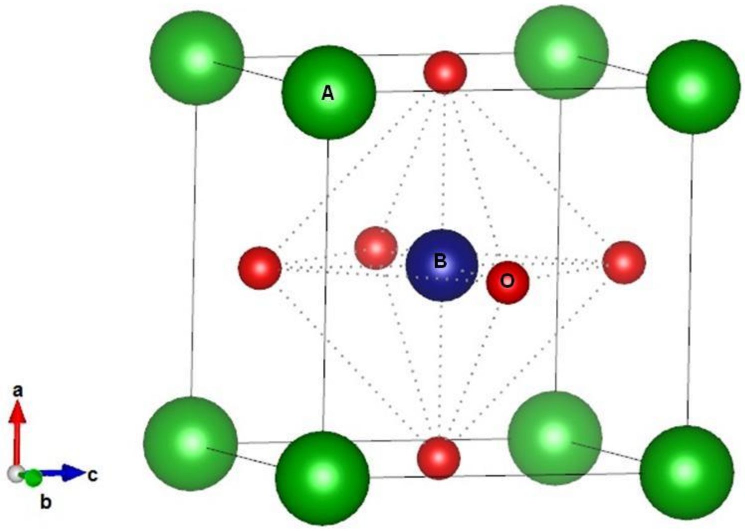

Fig. 1.7 – Schematic representation of the ideal perovskite structure, ABO_3 (adapted from [23]).

The mechanism of proton conduction in the material of perovskite-type structure is defined by the formation of proton defects, *i.e.*, formation of hydroxyl groups. Mobile protons can be incorporated in the perovskite structure as hydroxide defects which can be formed by the presence of water vapour (equation 1.8), where a H_2O molecule fills an oxide-ion vacancy, forming two hydroxyl groups by combination with a lattice oxygen, and/or in hydrogen containing atmospheres (equation 1.9) [11,23,29,36,37].

$$H_2O + O_O^x + V_O^{\bullet\bullet} \rightarrow 2OH_O^{\bullet} \tag{1.8}$$

$$H_2 + 2O_O^x \rightarrow 2OH_O^{\bullet} + 2e' \tag{1.9}$$

Proton incorporation can also occur by the consumption of positively charged holes in humid atmospheres according to the following reaction [23]:

$$H_2O + 2h^{\bullet} + 2O_O^x \rightarrow 2OH_O^{\bullet} + \frac{1}{2}O_2 \tag{1.10}$$

The proton transport mechanism can be described by two main mechanisms: the simplest one where the proton transfers by the diffusion of hydroxyl ions as a whole, leading to the diffusivity of OH^-, or a more complex mechanism denominated as the Grotthuss mechanism (represented in figure 1.8), where the proton transfers between fixed oxygen sites. The existence of the Grotthuss mechanism was considered a controversial diffusion mechanism for a long time but these days has become the generally accepted process for ionic motion in solid state proton conductors. It can be explained by a combination between a molecular reorientation around the oxygen and jump of the proton from oxygen to nearest neighbour ion. This process has been highlighted as the active process for ionic migration typically occurring in solid acid salts (CsH_2PO_4) and perovskites [11,38,39].

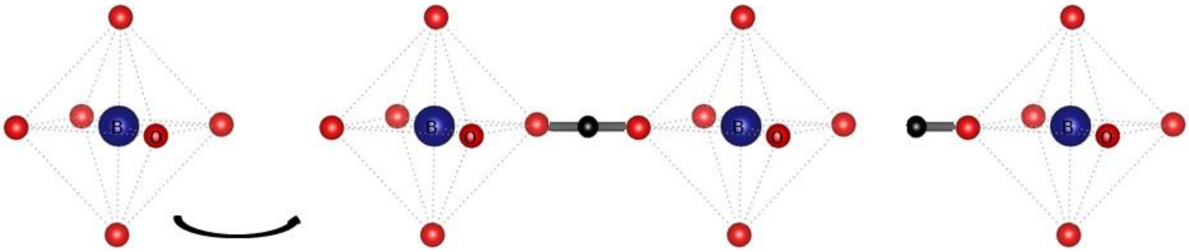

Fig. 1.8 – Schematic representation of the Grotthuss mechanism for proton transport in $BaZrO_3$ (adapted from [11]).

According to equation (1.8), it becomes clear that to generate protonic conductivity in the material of ABO_3 structure, the existence of oxide-ion vacancies is crucial [11,23,29,36,37]. These vacancies may be formed intrinsically by varying the ratio of the main constituents, or extrinsically to compensate an acceptor dopant. As an example, partial substitution of the B-site cation of the perovskite with a trivalent dopant M(III) would result in the creation of oxygen vacancies to achieve charge balance (equation 1.11). In this case the perovskite would assume the formula $AB_{1-x}M_xO_{3-\delta}$ [23].

$$2B_B^x + O_O^x + M_2O_3 \rightarrow 2M_B' + V_O^{\bullet\bullet} + 2BO_2 \tag{1.11}$$

In this case, the relation between dopant and oxygen vacancy concentration would be given by [23]:

$$[V_{\ddot{O}}] = \frac{1}{2}\,[M(III)] \tag{1.12}$$

However, the actual defect chemistry of doped ABO_3 perovskite structures can be complicated due to the possibility of partial substitution of the M dopant cation into the A-site instead of the B-site where oxygen vacancies would be consumed instead of being created. Many works were done on barium cerates to assess possible A-site substitution and preferential A-site substitution was shown for dopant cations of large ionic radius [40-43].

Additionally, lattice distortions can influence the conducting properties due to increasing the energy required for protonic migration. This implies that the choice of the dopant cations with respect to respective ionic radius and their dopant concentration can in general have a strong impact on the electrical performance. The extent of distortion of a perovskite structure from the ideal cubic structure can be described by the Goldschmidt tolerance factor [23].

In the early 1920s, Goldschmidt [44] proposed a tolerance factor (t) to study the stability of perovskites. Goldschmidt's tolerance factor (t), equation 1.13, is used to describe the distortion of the perovskite and the likelihood of perovskite formation. The tolerance factor is based on the geometrical packing of charge spheres.

$$t = \frac{(r_A + r_O)}{\sqrt{2}\,(r_B + r_O)} \tag{1.13}$$

"t" is determined by taking into account the ionic radii of the species A, B and O. For the ideal packed perovskite structure, which has a simple cubic structure, the tolerance factor presents a value t = 1. When distortions from the ideal configuration are present, "t" can assume different values: "t" values of most perovskites are in the range 0.75 - 1.0, resulting in different crystallographic systems such as orthorhombic, rhombohedral or tetragonal. A decrease in tolerance factor usually predicts a lower symmetry. Bhide *et al.* [45], also point out that the stability of perovskites (ABO_3) increases with increasing perovskite tolerance factor. In other words, this means that upon distortion from the cubic structure, due to increasing mismatch in the A-O and B-O bond lengths, the stability of the perovskite will decrease.

According to what was described, the lattice distortions are then responsible for the position of the oxygen sites and consequently may affect the mobility of oxygen vacancies.

Although, the tolerance factor is a useful guideline it is not the only condition that is required for the formation of the perovskite structure. It should be coupled with the octahedral factor, which is defined by r_B/r_O. In order to have perovskite formation, the octahedral factor should be higher than 0.425 [11,35,44].

In the early 1980s, Iwahara *et al.* [46] found several perovskite-type oxides that exhibit high proton conductivity at elevated temperatures. The most extensively studied are doped $SrCeO_3$, $BaCeO_3$, $BaZrO_3$ and $SrZrO_3$. The Ba-perovskites ($BaCeO_3$, $BaZrO_3$) have shown the most interesting proton conductivity properties duea combination of their high cell symmetry, their basicity and their ability to retain protonic species to high temperatures [23].

Sr-based compounds reveal larger lattice distortions due to the smaller ionic radius of Sr^{2+} (0.126 nm in eight-fold coordination) compared with Ba^{2+} (0.142 nm in eight-fold coordination). The larger distortions and the presence of two oxygen sites with different symmetry are probably the reasons why Sr-based perovskite oxides display high proton transport numbers, but smaller proton solubility and larger activation energy for proton transport with respect to the Ba-based perovskite oxide compounds [23].

$BaCeO_3$-based materials show high performance in terms of proton conductivity (equal or larger than 10^{-2} S/cm at 600ºC) that exceed that of some of the best oxide-ion conductors in the intermediate temperatures range due to a lower activation energy for ionic migration in the proton-conducting case. Thus a motivation to study this type of material in fuel cells is the possibility to decrease the operation temperature (500 - 700ºC), relatively to the high temperature solid oxide fuel cells based on oxide-ion conductors (800 - 1000ºC). This would give advantages with respect to cost, balance of plant and cell longevity. However, the most severe problem regarding barium cerates is their low chemical stability. It has been shown that they react with acidic gases, such as CO_2, and with water vapour to form carbonates and hydroxides, respectively (equations 1.14 and 1.15). Since the use of hydrocarbon fuels (i.e., methane) can lead to the production of CO_2 and H_2O, their chemical instability precludes their use with such fuels. On the other hand, their reactivity in the presence of water vapour also represents a harsh drawback since high water vapour partial pressures may be generated at the cathode during fuel cell operation [18,19,23].

$$BaCeO_3 + CO_2 \rightarrow BaCO_3 + CeO_2 \tag{1.14}$$

$$BaCeO_3 + H_2O \rightarrow Ba(OH)_2 + CeO_2 \tag{1.15}$$

In contrast to the cerate-based proton conductors, $BaZrO_3$-based oxides exhibit not only cubic symmetry, in agreement with their high tolerance factor (close to unity), but also superior stabilities in steam or CO_2 containing atmospheres that are advantageous for cell longevity. The cubic nature of their symmetry is also beneficial for ionic mobility, giving these materials attractive bulk conduction properties [11,18,19,23,47].

For the perovskite to be stable, the Gibbs energy of its formation must be lower than both the formation energy of the hydroxide and carbonate. Figure 1.9 shows the Gibbs energy of formation of barium hydroxide, barium carbonate and the formation of the perovskite oxides. $BaCeO_3$ exhibits relatively high formation energy compared to $BaZrO_3$ which demonstrates stability against hydroxide formation at all given partial pressures and temperatures. Although decomposition reactions of barium zirconate are thermodynamically expected below ~530ºC in pure CO_2, their slow kinetics allows the system to maintain stability [48].

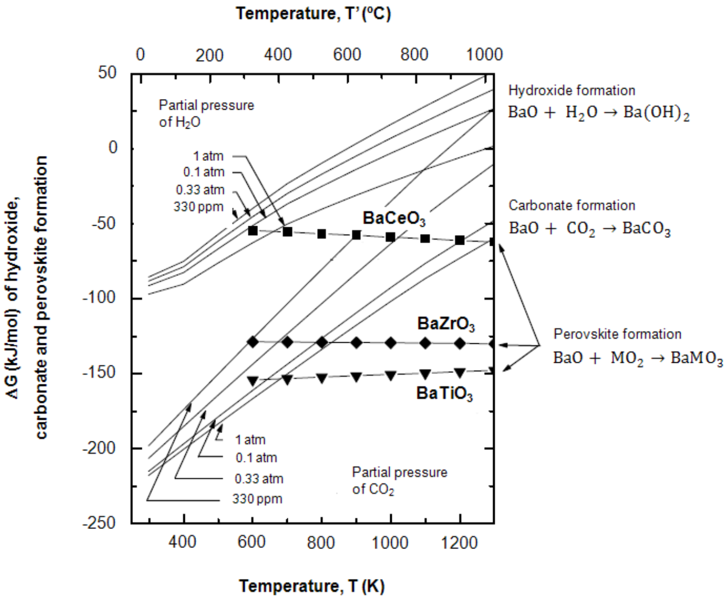

Fig. 1.9 – Gibbs energy of formation of barium hydroxide, barium carbonate, and perovskite from constituent oxides (adapted from [48]).

1.3.1.1 $BaZrO_3$ PROTON CONDUCTORS

Following that described previously, $BaZrO_3$-based materials have attracted special interest for use in electrochemical devices. They offer excellent chemical stability in a wide range of fuel cell operating conditions, such as CO_2-containing atmospheres, rendering them highly attractive to operate under aggressive carbonaceous environments, opening up the use of these devices in a range of alternative fuels. Furthermore, their cubic perovskite structure shows a high melting temperature 2600ºC, good mechanical strength, high thermal stability, and low coefficient of thermal expansion that are attractive for many high-temperature applications [11,18,49,50].

Barium zirconate materials exhibit a higher bulk proton conductivity compared with their cerate analogues. However, despite this potential, these materials exhibit inferior levels of total proton conductivity, due to highly resistive grain boundaries, compounded by poor grain growth. Thus, the total conductivity of $BaZrO_3$ materials is in general two orders of magnitude smaller than the conductivity of their $BaCeO_3$ based analogues measured at the same operating conditions (1.2 x 10^{-4} $S.cm^{-1}$ at 600ºC). Poor grain growth in $BaZrO_3$ based materials arises due to their highly refractory nature, leading to sintered samples with submicron average grain size and high grain boundary density. These factors further aggravate the poor protonic conductivity of the grain boundary, resulting in a poor overall conductivity [11,23,51,52].

The refractory nature of barium zirconate also leads to significant challenges to its implementation in fuel cells, namely its poor sinterability (*i.e.*, low densification rate) [23,51,52]. The extremely poor sinterability and low densification rate of barium zirconate materials are serious issues for ceramic processing of these materials. Typically, sintering of $BaZrO_3$ requires high sintering temperatures, 1600-1700ºC, to achieve full densities (> 95%), which are incompatible with most potential electrode materials and, thus, precludes the fabrication of co-sintered structures. The high sintering temperature requirement also can be responsible for BaO evaporation (stoichiometric losses) which can also lead to further reduction in the total conductivity and is accountable for abnormal grain growth that has been noted to result in inhomogeneous properties, both electrical and mechanical (table 1.6) [11,47,49,50,53-56].

Table 1.6 – Comparison of $BaZrO_3$ samples density under different sintering regimes and pressing conditions.

Sintering temperature	**Sintering time**	**Pressing conditions**	**Densification rate**	**Reference**
1700ºC	48 hours	Cold isostatic pressing (200 MPa)	98.5%	[54]
1600ºC + 1700ºC	6 hours + no soak	Cold isostatic pressing (200 MPa)	91%	[55]
1600ºC	2 hours	Cold isostatic pressing (225 MPa)	99%	[56]
1650ºC	2 hours	Uniaxial pressing (350 MPa)	99%	[50]
1600ºC	5 hours	Cold isostatic pressing (200 MPa)	94%	[47]
1650ºC	1 hour	Hot isostatic pressing (50 MPa)	98%	[49]

There is a compromise between the grain growth and the densification mechanisms during heat treatment, especially during the final stage of sintering. When the sintering rate is too fast and/or the isotherm temperature is too high, the grain growth is faster than the densification. Since the grain growth affects the distribution of grain size, a broad range of values of grain area is reached when only temperature or both temperature and heating time are increased [56,57].

Guillaume *et al.* [56] have studied why an abnormal grain growth mechanism is effective for $BaZrO_3$. Such behaviour is confirmed by microstructure analyses (fig. 1.10), where large pores are observed when the sintering temperature is higher than 1650ºC and/or the heating time is longer than 2 hours. Increasing further the isotherm temperature or the heating time leads to a decrease in density due to abnormal grain growth associated with the formation of trapped porosity, *i.e.*, an abnormal grain growth is effective for $BaZrO_3$ associated with the formation of trapped porosity. Guillaume concluded that full density of these materials (99%) is achieved at 1650ºC during 2 hours.

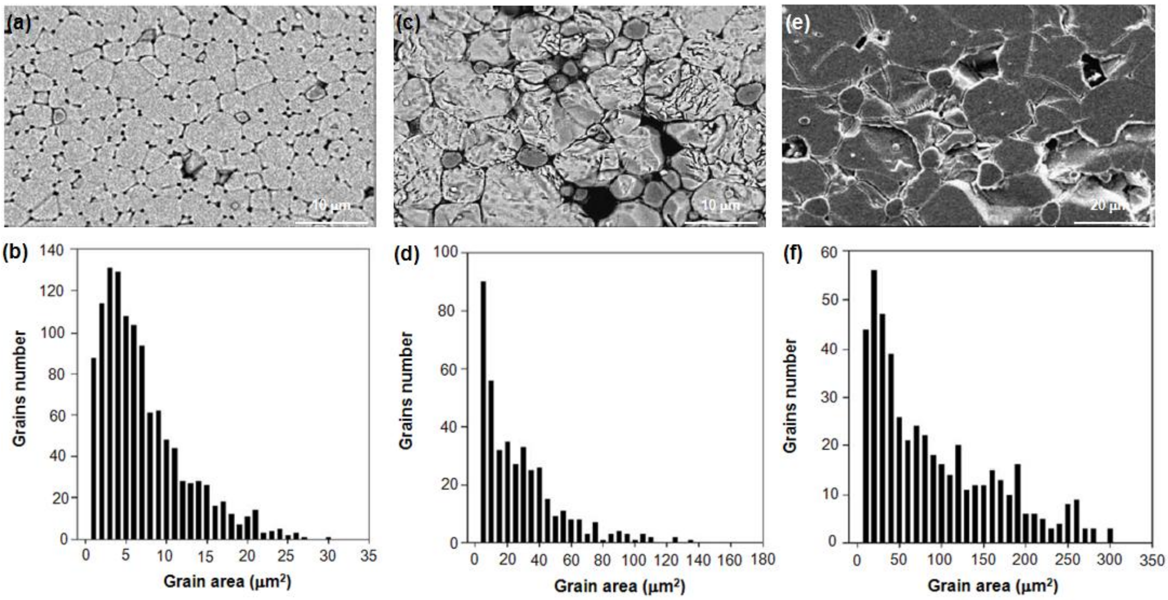

Fig. 1.10 - Scanning electron micrograph and grain area distribution plot of $BaZrO_3$ sintered at: (a) 1650ºC during 2 hours, (b) 1700ºC during 2 hours, and (c) 1700ºC during 48 hours (adapted from [56]).

The results compared in figure 1.11 clearly show that grain growth affects the distribution of the grain size, which is dependent on the sintering cycle (temperature and dwell time) [56].

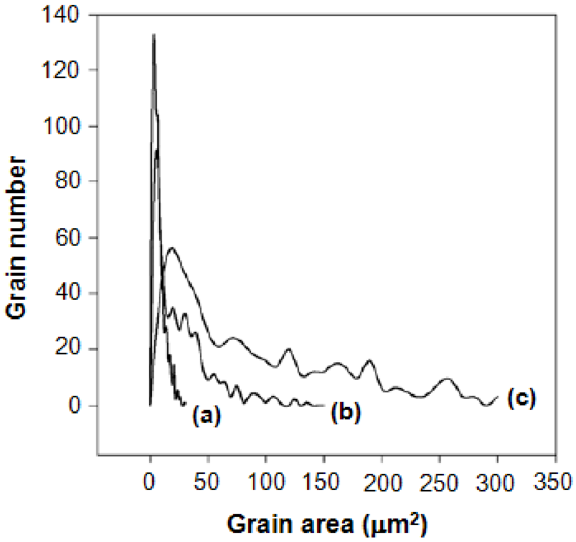

Fig. 1.11 - Comparative plot of grain size distribution for $BaZrO_3$ sintered at (a) 1650ºC for 2h, (b) 1700ºC for 2h and (c) 1700ºC for 48h (adapted from [56]).

On the other hand, the very high grain boundary resistances associated to these ceramics leads to poor proton conductivity [58-60]. Many studies have been performed in order to understand these low values of proton conductivity. In 1993, Kreuer *et al.* [61] showed that, in the case of barium cerates, the isothermal conductivity measured at elevated temperatures for long periods of time can drop by as much as two orders of magnitude and this phenomenon was attributed to the loss of BaO through evaporation. Later, Shima *et al.* [62] presented that in the case of barium zirconate, Ba-losses also happen and suggested that they could be responsible for the poor conductivity of $BaZrO_3$. In 1999, Kreuer [63] attributed this poor conductivity to the small grain sizes and high total grain boundary area due to the high refractory nature of this material. In 2004, Snijkers and co-workers [64] proposed that the achievement of the highest conductivities is affected by some form of phase transformation or segregation and/or by slow kinetic processes of water absorption. Additional attempts have also been made to attribute this factor to highly resistive grain boundary/impurity phases caused by intergranular phase formation during ceramic processing, perhaps related to the prolonged sintering at extreme temperatures [52,65], and/or space charge effects [66].

According to this description, a major target in the study of this material is to decrease the sintering temperature in order to avoid the deleterious effect that may arise due to barium losses and abnormal grain growth, and improve grain growth to maximise total proton conductivity. It is only in this way that profit can be taken from the advantageous high chemical stabilities of the $BaZrO_3$ based materials. These challenges are furthermore interrelated because processing approaches that lead to large-grained materials, such as prolonged sintering at extreme temperatures, often also result in lowered bulk or grain interior conductivities and poor chemical homogeneities [67].

Preparation of $BaZrO_3$ proton conductors

Challenges surrounding the use of barium zirconate materials centre on: (i) decrease the sintering temperature required to achieve full density, thus, preventing elemental loss, (ii) improve the grain boundary conductivity and iii) lower the high number-density of grain boundaries by enhancement of grain growth characteristics.

Highly pure and fine powder has been shown to be very crucial to produce dense ceramic bodies of $BaZrO_3$-materials with high strength and good microstructural features. A wide range of soft chemistry synthesis techniques have been attempted for this purpose with the aim to form nanometric powders with narrow size distributions: co-precipitation [68-70], sol-gel techniques [71-74], hydrothermal synthesis [75,76], thermal decomposition of nitrate [55], combustion synthesis [50,52,72], spray pyrolysis [77,78] and mechanochemical reaction [47]. However, several disadvantages have been found for typical soft chemistry routes such as the evaporation of solvents, non-homogeneity causing the formation of segregated phases or alteration of stoichiometry due to incomplete precipitation processes [79], high chemical costs and time consuming processes [71-74], as well as the discharge of pollutant gases [52,55,68,72]. Furthermore, the formation of $BaCO_3$ as an impurity phase due to the decomposition of organics was also presented as a common problem in many of the described techniques. In this case, additional calcinations steps are required to remove this impurity and may add to compositional inhomogeneity [52,55,68,72,74,79].

In order to obtain dense ceramics, some advanced pressing techniques are already known. Hot pressing (applying a pressure during the sintering) can also help the sintering rate as does a higher green density by isostatic pressing or rapid sintering process such as spark plasma sintering [49,58].

Moreover, control of Ba-loss on sintering can also give additional improvements in density as demonstrated by Magrez *et al.* [72] and Babilo *et al.* [52]. Ba-loss is a case in point that further impedes grain growth and conductivity. It can be reduced by covering the samples with sacrificial powder of the same composition.

Many authors have also shown that the sintering rate can be improved by adding sintering aids [51,53,55,80] which will have influence not only in the sintering temperature but potentially can also alter the grain boundary resistance due to preferential location sintering additive in the grain boundary [36]. Potential sintering additives will be discussed in the later Chapter 4.

1.3.1.2 YTTRIUM-DOPED $BaZrO_3$ PROTON CONDUCTORS (BZY)

Among various acceptor dopants suggested for barium zirconate the rare-earth elements are reported to be optimal for the generation of protonic conductivity [81-83]. According to that described in chapter 1.3.1, the mechanism of proton conduction in the perovskites is defined by the formation of proton defects (equation 1.18) that require the presence of oxygen vacancies. The formation of oxide-ion vacancies can be obtained by the partial substitution of the B cation by an acceptor dopant due to the requirement of valence charge balance (equation 1.11) - $AB_{1-x}M_xO_{3-\delta}$ [23]. Kreuer [29] has reported on the proton mobility in $BaZrO_3$ doped with Sc^{3+}, In^{3+}, Y^{3+} and Gd^{3+} (fig. 1.12) and has shown that $BaZrO_3$ doped with Y exhibits the highest proton mobility of these dopants. The presence of yttrium also can raise the tolerance factor producing low lattice distortion. The significantly smaller ionic radius of Y^{3+} (0.892 Å), when compared with that of Ba^{2+} (1.35 Å), also minimizes the site partition problem. Based on the above considerations, yttrium-doped barium zirconate ($BaZr(Y)O_{3-\delta}$, BZY) is an interesting parent compound for the development of proton conducting electrolyte for SOFC applications [19,29,35,36,47,67,80].

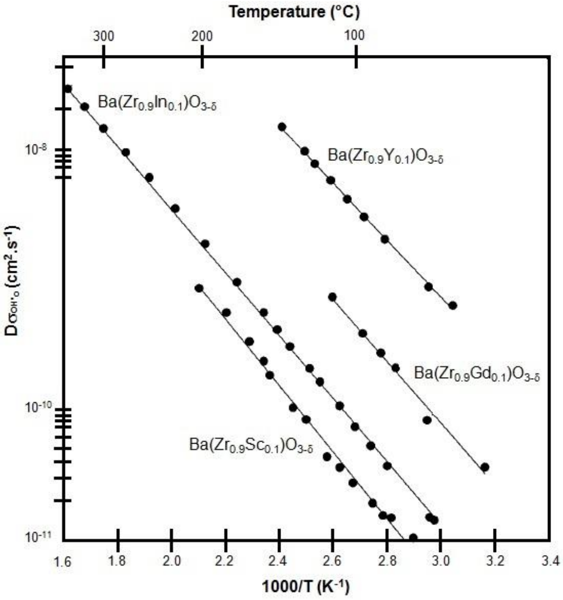

Fig. 1.12 – Proton mobility in $BaZrO_3$ doped with different acceptor dopants: Sc^{3+}, In^{3+}, Y^{3+} and Gd^{3+} (adapted from [56]).

Yttrium-doped barium zirconate ($BaZr(Y)O_{3-\delta}$, BZY) is thus widely recognised as one of the strongest candidates for incorporation in electrochemical devices due to good stability in CO_2 and higher proton mobility. It possesses relatively high bulk conductivity of about $1.0x10^{-2}$ $S.cm^{-1}$ at 450ºC [5], which can satisfy the conductivity requirement for application as an electrolyte in fuel cells [84], with a wide ionic domain [19,29,35,36,47,67,80].

Nonetheless, the required high sintering temperatures (1600ºC) to ensure proper densification levels can lead to barium losses. Moreover, poor grain growth leads to a large grain boundary contribution limiting its total electrical conductivity [23,29,81].

The total conductivity of yttrium-doped $BaZrO_3$ has been reported by many independent groups since 1995. However, its reported value varies widely, from around 1.3×10^{-6} [60] to high values of 1.0×10^{-2} $S.cm^{-1}$ [85] at 600 °C (table 1.7).

Table 1.7 - Conductivity of Y-doped $BaZrO_3$ as reported in the literature (adapted from [52]).

Composition	Sintering conditions	Conductivity	Conductivity measurement conditions	Reference
$BaZr_{0.9}Y_{0.1}O_{3-\delta}$	1400ºC, 10 hours in air	1.3×10^{-6} S/cm (bulk) at 605ºC	N_2 wet (room temperature water)	[16]
$BaZr_{0.9}Y_{0.1}O_{3-\delta}$	1715ºC, 30 hours in air	3.0×10^{-3} S/cm (bulk) at 600ºC	Air wet	[48]
$BaZr_{0.9}Y_{0.1}O_{3-\delta}$	1800ºC, 5 hours in air	1.1×10^{-3} S/cm (total) at 600ºC	H_2 wet (pH_2O = 0.017 atm)	[86]
$BaZr_{0.93}Y_{0.07}O_{3-\delta}$	1700ºC, 1 hour	5.0×10^{-4} S/cm (total) at 600ºC	Air wet (room temperature water)	[87]
$BaZr_{0.95}Y_{0.05}O_{3-\delta}$	1350ºC-1400ºC, 20-40 hours in air	1.8×10^{-6} S/cm (bulk) at 605ºC	N_2 wet (pH_2O = 0.031 atm)	[88]
$BaZr_{0.85}Y_{0.15}O_{3-\delta}$	1700ºC, 2 hours	1.6×10^{-3} S/cm (total) at 600ºC	N_2 wet (pH_2O = 0.023 atm)	[29]
$Ba_{1.1}Zr_{0.9}Y_{0.1}O_{3-\delta}$ (10% excess of BaO before sintering)	1500ºC, 24 hours	9×10^{-4} S/cm (total) at 500ºC	Air wet	[27]
$BaZr_{0.93}Y_{0.07}O_{3-\delta}$	1650ºC, 10 hours in air	3.8×10^{-3} S/cm (total) at 600ºC	N_2 wet (pH_2O = 0.025 atm)	[89]
$BaZr_{0.93}Y_{0.07}O_{3-\delta}$	1650ºC, 10 hours in air	4.2×10^{-3} S/cm (total) at 600ºC	Air wet (pH_2O = 0.025 atm)	[90]
$BaZr_{0.9}Y_{0.1}O_{3-\delta}$	1400ºC	2.8×10^{-4} S/cm (bulk) at 600ºC	Ar wet – 5% H_2 (pH_2O = 0.03 atm)	[55]
$BaZr_{0.95}Y_{0.05}O_{3-\delta}$	1800ºC	1.0×10^{-2} S/cm at 600ºC	Ar wet – O_2 (pH_2O = 0.023 atm)	[49]

The poor reproducibility of conductivity measurements represent a major challenge for the implementation of BZY in real devices and raises fundamental questions regarding the root of these variations and the proton transport mechanism [19,29,52].

As is shown in table 1.7, many different compositions of BZY have been tested. Iguchi and co-workers [19,91,92] have studied the relationship between chemical composition and grain boundary conductivity in Y-doped $BaZrO_3$ materials. In 2007, Iguchi [91] concluded that as Y concentration increased, the total and bulk conductivities also increase (figure 1.13).

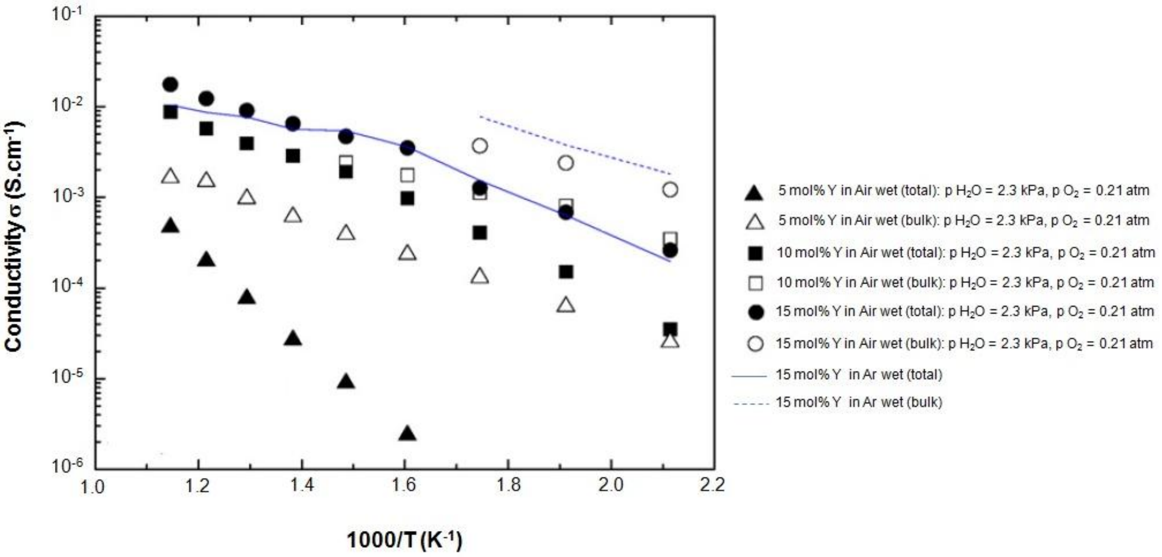

Fig. 1.13 - Comparison of total and bulk conductivities of the samples of BZY with different amounts of Y (5, 10 and 15 mol%) and different atmospheres (wet air and wet argon) (adapted from [91]).

Nonetheless, figure 1.13, clearly shows that the total conductivity is significantly lower than that of the bulk conductivity for all materials, corresponding to the large impact of a high grain boundary resistance. On the other hand, the grain boundary conductivity was shown to significantly increase with increasing Y content from 5 mol% to 15 mol% by about three orders of magnitude at 200ºC [91,92]. Thus, the chemical composition can exert important influences on the proton conductivity of both grain and grain boundary contributions, whereas the overall conductivity is predominantly limited by the level of grain boundary conductivity. Thus, the deviation in the total conductivities reported for this material in the literature is likely to be a factor of the different processing routes adopted, which may lead to chemical inhomogeneities, deviations in stoichiometry (e.g. Ba-loss) and/ or different grain sizes.

The presence of yttrium in barium zirconate-based materials has also been shown to be effective in terms of densification. Different studies have been performed with the purpose of understand the benefits of BZY.

In 2011, Bendjeriou-Sedjerari *et al.* [93] reported the influence of yttrium-doped $BaZrO_3$ (BZY) on densification compared with un-doped barium zirconate (BZO)(fig. 1.14).

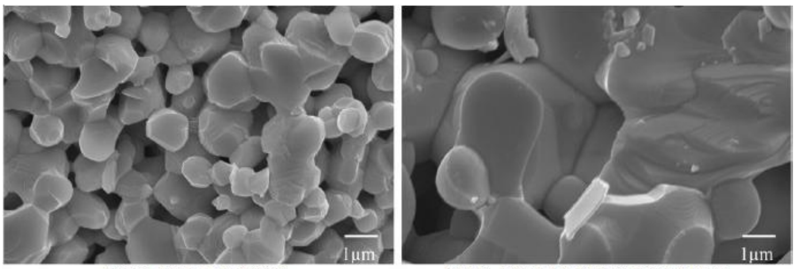

BaZrO$_3$ sintered at 1650°C.

BaZrO$_3$ sintered at 1650°C during 4 hours.

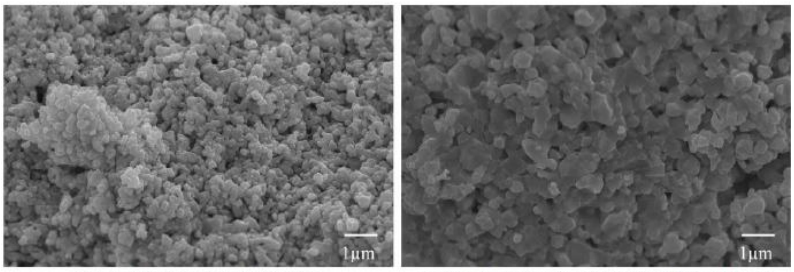

Y-doped BaZrO$_3$ sintered at 1650°C.

Y-doped BaZrO$_3$ sintered at 1650°C during 4 hours.

Fig. 1.14 - Effect of zirconium substitution by yttrium on BaZrO$_3$ after sintering at 1650ºC or during 4 hours at 1650ºC (adapted from [93]).

According to their results, the presence of Y proved to be disadvantageous during the rise of temperature but it had a positive effect on densification during the dwell of the sintering cycle. On the contrary, Figure 1.14 also shows that sintered BZY has a smaller final grain size when compared with un-doped BaZrO$_3$. This difference was suggested by Bendjeriou-Sedjerari [93] to be responsible for the low densification rate of BZO upon heating [93].

Iguchi *et al.* [19] presented the influence of the chemical composition in the densification of BZY samples. High densities of BZY samples (between ~93% and 100%) were achieved in samples prepared at 1800ºC (table 1.8).

Table 1.8 - Comparison of Y-doped $BaZrO_3$ samples density prepared at 1800ºC under different Y content, preparation method and sintering rates (adapted from [19]).

Composition	Preparation method	Sintering time	Densification
5 mol% Y	Solid state reaction	20 hours	96.7%
5 mol% Y	Pechini method	20 hours	98.0%
5 mol% Y	Pechini method	50 hours	97.3%
5 mol% Y	Pechini method	200 hours	95.9%
10 mol% Y	Solid state reaction	20 hours	97.3%
15 mol% Y	Solid state reaction	20 hours	100.0%
30 mol% Y	Solid state reaction	20 hours	92.5%

Iguchi *et al.* [19] concluded that 15 mol% of Y-doped attained the highest final density. Nonetheless problems associated to the extremely high sintering temperature of 1800ºC still exist.

In summary, BZY is a promising material of high bulk conductivity, but drastically limited by poor grain boundary conductivity. It also suffers from poor densification properties requiring extreme conditions (high sintering temperatures and/or high sintering rates) and poor grain growth. With the aim of improving these factors, various co-dopants and sintering aids for yttrium-doped barium zirconate materials will be studied in the present work.

1.3.2 NEW FAMILY OF OXIDE-ION CONDUCTORS

Much research has been dedicated to the improvement of material properties for solid oxide fuel cells (SOFC), searching for new compositions and/or ways of improving the performance of existing materials. According to that described previously, one of the major challenges in this study is lowering the operating temperatures to the intermediate temperature regime, *i.e.* lower than 700ºC, while maintaining good electrochemical performances [7,29,30]. The solid electrolyte plays a central role in this goal, since its ionic conductivity determines the best operating temperature range. The search for novel ionic conductors therefore remains a highly important line of research.

Recently, in 2012, a superior oxide-ion electrolyte family has been discovered showing an oxide-ion conductivity of $\geq 10^{-2}$ S.cm^{-1} in the temperature range 500 - 600ºC, one of the key elements to the realization of intermediate temperature-solid oxide fuel cells (IT-SOFC). Additionally, its high stability and electrochemical performance make this material an ideal solid electrolyte for IT-SOFC [32,33,94].

The material shows a 2D planar layered structure different from the fluorite and the perovskite structures, with a generic formula $Sr_{3-x}A_xM_3O_{9-0.5x}$ (A = N or K and M = Si or Ge). It may be in the form of a single-phase polycrystalline solid having a monoclinic crystal structure, with the space group C12/c1 [30,32,94].

The monoclinic $Sr_{3-x}A_xM_3O_{9-0.5x}$ (A = N or K and M = Si or Ge) structure is based on completely novel structure that may provide an alternative mechanism for oxide-ion transport involving interstitial oxygen as well as mobile vacancies [30,94].

In typical materials based on fluorite or perovskite-type crystallographic structures, oxide ion conductivity is induced by the introduction of oxygen vacancies. This type of defects appears by the substitution of a lower valence cation producing oxygen vacancies as defects that are created by charge compensation for the acceptor dopant cation. O^{2-} conduction then proceeds through oxide ion “jumps” via the formed oxygen vacancy defects [95,96].

In contrast, according to Goodenough and co-workers [30,32,94], the $Sr_{3-x}A_xM_3O_{9-0.5x}$ (A = N or K and M = Si or Ge) material may exhibit acceptable oxide ion conductivity due to the presence of either a terminal oxygen vacancy or an interstitial oxide-ion. The presence of these defects may be understood by first considering its location in the tetrahedral $SrMO_3$ complex, M = Si or Ge (fig. 1.15) [32,94,97].

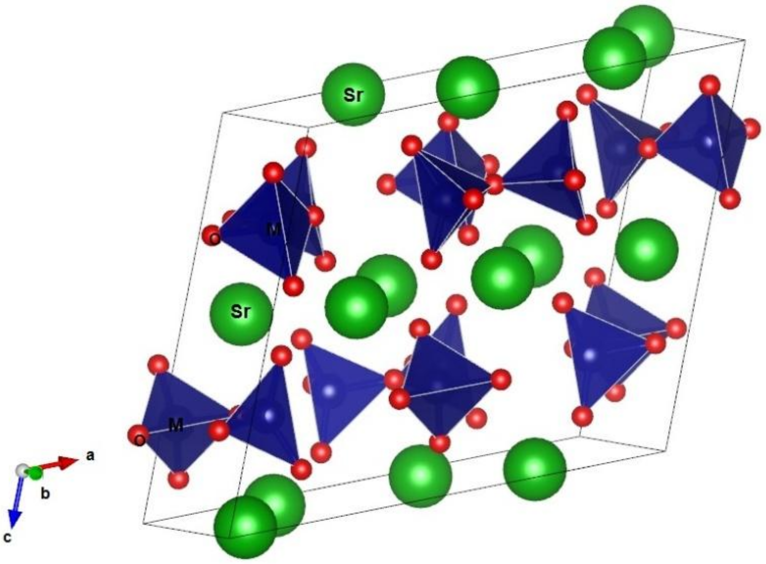

Fig. 1.15 – Schematic representation of the monoclinic $SrMO_3$ (M = Si or Ge) complex with the space group C12/c1 (adapted from [32]).

The $SrMO_3$ complex contains (001) planes of isolated M_3O_9 (M = Si or Ge) units of three MO_4 complexes in which each MO_4 unit shares corners with two other tetrahedra of the M_3O_9 unit. These units lie within the a-b planes that are separated from one another by a close-packed layer of large Sr^{2+} ions, each coordinated above and below by three terminal coplanar oxide ions belonging to three different M_3O_9 units [32,94].

Substitution of K^+ or Na^+ for Sr^{2+} in the material, represented in figure 1.16, introduces mobile oxygen vacancies and steric constraints prevent the vacancies from being eliminated by a corner sharing M_3O_9 unit [33,94].

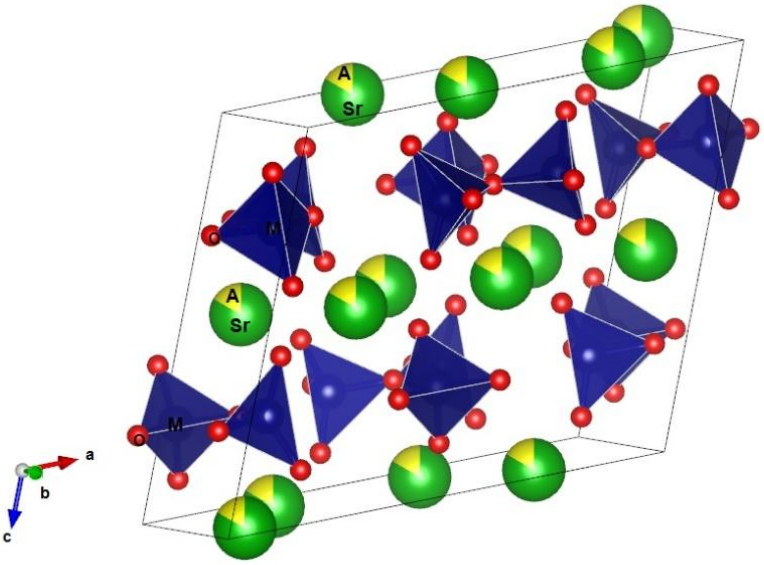

Fig. 1.16 – Schematic representation of the monoclinic structure of $Sr_{3-x}A_xM_3O_{9-0.5x}$, where A = N or K and M = Si or Ge, with the space group C12/c1 (adapted from [32]).

Wei *et al.* [33] suggested that the oxygen vacancies are retained by the steric hindrance promoted by the substitution of A^+ (A = K or Na) for Sr^{2+}. These vacancies will occupy primarily M_3O_9 (M = Si and Ge) complexes at lower temperatures with increasing apical-site occupancy as the temperature is raised, and would be expected to jump between clusters following generally the double well potential model [33,94].

Lastly, this type of ionic conduction, promoted by the use of steric hindrance to stabilize a terminal-oxygen vacancy on a tetrahedral anion complex, can be considered as a new design principle for an ionic conductor.

1.3.2.1 (Ba,Sr)GeO_3 OXIDE-ION CONDUCTORS

Singh *et al.* [30] have concluded that in the system of $Sr_{3-x}A_xM_3O_{9-0.5x}$ where A = N or K and M = Si or Ge, Ge analogue generally give a high oxide-ion conductivity in comparison with Si analogues.

According to this study, the current work is focused on doping of $SrGeO_3$ to determine whether the vacancies could give a competitive ionic conductivity.

The introduction of a cation at the Sr-site of $SrGeO_3$ causes the reduction of the unit-cell volume. It will lead to the introduction of terminal-oxygen vacancies on tetrahedral anion complexes ions which may provide a high oxide-ion conductivity [30,32,97].

The occupancy factors of the oxygen atoms in $SrGeO_3$-doped system were described by Martinez-Coronado *et al.* [32], revealing the presence of oxygen vacancies by the substitution of Na^+ or K^+ for Sr^{2+}. In the Na samples, the oxygen vacancies are located at all oxygen atom positions, being more pronounced at the in-plane O3 and O5 site at low temperatures (400ºC). For K samples, the oxygen vacancies are concentrated in a specific plane (at the in-plane O3 and O5 sites). Additionally, no oxygen interstitials were evident.

Substitution of a large K^+ ion for Sr^{2+} was described to be possible in the range $0 < x \leq 0.25$ of $Sr_{1-x}K_xGeO_{3-0.5x}$, reaching oxide-ion conductivity higher than 10^{-2} $S.cm^{-1}$ by 700ºC. However, two slopes were clearly seen showing two different activation energies for oxide-ion conduction in the low- and high-temperature regions [30]. In order to understand this behaviour and since potassium doping showed better oxide-ion conductivity compared to un-doped $SrGeO_3$, $Sr_{1-x}K_xGeO_{3-0.5x}$ materials will be in the base of the present work.

The large difference in ionic radius of Sr^{2+} (0.126 nm) compared with Ba^{2+} (0.142 nm) may lead to significant lattice distortion in the current materials. Wei *et al.* [33] suggested that the oxygen vacancies in the current materials could be retained by the steric hindrance promoted by the substitution of larger cations for Sr^{2+}. Based on this observation, $Ba_{1-x}K_xGeO_{3-0.5x}$ materials were also studied to understand if a larger ionic radius in the close packed alkaline earth metal layers could impact the oxide-ion transport.

1.4 REFERENCES

[1] Stambouli, A.B. and Traversa, E. (2002). “Fuel Cells, an alternative to standard sources of energy.” Renewable and Sustainable Energy Reviews **6(3):** 297-306.

[2] Ormerod, R.M. (2003). “Solid oxide fuel cells.” Chemical Society Reviews **32:** 17-28.

[3] Andújar, J.M., Segura, F. (2009). “Fuel cells: History and updating. A walk along two centuries.” Renewable and Sustainable Energy Reviews **13(9):** 2309-2322.

[4] www.fuelcells.org; accessed December 2, 2011; activity of the Breakthrough Technologies Institute (BTI); created in 1993.

[5] Yamazaki, Y., Hernandez-Sanchez, R. and Haile, S.M. (2009). “High Total Proton Conductivity in Large-Grained Yttrium-Doped Barium Zirconate.” Chemistry of Materials **21(13):** 2755-2762.

[6] Mekhilef S., Saidur, R. and Safari, A. (2012). “Comparative study of different fuel cell technologies.” Renewable and Sustainable Energy Reviews **16(1):** 981-989.

[7] Haile, S.M. (2003). “Fuel cell materials and components.” Acta Materialia **51:** 5981-6000.

[8] www.renewableenergyworld.com/rea/tech/hydrogen; accessed December 2, 2011; activity of Renewable Energy Network for News & Information; created in 1999.

[9] Minh, N.Q. (1993). “Ceramic Fuel Cells.” Journal of the American Ceramic Society **76(3):** 563-568.

[10] Kjølseth, C., Fjeld, H. and Vestre, P.K. “Proton ceramic fuel cell.” Patent WO 2011/131657 A1 (2011).

[11] Souza, E.C.C. and Muccillo R. (2010). “Properties and Applications of Perovskite Proton Conductors.” Materials Research **13(3):** 385-394.

[12] Nasani, N., Ramasamy, D., Mikhalev, S., Kovalevsky, A.V. and Fagg, D.P. (2015). “Fabrication and electrochemical performance of a stable, anode supported thin in $BaCe_{0.4}Zr_{0.4}Y_{0.2}O_{3-\delta}$ electrolyte Protonic Ceramic Fuel Cell.” Journal of Power Sources **278:** 582-589.

[13] www.csa.com/discoveryguides/fuelcel/overview; accessed December 3, 2011; activity of ProQuest Information and Learning and CSA (part of Cambridge Information Group); created in 2001.

[14] Kee, R. J. and Zhu, H.. (2004). “Solid-oxide fuel cells (SOFC) with hydrocarbon and hydrocarbon-derived fuels.” Presented on International Symposium on Combustion, July 2004.

[15] U.S. Department of Energy, Office of Fossil Energy (2004). ”Fuel Cell Handbook.” EG&G Technical Services, Inc, 7th Edition.

[16] http://www.doitpoms.ac.uk/tlplib/fuel-cells/high_temp_sofc.php; accessed December 3, 2011; activity of DoITPoMS Teaching and Learning Packages (TLPs); created in 2004.

[17] Park, H.-G., Moon, H., Park, S.-C., Lee, J.-J., Yoon, D., Hyun, S.-H. and Kim, D.-H. (2010). “Performance improvement of anode-supported electrolytes for planar solid oxide fuel cells via a tape-casting/lamination//co-firing technique.” Journal of Power Sources **195(9):** 2463-2469.

[18] Oyama Y., Kojima A., Li X., Cervera R.B., Tanaka K. and Yamaguchi S. (2011). “Phase relation in the $BaO-ZrO_2-YO_{1.5}$ system: Presence of separate $BaZrO_3$ phases and complexity in phase formation.” Solid State Ionics **197(1):** 1-12.

[19] Iguchi, F., Tsurui, T., Sata, N., Nagao Y. and Yugami, H. (2009). “The relationship between chemical composition distributions and specific grain boundary conductivity in Y-doped $BaZrO_3$ proton conductors.” Solid State Ionics **180:** 563-568.

[20] Elagonvan, S. and Hartvigsen, J.J. (2007). “Intermediate Temperature Reversible Fuel Cells.” International Journal of Applied Ceramic Technology **4(2):** 109-118.

[21] Shao, Z., Zhou, W. and Zhu, Z. (2012). “Advanced synthesis of materials for intermediate-temperature solid oxide fuel cells.” Progress in Materials Science **57:** 804-874.

[22] Fabbri, E., D’Epifanio, A., Di Bartolomeo, E., Licoccia, S. and Traversa, E. (2008). “Tailoring the chemical stability of $Ba(Ce_{0.8-x}Zr_x)Y_{0.2}O_{3-\delta}$ protonic conductors for Intermediate Temperature Solid Oxide Fuel Cells (IT-SOFCs).” Solid State Ionics **179(15-16):** 558-564.

[23] Fabbri, E., Pergolesi, D. and Traversa, E. (2010). “Materials challenges toward proton-conducting oxide fuel cells: a critical review.” Chemical Society Reviews **39:** 4355-4369.

[24] Dias, P.A.N., Nasani, N., Horozov, T.S. and Fagg, D.P. (2013). “Non-aqueous stabilized suspensions of $BaZr_{0.85}Y_{0.15}O_{3-\delta}$ proton conducting electrolyte powders for thin film preparation.” Journal of the European Ceramic Society **33(10):** 1833-1840.

[25] Guo, Y., Lin, Y., Ran, R. and Shao, Z. (2009). “Zirconium doping effect on the performance of proton-conducting $BaZr_yCe_{0.8-y}Y_{0.2}O_{3-\delta}$ ($0.0 \leq y \leq 0.8$) for fuel cell applications.” Journal of Power Sources **193(2):** 400-407.

[26] http://www.cnrs-imn.fr/index.php/en/research-topics-st2e/development-of-new-materials-for-fuel-cell-applications/101-new-materials-to-replace-reference-electrolytes-for-pcfc-and-sofc; accessed May 9, 2013; activity of Institut des Matériaux Jean Rouxel (IMN), Université de Nantes; created in 2011.

[27] Goodenough, J.B. (1997). “Ceramic solid electrolytes.” Solid State Ionics **94:** 17-25.

[28] http://www1.eere.energy.gov/hydrogenandfuelcells/fuelcells/fc_types.html; accessed May 13, 2013; activity of U.S. Department of Energy (Energy Efficiency & Renewable Energy); created in 2009.

[29] Kreuer, K.D. (2003). “Proton-Conducting Oxides.” Annual Reviews Materials Research **33:** 333-359.

[30] Singh, P. and Goodenough, J.B. (2012). “$Sr_{1-x}K_xSi_{1-y}Ge_yO_{3-0.5x}$: a new family of superior oxide-ion conductors.” Energy & Environmental Science **5:** 9626-9631.

[31] Singh, P. and Goodenough, J.B. (2013). “Monoclinic $Sr_{1-x}Na_xSiO_{3-0.5x}$: New Superior Oxide Ion Electrolytes.” Journal of the American Chemical Society **135:** 10149-10154.

[32] Martinez-Coronado, R., Singh, P., Alonso-Alonso, J. and Goodenough, J.B. (2014). “Structural investigation of the oxide-ion electrolyte with SrMO3 (M = Si/Ge) structure.” Journal of the Materials Chemistry A **2:** 4355-4360.

[33] Wei, T., Singh, P., Gong, Y., Goodenough, J.B., Huang, Y. and Huang, K. (2012). “$Sr_{3-3x}Na_{3x}Si_3O_{9-1.5x}$ ($x = 0.45$) as a superior oxide-ion electrolyte for intermediate temperature-solid oxide fuel cells.” Energy & Environmental Science **7:** 1680-1684.

[34] Li, C., Soh, K.C.K. and Wu, P. (2004). “Formability of ABO_3 perovskites.” Journal of Alloys and Compounds **372:** 40-48.

[35] Giannici, F., Shirpour, M., Longo, A., Martorana, A., Merkle, R. and Maier, J. (2011). “Long-Range and Short-Range Structure of Proton-Conducting Y:$BaZrO_3$.” Chemistry of Materials **23(11):** 2994-3002.

[36] Han, D., Nose, Y., Shinoda, K. and Uda, T. (2012). "Site selectivity of dopants in $BaZr_{1-y}M_yO_{3-\delta}$ (M = Sc, Y, Sm, Eu, Dy) and measurement of their water contents and conductivities." Solid State Ionics **213:** 2-7.

[37] Haile, S.M., Staneff, G. and Ryu, K.H. (2001). "Non-stroichiometry, grain boundary transport and chemical stability of proton conducting perovskites." Journal of Materials Science **36:** 1149-1160.

[38] Agmon, N. (1995). "The Grotthuss mechanism." Chemical Physics Letters **244:** 456-462.

[39] Kreuer, K.D., Fuchs, A. And Maier, J. (1995). "H/D isotope effect of proton conductivity and proton conduction mechanism in oxides." Solid State Ionics **77:** 157-162.

[40] Wu, J., Davis, R.A., Islam, M.S. and Haile, S.M. (2004). "Defect chemistry and transport properties of $Ba_xCe_{0.85}M_{0.15}O_{3-\delta}$." Journal of Materials Research **19(8):** 2366-2376.

[41] Davies, R.A., Islam, M.S. and Gale, J.D. (1999). "Dopant and proton incorporation in perovskite-type zirconates." Solid State Ionics **126:** 323-335.

[42] Glöckner, R., Islam, M.S. and Norby, T. (1999). "Protons and other defects in $BaCeO_3$: a computational study." Solid State Ionics **122:** 145-156.

[43] Buscaglia, M.T., Buscaglia, V., Viviani, M. and Nanni, P. (2001). "Atomistic Simulation of Dopant Incorporation in Barium Titanate." Journal of American Ceramic Society **84(2):** 376-384.

[44] Goldschmidt, V.M. (1926). Skrifer Norske Videnskaps-Akad. Oslo, I. Mat.-Nat., Kl: 8.

[45] Bhide, S.V. and Virkar, V.K. (1999). "Stability of $BaCeO_3$-Based Proton Conductors in Water-Containing Atmospheres." Journal of The Electrochemical Society **146(6):** 2038-2044.

[46] Iwahara, H., Esaka, T., Uchida, H. and Maeda, N. (1981). "Proton conduction in sintered oxides and its application to steam electrolysis for hydrogen production." Solid State Ionics **3/4:** 359-363.

[47] Antunes, I., Brandão, A., Figueiredo, F.M., Frade, J.R., Grácio, J. and Fagg, D.P. (2009). "Mechanosynthesis of nanopowders of the proton-conducting electrolyte material $Ba(Zr,Y)O_{3-\delta}$." Journal of Solid State Chemistry **182(8):** 2149-2156.

[48] Uda, T., Babilo, P. and Haile, S.M. (2005). "Thermodynamic Analysis and Conductivity of Yttrium Doped Barium Zirconate." Presented on 207th ECS Meeting, Quebec City, Canada.

[49] Dahl, P.I., Lein, H.L., Yu, Y., Tolchard, J., Grande, T., Einarsrud, M.-A., Kjølseth, C., Norby, T. and Haugsrud (2011). "Microstructural characterization and electrical properties of spray pyrolyzed conventionally sintered or hot-pressed $BaZrO_3$ and $BaZr_{0.9}Y_{0.1}O_{3-\delta}$." Solid State Ionics **182(1):** 32-40.

[50] Kumar, H.P., Vijayakumar, C., George, C.N., Solomon, S., Jose, R., Thomas, J.K. and Koshy, J. (2008). "Characterization and sintering of $BaZrO_3$ nanoparticles synthesized through a single-step combustion process." Journal of Alloys and Compounds **458:** 528-531.

[51] Tao, S. and Irvine, J.T.S. (2006). "A Stable, Easily Sintered Proton-Conducting Oxide Electrolyte for Moderate-Temperature Fuel Cells and Electrolyzers." Advanced Materials **18(12):** 1581-1584.

[52] Babilo, P., Uda, T. and Haile, S.M. (2007). "Processing of yttrium-doped barium zirconate for high-proton conductivity." Journal of Materials Research **22(5):** 1322-1330.

[53] Babilo, P. and Haile, S.M. (2005). "Enhanced Sintering of Yttrium-Doped Barium Zirconate by Addition of ZnO." Journal of the American Ceramic Society **88(9):** 2362-2368.

[54] Erb, A., Walker, E. and Flükiger, R. (1995). “$BaZrO_3$: the solution for the crucible corrosion problem during the single crystal growth of high-Tc superconductors $REBa_2Cu_3O_{7-\delta}$; RE = Y, Pr.” Physica C **245:** 245-251.

[55] Azad, A.-M, Subramaniam, S. and Dung, T.W. (2002). “On the development of high density barium metazirconate ($BaZrO_3$) ceramics.” Journal of Alloys and Compounds **334:** 118-130.

[56] Guillaume, B., Boschini, F., Garcia-Cano, I., Rulmont, A., Cloots, R. and Ausloos, M. (2005). “Optimization of $BaZrO_3$ sintering by control of the initial powder size distribution; a factorial design statistical analysis.” Journal of the European Ceramic Society **25(16):** 3593-3604.

[57] Imashuku, S., Uda, T. and Awakura, Y. (2007). “Sintering Properties of Trivalent Cation-Doped Barium Zirconate at 1600ºC.” Electrochemical and Solid-State Letters **10(10):** B175-B178.

[58] Iwahara, H., Yajima, T., Hibino, T., Ozaki, K. and Suzuki, H. (1993). “Protonic conduction in calcium, strontium and barium zirconates.” Solid State Ionics **61:** 65-69.

[59] Manthiram, A., Kuo, J.F. and Goodenough, J.B. (1993). “Characterization of oxygen-deficient perovskites as oxide-ion electrolytes.” Solid State Ionics **62:** 225-234.

[60] Slade, R.C.T., Flint, S.D. and Singh, N. (1995). “Investigation of protonic conduction in Yb- and Y-doped barium zirconates.” Solid State Ionics **82:** 135-141.

[61] Kreuer, K.D., Schönherr, E. and Maier, J. (1993). “Phase separation and grain boundary proton conductivity in $BaCeO_3$ based ceramics.” Presented on 14th RisØ International Symposium on Materials Science, Roskilde, Denmark.

[62] Shima, D. and Haile, S.M. (1997). “The influence of cation non-stoichiometry on the properties of un-doped and gadolinia-doped barium cerate.” Solid State Ionics **97:** 443-455.

[63] Kreuer, K.D. (1999). “Aspects of the formation and mobility of protonic charge carriers and the stability of perovskite-type oxides.” Solid State Ionics **125:** 285-302.

[64] Snijkers, F.M.M., Buekenhoudt, A., Cooymans, J. and Luyten, J.J. (2004). “Proton conductivity and phase composition in $BaZr_{0.9}Y_{0.1}O_{3-\delta}$.” Scripta Materialia **50(5):** 655-659.

[65] Groβ, B., Beck, Ch., Meyer, F., Krajewski, Th., Hempelmann, R. and Altgeld, H. (2001). “BaZr0.85Me0.15O2.925 (Me = Y, In and Ga): crystal growth, high-resolution transmission electron microscopy, high-temperature X-ray diffraction and neutron scattering experiments.” Solid State Ionics **145:** 325-331.

[66] Kjølseth, C., Fjeld, H., Prytz, Ø., Dahl, P.I., Estournès, C., Haugsrud, R. and Norby, T. (2010). “Space-charge theory applied to the grain boundary impedance of proton conducting $BaZr_{0.9}Y_{0.1}O_{3-\delta}$.” Solid State Ionics **181:** 268-275.

[67] Yamazaki, Y., Hernandez-Sanchez, R. and Haile, S.M. (2010). “Cation non-stoichiometry in yttrium-doped barium zirconate: phase behaviour, microstructure, and proton conductivity.” Journal of Materials Chemistry **20:** 8158-8166.

[68] Robertz, B., Boschini, F., Cloots, R. and Rulmont, A. (2001). “Importance of soft solution processing for advanced $BaZrO_3$ materials.” International Journal of Inorganic Materials **3(8):** 1185-1187.

[69] Reddy, S.B., Rao, K.P. and Rao, M.S.R. (2007). “Nanocrystalline barium zirconate titanate synthesized at low temperature by an aqueous co-precipitation technique.” Scripta Materialia **57(7):** 591-594.

[70] Boschini, F., Rulmont, A., Cloots, R. and Vertruyen, B. (2009). “Rapid synthesis of submicron crystalline barium zirconate $BaZrO_3$ by precipitation in aqueous basic solution below 100ºC.” Journal of the European Ceramic Society **29(8):** 1457-1462.

[71] Cervera, R.B., Oyama, Y. and Yamaguchi, S. (2007). “Low temperature synthesis of nanocrystalline proton conducting $BaZr_{0.8}Y_{0.2}O_{3-\delta}$ by sol-gel method.” Solid State Ionics **178:** 569-574.

[72] Magrez, A. and Schober, T. (2004). “Preparation, sintering, and water incorporation of proton conducting $Ba_{0.99}Zr_{0.8}Y_{0.2}O_{3-\delta}$: comparison between three different synthesis techniques.” Solid State Ionics **175:** 585-588.

[73] Khani, Z., Taillades-Jacquim, M., Taillades, G., Marrony, M., Jones, D.J. and Rozière, J. (2009). “New synthesis of nanopowders of proton conducting materials. A route to densified proton ceramics.” Journal of Solid State Chemistry **182(4):** 790-798.

[74] Sin, A., El Montaser, B. and Odier, P. (2002). “Synthesis and Sintering of Large Batches of Barium Zirconate Nanopowders.” Journal of the American Ceramic Society **85(8):** 1928-1932.

[75] Kolen’ko, Y.V., Burukhin, A.A., Churagulov, B.R., Oleinikov, N.N. and Vanetsev, A.S. (2002). “On the Possibility of Preparing Fine-Particle Barium Zirconate by Hydrothermal Synthesis.” Inorganic Materials **38(3):** 252-255.

[76] Phulé, P.P. and Grundy, D.C. (1994). “Pathways for the low temperature synthesis of nano-sized crystalline barium zirconate.” Materials Science and Engineering: B **23(1):** 29-35.

[77] Bućko, M.M. and Oblakowski, J. (2007). “Preparation of $BaZrO_3$ nanopowders by spray pyrolysis method.” Journal of the European Ceramic Society **27:** 3625-3628.

[78] Stuart, P.A., Unno, T., Ayres-Rocha, R., Djurado, E. and Skinner, S.J. (2009). “The synthesis and sintering behaviour of $BaZr_{0.9}Y_{0.1}O_{3-\delta}$ powders prepared by spray pyrolysis.” Journal of the European Ceramic Society **29(4):** 697-702.

[79] Taglieri, G., Tersigni, M., Villa, P.L. and Mondelli, C. (1999). “Synthesis by the citrate route and characterisation of $BaZrO_3$, a high tech ceramic oxide: preliminary results.” International Journal of Inorganic Materials **1(1):** 103-110.

[80] Peng, C., Melnik, J., Jinxia, L., Luo, J., Sanger, A.R. and Chuang, K.T. (2009). “ZnO-doped $BaZr_{0.85}Y_{0.15}O_{3-\delta}$ proton conducting electrolytes: characterization and fabrication of thin films.” Journal of Power Sources **190(2):** 447-452.

[81] Kreuer, K.D., Adams, St., Münch, W., Fuchs, A., Klock, U. and Maier, J. (2001). “Proton conducting alkaline earth zirconates and titanates for high drain electrochemical applications.” Solid State Ionics **145:** 295-306.

[82] Bohn, H.G. and Schober, T. (2000). “Electrical Conductivity of the High-Temperature Proton Conductor $BaZr_{0.9}Y_{0.1}O_{2.95}$.” Journal of the American Ceramic Society **83(4):** 768-772.

[83] Schober, T. and Bohn, H.G. (2000). “Water vapour solubility and electrochemical characterization of the high temperature proton conductor $BaZr_{0.9}Y_{0.1}O_{2.95}$.” Solid State Ionics **127:** 351-360.

[84] Steele, B.C.H. and Heinzel, A. (2001). “Materials for fuel-cell technologies.” Nature **414:** 345-352.

[85] Iguchi, F., Yamada, T., Sata, N., Tsurui, T. and Yugami, H. (2006). “The influence of grain structures on the electrical conductivity of a $BaZr_{0.95}Y_{0.05}O_3$ proton conductor.” Solid State Ionics **177:** 2381-2384.

[86] Katahira, K., Kohchi, Y., Shimura, T. and Iwahara, H. (2000). “Protonic conduction in Zr-substituted $BaCeO_3$.” Solid State Ionics **138:** 91-98.

[87] Gorelov, V.P., Balakireva, V.B., Kleshchev, Y.N. and Brusentsov, V.P. (2001). “Preparation and Electrical Conductivity of $BaZr_{1-x}R_xO_{3-\alpha}$ (R = Sc, Y, Ho, Dy, Gd, In).” Inorganic Materials **37(5):** 535-538.

[88] Laidoudi, M., Talib, I.A. and Omar, R. (2002). “Investigation of the bulk conductivity of $BaZr_{0.95}M_{0.05}O_{3-\alpha}$ (M = Al, Er, Ho, Tm, Yb and Y) under wet N_2.” Journal of Physics D: Applied Physics **35(4):** 397-401.

[89] Wang, W. and Virkar, A.V. (2005). “Ionic and electron-hole conduction in $BaZr_{0.93}Y_{0.07}O_{3-\delta}$ by 4-probe dc measurements.” Journal of Power Sources **142:** 1-9.

[90] Savaniu, C.D., Canales-Vazquez, J. and Irvine, J.T.S. (2005). “Investigation of proton conducting $BaZr_{0.9}Y_{0.1}O_{2.95}$: $BaCe_{0.9}Y_{0.1}O_{2.95}$ core-shell structures.” Journal of Materials Chemistry **15:** 598-604.

[91] Iguchi, F., Sata, N., Tsurui, T. and Yugami, H. (2007). “Microstructures and grain boundary conductivity of $BaZr_{1-x}Y_xO_3$ (x = 0.05, 0.10, 0.15) ceramics.” Solid State Ionics **178:** 691-695.

[92] Iguchi, F., Tokikawa, T., Myoski, T., Tsurui, T., Nagao, Y., Sata, N. And Yugami, H. (2007). “Performance of $BaZrO_3$ based Proton Conductors as an Electrolyte for Intermediate Temperature Operating SOFC.” Electrochemical Society Transactions **7(1):** 2331-2336.

[93] Bendjeriou-Sedjerari, B., Loricourt, J., Goeuriot, D. and Goeuriot, P. (2011). “Sintering of $BaZrO_3$ and $SrZrO_3$ perovskites: Role of substitutions by yttrium or ytterbium.” Journal of Alloys and Compounds **509(21):** 6175-6183.

[94] Goodenough, J.B. and Singh, P. “Monoclinic Sr1-xAxSi1-yGeyO3-0.5x, wherein A is K or Na, oxide ion conductor.” Patent US 2014/0080019 A1 (2014).

[95] Kendrick, E. and Slater, P.R. (2009). “Understanding fast ion conduction in solids: synergy between modelling and experiment.” Presented at Supergen/RCEP Conference, Oxford 2008.

[96] Malavasi, L., Fisher, C.A.J. and Islam, M.S. (2010). “Oxide-ion and proton conducting electrolyte materials for clean energy application: structural and mechanistic features.” Chemical Society Reviews **39:** 4370-4387.

[97] Nishi, F. (1997). “Strontium Metagermanate, $SrGeO_3$.” Acta Crystallographica Section C **53:** 399-401.

CHAPTER 2. OBJECTIVES AND MOTIVATIONS

The main objective of this dissertation is the development and processing of novel ionic conducting ceramic materials for use as electrolytes in proton ceramic and solid oxide fuel cells (PCFCs and SOFCs, respectively). Research aims to develop new processing routes and/or materials based on nanometric ceramic oxide powders showing superior electrochemical behaviour and chemical stability, prepared by manipulation of mechanochemical processes.

As described in chapter 1, PCFCs require electrolyte materials with high proton conductivity at intermediate temperatures (500-700ºC) such as reported for perovskite zirconate oxides containing alkaline earth metal cations [1,2]. The flexibility of the perovskite structure to accommodate a wide range of cations results in a diverse number of properties, ranging from insulating, semiconducting, superconducting and, the present work's motivation, ionically conducting. Perovskite, proton conducting, electrolyte materials based on the cerates or zirconates of barium doped with yttrium or lanthanide oxides have received extensive study for a large number of applications [3-5].

For such purpose, research work specifically focused on the development of proton conductors based on barium zirconate ($BaZrO_3$), with special interest in yttrium-doped barium zirconate - $BaZr(Y)O_{3-\delta}$, since it is nowadays widely recognised as one of the strongest candidates for incorporation in electrochemical devices due to its good stability in CO_2 atmospheres and high proton conductivity [4,6]. Nonetheless, despite offering high bulk proton conductivity, widespread application of this material is limited by its high levels of grain-boundary resistance, poor sinterability and grain growth. These are the major challenges involving these materials, providing considerable research work.

Several recent studies have focused on strategies to minimise grain boundary resistance by promoting grain growth. Efforts such as reactive sintering [7], introduction of sintering additives [8-12] or doping strategies [13-15] have been suggested. Although, such efforts have been numerous, only fractional improvements in conductivity have been achieved to date [7-15]. Thus, this thesis aims to extend such works through two main investigation strategies: i) the use of alternative sintering additives and ii) a detailed analysis of doping strategies and their impact on crystallographic structure, compositional homogeneity and protonic transport.

$BaZrO_3$ containing 15 mol% of Y (BZY) was chosen as base material for further study. Minor additions of oxides of zinc, phosphorous and boron were added as possible sintering additives, which were chosen based on the structural Goldschmidt tolerance factor for perovskites.

On the other hand, one of the major challenges for electrolyte materials to be used in solid oxide fuel cells (SOFCs) is lowering the operating temperature to the intermediate temperature regime, < 700ºC, while maintaining good electrochemical performances such as: high ionic conductivity, low electronic conductivity, stability in both oxidizing and reducing environments, good mechanical properties and long-term stability with respect to dopant segregation [16,17]. Three electrolyte systems are known, namely yttria-stabilized zirconia (YSZ), strontium and magnesium-doped lanthanum gallate (LSGM), and gadolinium- or samarium-doped ceria (CGO or CSO). However, each system offers advantages and disadvantages. On one hand, YSZ fulfils electrical requirements at high temperatures and has good high temperature mechanical properties, but problems related to its reactivity with perovskite oxide electrodes containing lanthanum at high temperature can occur and $La_2Zr_2O_7$ resistive layers can be formed. Although, LSGM has higher ionic conductivity compared with YSZ and is more compatible with lanthanum transition-metal oxide perovskite cathodes, on the anode-electrolyte side, composite LSGM-NiO anodes are less compatible with LSGM due to NiO reactivity. Finally, Ceria doped with rare earth metals has received considerable attention as an alternative electrolyte. It shows the highest conductivity at lower temperature but in reducing conditions Ce^{4+} is reduced to Ce^{3+} which results in the introduction of electronic conductivity thereby reducing fuel cell efficiency [18].

Recently, Goodenough *et al.* [19] reported a superior oxide-ion electrolyte family of monoclinic doped $SrMO_3$-based oxide ion conductors (M = Si, Ge) as promising candidates for intermediate temperature-solid oxide fuel cells (IT-SOFC), which shows good ionic conductivity values ($\sigma \geq 10^{-2}$ $S.cm^{-1}$), at intermediate temperatures (625ºC). The introduction of a cation at the Sr-site of $SrMO_3$, such as K^+, was shown to cause reduction of the unit-cell volume, which led to the introduction of terminal-oxygen vacancies on tetrahedral anion complexes ions, providing elevated oxide-ion conductivity. Terminal-oxygen vacancies can be formed by the not accommodation in corner sharing with a neighbouring M_3O_9 unit, or by distortion promoted accommodation creating an interstitial mobile oxide ion. In order to stabilize terminal-oxygen vacancy in a tetrahedral anion complex, steric hindrance in the system is used and represents a novel design principle for oxide-ion electrolytes. This research assessed if these materials could be formed by mechanochemical process and the role of the ionic radius of the alkaline earth metal cation (namely, potassium) on the crystallographic structure, compositional homogeneity and ionic transport.

2.1 REFERENCES

[1] Minh, N.Q. (1993). “Ceramic Fuel Cells.” Journal of the American Ceramic Society **76(3):** 563-568.

[2] Kjølseth, C., Fjeld, H. and Vestre, P.K. “Proton ceramic fuel cell.” Patent WO 2011/131657 A1 (2011).

[3] Haile, S.M. (2003). “Fuel cell materials and components.” Acta Materialia **51(19):** 5981-6000.

[4] Kreuer, K.D. (2003). “Proton-Conducting Oxides.” Annual Reviews Materials Research **33:** 333-359.

[5] Iwahara, H., Esaka, T., Uchida, H. and Maeda, N. (1981). “Proton conduction in sintered oxides and its application to steam electrolysis for hydrogen production.” Solid State Ionics **3/4:** 359-363.

[6] Bohn, H.G. and Schober, T. (2000). “Electrical Conductivity of the High-Temperature Proton Conductor $BaZr_{0.9}Y_{0.1}O_{2.95}$.” Journal of the American Ceramic Society **83(4):** 768-772.

[7] Yamazaki, Y., Hernandez-Sanchez, R. and Haile, S.M. (2009). “High Total Proton Conductivity in Large-Grained Yttrium-Doped Barium Zirconate.” Chemistry of Materials **21(13):** 2755-2762.

[8] Babilo, P. and Haile, S.M. (2005). “Enhanced Sintering of Yttrium-Doped Barium Zirconate by Addition of ZnO.” Journal of the American Ceramic Society **88(9):** 2362-2368.

[9] Tao, S. and Irvine, J.T.S. (2006). “A Stable, Easily Sintered Proton-Conducting Oxide Electrolyte for Moderate-Temperature Fuel Cells and Electrolyzers.” Advanced Materials **18(12):** 1581-1584.

[10] Ricote, S. and Bonanos, N. (2010). “Enhanced sintering and conductivity of cobalt or nickel doped solid solution of barium cerate and zirconate.” Solid State Ionics **181:** 694-700.

[11] Tong, J.H., Clark, D., Bernau, L., Sanders, M. and O’Hayre, R. (2010). “Solid-state reactive sintering mechanism for large-grained yttrium-doped barium zirconate proton conducting ceramics.” Journal of Materials Chemistry **20:** 6333-6341.

[12] Park, J.-S., Lee, J.-H., Lee, H.-W. and Kim, B.-K. (2010). “Low temperature sintering of $BaZrO_3$-based proton conductors for intermediate temperature solid oxide fuel cells.” Solid State Ionics **181:** 163-167.

[13] Ito, N., Matsumoto, H., Kawasaki, Y., Okada, S. and Ishihara, T. (2008). “Introduction of In or Ga as a second dopant to $BaZr_{0.9}Y_{0.1}O_{3-\delta}$ to achieve better sinterability.” Solid State Ionics **179:** 324-329.

[14] Imashuku, S., Uda, T., Nose, Y. and Awakura, Y. (2010). “Effect of isovalent cation substitution on conductivity and microstructure of sintered yttrium-doped barium zirconate.” Journal of Alloys and Compounds **490:** 672-676.

[15] Ryu, K.H. and Haile, S.M. (1999). “Chemical stability and proton conductivity of doped $BaCeO_3$-$BaZrO_3$ solid solutions.” Solid State Ionics **125:** 355-367.

[16] Wei, T., Singh, P., Gong, Y., Goodenough, J.B., Huang, Y. and Huang, K. (2014). “$Sr_{3-3x}Na_{3x}Si_3O_{9-1.5x}$ (x = 0.45) as a superior oxide-ion electrolyte for intermediate temperature-solid oxide fuel cells.” Energy & Environmental Science **7:** 1680-1684.

[17] Tealdi, C., Malavasi, L., Uda, I., Ferrara, C., Berbenni, V. and Mustarelli, P. (2014). “Nature of conductivity in $SrSiO_3$-based fast ion conductors.” Chemical Communications **50:** 14732-14735.

[18] Jacobson, A.J. (2010). “Materials for Solid Oxide Fuel Cells.” Chemistry of Materials **22(3):** 660-674.

[19] Singh, P. and Goodenough, J.B. (2012). “$Sr_{1-x}K_xSi_{1-y}Ge_yO_{3-0.5x}$: a new family of superior oxide-ion conductors.” Energy & Environmental Science **5:** 9626-9631.

CHAPTER 3. EXPERIMENTAL PROCEDURES

3.1 SYNTHESIS METHOD: MECHANOCHEMICAL AND/OR MECHANOSYNTHESIS

The term mechanochemistry was introduced by Ostwald and was used to describe a mechanism where mechanical force can be used to induce chemical reactions [1]. However, nowadays different terms are in use to describe different synthesis techniques related to the use of mechanical energy, such as mechanical alloying, mechanochemical processing, mechanical activation or mechanosynthesis [2].

The current work reports the formation of $BaZrO_3$ and $BaGeO_3$ based nanopowders by room temperature mechanosynthesis. The processing of nanocrystalline materials using mechanosynthesis is of particular interest in the preparation of a variety of functional ceramic materials, such as complex oxides with perovskite and spinel structures, layer structures, magnetic materials or ceramic nanocomposites. Compared with alternative synthesis techniques, mechanosynthesis is a cheap, quick and efficient method that can achieve highly reactive and homogeneous nanopowders. Additionally, it has been recognized that powder mixtures can be mechanically activated to induce reactions at temperatures much lower than normally required. These mechanical processes offer the advantage that they are non-polluting processes in the formation of nanostructured powders which can exhibit high compatibility and improved sinterability to allow the formation of ceramic materials at lower temperature. For example, the density and grain growth of $BaZrO_3$-based samples obtained by mechanosynthesized powder compacts show highly competitive levels, in comparison with the same materials formed by alternative powder preparation in similar sintering conditions (table 3.1). Furthermore, the formation of $BaCO_3$ as an impurity phase on decomposition of organics is also a common problem of soft chemical synthesis route, requiring additional calcination steps to remove and may add to compositional inhomogeneity and powder coarsening, defeating the primary purpose of such low temperature synthesis techniques. Antunes *et al.* [4] showed that mechanosynthesis offers a method of producing of $BaZrO_3$-related nanopowders with very low contamination levels of barium carbonate, with levels only detectable by FT-IR, a technique of very high sensitivity (fig. 3.1) [3].

Table 3.1 – Comparison of density of mechanosynthesized composition x = 0.148 after 420 minutes of milling time with literature values for $BaZr_{1-x}Y_xO_{3-\delta}$ prepared by different synthesis techniques in similar sintering conditions (adapted from [4]).

x	Preparation method	Densification rate	Sintering temperature	Ramp rate	Dwell	Covered	Reference
0.1	Sol-gel-acrylates	95%	1500ºC	1.5ºC.min^{-1}	15 hours	Yes	[5]
0.1	Spray pyrolysis	90.6%	1500ºC	n/a	1 hour	n/a	[6]
0.1	Spray pyrolysis	68%	1500ºC	n/a	n/a	n/a	[7]
0.1	Sol-gel	65%	1500ºC	n/a	n/a	n/a	[7]
0.1	Solid state	64%	1500ºC	n/a	n/a	n/a	[7]
0.1	Spray dried	59%	1500ºC	n/a	n/a	n/a	[7]
0.148	Mechanosynthesis	90.2%	1500ºC	5ºC.min^{-1}	10 hours	Yes	[4]
0.2	Sol-gel-alkoxides	99%	1500ºC	n/a	20 hours	n/a	[8]
0.2	Sol-gel-polyacrymide	95%	1500ºC	n/a	10 hours	Surface removed	[9]

* n/a: not available data

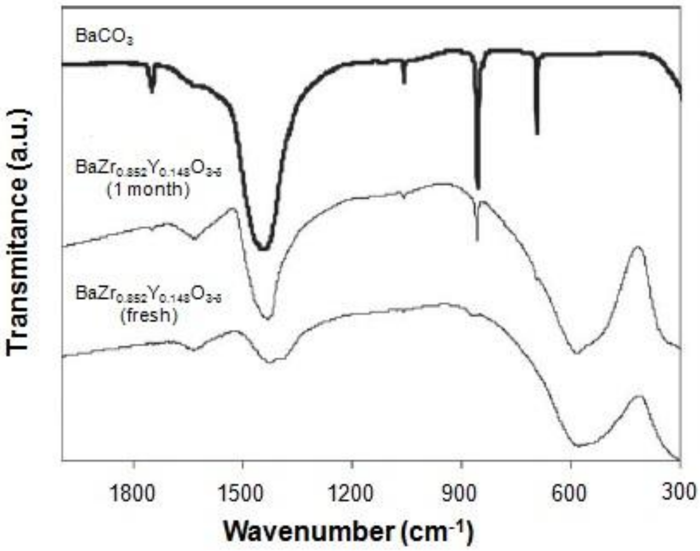

Fig. 3.1 - Comparison between FT-IR spectra of undried $BaCO_3$ commercial powder with mechanosynthesized $BaZr_{0.852}Y_{0.148}O_{3-\delta}$ fresh powder and after 1 month of exposure at atmospheric (adapted from [4]).

Mechanosynthesis is performed in a high energy planetary ball mill. During ball milling the powders particles in the container are repeatedly deformed, cold-welded, fractured and re-welded. Nonetheless, the energy imparted is mostly lost in the form of heat and only a minor amount is spent in the elastic and plastic deformation of the powder particles [10].

The planetary ball mill owes its name to the planet-like movement of its milling containers, which are arranged on a rotating support disk with a special drive mechanism that rotates them around their own axes. The centrifugal forces produced by the vials rotating around their own axes and by the rotational support disk act on the material being processed and on the milling balls. Since the two rotational movements occur in opposite directions, their superimposition gives rise to the so-called Coriolis forces: the combined centrifugal forces lift off the milling balls across the inner chamber of the container and make them collide against the opposing inner wall of the container particles [10,11]. Figure 3.2 shows a schematic representation of the working principle of a planetary ball mill.

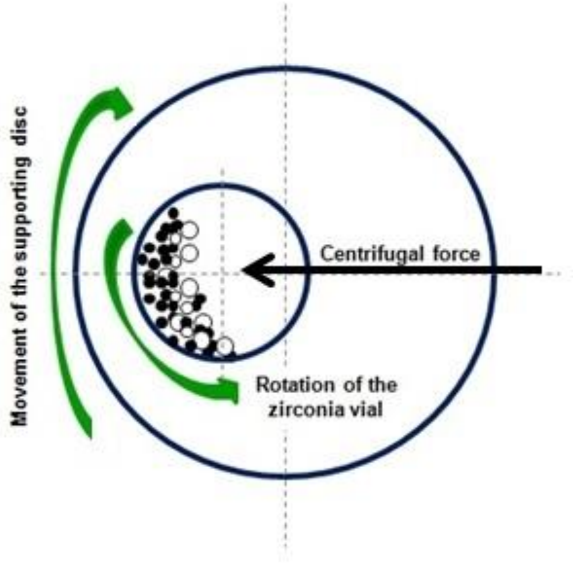

Fig. 3.2 - Schematic representation of a high energy planetary ball mill shown in a horizontal section (adapted from [11]).

The material used for the milling containers and balls must be suitably selected due to the high-energy impact of the milling balls on its inner walls. In order to minimize contamination by the impact of the balls on the milling media, it is a benefit if the vials and the spheres could be made of the same material as the processing powder particles [10].

According to the described assumptions, in the current work, the milling experiments were conducted in a planetary ball mill (Retsch PM200 – fig. 3.3a) with constant planetary rotation of 650 rpm using 125 cm^3 tetragonal zirconia vials (Retsch – fig. 3.3b) and balls (TOSOH Co. – fig. 3.3c).

Fig. 3.3 – (a) High energy planetary ball mill (Retsch PM200), (b) 125 cm^3 tetragonal zirconia vials (Retsch) and (c) tetragonal zirconia balls with 10 mm and 15 mm of diameter (TOSOH Co.).

The size of the balls has also influence in the milling efficiency through the impact for generated particles. Two different sizes were chosen: 10 mm and 15 mm. The weight ratio between the balls and the powder must also be considered once higher ball weight proportions increase the number of collisions per unit of time and, consequently, the energy transferred to the powder particles, reducing the processing time [10]. So, the ball to powders weight ratio used was around 10:1.

Lastly, the extent to which the container is filled must also be carefully analysed once the balls and the powders should be allowed to move freely. It means that the container should not be occupied with more than 50% of its total volume, which means that the maximum amount of powder is 5 g.

According to Antunes and co-workers [4] $BaZrO_3$-based materials prepared by mechanosynthesis produce heat due to the exothermic reaction. In order to avoid excess build-up of heat, the milling was performed during periods of 5 minutes with a subsequent pause for the same period of time. After each interruption, the direction of rotation was reversed. As some gas product is also produced, the vials were regularly opened to release this gas, as this has been shown to be important to assist reaction progression.

Produced powders often shows agglomerates up to 100 μm with low densities, consisting of aggregates which are comprised of composites of nanosized crystallites (fig. 3.4).

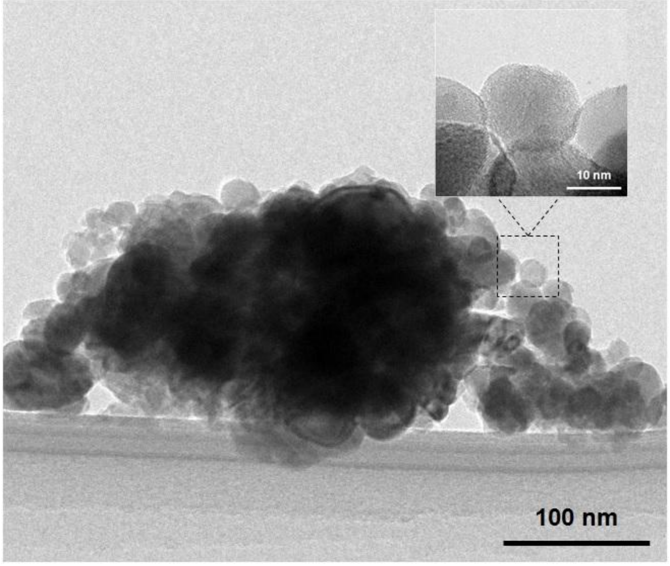

Fig 3.4 - TEM image of $BaZr_{0.852}Y_{0.148}O_{3-\delta}$ powder produced by mechanosynthesis showing agglomerate composed by aggregates of nanosized crystallites. The inset shows an example of a nanocrystallite.

3.2 POWDER SYNTHESIS

3.2.1 $Ba(Zr,Y)O_{3-\delta}$: MATERIALS PREPARATION

Powders of $Ba(Zr,Y)O_{3-\delta}$ were synthesized by the mechanosynthesis method [4]. According to Antunes [4], high energy milling of BaO_2 with high purity ZrO_2 and/or $(ZrO_2)_{0.92}(Y_2O_3)_{0.08}$ precursors at 650 rpm in zirconia vials, leads to mechanochemical reaction and the formation of the correspondent perovskite: $BaZrO_3$ and/or $BaZr_{0.852}Y_{0.148}O_{3-\delta}$, respectively. These experiments were preceded by thermodynamic analysis for use as a guide in the selection of the most favourable precursors to achieve the one step mechanosynthesis of each material composition and experimentally checked. $BaCO_3$ was proven to be not effective for the mechanochemical reaction, a factor that can be related with its higher thermodynamic stability in comparison with BaO_2, as predicted by the thermodynamic analysis software.

According to the described assumption, for $BaZrO_3$, stoichiometric quantities of precursors: barium peroxide (Sigma-Aldrich, 95% purity), with zirconium (IV) oxide (TZ-0Y, TOSOH Co.) were used, while the preparation of $BaZr_{0.852}Y_{0.148}O_{3-\delta}$ was performed using barium peroxide (Riedel-de-Häen, 99% purity) with $(ZrO_2)_{0.92}(Y_2O_3)_{0.08}$ (TZ-8Y, TOSOH Co.), or ZrO_2 (TZ-0Y, TOSOH Co.) and Y_2O_3 feinst (Herman C. Starck Berlin). The commercial powder of barium peroxide is a mixture of 95 mol% BaO_2 and 5 mol% $BaCO_3$. Thus, in order to calculate the exact quantities of each component, thermogravimetric analysis (TGA) in flowing CO_2 were performed, using a Netzsch STA 449F3 (fig. 3.5) with a 1600°C rod by complete carbonation of a sample in flowing CO_2.

The milling experiments were conducted in the planetary ball mill at 650 rpm and the grinding time was 7 hours. The final powder was kept in vacuum dessicator to avoid humidification and carbonation in air.

Fig. 3.5 – TGA/DSC from Netzsch (STA 449F3).

3.2.2 (Ba,Sr)GeO_3: MATERIALS PREPARATION

Powders of (Ba,Sr)GeO_3 were also synthesized by the mechanosynthesis method from a stoichiometric amount of mixed BaO_2 (Sigma-Aldrich, 95% purity) or SrO_2 (Sigma-Aldrich, 98% purity) and high purity GeO_2 (Sigma-Aldrich, ≥99.99% trace metal basis). Powders were mixed in a high energy planetary ball mill at 650 rpm in zirconia vials for 5 hours. Samples were isostatically pressed at 200 MPa and heated at 1100ºC for 5 hours.

As previously noted, the commercial powder of barium peroxide is a mixture of 95 mol% BaO_2 and 5 mol% $BaCO_3$. Correspondingly, the commercial powder of strontium peroxide is a mixture of 98% SrO_2 and 2 mol% of $SrCO_3$. Hence, according to that described in the previous section (3.2.1), the exact quantities of each component were confirmed by thermogravimetric analysis (TGA) in flowing CO_2 with a 1600°C rod by complete carbonation of a reference sample.

3.3 MATERIALS CHARACTERIZATION: METHODS AND WORKING PRINCIPLES

3.3.1 X-RAY DIFFRACTION: PHASE ANALYSIS, LATTICE PARAMETERS AND CRYSTALLITE SIZE

X-ray diffraction is one of the most powerful tools for crystalline phase identification. It is, performed by comparing the position intensities of the diffraction peaks against a library of phase information. Coexisting phases can be identified with a detection limit of ~ 1 wt% for similar diffracting powers and quantified from the relative integrated intensity of the peaks [12].

In this work, the progression of reactions were monitored by X-ray diffraction (XRD) analysis of powder samples collected at regular periods of time, using a Rigaku Geigerflex diffractometer in the range $10 \leq 2\theta \leq 90°$ with Cu $K\alpha$ radiation, and scan rate of $1.5°.min^{-1}$ (fig. 3.6). The millings were stopped when no further crystallographic changes were observed.

Fig. 3.6 – X-ray-diffractometer (Rigaku Geigerflex).

Cell parameters can be determined from the x-ray patterns through the central position of each diffraction peak and are sensitive to the material chemical composition. Rietveld refinement is a technique used in the characterisation of crystalline materials. This method uses a least squares approach to refine a theoretical line profile until it matches the measured profile.

In the current work, unit-cell parameters were determined from the diffraction data using Fullprof software. The program has been mainly developed for Rietveld analysis (structure profile refinement) of XRD data collected at constant or variable step in scattering angle 2θ. It also allows the determination of shape and symmetry parameters as well as preferred orientation and strain [13].

All XRD patterns exhibit peak broadening which may arise due to the combined effect of a crystallite size in a nanometric range and lattice strain, both typical consequences of high energy milling. Crystallite size is commonly defined as the size of the crystalline domains. On the other hand, lattice strain is usually a consequence of the crystalline defects induced by milling. The Scherrer equation and the Williamson-Hall method can be used to access the two contributions to the peak broadening observed in the X-ray diffractograms perovskite nanopowders. However, the Scherrer equation attributes peak broadening exclusively to crystal size, not taking into account microstrain (equation 3.1) [14]:

$$D = \frac{k\,\lambda}{\beta\ \cos\theta} \tag{3.1}$$

where k is a shape factor, λ is a X-ray wavelength, β is full width at half maximum and θ is the X-ray angle.

On the other hand, the Williamson-Hall approach enables to separate the two effects: crystallite size and microstrain effect (equation 3.2) [15]:

$$\left(\frac{\beta *}{d *}\right)^2 \approx \frac{1}{\varepsilon}\left(\frac{\beta *}{d *^2}\right) + \left(\frac{\eta}{2}\right)^2 \tag{3.2}$$

where β* is the integral breath and d* is the interplanar distance, both in reciprocal space units; ε is the average apparent diameter; and η is the mean lattice strain.

The Williamson-Hall method has been used in the calculations of crystallite size in the current work, once it is a more precise approach. According to equation 3.2, the representation of β* and d*, *i.e.* β*/(d*)2 vs $(\beta*/d*)^2$x10^4, gives the Williamson-Hall plot. Linear regression of this plot allows to estimate the crystallite size, ε (calculated from the slope of the regression), and the mean lattice strain, η (calculated from the intersection at the origin) [4].

3.3.2 SCANNING ELECTRON MICROSCOPY (SEM): MICROSTRUCTURE ANALYSIS AND CHEMICAL COMPOSITION

Scanning electron microscopy (SEM) is a powerful technique capable of producing images of a sample by scanning it with a focused beam of electrons. The electrons interact with atoms in the sample, producing various signals that can be detected and that contain information about the sample's surface: topography and composition. SEM can produce images with resolution of around 1 nm [16].

The scanning electron microscope is a machine comprised of an electron generating component, the gun; a column through which the electron beam travels; a series of lenses to shape the electron beam; the sample chamber; and a series of vacuum pumps to keep the equipment interior under vacuum [17].

In the current work, microstructural detail and chemical composition was investigated by scanning electron microscopy (SEM) using a Hitachi 4100S instrument (fig. 3.7) coupled with energy dispersive X-ray spectroscopy (EDS). Generally, bulk samples were analysed as a fracture section or a polished top surface. A carbon coating was applied to the sample to provide conductive path, and to avoid charging of the sample inside the microscope.

Average grain sizes were calculated from SEM images, using the image processing program Image J 1.37v software (Wayne Rasband, National Institutes of Health, USA). This software determines the number of grains per unit area. In order to have a correct approach of the grain size, at least a total of 200 grains were measured in different locations on the sample (multiple pictures).

Fig. 3.7 - Scanning electron microscope (Hitachi 4100S instrument).

3.3.3 DENSIFICATION: TEMPERATURE DEPENDENCE AND SHRINKAGE RATE

Densification measurements were performed in two ways: direct measurements of sample dimensions and weight (geometric measurements) and linear shrinkage after sintering.

In order to study the densification and the temperature dependence of the linear shrinkage rate, rectangular green compacts of as prepared material (1.4 × 0.5 × 0.3 cm^3) were isostatically pressed at 300 MPa during 15 minutes. The green compact was assessed dynamically using a Linseis L70/2001 dilatometer (fig. 3.8). Data was collected at a constant heating rate of $10°C.min^{-1}$ to 1500ºC under atmospheric conditions. The relative density (ρ_r) was corrected for thermal expansion using the following equation [18]:

$$\rho_r = \frac{\rho_i \times 100}{\rho_t(T) \times \left(1 + \frac{PLC_s(T)}{100}\right)^3} \tag{3.3}$$

where ρ_i is the initial density (direct measured of sample dimensions and weight, *i.e.*, geometric measurement), $\rho_t(T)$ is the theoretical density as a function of temperature, and $PLC_s(T)$ is the percentage linear change of the sample in the axial direction as a function of temperature. The value of $\rho_t(T)$ was determined by dilatometry using the expression:

$$\rho_t(T) = \frac{\rho_t\ (25)}{\left(1 + \frac{PLC_p(T)}{100}\right)^3} \tag{3.4}$$

where $\rho_t(25)$ is the room temperature theoretical density and $PLC_p(T)$ is the percentage linear change of a pre-densified sample in the axial direction as a function of temperature.

Fig. 3.8 - Linseis L70/2001 dilatometer.

3.3.4 CONDUCTIVITY CHARACTERIZATION: IMPEDANCE SPECTROSCOPY

Impedance spectroscopy is a powerful analytical tool for characterizing electrical properties of materials and their interfaces with electrodes. It has the capability to distinguish different responses contribution to the total resistance and is commonly conducted in a symmetric cell configuration, denoting two identical electrodes applied to the faces of the sample with uniform gas on both sides. A small electrical perturbation voltage is applied (equation 3.5) and the response is measured by equation 3.6:

$$v(t) = V_0 \, sin(wt) \tag{3.5}$$

$$i(t) = I_0 sin\,(wt + \theta) \tag{3.6}$$

The voltage "*v*" and resultant current "*i*" will be in phase only for a pure resistor, *i.e.* θ = 0º, whilst for a pure capacitor "*i*" would lead "*w*" by a phase angle of 90º (θ = 90º). It means that a real system would consist of both a capacitive and a resistive term [19].

The A.C. impedance can be described by equation 3.7, *i.e.* the ratio between the A.C. voltage and the A.C. current in the frequency domain [19].

$$Z(j, w) = \frac{V_0 \, e^{\,jwt}}{I_0 \, e^{\,j\,(wt + \theta)}} = Z_0 \, e^{-j\theta} \tag{3.7}$$

The complex impedance is typically represented in a Nyquist plot (fig. 3.9), where the imaginary part of the impedance is plotted as a function of the real part. According to figure 3.9, there are three arcs, each one responsible for a distinct phenomenon: grain interior/bulk (arc 1), grain boundary (arc 2) and electrode (arc 3) [20].

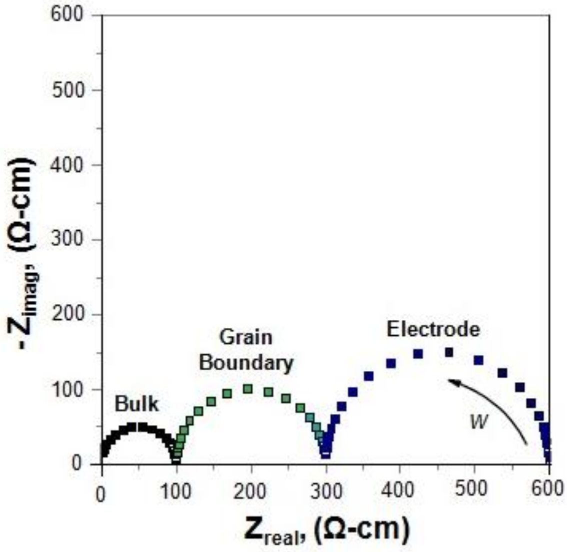

Fig. 3.9 - Example of a Nyquist plot for three unique processes: grain interior/bulk, grain boundary and electrode (adapted from [20]).

Each process is characterized by a typical capacitance value as shown in table 3.2.

Table 3.2 - Typical capacitance values shown together with the component phenomenon responsible (adapted from [20]).

Capacitance	**Phenomenon responsible**
10^{-12}	Grain interior / bulk
10^{-11}-10^{-8}	Grain boundary
10^{-7}-10^{-5}	Electrode

The characteristic frequency is a material constant and independent of sample geometries (equation 3.8) [19]:

$$w_0 = \frac{1}{R\,C} \tag{3.8}$$

The unique processes of the polycrystalline materials are modelled as RC circuits in series as shown in fig. 3.10. For each arc in the plot, the resistor describes the resistance of the process to a moving charge, while the capacitance describes the dielectric response of the process [21].

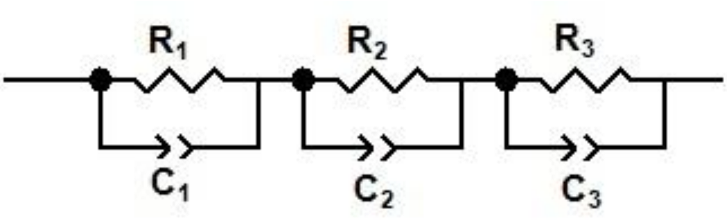

Fig. 3.10 - Equivalent circuit to model a three-process system.

The three phenomenon responses from impedance spectroscopy can be described by the “brick layer model” (fig. 3.11). It was adopted to optimize the full extent of information that can be extracted from the measured electrical data [22].

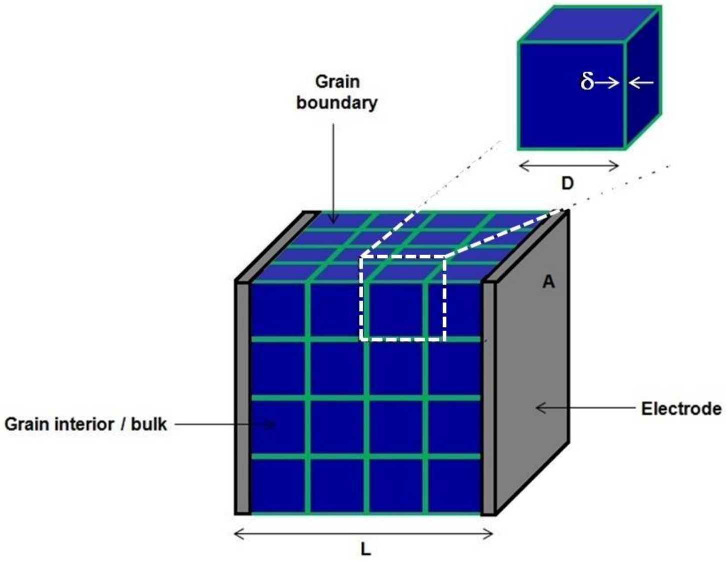

Fig. 3.11 - “Brick layer model” of a polycrystalline material (adapted from [22]).

From figure 3.11, L is the sample length, A is the sample cross sectional area, D is the average grain size and δ is the average grain boundary thickness. When $\sigma_i > \sigma_{gb}$ and δ >> D, the current will follow the grain interiors only passing through the series grain boundaries as a means to get from one grain to another. This will result in two distinguishable arcs, where the high frequency arc is assigned to the grain interior and the low frequency one is identified as the total grain boundary response [22].

According to what is shown in the Nyquist plot (fig. 3.10), the resistance due to the grain interior and total grain boundary can be easily extracted. Given that the characteristic frequencies are sufficiently different from one another, a complete semi-circular arc can be seen where the diameter reveals the resistance for that specific process (R). The resistivity (ρ) and the conductivity (σ) can be calculated by [23]:

$$\sigma = \frac{1}{\rho} = \frac{L}{R\,A} \tag{3.9}$$

where L and A are sample dimensions, length and cross sectional area, respectively.

From equation 3.9, the total grain boundary conductivity is a measure of both the grain boundary geometry and the inherent properties of the grain boundaries. Using the brick layer model, it can be estimated as [23]:

$$\delta_{g.b.} = \frac{L}{A}\left(\frac{C_{bulk}}{C_{gb}}\right)\frac{1}{R_{gb}} \tag{3.10}$$

where R_{gb} is the grain boundary resistance extracted from the impedance spectra, and C_{bulk} and C_{gb} are the bulk and boundary capacitances, respectively.

In this approximation, it is assumed that the dielectric constants are equal in the grain interior and grain boundary. Resulting in the ration of the capacitances being equal to the ration of grain boundary thickness (δ) to average grain size (D) [23]:

$$\frac{C_{bulk}}{C_{gb}} = \frac{\frac{A}{L}\,\varepsilon_{bulk}\,\varepsilon_0}{\frac{A}{L}\,\frac{D}{\delta}\,\varepsilon_{gb}\,\varepsilon_0} = \frac{\delta}{D} \tag{3.11}$$

Electrical-conductivity measurements were on samples prepared by isostatically pressing the as-prepared powders to 300 MPa for 15 minutes. The sintering conditions depended on the presence and type of sintering additive. Platinum wire was attached to the samples in a pseudo 4-point configuration using porous Pt-paste. Impedance spectroscopy was carried out using an Electrochemie Autolab PGSTAT302N analyser (fig. 3.12) in the frequency range 10^{-2} – 10^{6} Hz applying signal amplitude of 50 mV. Data was collected on cooling in different atmospheres, monitored by an inbuilt oxygen sensor. Stability was confirmed by performing repeated impedance measurements at each temperature. Humidification was achieved by bubbling the gas through water then a saturated KCl solution in contact with solid KCl, producing approximately 86% relative humidity at room temperature. The impedance data were de-convoluted using the ZView program to obtain contributions ascribed to bulk, grain boundaries and external interfaces, as suggested by typical capacitance values in the ranges of ~1 pF/cm^2, about 0.1-1 nF/cm^2, and about 0.1-1 μF/cm^2, respectively [24].

Fig. 3.12 - Electrochemie Autolab PGSTAT302N analyser.

Activation energies (Ea) for the bulk and specific grain boundary conductivities were calculated by the standard Arrhenius equation (equation 3.12) where A_o is the pre-exponential factor.

$$\sigma = \frac{A_o}{T} exp\left[-\frac{Ea}{RT}\right] \tag{3.12}$$

An example of a typical impedance spectrum for BZY-based materials is shown in fig. 3.13. In this case, the impedance response can be seen to be dominated by the grain boundary response [25]. Bulk response is only observable at the highest frequencies.

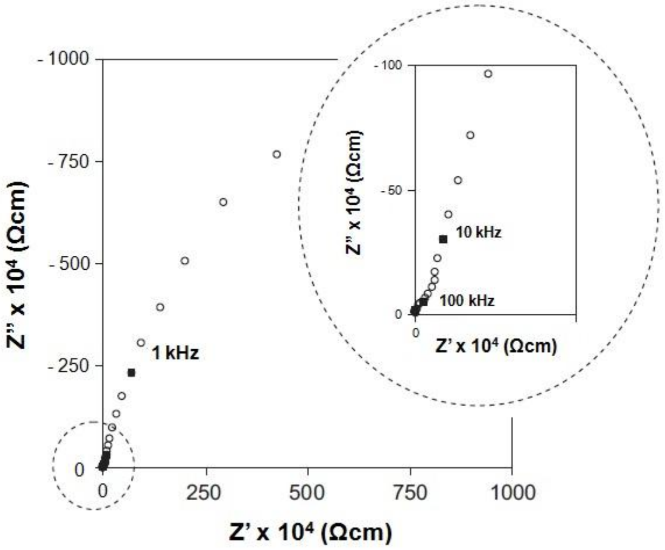

Fig. 3.13 - Typical impedance spectrum at low temperatures. The grain boundary response dominates the spectra. The inset reveals the bulk response at the highest frequencies (adapted from [25]).

3.4 REFERENCES

[1] Beyer, M.K. and Clause-Schaumann, H. (2005). “Mechanochemistry: the mechanical activation of covalent bonds.” Chemical Reviews **105(8):** 2921-2948.

[2] Zyryanov, V. (2005). “Ultrafast Mechanochemical Synthesis of Mixed Oxides.” Inorganic Materials **41(4):** 378-392.

[3] Xue, J.M., Zhou, Z.H. and Wang, J. (2004). “Nanocrystalline Ceramics by Mechanochemical Activation.” Encyclopedia of Nanoscience and Nanotechnology. H.S. Nalwa, American Scientific Publishers **6:** 417-433.

[4] Antunes, I., Brandão, A., Figueiredo, F.M., Frade, J.R., Grácio, J. and Fagg, D.P. (2009). “Mechanosynthesis of nanopowders of the proton-conducting electrolyte material $Ba(Zr,Y)O_{3-\delta}$.” Journal of Solid State Chemistry **182(8):** 2149-2156.

[5] Khani, Z., Taillades-Jacquin, M., Taillades, G., Marrony, M., Jones, D.J. and Rozière, J. (2009). “New synthesis of nanopowders of proton conducting materials. A route to densified proton ceramics.” Journal of Solid State Chemistry **182(4):** 790-798.

[6] Stuart, P.A., Unno, T., Ayres-Rocha, R., Djurado, E. and Skinners, S.J. (2009). “The synthesis and sintering behaviour of $BaZr_{0.9}Y_{0.1}O_{3-\delta}$ powders prepared by spray pyrolysis.” Journal of the European Ceramic Society **29(4):** 697-702.

[7] Azad, A.K., Savaniu, C., Tao, S., Duval, S., Holtappels, P., Ibberson, R.M. and Irvine, J.T.S. (2008). “Structural origins of the differing grain conductivity values in $BaZr_{0.9}Y_{0.1}O_{2.95}$ and indication of novel approach to counter defect association.” Journal of Materials Chemistry **18:** 3414-3418.

[8] Cervera, R.B., Oyama, Y. and Yamaguchi, S. (2007). “Low temperature synthesis of nanocrystalline proton conducting $BaZr_{0.8}Y_{0.2}O_{3-\delta}$ by sol-gel method.” Solid State Ionics **178:** 569-574.

[9] Magrez, A. and Schober, T. (2004). “Preparation, sintering and water incorporation of proton conducting $Ba_{0.99}Zr_{0.8}Y_{0.2}O_{3-\delta}$: comparison between three different synthesis techniques.” Solid State Ionics **175:** 585-588.

[10] Suryanarayana, C. (2001). “Mechanical alloying and milling.” Progress in Materials Science **46:** 1-184.

[11] Gu, D. and Shen, Y. (2009). “Microstructures and properties of high Cr content coatings on inner surfaces of carbon steel tubular components prepared by a novel mechanical alloying method.” Applied Surface Science **256(1):** 223-230.

[12] Zhao, Z., Buscaglia, V., Viviani, M., Buscaglia, M.T., Mitoseriu, L., Testino, A., Nygren, M., Johnsson, M. and Nanni, P. (2004). “Grain-size effects on the ferroelectric behaviour of dense nanocrystalline $BaTiO_3$ ceramics.” Physical Review B **70:** 1-8.

[13] Rodriguez-Carvajal, J. (1993). “Recent advances in magnetic structure determination by neutron powder diffraction.” Physica B **192:** 55-69.

[14] Patterson, A.L. (1939). “The Scherrer Formula for X-ray Particle Size Determination.” Physical Review **56:** 978-982.

[15] Williamson, G.K. and Hall, W.H. (1953). “X-ray line broadening from filled aluminium and wolfram.” Acta Metallurgica **1:** 22-31.

[16] http://www.ammrf.org.au/myscope/sem/practice/principles/; accessed on October 6, 2013; activity of the Australian Microscopy & Microanalysis Research Facility; created in 2011.

[17] http://www.ammrf.org.au/myscope/sem/practice/principles/; accessed on October 6, 2013; activity of the Australian Microscopy & Microanalysis Research Facility; created in 2011.

[18] Nicholas, J.D. and De Jonghe, L.C. (2007). “Prediction and evaluation of sintering aids for cerium gadolinium oxide.” Solid State Ionics **178:** 1187-1194.

[19] MacDonald, J.R. and Johnsson, W.B. (1988). “Impedance spectroscopy.” J.R. MacDonald Wiley and Sons, New York.

[20] Maxwell, J.C. (1954). “A treatise on electricity and magnetism.” Clarendon Press, Oxford, 2nd edition.

[21] Brandão, A.D., Antunes, I., Frade, J.R., Torre, J., Mikhalev, S.M. and Fagg, D.P. (2012). “Mechanochemical preparation, sintering aids and hybrid microwave sintering in the proton conductor $Sr_{0.02}La_{0.98}Nb_{1-x}V_xO_{4-\delta}$, x = 0.015.” International Journal of Hydrogen Energy **37(8):** 7252-7261.

[22] Haile, S.M., West, D.L. and Campbell, J. (1998). “The role of microstructure and processing on the proton conducting properties of gadolinium-doped barium cerate.” Journal of Materials Research **13(6):** 1576-1595.

[23] Haile, S.M., Staneff, G. and Ryu, K.H. (2001). “Non-stoichiometry, grain boundary transport and chemical stability of proton conducting perovskites.” Journal of Materials Science **36(5):** 1149-1160.

[24] Bauerle, J.E. (1969). “Study of solid electrolyte polarization by a complex admittance method.” Journal of Physics and Chemistry of Solids **30(12):** 2657-2670.

[25] Yamazaki, Y., Hernandez-Sanchez, R. and Haile, S.M. (2010). “Cation non-stoichiometry in yttrium-doped barium zirconate: phase behaviour, microstructure, and proton conductivity.” Journal of Materials Chemistry **20:** 8158-8166.

CHAPTER 4. Ba(Zr,Y)$O_{3-\delta}$ MATERIALS: SINTERING ADDITIVES

Yttrium-doped barium zirconate (BZY) is considered to be one of the most promising materials for application in IT-SOFC due to its good stability in CO_2 and high bulk proton conductivity [1,2]. Nevertheless, several challenges still exist for its implementation in functional devices, as outlined in Chapter 1. This material exhibits a high grain-boundary resistance that is compounded by poor densification and poor grain growth, requiring high sintering temperatures (~1700ºC) for its fabrication [3-8]. With the aim of improving these factors, several studies have focused on strategies to minimise grain boundary resistance by the promotion of grain growth, such as: reactive sintering [9], the introduction of sintering aids [10-14] or by doping strategies [15-17]. In this section, the effect of various potential co-dopants and sintering aids is studied.

Babilo *et al.* [10] provided an initial screening of all transition elements from Sc to Zn as potential sintering additives for yttrium-doped barium zirconate materials and showed NiO, CuO, and ZnO to be the most effective additives for enhancing barium zirconate densification. For the ZnO-case, these authors highlighted an optimal additive concentration of 4 mol% Zn that allowed peak densification at 1300ºC. Further increases in sintering temperature lead to decreases in density, possibly due to Zn volatilisation. Despite such valuable gains in densification, Zn-additions were observed to deplete levels of proton conductivity when compared to literature data of additive-free compositions [3-8]. Subsequent works, in general, reinforce these conclusions [10,11,18]. Ricote *et al.* [12] showed that improvements in densification could be obtained for minor Ni and Co additions (1-2 mol%), but noted that grain growth was only improved in the case of Ni-doping, an observation supported by Tong *et al.* [13] who studied slightly higher Ni-additive concentrations (3.5 to 7.5 mol%). Both groups reported depletions in conductivity with Ni-additions in the low temperature range, while slightly enhanced total conductivities were obtained at temperatures in excess of 500ºC for the more Ni-rich samples [13]. In all cases, the activation energy for total conductivity was shown to be seriously increased by addition of Ni as a sintering additive, suggesting an impairment of ionic motion or a shift to a larger electronic component. Cu-additions have been shown to mirror the results for Ni-additions. Park *et al.* [14] showed that Cu-additives enhance grain growth and stimulate densification, but have a negative impact on levels of total conductivity and activation energy for conduction.

Thus, despite their noted improvements in densification, the negative effects of these sintering additives on the levels of total conductivity needs to be fully understood. To date, the exact role of these additives in the enhanced sintering mechanism has not been clarified. Several authors have pointed out that there may be slight solubility of these sintering additives in the main perovskite phase due to compatible lattice parameters for a B-site location. Hence, the current work offers an assessment of different methods to encompass these sintering additives in the proton ceramic with examination of their respective impacts on final levels of total conductivity. In the current work one will focus on Zn additions for this goal.

A slightly different approach can also be suggested, involving the search for redox stable sintering additives with ionic sizes much smaller than the average B-site ionic radius. Here, due to their small ionic size, these additives may be considered less likely to be accommodated in the bulk perovskite material and, hence, less likely to influence bulk conductivity. Lithium may be one potential additive that could fulfil these prerequisites, however, Tong *et al.* [13], showed LiF_2 to be relatively ineffective at improving densification when added to barium zirconate based materials. Phosphorous additions have been studied as potential sintering additives in analogous $BaTiO_3$ materials, with improvements in densification being obtained. However, the presence of barium phosphate as a secondary phase was shown to impact conductivity with the varying effects being obtained depending on sintering temperature. Although conductivities were impaired at sintering temperatures below 1275ºC, higher sintering temperatures lead to slight enhancements over the P-free base composition [19]. Additionally, Lee *et al.* [20] studied the densification of the material $Ba_{0.997}Y_{0.003}TiO_{3-\delta}$, as a function of boron additives in the form of BN or BaB_2O_4 additions. In their work, the densification temperature could be decreased by approximately 200ºC with respect to the additive free composition on addition of 4 mol% BN or 4 mol% BaB_2O_4 [20,21]. Moreover, for small additive levels, improvements in conductivity over the base material were also noted [21].

This chapter is, therefore, constituted by three individual studies concerning the use of sintering additives, such as oxides of Zn, P, and B, on $BaZrO_3$-based materials. From the use of these additives, it is hoped to confront the main issues limiting the performance of $BaZrO_3$-based materials, *i.e.* to lower sintering temperatures and increase grain size, which have the potential to enhance subsequent grain boundary conductivities, leading to gains in total proton conductivity.

The first work is related to study the potential of ZnO as a sintering additive, as a function of the adopted substitution mechanism. The effect of the addition method on the microstructure, lattice parameter, grain growth and conductivity (bulk and grain-boundary) of the bulk protonic ceramic are outlined, as well as an investigation of potential elemental segregation.

The following study concerns the study of the influence of phosphorous additions on the sintering and electrical transport properties of the proton-conducting perovskite $BaZr_{0.85}Y_{0.15}O_{3-\delta}$. The effect of P_2O_5 additions was studied in order to assess both the feasibility of the use of phosphate esters in BZY thin film preparation and the potential of phosphorus as a sintering additive. To understand the effect of phosphorus additions a barrage of tests were performed, such as: dilatometric measurements, XRD, SEM as well as impedance measurements.

The final section presents results for the densification of un-doped and Y-doped $BaZrO_3$ (BZO and BZY, respectively) with boron additions, using H_3BO_3, as a potential sintering additive. The effect of the solution doping method was an additional focus of this work. The study was based on dilatometric measurements complemented by XRD, SEM, Raman and FT-IR analyses, to understand the different mechanisms of B-addition.

4.1 OPTIMIZING THE SOLID SOLUTION MECHANISM FOR Zn-ADDITION TO Ba(Zr,Y)O$_{3-\delta}$

4.1.1 INTRODUCTION

Zinc oxide (ZnO) has been observed to be an effective sintering aid for BZY proton conducting electrolytes, lowering the sintering temperature from >1700ºC to 1300ºC, enhancing both densification to 93% of theoretical density and uniform grain growth. Despite such valuable gains, Zn-additions were observed to deplete levels of proton conductivity when compared to literature data of additive-free compositions [8,10,11,18,22]. By observing changes in lattice parameter, such depletions were suggested to be due to partial Zn-solubility in the main perovskite phase [18]. This has lead authors to suggest three possible mechanisms for Zn addition: a) $BaZr_{1-y-x}Zn_xY_yO_{3-\delta}$ [10], b) (1-x)$BaZr_{1-y}Y_yO_{3-\delta}$+xZnO [10,18] and c) $BaZr_{1-y}Y_{y-x}Zn_xO_{3-\delta}$ [18,22]. Nonetheless, to date, a direct comparison between these methods has not been presented. Following the discussion presented in the introduction, Chapter 1, the ability to achieve reproducibility in the conduction behaviour of $BaZrO_3$-based materials is highly dependent on their powder processing route. Thus, for the current study potential processing differences between these Zn addition methods for $BaZrO_3$-powders are avoided by the preparation of all materials by mechanosynthesis. It should further noted that the work of Tao *et al.* [18] discussed mechanism case c) in its introduction, however, the conductivity measurements presented were those of a different mechanism: (1-x)$BaZr_{1-y}Y_yO_{3-\delta}$-xZnO (mechanism b).

In mechanism a), the zirconium cation, Zr (IV), is partially substituted with a divalent cation, Zn (II). For charge compensation, oxide-ion vacancies are introduced (equation 4.1). This substitution mechanism would lead to a significantly higher oxygen vacancy concentration in comparison to substitution mechanism c) where the trivalent cation Y (III) is partially substituted by Zn (II), (equation 4.2). A higher oxygen vacancy concentration could increase the number of protonic carriers formed by hydration (described by equation 1.8) giving a positive boost to conductivity or, conversely, lead to negative effects such as poor stability or the formation of associated defects that may hinder protonic migration [8,10,23,24]. It is, therefore, necessary to experimentally test for these effects.

Mechanism a: $BaZr_{1-x-y}Zn_xY_yO_{3-\delta}$: $BaO_2 + (1-x-y)\,ZrO_2 + x\,ZnO + y\,YO_{1.5} \rightarrow$

$$Ba_{Ba}^{x} + (1-x-y)\,Zr_{Zr}^{x} + x\,Zn_{Zr}^{//} + y\,Y_{Zr}^{/} + (x+0.5y)\,V_{O}^{\cdot\cdot} + (3-x-0.5y)\,O_{O}^{x} \qquad (4.1)$$

$$\text{Mechanism c: } BaZr_{1-y}Y_{y-x}Zn_xO_{3-\delta}: \quad BaO_2 + (1-y)\,ZrO_2 + (y-x)\,YO_{1.5} + x\,ZnO \rightarrow \\ Ba_{Ba}^{x} + (1-y)\,Zr_{Zr}^{x} + x\,Zn_{Zr}^{//} + (y-x)\,Y_{Zr}^{/} + (0.5x+0.5y)\,V_{O}^{\cdot\cdot} + (3-0.5x-0.5y)\,O_{O}^{x} \tag{4.2}$$

Furthermore, assuming complete solubility of Zn in the perovskite lattice, the adoption of mechanism b) may induce sub-stoichiometry on A-site, where Zn is preferentially located on the B-site due to its more compatible ionic size – equation 4.3. This may have negative potential impacts on performance as in 2010, Yamazaki and his group [7] reported that the presence of Ba-deficiency in the parent BZY material was responsible for impaired grain growth and conductivity depletion. These authors related these effects to subsequent yttrium crossover to the A-site to accommodate the Ba vacancies that in turn by would result in a depleted number of oxygen vacancies to achieve charge balance.

$$\text{Mechanism b: } (1-x)BaZr_{1-y}Y_yO_{3-\delta} + x\,ZnO: \quad (1-x)\,BaO_2 + (1-x)(1-y)\,ZrO_2 + (1-x)y\,YO_{1.5} + x\,ZnO \rightarrow \\ (1-x)\,Ba_{Ba}^{x} + (1-x)(1-y)\,Zr_{Zr}^{x} + x\,Zn_{Zr}^{//} + (1-x)y\,Y_{Zr}^{/} + [x+0.5y(1-x)]\,V_{O}^{\cdot\cdot} \\ + [3-x+0.5y(1-x)]\,O_{O}^{x} \tag{4.3}$$

Furthermore, on excess addition of ZnO using substitution mechanism b) Peng *et al.* [8] observed the presence of Y_2O_3 as a secondary phase. Such yttrium expulsion from the perovskite phase may suggest that mechanism c) is the preferred substitution mechanism occurring in these materials at high Zn contents, perhaps overriding their nominal stoichiometry or that yttrium is expelled from the perovskite phase on extensive Ba-deficiency [7]. Hence, the current work aims to provide a detailed analysis of these mechanisms, with special focus on phase purity, potential elemental segregation and Zn solubility in the parent perovskite phase.

When one compares the perovskite tolerance factors of these three possible mechanisms one observes that an increase in tolerance factor arises only for mechanism c - fig. 4.1 (note this calculation is made for mechanism b assuming total solubility of Zn in the perovskite phase, equation 4.3, and partial crossover of yttrium to the A-site to accommodate Ba vacancies)

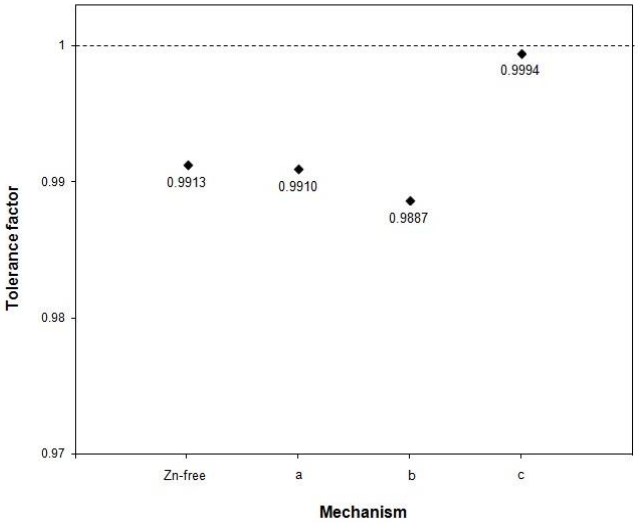

Fig. 4.1 – Tolerance factor comparison between Zn-free BZY and BZY doped with ZnO by three different mechanisms: a) $BaZr_{1-x-y}Zn_xY_yO_{3-\delta}$, b) (1-x) $BaZr_{1-y}Y_yO_{3-\delta}$ + x ZnO and c) $BaZr_{1-y}Y_{y-x}Zn_xO_{3-\delta}$.

Links between thermodynamic stability and tolerance factor are well known [25]. According to that described in section 1.3.1, the tolerance factor (t) of the ideal cubic close packed perovskite structure is that of unity. When distortions from the ideal perovskite configuration are present, “t” can be between 0.75 and 1, resulting in lower crystallographic symmetries, offering inferior thermodynamic stability and, commonly, also impaired ionic motion [26,27].

Babilo *et al.* [28] highlighted an optimal additive concentration of 4 mol% Zn, which allowed peak densification values of 95% that of the theoretical to be attained at 1300ºC, while remaining significantly lower than that causing elemental segregation.

In this work a comparison between the three described mechanisms will be performed for the base composition $BaZr_{0.852}Y_{0.148}O_{3-\delta}$ with respect to sintering behaviour and resultant conductivity for a fixed Zn content of 4 mol%: $BaZr_{0.852}Y_{0.108}Zn_{0.04}O_{3-\delta}$ (mechanism a), $0.96BaZr_{0.852}Y_{0.148}O_{3-\delta}+0.04ZnO$ (mechanism b) and $BaZr_{0.812}Zn_{0.04}Y_{0.148}O_{3-\delta}$ (mechanism c). It is possible that vast differences in conductivity may result due to the changing tolerance factor and associated defect chemistry [10,11,18].

4.1.2 PROCESSING METHODOLOGY

Zinc oxide was used as a potential sintering additive for $BaZr_{0.852}Y_{0.148}O_{3-\delta}$ (BZY), produced from BaO_2 (Sigma-Aldrich, 95% purity), ZrO_2 (TZ-0Y, TOSOH Co.) and Y_2O_3 feinst (Herman C. Starck Berlin). 4 mol% of ZnO (Sigma-Aldrich , ≥ 99% purity) was added to the system as a one-step reaction for Zr- and Y-deficient compositions, such as $BaZr_{0.852}Y_{0.108}Zn_{0.04}O_{3-\delta}$ (mechanism a) and $BaZr_{0.812}Zn_{0.04}Y_{0.148}O_{3-\delta}$ (mechanism c), respectively; and in a two-step process for Ba-deficient composition, $0.96BaZr_{0.852}Y_{0.148}O_{3-\delta}+0.04ZnO$ (mechanism b). In mechanisms a) and c), stoichiometric amounts of BaO_2, ZrO_2, Y_2O_3 and ZnO were mixed in a high energy ball mill (650 rpm for 7 hours). On the other hand, powders of $0.96BaZr_{0.852}Y_{0.148}O_{3-\delta}$ + 0.04ZnO (mechanism b) were prepared in two steps: starting with the preparation of $BaZr_{0.852}Y_{0.148}O_{3-\delta}$, synthesized by mechanosynthesis under identical conditions, (650rpm for 7 hours); while in the second stage of the reaction, the final powder was intimately mixed with stoichiometric amount of 4 mol% of ZnO for a further 3 hours at a rotation speed of 200 rpm.

Green pellets were obtained after being pressed isostatically at 300 MPa for 15 minutes.

Densification studies were assessed dynamically on green pellets by dilatometer measurements. Further assessment of density was assessed on green samples sintered at 1300ºC for 5 hours in air. Phase analysis and determination of lattice parameters were performed by X-ray diffraction (XRD) coupled with Reitveld refinement.

Microstructural detail was investigated on polished and thermally etched sintered samples by scanning electron microscopy (SEM) and transmission electron microscopy (TEM), using a Philips CM200 FEG coupled with STEM-XEDS equipment (Genessis 4000).

To characterize the electrical properties, measurements were performed on sintered pellets using electrodes formed by porous platinum paint. Data were collected on cooling in different flowing dry and wet atmospheres: N_2 and O_2 with repeated experiments performed after 1 hour at each temperature to confirm the attainment of stability. The electrical properties were also studied as a function of oxygen partial pressure (pO_2): various pO_2 values, obtained by mixing O_2 and N_2, were used in this work using dwell times of 2 hours under each condition, where stability was confirmed by repeated measurements after an additional dwell time of 1 hour.

4.1.3 RESULTS AND DISCUSSION

4.1.3.1 DENSIFICATION

The difference in sintering behavior between Zn-free and Zn-doped BZY is particularly evident in fig. 4.2 with large gains in densification being offered by the Zn-containing samples. However, densification levels are shown to not vary significantly between the three substitutions mechanisms.

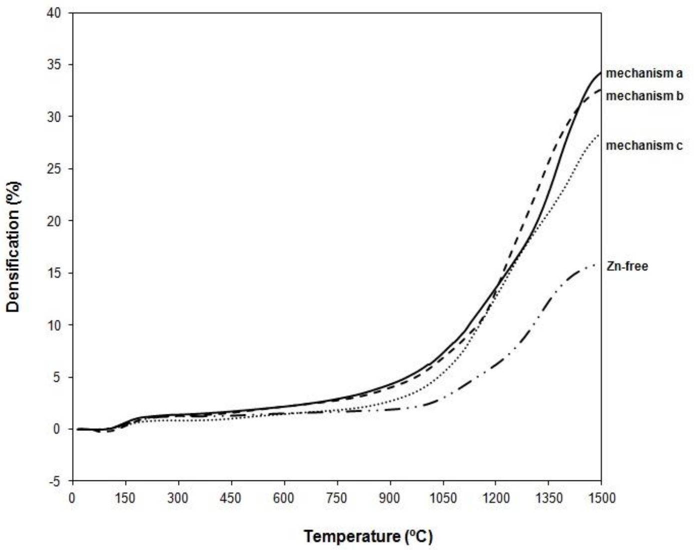

Fig. 4.2 - Densification behaviour of Zn-free and ZnO-doped BZY by three different mechanisms: a) $BaZr_{0.812}Zn_{0.04}Y_{0.148}O_{3-\delta}$, b) $0.96BaZr_{0.852}Y_{0.148}O_{3-\delta} + xZnO$ and c) $BaZr_{0.852}Y_{0.108}Zn_{0.04}O_{3-\delta}$.

From fig. 4.2, it is possible to conclude that the presence of zinc promotes densification to ~ 35% comparing to the Zn-free material, corresponding to final densities in excess of 98% that of the theoretical.

Fig. 4.3 compares the temperature dependence of the linear shrinkage rate as a function of the substitution mechanism on Zn additions. The presence of ZnO produces an increase in the maximum shrinkage rate for all mechanisms, while the temperature of maximum shrinkage rate is noted to shift to lower temperatures (just below 1300ºC) for mechanisms b) and c).

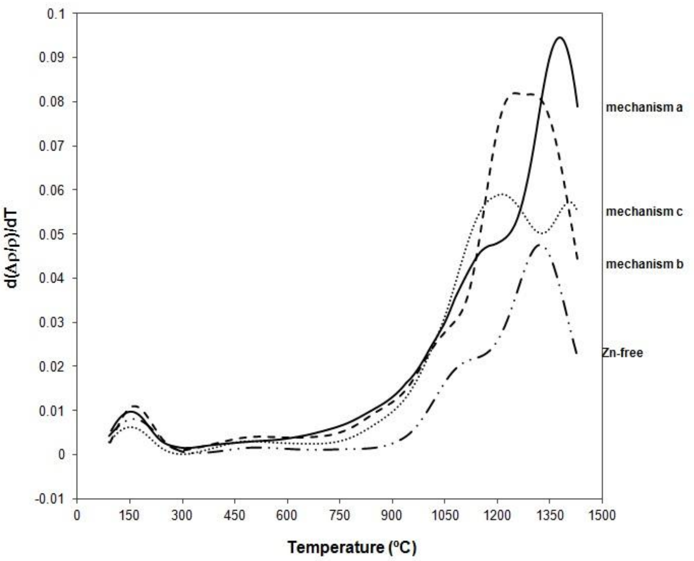

Fig. 4.3 - Temperature dependence of the linear shrinkage rate of Zn-free and Zn-modified $BaZr_{0.852}Y_{0.148}O_{3-d}$ as a function of substitution mechanism.

As evident from fig. 4.3, mechanism a) offers the maximum shrinkage rate of all mechanisms.

Based on further measurements, after firing fresh pelleted samples with and without ZnO additions at 1300ºC for 5 hours, the Zn-free $BaZr_{0.852}Y_{0.148}O_{3-\delta}$ did not reach full density, giving a final density lower than 80% that of the theoretical density, in comparison to the ZnO-added samples, which were all shown to be above ~ 98% dense.

4.1.3.2 PHASE ANALYSIS AND MICROSTRUCTURE

Fig. 4.4 shows the XRD patterns of Zn-doped BZY pellets sintered at 1300ºC for 5 hours. A single, well crystallized phase was obtained for all the compositions. The identified phase of the ZnO-added samples is that of the cubic perovskite structure (JCPDS #01-072-7549) which is similar to the Zn-free $BaZr_{0.852}Y_{0.148}O_{3-\delta}$ material prepared at 1600ºC for 5 hours, presented by Antunes *et al.* [6].

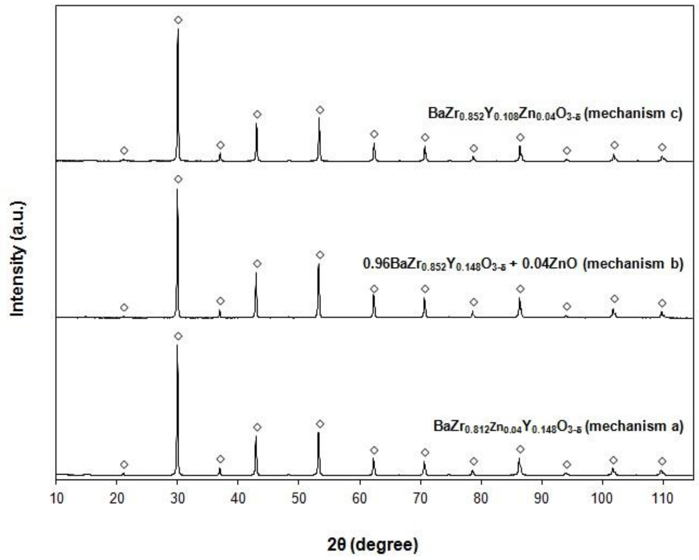

Fig. 4.4 - XRD patterns of sintered pellets of BZY doped with ZnO by three different mechanisms: a) $BaZr_{0.812}Zn_{0.04}Y_{0.148}O_{3-\delta}$, b) $0.96BaZr_{0.852}Y_{0.148}O_{3-\delta}+xZnO$ and c) $BaZr_{0.852}Y_{0.108}Zn_{0.04}O_{3-\delta}$, at 1300ºC for 5 hours. The markers (◊) identify the $BaZrO_3$- based phase (cubic perovskite structure).

No secondary phases and/or impurities were detected in any mechanism at the resolution of the XRD technique. The consequence of Zn incorporation into the parent $BaZr_{0.85}Y_{0.15}O_{3-\delta}$ material induces lattice parameter changes (fig. 4.5).

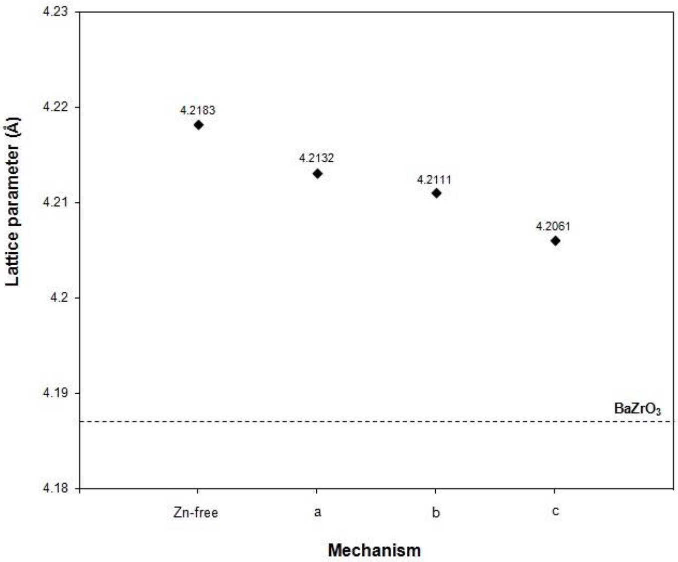

Fig. 4.5 - Lattice parameters evolution of Zn-free and Zn-modified $BaZr_{0.852}Y_{0.148}O_{3-\delta}$ samples fired at 1300ºC for 5 hours.

From fig. 4.5 it is possible to conclude that the lattice parameters of the perovskite oxides are very sensitive to the mechanism of Zn-addition. In all cases the lattice parameter of the Zn-containing materials is observed to be lower than that of the parent BZY. In the case of mechanism c), this decrease in lattice parameter can be explained by the partial substitution of large yttrium cations with smaller Zn cations on the perovskite B-site. Conversely, in mechanism a) Zn substitutes Zr cations of similar ionic radius. Thus, although the decrease in lattice parameter in mechanism a) is small and the lowest of all mechanisms with respect to BZY, the observed decrease cannot result from considerations of cation size. However, an alternative explanation can be found on considering that Zn-additions in both mechanisms a) and c) function as acceptor dopants that promote the formation of oxygen vacancies (described by equations 4.1 and 4.2) in order to achieve charge compensation. From the work of Chatzichristodoulou *et al.* [29] it is known that the formation of oxygen vacancies can lead to a decrease in lattice parameter due to a slightly smaller effective radius of an oxide-ion vacancy than that of an oxide-ion, a trend that is in agreement with the current result. In the case of mechanism b), Yamazaki *et al.* [7] have shown that with increasing Ba deficiency in the parent BZY phase the lattice constant monotonically decreases. Thus, the decrease in the lattice parameter in the sample formed by mechanism b) can also be attributed to the creation of barium deficiency upon Zn solubility into the perovskite phase, as described by equation (4.3).

From the scanning electron microscopy (SEM) images the microstructure of Zn-modified BZY sintered samples show high levels of densification (fig. 4.6), independent of the Zn-addition mechanism. The images (examined in combination with EDS chemical analysis) furthermore reveal that BZY doped with ZnO systems are free of secondary phases at this additive level in agreement with the work of Babilo *et al.* [28].

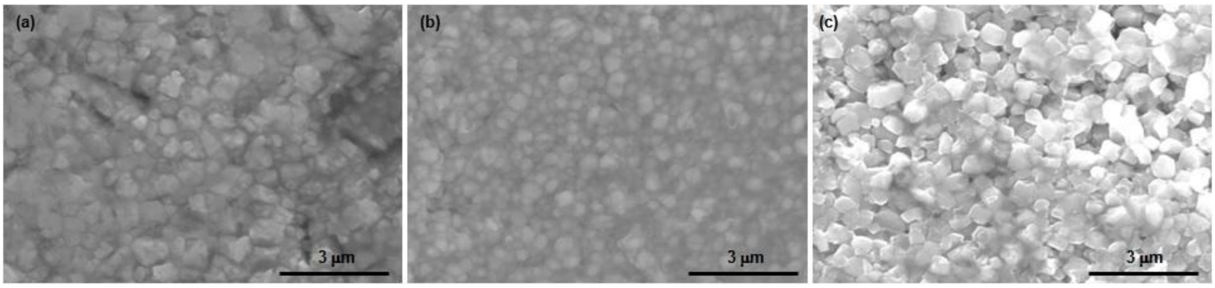

Fig. 4.6 - SEM surface micrograph of sintered (1300ºC, 5 hours) Zn-modified $BaZr_{0.85}Y_{0.15}O_{3-\delta}$ as a function of substitution mechanism: a) $BaZr_{0.812}Zn_{0.04}Y_{0.148}O_{3-\delta}$, b) $0.96BaZr_{0.852}Y_{0.148}O_{3-\delta}+0.04ZnO$ and c) $BaZr_{0.852}Y_{0.108}Zn_{0.04}O_{3-\delta}$.

For comparative purposes, Fig. 4.7 shows a scanning electron micrograph (SEM) of Zn-free $BaZr_{0.852}Y_{0.148}O_{3-\delta}$ sintered at 1300ºC for 5 hours. From the picture it is possible to conclude that BZY system has considerable porosity after sintering at this low temperature, confirming that densification is far from being complete. As previously mentioned at 1300ºC, the density of un-modified BZY is lower than 80%, while zinc oxide is shown to be an effective sintering aid for BZY, reducing sintering temperatures (from 1600ºC to 1300ºC) and reaching full densities at this lower temperature of 98% dense. In comparison Zn-free BZY must be sintered at much higher temperatures to achieve similar densities, for example ~ 90% of theoretical density at 1600ºC for 5 hours [6].

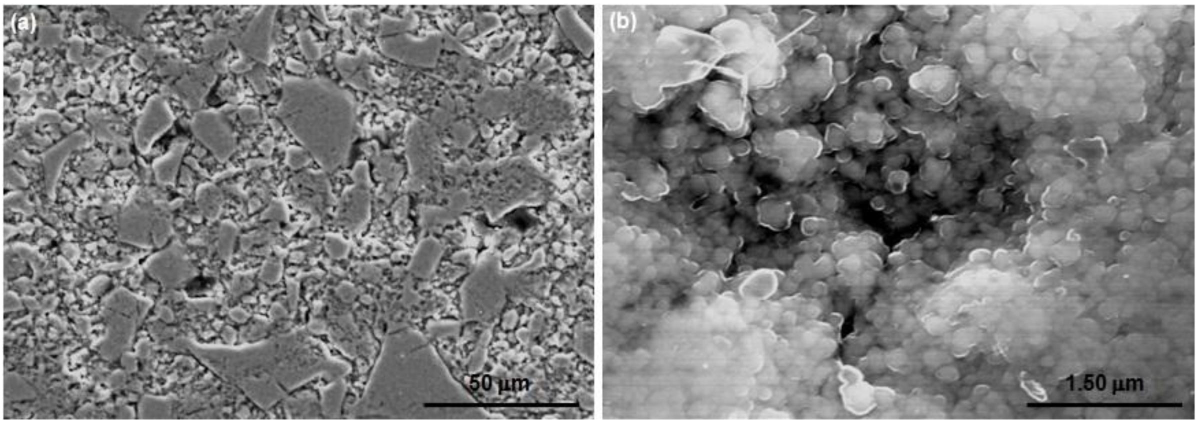

Fig. 4.7 - SEM surface micrographs of Zn-free BZY sintered sample at 1300ºC for 5 hours: a) low magnification (600 x) and b) high magnification (20000 x).

Despite the fact that all Zn-containing materials are shown to be fully dense, the mechanism of ZnO addition is noted to have distinct impacts on resultant microstructure. This is highlighted by table 4.1 that shows that different mechanisms lead to different grain growth with larger grain size being obtained from mechanisms a) and c). Nonetheless, all samples show unimodal grain size distributions (fig. 4.8).

Table 4.1 - Average grain sizes of un-modified and Zn-modified BZY sintered samples (1300ºC, 5 hours), calculated from SEM images.

Sample	**Grain size (nm)**
$BaZr_{0.812}Zn_{0.04}Y_{0.148}O_{3-d}$ (mechanism a)	479.4 ± 21.8
$0.96BaZr_{0.852}Y_{0.148}O_{3-d}+0.04ZnO$ (mechanism b)	145.6 ± 8.2
$BaZr_{0.852}Y_{0.108}Zn_{0.04}O_{3-d}$ (mechanism c)	536.6 ± 22.3

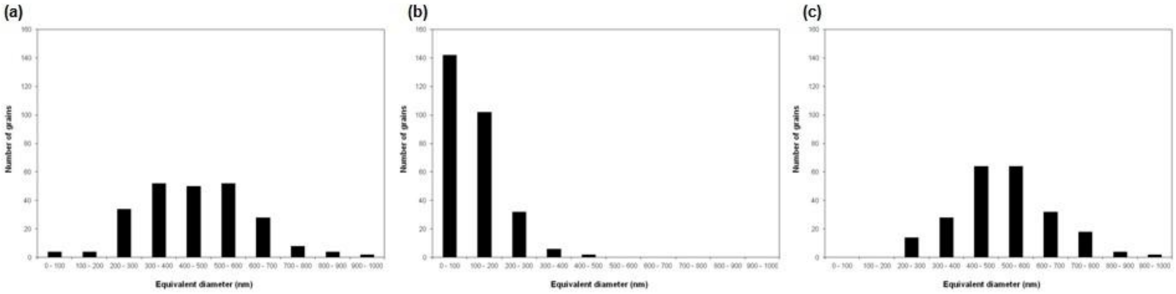

Fig. 4.8 - Grain size distribution for sintered Zn modified BZY samples: a) $BaZr_{0.812}Zn_{0.04}Y_{0.148}O_{3-\delta}$ - mechanism a, b) $0.96BaZr_{0.852}Y_{0.148}O_{3-\delta}+0.04ZnO$ - mechanism b, and c) $BaZr_{0.852}Y_{0.108}Zn_{0.04}O_{3-\delta}$ - mechanism c.

Mirroring that noted in the literature for the parent BZY material, the formation of Ba-deficiency by mechanism b) leads to depleted grain growth [7]. One can hypothesize that impairment of grain growth on increasing barium loss may arise due to the segregation of secondary phases, such as Y_2O_3 to the grain boundary, that pin grains preventing growth [30] or, alternatively, due to a decrease in cation diffusion rates [7]. The latter analogy implies that Ba-deficiency would be partially accommodated by dopant partitioning across the A and B sites, leading to resultant decreases in point defect concentrations and impairment of grain growth [31,32].

Additionally, the distribution of Zn within the polycrystalline perovskite can also justify the differences in grain size of Zn-modified BZY samples. While the XRD and SEM studies indicate that all the samples do not show any bulk secondary phases, which may have served to enhance sintering, these techniques provide little information about Zn distribution, *i.e.*, if there is any difference in Zn concentration between bulk (grain interiors) and grain boundary regions. Figure 4.9 shows examples of the transmission electron microscopic images (TEM) of samples of each Zn-addition mechanism. The yellow and red squares represent the points where the chemical analysis for Zn distribution was performed. The qualitative analysis was made by STEM-XEDS analysis of 50 points inside the grain interiors (bulk) and 30 points at the grain boundaries and triple points.

Table 4.2 summarises these results to clarify the Zn distribution in each sample for each mechanism.

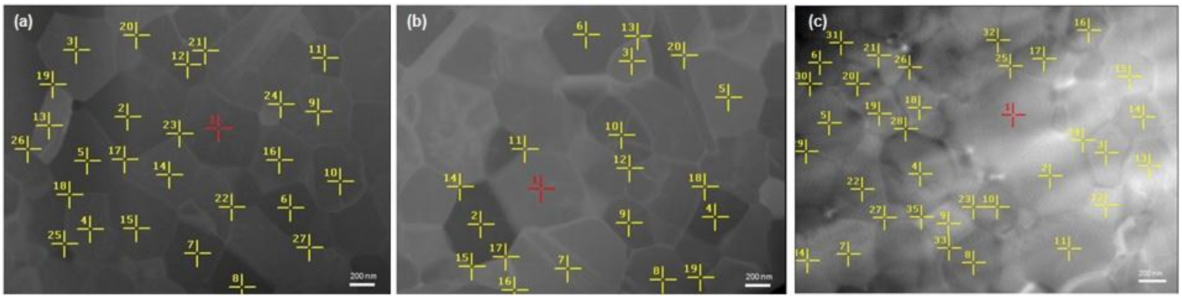

Fig. 4.9 – Scanning transmission electron microscopic images of sintered (1300ºC, 5 hours) Zn-modified $BaZr_{0.85}Y_{0.15}O_{3-\delta}$ as a function of substitution mechanism: a) $BaZr_{0.812}Zn_{0.04}Y_{0.148}O_{3-\delta}$, b) $0.96BaZr_{0.852}Y_{0.148}O_{3-\delta}+0.04ZnO$ and c) $BaZr_{0.852}Y_{0.108}Zn_{0.04}O_{3-\delta}$.

Table 4.2 - Chemical compositional comparison of the bulk and Grain Boundary/Triple points in the Zn-modified BZY sintered samples (1300ºC, 5 hours), calculated from TEM/STEM images.

Sample	**Bulk (atomic %)**	**Grain boundary / Triple points (atomic %)**
$BaZr_{0.812}Zn_{0.04}Y_{0.148}O_{3-\delta}$ (mechanism a)	1.183 ± 0.170	2.644 ± 1.481
$0.96BaZr_{0.852}Y_{0.148}O_{3-\delta}+0.04ZnO$ (mechanism b)	0.882 ± 0.227	6.128 ± 1.565
$BaZr_{0.852}Y_{0.108}Zn_{0.04}O_{3-\delta}$ (mechanism c)	0.944 ± 0.225	2.417 ± 1.851

From table 4.2 it is possible to conclude that there are no significant differences in the amount of zinc inside the grains (bulk) for all Zn-added mechanisms and that this concentration is close to the expected stoichiometry for the additive level of 4mol% Zn (~0.8 atomic %). In contrast, there is a distinct enrichment of Zn in the grain boundary of all the samples, which previously has been suggested to be responsible for the enhanced densification behavior [10]. However, in light of the chemical analysis, mechanism b) shows much larger differences in Zn amounts between bulk and grain boundaries/triple points than the other mechanisms, having substantial concentrations of Zn at the grain boundary. This segregation of Zn in this mechanism could affect electrical conductivities as well as possibility being responsible for the reduced grain size of this mechanism. In this respect, this behaviour was also described by Caballero *et al.* [33] for small Zn additions to $BaTiO_3$ where, besides the improvement in densification, the similar coating of grains by ZnO dramatically inhibited grain growth.

4.1.3.3 ELECTRICAL MEASUREMENTS

The conductivity behavior of the Zn-modified BZY samples was assessed by A.C. impedance spectroscopy under wet N_2 and O_2 atmospheres. Example impedance spectra for these compositions are shown in figure 4.10. Impedance spectra were fitted by a series combination of distributed RQ elements, where the fitting parameters extracted for each distributed arc are the resistance value, R, the pseudocapacitance Q, of the constant phase element and the parameter n, parameters that can be related to the true capacitance by the equation (4.4):

$$C = R^{\frac{1-n}{n}} Q^{\frac{1}{n}} \tag{4.4}$$

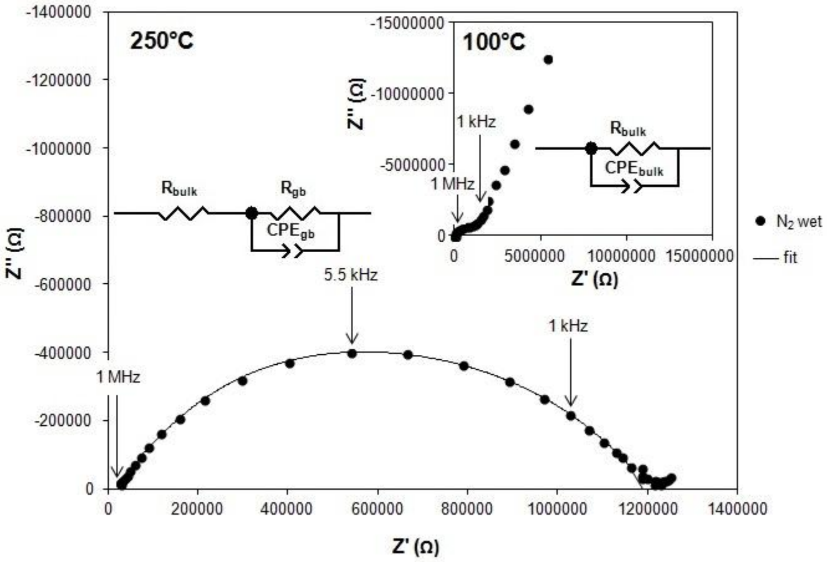

Fig. 4.10 - Typical impedance spectra and respective equivalent circuit measured at 250°C in wet nitrogen atmospheres Zn-modified $BaZr_{0.85}Y_{0.15}O_{3-\delta}$ from mechanism a) - $BaZr_{0.812}Zn_{0.04}Y_{0.148}O_{3-\delta}$. Inset image shows the impedance spectra measured at lower temperatures (100ºC) in wet nitrogen atmosphere of Zn-modified $BaZr_{0.85}Y_{0.15}O_{3-\delta}$ from mechanism a) - $BaZr_{0.812}Zn_{0.04}Y_{0.148}O_{3-\delta}$, showing the bulk response at higher Z' frequencies.

The inset of the figure shows a typical impedance response measured at low temperature (100ºC) consisting of a bulk response, observable at high frequency, with capacitance values in the pF/cm^2 range, followed by a partial grain boundary response at lower frequencies. In contrast, the main image of fig.4.10 shows example impedance spectra measured at a more elevated temperature (250ºC) under similar conditions. At such higher temperatures, the bulk response becomes unresolvable in the frequency window of the experiment and is revealed only as an offset along the real Z' axis at the highest frequency, while intermediate to low frequencies reveal the grain boundary response, with capacitance values in the range 10^{-10}-10^{-9} F/cm^2. Correspondingly, the impedance responses were modeled by the equivalent circuit presented in the images. The total conductivity was taken as the sum of the bulk and grain boundary components.

Figures 4.11 and 4.12 show the temperature dependences of the extracted total and bulk conductivities of the Zn containing samples and those of the base BZY composition measured under wet O_2 and wet N_2 atmospheres, respectively. In the plotted temperature range (100ºC-400ºC), the total conductivity is shown to be significantly lower than that of the bulk, highlighting a dominant grain boundary contribution to total conductivity. The activation energies of the bulk response are calculated to be similar for compositions mechanism a) and c), with values in the region of 0.41-0.45eV under all atmospheres, Table 4.3 in agreement with that of the un-doped material BZY; values that can be considered characteristic of proton conduction [34]. In contrast the respective activation energy for mechanism b) is shown to be slightly lower than the other Zn-containing samples. The total conductivities of all Zn-containing materials appear to converge at the highest temperature measured in all conditions and to be lower than that of the un-doped BZY material, whereas bulk conductivity is marginally higher in the Zn-free BZY and Zn-modified BZY in mechanism b) samples at the lowest temperatures.

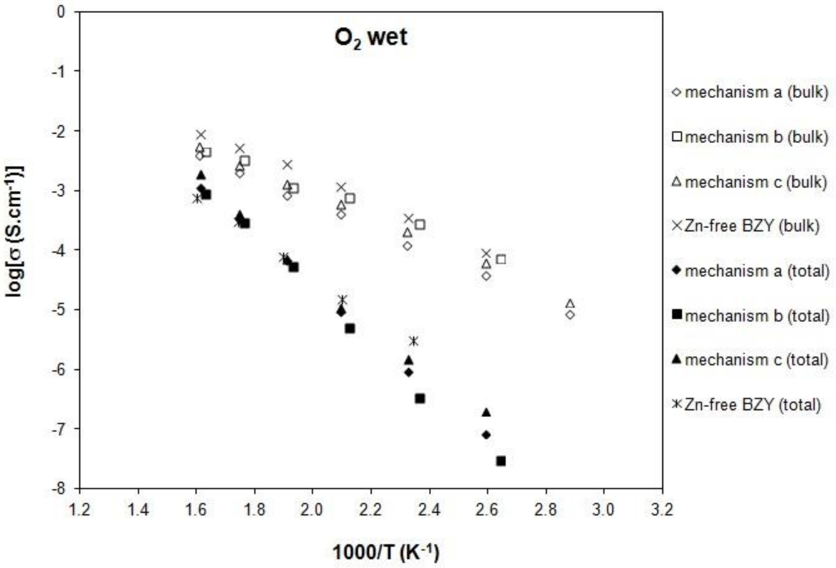

Fig. 4.11 - Temperature dependence of the extracted total and bulk conductivities of the Zn-free and Zn-modified BZY samples measures in wet O_2 atmospheres.

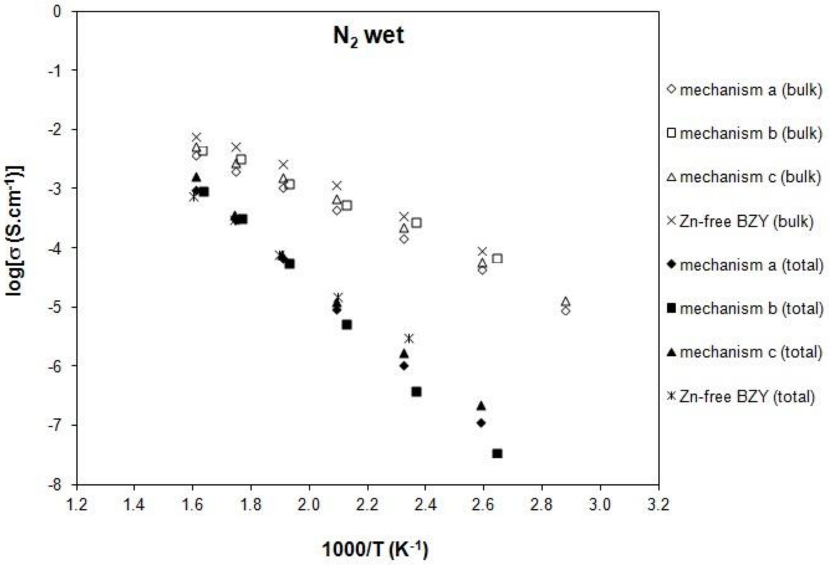

Fig. 4.12 - Temperature dependence of the extracted total and bulk conductivities of the Zn-free and Zn-modified BZY samples measures in wet N_2 atmospheres.

In order to discuss the much larger grain boundary contribution to total conductivity, it is necessary to firstly normalize the data to accommodate the differing grain sizes of the samples noted previously in section 4.1.3.2. To this end, the term $\sigma_{gb}^* = \sigma_{gb}/D$ is introduced, where σ_{gb} is the uncorrected grain boundary conductivity and D is the mean grain size of each dense ceramic calculated by SEM assessment, table 4.1 (note that for Zn-free BZY samples the mean grain size was considered to be around 910 nm, as described by Antunes *et al.* [6]). This approach is typically used in the literature to provide an estimation of the characteristic grain boundary properties independent of variations in microstructure on the assumption that the proportionally factor of the grain boundary thickness remains effectively constant [7]. The normalized grain boundary conductivity is shown in figures 4.13 and 4.14 as a function of temperature in wet O_2 and N_2 atmospheres, respectively. The figures highlight that the Zn-containing samples all offer higher normalized grain boundary conductivities with increasing temperature than the Zn-free BZY material, due to possessing significantly higher activation energies for conduction, table 4.3. This phenomenon is most likely to be related to the segregation of Zn to the grain boundaries of these materials, as observed by chemical composition calculated from TEM/STEM (table 4.2) analysis in the previous section 4.1.3.2. In this respect it should be noted that ZnO is reported to be an n-type electronic conductor with a conduction mechanism traditionally explained to result from the presence of oxygen vacancies or zinc interstitials [35]. In support of this suggestion, the sample recorded to contain the largest quantity of Zn located in the grain boundary, Zn-modified BZY from mechanism b), section 4.1.3.2, shows a distinct increase in activation energy on moving to the more reducing wet N_2 conditions to yield an activation energy for this composition that notably exceeds that of the other Zn samples under this atmosphere, table 4.3, as would be expected for an increasing n-type electronic contribution to grain boundary conductivity.

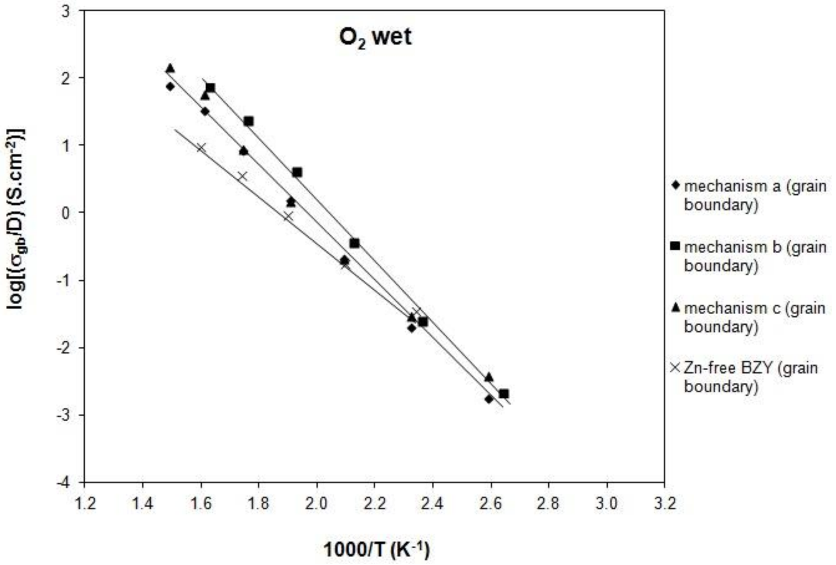

Fig. 4.13 - Temperature dependence of the normalized grain boundary conductivity (σ_{gb}* = σ_{gb}/D) of the Zn-free and Zn-modified BZY samples measures in wet O_2 atmospheres.

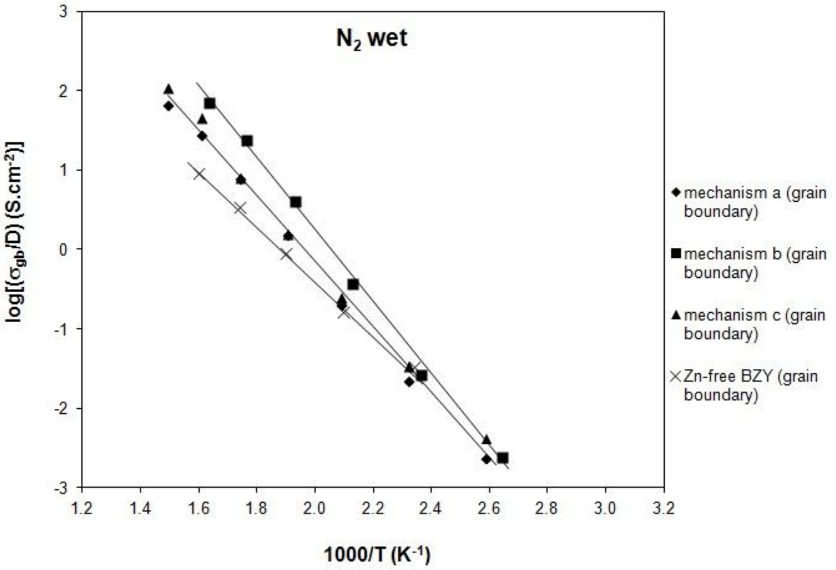

Fig. 4.14 - Temperature dependence of the normalized grain boundary conductivity (σ_{gb}* = σ_{gb}/D) of the Zn-free and Zn-modified BZY samples measures in wet N_2 atmospheres.

The differing grain boundary activation energies of the samples, coupled with their respective differences in grain sizes, leads their total conductivities to be relatively similar at the highest temperatures of figures 4.11 and 4.12, despite an initially lower conductivity of the mechanism b) sample measured at low temperatures. Figures 4.11 and 4.12 further highlight that the bulk conductivity takes an increasing important role in the total conductivity with increasing temperature, due to its substantially lower activation energy for conduction than that of the grain boundary (table 4.3).

Table 4.3 - Activation energies of total (Ea_{total}), bulk (Ea_{bulk}) and normalized grain boundary (Ea_{gb^*}, calculated from the normalized grain boundary conductivity: $\sigma_{gb}^* = \sigma_{gb}/D$) of the Zn-free and Zn-modified BZY samples measures in wet O_2 and N_2 atmospheres, measured at low temperatures (100ºC - 350ºC).

Sample	**Wet O_2**			**Wet N_2**		
	Ea_{total} (eV)	**Ea_{bulk}** (eV)	**Ea_{gb^*}** (eV)	**Ea_{total}** (eV)	**Ea_{bulk}** (eV)	**Ea_{gb^*}** (eV)
$BaZr_{0.852}Y_{0.148}O_{3-\delta}$ (Zn-free)	0.64 ± 0.01	0.44 ± 0.01	0.66 ± 0.01	0.64 ± 0.01	0.42 ± 0.02	0.66 ± 0.01
$BaZr_{0.812}Zn_{0.04}Y_{0.148}O_{3-\delta}$ (mechanism a)	0.89 ± 0.01	0.45 ± 0.01	0.92 ± 0.02	0.85 ± 0.02	0.43 ± 0.01	0.88 ± 0.02
$0.96BaZr_{0.852}Y_{0.148}O_{3-\delta}+0.04ZnO$ (mechanism b)	0.92 ± 0.03	0.39 ± 0.02	0.93 ± 0.03	0.92 ± 0.04	0.39 ± 0.02	0.99 ± 0.04
$BaZr_{0.852}Y_{0.108}Zn_{0.04}O_{3-\delta}$ (mechanism c)	0.85 ± 0.03	0.43 ± 0.01	0.88 ± 0.04	0.83 ± 0.02	0.43 ± 0.01	0.85 ± 0.03

The oxide-ion vacancies and electron-holes that form due to charge compensation of the acceptor dopants in these materials may be replaced by protons in a water- and/or hydrogen-containing atmosphere at elevated temperatures. The concentrations of each of these defects have a functional dependency on both oxygen and water vapour partial pressure (pO_2 and pH_2O, respectively), as well as on temperature, so that the nature of the defect concentration profiles relies on external equilibrium. It is important, therefore, for the defect structure of protonic conductors to be clearly understood because both transport and thermodynamic properties are strongly influenced by the nature of the defect system [36]. In order to investigate these phenomena in more depth, the relative conductivities of holes, oxide-ions and protons are separated in the subsequent section (4.1.3.4) using the experimental method of Lim *et al.* [37] and Baek [38] in the temperature range (600ºC - 800ºC) for which the role of the bulk conductivity becomes more significant.

The addition of ZnO can generate different point defects which give rise to improved oxygen vacancy concentration and, therefore, can influence the effective concentration of protons able to participate in the charge transport process. In order to describe the defect chemistry of the mechanisms of Zn addition, equations 4.1, 4.2 and 4.3, are simplified by the general composition $Ba_{1-z}Zr_{1-x-y}Zn_xY_yO_{3-\delta}$, where z is the effective A-site deficiency and x and y are the Zn and Y contents on the B-site, respectively, In this way the studied Zn-containing compositions can be described by equations 4.5, 4.6 and 4.7, upon the assumption that Zn is fully soluble in the bulk material in each case.

Mechanism a: $BaZr_{1-x-y}Zn_xY_yO_{3-\delta}$ (4.5)

where x = 0.04, y = 0.15 and z = 0.

Mechanism b: $(1-z)BaZr_{1-x-y}Zn_xY_yO_{3-\delta}$ (4.6)

where x = 0.038, y = 0.144 and z = 0.038.

Mechanism c: $BaZr_{1-x-y}Zn_xY_yO_{3-\delta}$ (4.6)

where x = 0.04, y = 0.11 and z = 0.

4.1.3.4 TRANSPORT PROPERTIES

In order to elucidate the conductivity mechanism, the electrical properties of Zn-modified BZY samples were studied in various oxygen and water vapor atmospheres as a function of temperature. Analytical analysis, based on the proposed defect structure of the material, was performed using plots of total conductivity, σ_{total} *vs* $pO_2^{1/4}$.

<u>Defect chemistry</u>

Hydration of oxygen vacancies present in a ceramic oxide proton conductor when exposed to water containing atmospheres can be described by the following (equation 1.8) [23,39]:

$$H_2O + O_O^x + V_O^{\bullet\bullet} \xrightarrow{K_H} 2OH_O^{\bullet} \tag{1.8}$$

where the equilibrium constant for the exchange of water (hydration) - $K_{H,}$ is given by:

$$K_H = \frac{[OH_O^{\bullet}]^2}{[V_O^{\bullet\bullet}]\, pH_2O} \tag{4.7}$$

This reaction is accompanied by the competing equilibrium of oxygen vacancies and gaseous oxygen from the surrounding atmosphere producing electron-holes, described by equation 4.8 [39]:

$$V_O^{\bullet\bullet} + \frac{1}{2}\, O_2\,(g) \overset{K_h}{\leftrightarrow} O_O^x + \, 2h^{\bullet} \tag{4.8}$$

where the corresponding equilibrium constant – $K_{h,}$ is given by:

$$K_h = \frac{p^2}{[V_O^{\bullet\bullet}]\; pO_2^{1/2}} \tag{4.9}$$

From these basic equations and the effective charge neutrality condition for an acceptor dopant single negative effective charge, the conductivity behaviour of a typical high-temperature proton conductor (HTPC) containing a 3+ acceptor dopant, such as Y, was described by Lim *et al.* [37] and Baek [38], based on relations modified from those originally published by Frade [40]. These authors showed that the partial conductivities of each charge carrier could be described by the following formulas:

$$\sigma_{OH^{\bullet}} = \sigma_{OH^{\bullet}}^{*}\left[\left(1 + \frac{\alpha}{p_{H2O}}\right)^{1/2} - 1\right]\left(\frac{p_{H2O}}{(1+\,\alpha)^{1/2} -\, 1}\right) \tag{4.10}$$

$$\sigma_{V_O^{\bullet\bullet}} = \sigma_{V_O^{\bullet\bullet}}^{*}\left[\left(1 + \frac{\alpha}{p_{H2O}}\right)^{1/2} - 1\right]^2 \left(\frac{p_{H2O}}{\alpha}\right) \tag{4.11}$$

$$\sigma_p = \sigma_p^{*}\left[\left(1 + \frac{\alpha}{p_{H2O}}\right)^{1/2} - 1\right]\left(\frac{p_{H2O}}{\alpha}\right)^{1/2} p_{O_2}^{1/4} \tag{4.12}$$

Where $\sigma_{OH^{\bullet}}^{*}$ is the protonic conductivity at pH$_2$O = 1atm, σ_p^{*} is the hole conductivity at pO$_2$ = 1 atm and pH$_2$O = 0 atm, $\sigma_{V_O^{\bullet\bullet}}^{*}$ is the oxygen ion conductivity when pH$_2$O = 0 atm and α is a constant determined by the following relationship:

$$\alpha = \frac{8\, l}{K_H} \tag{4.13}$$

where $l = \frac{[M_B^{/}]}{V_M}$, $M_B^{/}$ is the concentration of the singly charged acceptor dopant, V_M is the molar volume of the system and K_H is the equilibrium constant corresponding to hydration (equation 4.7).

The experimental method of these authors involved measuring the conductivity of the mixed conductor as a function of partial pressure of oxygen over a wide temperature range. In the case of proton conductors, the defect concentration is controlled by the acceptor dopant concentration. Therefore, the ionic conductivity is usually independent of oxygen partial pressure. On the contrary, the electron or electron-hole conductivity varies significantly with oxygen partial pressure with the electronic defect concentration being significantly influenced by small deviations in the material composition with respect to oxygen. Thus, the contributions of ionic and electronic conductivities and transport number as well as the ionic conduction domain could be assessed by measuring the conductivity as a function of pO_2 and temperature by fitting experimental data to an acceptable defect model [41].

In the present case, equations 4.1, 4.2 and 4.3 highlight the presence of three different negatively charged species that can be involved in the defect chemistry, $Zn_{Zr}^{//}$, $V_{Ba}^{//}$ and $Y_{Zr}^{/}$ for the Zn-containing BZY materials.

Thus, the electroneutrality equation for the current compositions must include these species to be given by the relationship:

$$[2V_O^{\bullet\bullet}] + p + [OH^{\bullet}] \quad = 2[Zn_{Zr}^{//}] + 2[V_{Ba}^{//}] + [Y_{Zr}^{/}] \tag{4.14}$$

which for the case that p << $[2V_O^{\bullet\bullet}]$ can be simplified to

$$[2V_O^{\bullet\bullet}] + [OH^{\bullet}] \quad \approx 2[Zn_{Zr}^{//}] + 2[V_{Ba}^{//}] + [Y_{Zr}^{/}] \tag{4.15}$$

From equations 4.7, 4.8 and 4.15 it can be deduced that the equations of Lim *et al.* [37] and Baek [38] (equations 4.10 to 4.13) continue to hold for the present materials, with the minor modification that

$$\alpha = \frac{8\,(2[Zn_{Zr}^{//}] + 2[V_{Ba}^{//}] + [Y_{Zr}^{/}])}{K_H\, V_M} \tag{4.16}$$

to reflect the more extensive electroneutrality equation 4.15. Based on equations 4.5, 4.6 and 4.7, this relationship can be written as

$$\alpha = \frac{8\,(2x + 2z + y)}{K_H\, V_M} \tag{4.17}$$

where, x, y, and z describe the compositions formed by each Zn addition mechanism.

The total conductivity is given by the sum of the partial conductivities:

$$\sigma_{total} = \sigma_{OH^\bullet} + \sigma_{V_O^{\bullet\bullet}} + \sigma_p \tag{4.18}$$

Equations 4.10 to 4.12 highlight that only σ_p shows direct dependency on pO_2 and, thus, total conductivity can be represented by:

$$\sigma_{total} = a + b\, pO_2^{1/4} \tag{4.19}$$

where $a = \sigma_{OH^{\cdot}} + \sigma_{V_O^{\cdot\cdot}}$ and $b = \sigma_p^* \left[\left(1 + \frac{p_{H2O}}{\alpha}\right)^{1/2} - \left(\frac{p_{H2O}}{\alpha}\right)^{1/2}\right]$.

From equations 4.10 and 4.11, the intercept (a) can be written as:

$$a = \sigma_{OH^\bullet}^* \left[\left(1 + \frac{\alpha}{p_{H2O}}\right)^{1/2} - 1\right] \left(\frac{p_{H2O}}{(1+\alpha)^{1/2} - 1}\right) + \sigma_{V_O^{\bullet\bullet}}^* \left[\left(1 + \frac{\alpha}{p_{H2O}}\right)^{1/2} - 1\right]^2 \left(\frac{p_{H2O}}{\alpha}\right) \tag{4.20}$$

By measuring the gradients of plots of σ_{total} *vs* $pO_2^{1/4}$ at two different water vapor pressures ($pH_2O_{,1}$ and $pH_2O_{,2}$, α can be determined from the ratio of two gradients as follows:

$$\frac{b_1}{b_2} = \frac{\left[\left(1 + \frac{p_{H2O,1}}{\alpha}\right)^{1/2} - \left(\frac{p_{H2O,1}}{\alpha}\right)^{1/2}\right]}{\left[\left(1 + \frac{p_{H2O,2}}{\alpha}\right)^{1/2} - \left(\frac{p_{H2O,2}}{\alpha}\right)^{1/2}\right]} \tag{4.21}$$

After determination of α, σ_p^* and K_H can be calculated. Additionally, by measuring the intercepts of plots of σ_{total} *vs* $pO_2^{1/4}$ measured at two different water vapor pressures, the constants $\sigma_{OH^\bullet}^*$ and $\sigma_{V_O^{\bullet\bullet}}^*$ can be determined.

When the constants σ_p^*,$\sigma^*_{OH^{\bullet}}$, $\sigma^*_{V_O^{\bullet\bullet}}$ and α are known, the partial conductivities and total conductivity can subsequently be obtained [37,38,40].

The experimental plots of total conductivity against $pO_2^{1/4}$ measured in dry and wet atmospheres are shown in figures 4.15 and 4.16, respectively.

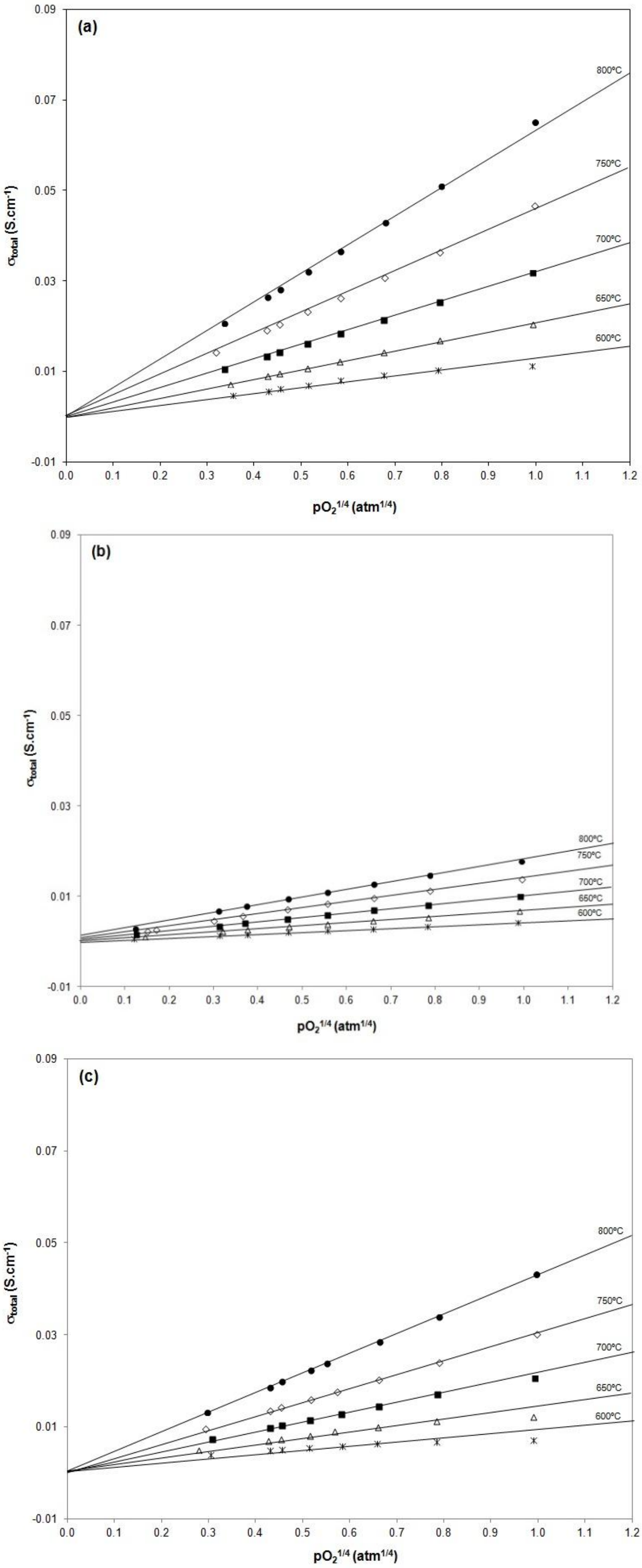

Fig. 4.15 - Total conductivity of Zn-modified BZY *vs* $pO_2^{1/4}$ under dry conditions ($pH_2O = 1.66 \times 10^{-5}$ atm) at various temperatures: a) $BaZr_{0.812}Zn_{0.04}Y_{0.148}O_{3-\delta}$, b) $0.96BaZr_{0.852}Y_{0.148}O_{3-\delta}+0.04ZnO$ and c) $BaZr_{0.852}Y_{0.108}Zn_{0.04}O_{3-\delta}$.

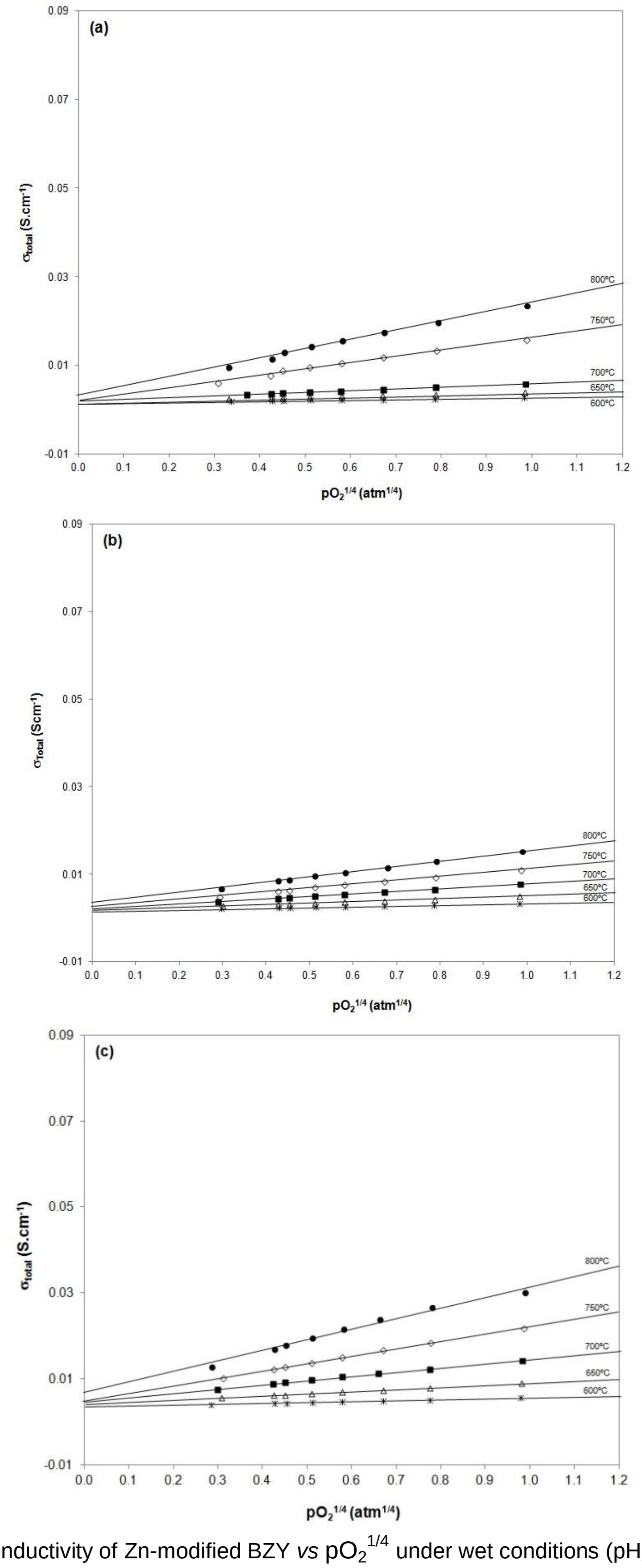

Fig. 4.16 - Total conductivity of Zn-modified BZY *vs* $pO_2^{1/4}$ under wet conditions (pH_2O = 0.033 atm) at various temperatures: a) $BaZr_{0.812}Zn_{0.04}Y_{0.148}O_{3-\delta}$, b) $0.96BaZr_{0.852}Y_{0.148}O_{3-\delta}$+0.04ZnO and c) $BaZr_{0.852}Y_{0.108}Zn_{0.04}O_{3-\delta}$.

Excellent linear relationships between σ_{total} and $pO_2^{1/4}$ suggested that the described defect model is valid for the current material. In dry conditions (fig. 4.15), the results also show that the relationship between σ_{total} and $pO_2^{1/4}$ tends to for the same value intercept, being effectively zero in mechanisms a) and c). These results suggest that under these extremely dry conditions (obtained using a commercial Varian moisture filter) both oxygen vacancy conductivities, $\sigma^*_{V_O^{\bullet\bullet}}$, and proton conductivity $\sigma^*_{OH^{\bullet}}$ are effectively negligible.

The gradients and intercepts of σ_{total} and $pO_2^{1/4}$ obtained by linear fitting are reported in tables 4.4, 4.5 and 4.6. The extracted values of the gradients (related to hole conduction) can be observed to be greater and with lower value intercepts (related to ionic conduction) in dry conditions than in wet conditions. From equation 4.20, this behavior suggests that the hole contribution to total conductivity increases, while the ionic contribution decreases with decreasing pH_2O.

Table 4.4 - The gradients and intercepts of σ_{total} and $pO_2^{1/4}$ obtained by linear fitting for $BaZr_{0.812}Zn_{0.04}Y_{0.148}O_{3-\delta}$ (mechanism a).

Temperature (°C)	**Dry conditions** ($pH_2O = 1.66 \times 10^{-5}$ atm)		**Wet conditions** ($pH_2O = 0.033$ atm)	
	Gradient (b) ($S.cm^{-1}.atm^{-1/4}$)	**Intercept (a)** ($S.cm^{-1}$)	**Gradient (b)** ($S.cm^{-1}.atm^{-1/4}$)	**Intercept (a)** ($S.cm^{-1}$)
600	0.0129	~0	0.0012	0.0016
650	0.0210	~0	0.0023	0.0017
700	0.0317	~0	0.0038	0.0021
750	0.0457	~0	0.0141	0.0021
800	0.0635	~0	0.0205	0.0034

Table 4.5 - The gradients and intercepts of σ_{total} and $pO_2^{1/4}$ obtained by linear fitting for $0.96BaZr_{0.852}Y_{0.148}O_{3-\delta}+0.04ZnO$ (mechanism b).

Temperature (°C)	**Dry conditions** ($pH_2O = 1.66 \times 10^{-5}$ atm)		**Wet conditions** ($pH_2O = 0.033$ atm)	
	Gradient (b) ($S.cm^{-1}.atm^{-1/4}$)	**Intercept (a)** ($S.cm^{-1}$)	**Gradient (b)** ($S.cm^{-1}.atm^{-1/4}$)	**Intercept (a)** ($S.cm^{-1}$)
600	0.0042	0.00001	0.0016	0.0016
650	0.0067	0.0002	0.0032	0.0019
700	0.0098	0.0004	0.0058	0.0020
750	0.0136	0.0006	0.0087	0.0025
800	0.0167	0.0015	0.0120	0.0033

Table 4.6 - The gradients and intercepts of σ_{total} and $pO_2^{1/4}$ obtained by linear fitting for $BaZr_{0.852}Y_{0.108}Zn_{0.04}O_{3-\delta}$ (mechanism c).

Temperature (°C)	**Dry conditions** ($pH_2O = 1.66 \times 10^{-5}$ atm)		**Wet conditions** ($pH_2O = 0.033$ atm)	
	Gradient (b) ($S.cm^{-1}.atm^{-1/4}$)	**Intercept (a)** ($S.cm^{-1}$)	**Gradient (b)** ($S.cm^{-1}.atm^{-1/4}$)	**Intercept (a)** ($S.cm^{-1}$)
600	0.0093	~0	0.0022	0.0035
650	0.0145	~0	0.0049	0.0041
700	0.0217	~0	0.0097	0.0047
750	0.0309	~0	0.0173	0.0048
800	0.0432	~0	0.0247	0.0067

From the gradients of σ_{total} and $pO_2^{1/4}$ at two different water pressures, α was calculated for each temperature and the water uptake equilibrium constant, K_H, was calculated (tables 4.7, 4.8 and 4.9).

Table 4.7 – Calculated α, K_H, σ_p^*, $\sigma^*_{OH^\bullet}$, $\sigma^*_{V_O^{\bullet\bullet}}$ at different temperatures for $BaZr_{0.812}Zn_{0.04}Y_{0.148}O_{3-\delta}$ (mechanism a).

Temperature (°C)	**α** (atm)	**K_H** ($atm^{-1}.cm^{-3}$)	**σ_p^*** ($S.cm^{-1}$)	**$\sigma^*_{OH^\bullet}$** ($S.cm^{-1}$)	**$\sigma^*_{V_O^{\bullet\bullet}}$** ($S.cm^{-1}$)
600	8.89×10^{-4}	$2.77 \times 10^{+25}$	1.47×10^{-2}	1.61×10^{-3}	~0
650	1.32×10^{-3}	$1.87 \times 10^{+25}$	2.34×10^{-2}	1.72×10^{-3}	~0
700	1.61×10^{-3}	$1.53 \times 10^{+25}$	3.50×10^{-2}	2.12×10^{-3}	~0
750	1.43×10^{-2}	$1.72 \times 10^{+24}$	4.73×10^{-2}	2.30×10^{-3}	~0
800	1.59×10^{-2}	$1.55 \times 10^{+24}$	6.55×10^{-2}	3.75×10^{-3}	~0

Table 4.8 – Calculated α, K_H, σ_p^*, $\sigma^*_{OH^\bullet}$, $\sigma^*_{V_O^{\bullet\bullet}}$ at different temperatures for $0.96BaZr_{0.852}Y_{0.148}O_{3-\delta}+0.04ZnO$ (mechanism b).

Temperature (°C)	**α** (atm)	**K_H** ($atm^{-1}.cm^{-3}$)	**σ_p^*** ($S.cm^{-1}$)	**$\sigma^*_{OH^\bullet}$** ($S.cm^{-1}$)	**$\sigma^*_{V_O^{\bullet\bullet}}$** ($S.cm^{-1}$)
600	2.45×10^{-2}	$1.29 \times 10^{+24}$	4.31×10^{-3}	1.84×10^{-3}	8.01×10^{-6}
650	4.80×10^{-2}	$6.61 \times 10^{+23}$	6.82×10^{-3}	2.38×10^{-3}	1.18×10^{-4}
700	1.04×10^{-1}	$3.05 \times 10^{+23}$	9.92×10^{-3}	2.79×10^{-3}	3.38×10^{-4}
750	1.47×10^{-1}	$2.15 \times 10^{+23}$	1.37×10^{-2}	3.69×10^{-3}	5.32×10^{-4}
800	2.78×10^{-1}	$1.14 \times 10^{+23}$	1.68×10^{-2}	4.90×10^{-3}	1.44×10^{-3}

Table 4.9 – Calculated α, K_H, σ_p^*, $\sigma^*_{OH^\bullet}$, $\sigma^*_{V_O^{\bullet\bullet}}$ at different temperatures for $BaZr_{0.852}Y_{0.108}Zn_{0.04}O_{3-\delta}$ (mechanism c).

Temperature (°C)	**α** (atm)	**K_H** ($atm^{-1}.cm^{-3}$)	**σ_p^*** ($S.cm^{-1}$)	**$\sigma^*_{OH^\bullet}$** ($S.cm^{-1}$)	**$\sigma^*_{V_O^{\bullet\bullet}}$** ($S.cm^{-1}$)
600	7.52×10^{-3}	$2.72 \times 10^{+24}$	9.73×10^{-3}	3.68×10^{-3}	~0
650	1.78×10^{-2}	$1.15 \times 10^{+24}$	1.49×10^{-2}	4.57×10^{-3}	~0
700	3.88×10^{-2}	$5.27 \times 10^{+23}$	2.21×10^{-2}	5.76×10^{-3}	~0
750	8.28×10^{-2}	$2.47 \times 10^{+23}$	3.14×10^{-2}	6.76×10^{-3}	~0
800	9.01×10^{-2}	$2.27 \times 10^{+23}$	4.38×10^{-2}	9.61×10^{-3}	~0

The temperature dependence of the equilibrium constant of water dissolution of each mechanism is shown in figures 4.17, 4.18 and 4.19. The standard solution enthalpy for water uptake for each mechanism was determined according to the slope of ln(K) vs. 1000/T. These values are -125.5 kJ/mol for mechanism a), -93.4 kJ/mol for mechanism b) and -102.3 kJ/mol for mechanism c). These values are lower in absolute terms than that of $BaZr_{0.85}Y_{0.15}O_{3-\delta}$, -83.4 kJ/mol [42] which are in agreement with the expected trends shown in the literature since the occupation of perovskite proton conductors with Zn would induce more negative hydration enthalpies due to the higher basicity levels of the corresponding oxides [37,43].

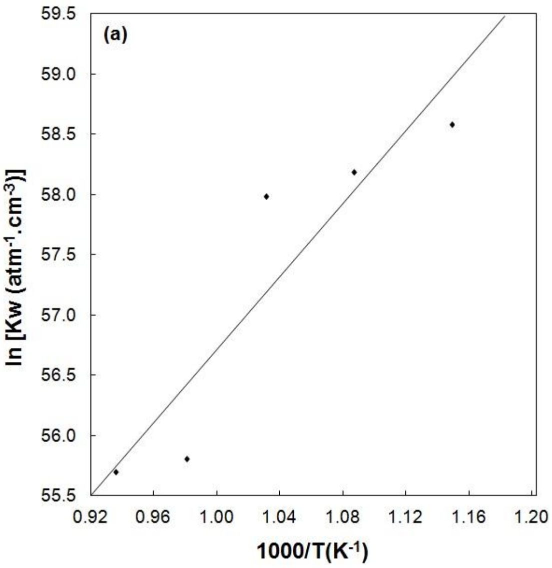

Fig. 4.17 – The equilibrium constant of hydration as a function of temperature mechanism a): $BaZr_{0.812}Zn_{0.04}Y_{0.148}O_{3-\delta}$.

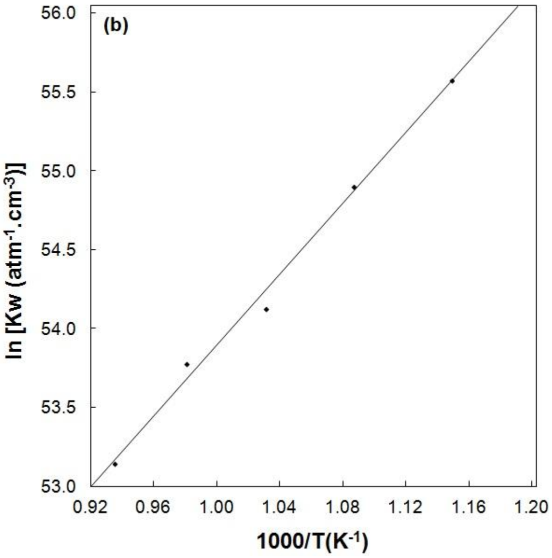

Fig.4.18 – The equilibrium constant of hydration as a function of temperature mechanism b): $0.96BaZr_{0.852}Y_{0.148}O_{3-\delta}+0.04ZnO$.

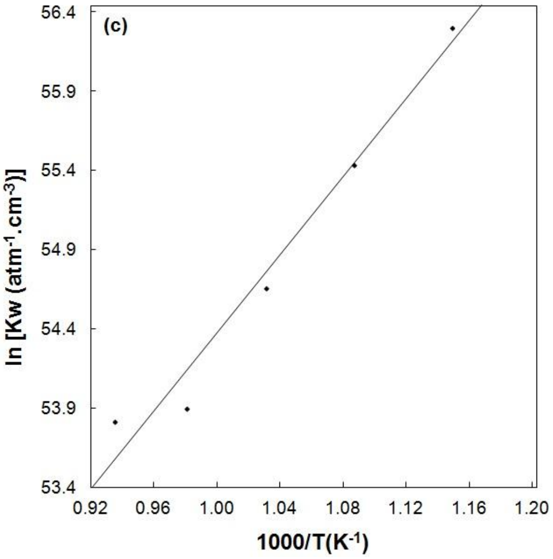

Fig. 4.19 – The equilibrium constant of hydration as a function of temperature mechanism c): $BaZr_{0.852}Y_{0.108}Zn_{0.04}O_{3-\delta}$

From figures 4.17 to 4.19 it is expected that the concentration of protons decreases with increasing the temperature due to the exothermic water dissolution [37].

By determination of the constants $\sigma^{*}_{OH_O^{\bullet}}$, $\sigma^{*}_{V_O^{\bullet\bullet}}$ and α, reported in tables 4.7, 4.8 and 4.9, the partial conductivities of protons, oxygen vacancies and holes can be calculated using equations 4.10 to 4.12, at different temperatures and atmospheres. Figures 4.20 and 4.21 shows the calculated dependences of partial conductivities as a function of the water vapour pressure under N_2 and O_2 atmospheres at 600°C and 800°C, respectively.

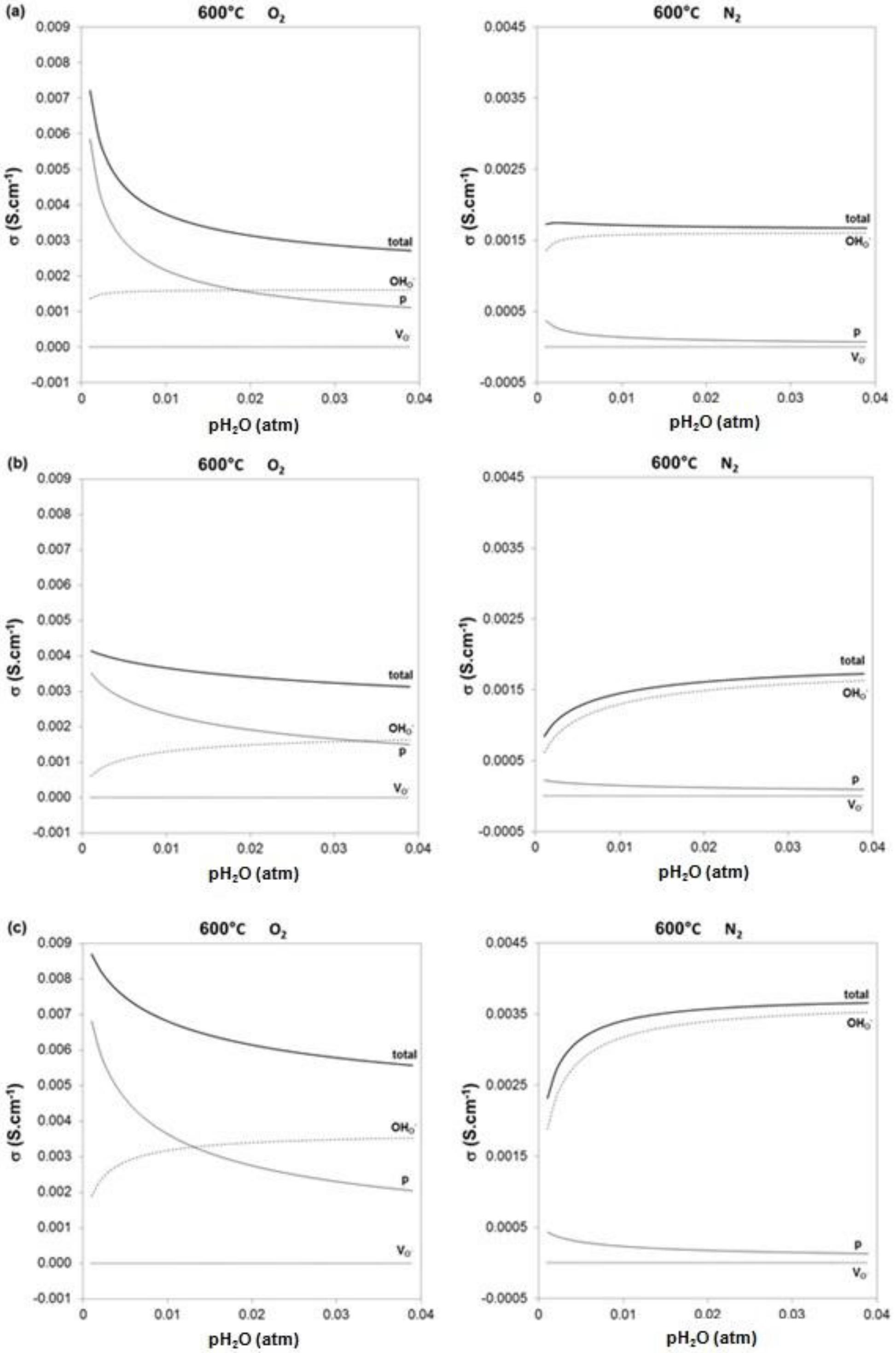

Fig. 4.20 – Total and partial conductivities dependence of Zn-modified samples *vs* pH_2O under different atmospheres (N_2 and O_2) at 600ºC: a) $BaZr_{0.812}Zn_{0.04}Y_{0.148}O_{3-\delta}$, b) $0.96BaZr_{0.852}Y_{0.148}O_{3-\delta}$+0.04ZnO and c) $BaZr_{0.852}Y_{0.108}Zn_{0.04}O_{3-\delta}$.

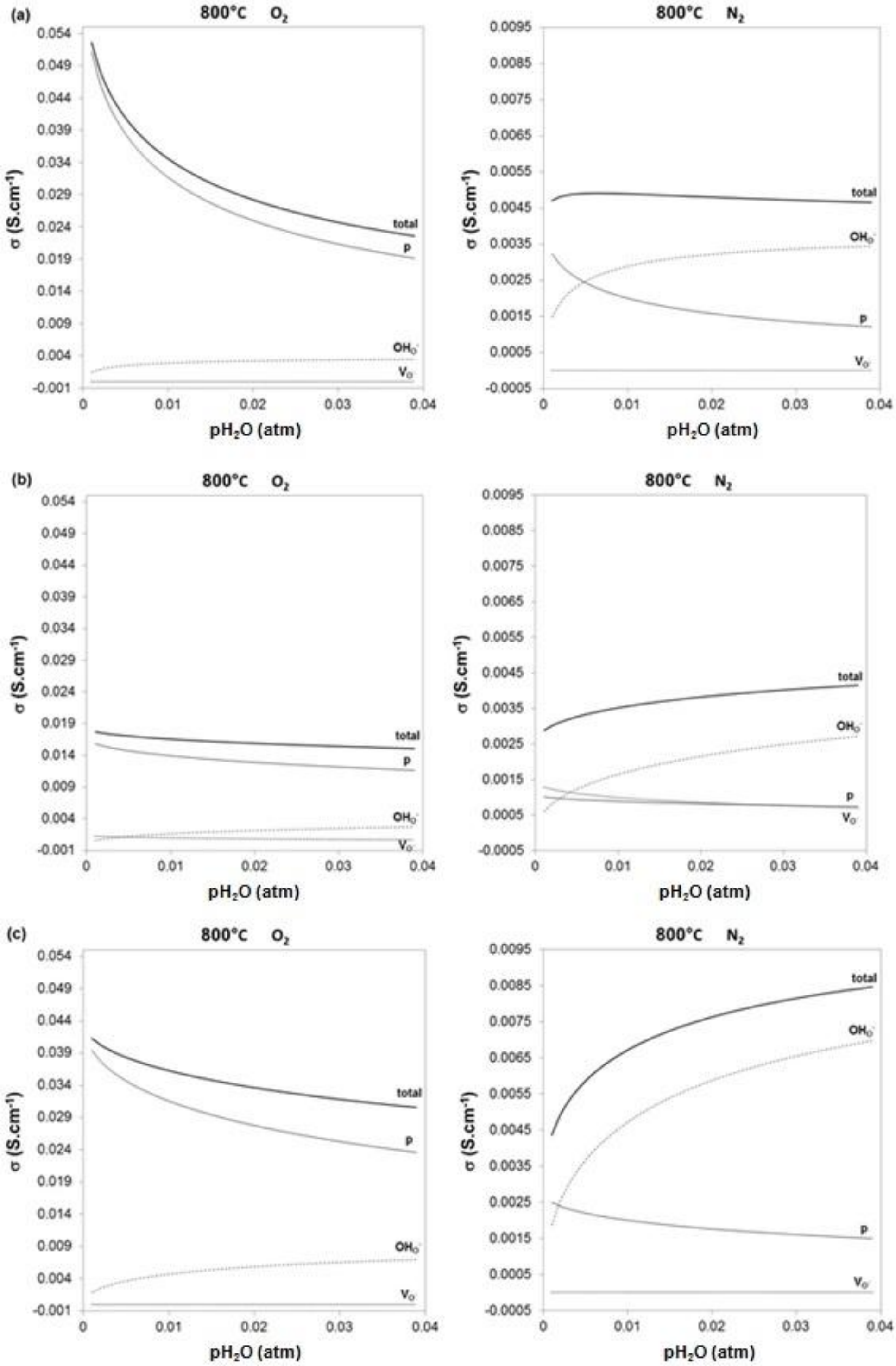

Fig. 4.21 – Total and partial conductivities dependence of Zn-modified samples *vs* pH$_2$O under different atmospheres (N$_2$ and O$_2$) at 800ºC: a) BaZr$_{0.812}$Zn$_{0.04}$Y$_{0.148}$O$_{3-\delta}$, b) 0.96BaZr$_{0.852}$Y$_{0.148}$O$_{3-\delta}$+0.04ZnO and c) BaZr$_{0.852}$Y$_{0.108}$Zn$_{0.04}$O$_{3-\delta}$.

From figures 4.20 and 4.21 it is clear that under O$_2$ conditions and high temperatures, the total conductivity is strongly dominated by the hole conductivity, while proton conductivity is dominant only at temperatures below 600°C and high water vapour pressures. Conversely, in a nitrogen atmosphere, proton conductivity is observed to be dominant for both temperatures and is shown to increase as pH_2O increases. In all cases oxide-ion conductivity is noted to be negligible. These results highlights the competitive nature of hydration, equation 1.8, and the production of holes, equation 4.8, a feature that is common for such perovskite ceramic proton conductors [2,43].

According to the figures 4.20 and 4.21, mechanism b) shows the lowest total conductivity in all conditions while, mechanisms a) and c) typically show similar and higher conductivities.

The low conductivity levels of mechanism b) can be explained by possible partitioning of yttrium over the A and B-sites to combat the induced Ba deficiency that would be expected to arise on Zn solubility in the BZY matrix, equation 4.2. Such a suggestion has previous been offered to account for the lower conductivity measured in Ba deficient BZY materials in the literature [7,44] Such crossover of yttrium to the A-site would deplete the oxygen vacancy concentration, lowering both the number of holes and/or the extent of hydration by equations 4.8 and 1.8, respectively.

The partial conductivities of protons, oxygen vacancies and holes measured under oxygen or nitrogen atmospheres at pH_2O = 0.033 atm. are shown in figure 4.22 in the form of Arrhenius plots for each mechanism. It is clear that, in an oxygen atmosphere, p-type electronic conductivity dominates the total conductivity across almost all the temperature range. In contrast, protonic conductivity is shown to dominate the total conductivity in nitrogen atmosphere. In all cases oxide-ion conductivity is negligible, as previously noted, and is, therefore, not plotted.

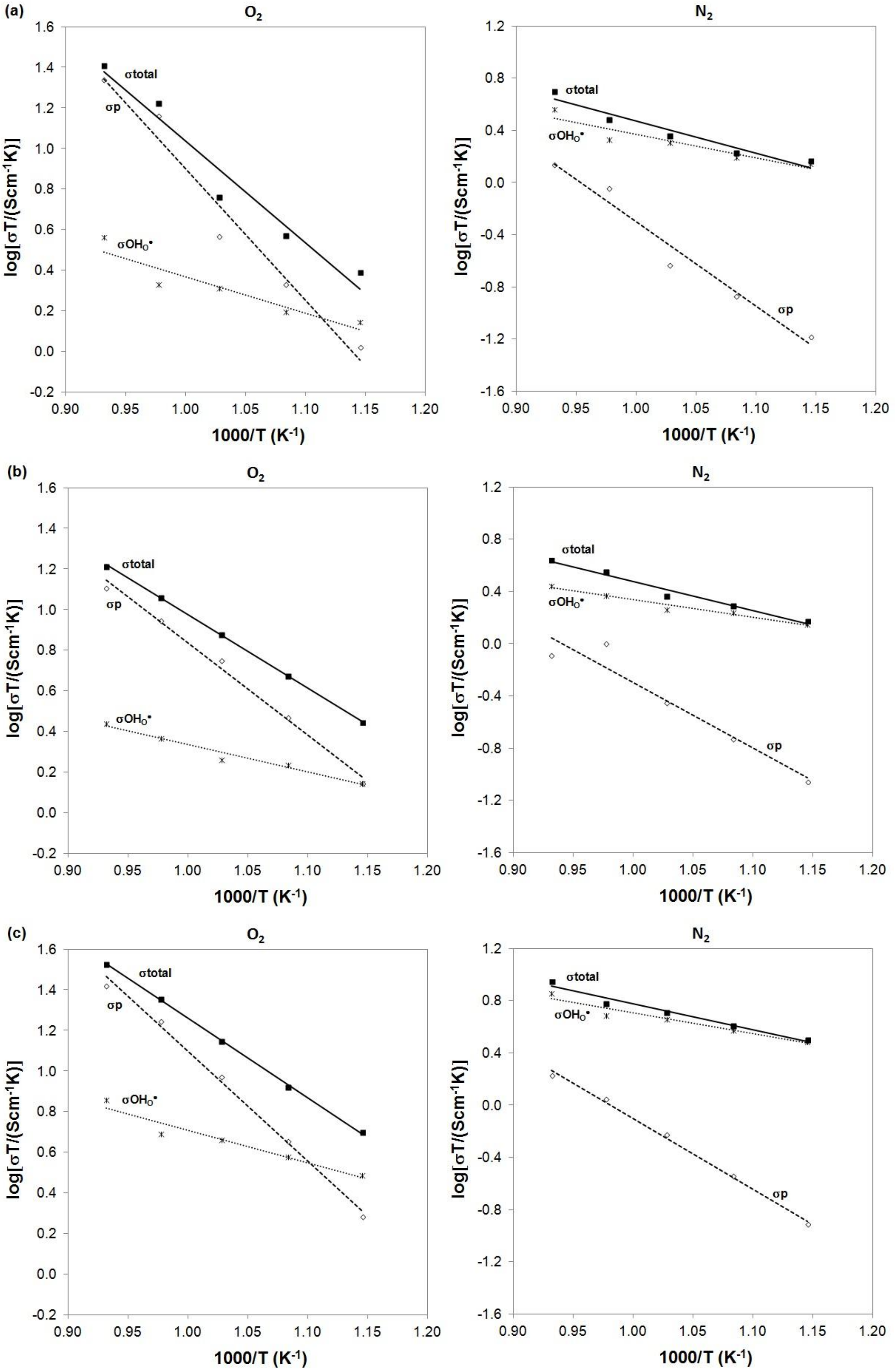

Fig. 4.22 – Total and partial conductivities of Zn-modified BZY *vs* reciprocal temperature at pH_2O = 0.033 atm in O_2 and N_2 atmospheres: a) $BaZr_{0.812}Zn_{0.04}Y_{0.148}O_{3-\delta}$, b) $0.96BaZr_{0.852}Y_{0.148}O_{3-\delta}$+0.04ZnO and c) $BaZr_{0.852}Y_{0.108}Zn_{0.04}O_{3-\delta}$.

The activation energies calculated from ln(σT) vs. 1000/T plots (figure 4.22) are shown in table 4.10 and are observed to be similar between N_2 and O_2 atmospheres. Nonetheless, the activation energies of protonic and p-type conduction is noted to increase in the order mechanism b) < mechanism c) < mechanism a), indicating a decrease in the mobility of both protons and holes in this sequence. This result concurs with the bulk activation energy trends measured at lower temperatures in table 4.3, reinforcing the importance of the bulk response in the total conductivity measured at these higher temperatures.

The activation energies for proton conduction in all the mechanisms are lower than the previously reported for barium zirconates (0.44 eV) [34] measured at low temperatures. While, the activation energies for hole conduction are of similar magnitude to those previously reported in the literature [43,45].

Table 4.10 – Activation energies (Ea) calculated at pH_2O = 0.033 atm in oxygen and nitrogen atmospheres of studied Zn-modified systems: mechanism a) - $BaZr_{0.812}Zn_{0.04}Y_{0.148}O_{3-\delta}$, mechanism b) - $0.96BaZr_{0.852}Y_{0.148}O_{3-\delta}+0.04ZnO$ and mechanism c) - $BaZr_{0.852}Y_{0.108}Zn_{0.04}O_{3-\delta}$.

Sample	**Wet O_2** (pH_2O = 0.033 atm)		**Wet N_2** (pH_2O = 0.033 atm)	
	Ea $\sigma_{OH^\bullet}$ (eV)	**Ea σ_p** (eV)	**Ea $\sigma_{OH^\bullet}$** (eV)	**Ea σ_p** (eV)
$BaZr_{0.812}Zn_{0.04}Y_{0.148}O_{3-\delta}$ (mechanism a)	0.36 ± 0.03	1.29 ± 0.02	0.36 ± 0.02	1.29 ± 0.02
$0.96BaZr_{0.852}Y_{0.148}O_{3-\delta}+0.04ZnO$ (mechanism b)	0.27 ± 0.01	0.90 ± 0.01	0.27 ± 0.01	1.00 ± 0.03
$BaZr_{0.852}Y_{0.108}Zn_{0.04}O_{3-\delta}$ (mechanism c)	0.31 ± 0.02	1.07 ± 0.01	0.31 ± 0.02	1.07 ± 0.01

4.1.3.5 CHEMICAL STABILITY

The influence of ZnO on the chemical stability of yttrium-doped barium zirconate was also investigated in this work. According to the electrical conductivity measurements, Zn-modified samples show a stable behaviour under oxidizing conditions under the operation temperatures. However, the stability of zinc in reducing operating conditions is under question. According to the thermodynamic tables - Ellingham diagram (fig. 4.23) [46], all the successful transition element sintering additives (Cu, Co, Ni and Zn) can be predicted to be susceptible to reduction under normal conditions [10,11].

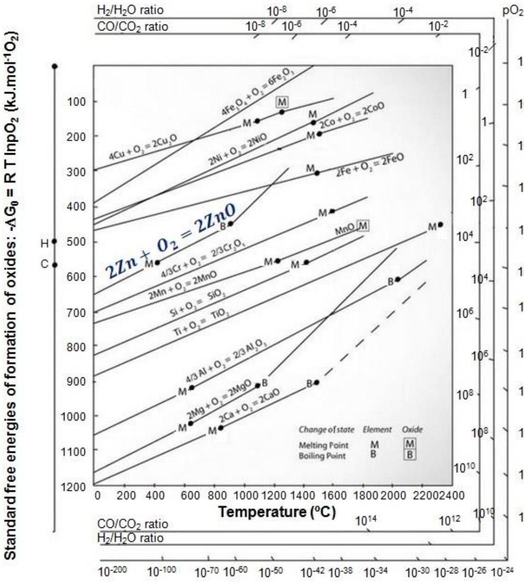

Fig. 4.23 – The Ellingham diagram of metal oxides (adapted from [46]).

Moreover, figure 4.24 highlights that under increasing temperature and/or lowering oxygen partial pressure the vapor partial pressure of zinc increases sharply, predicting potential Zn losses under these conditions.

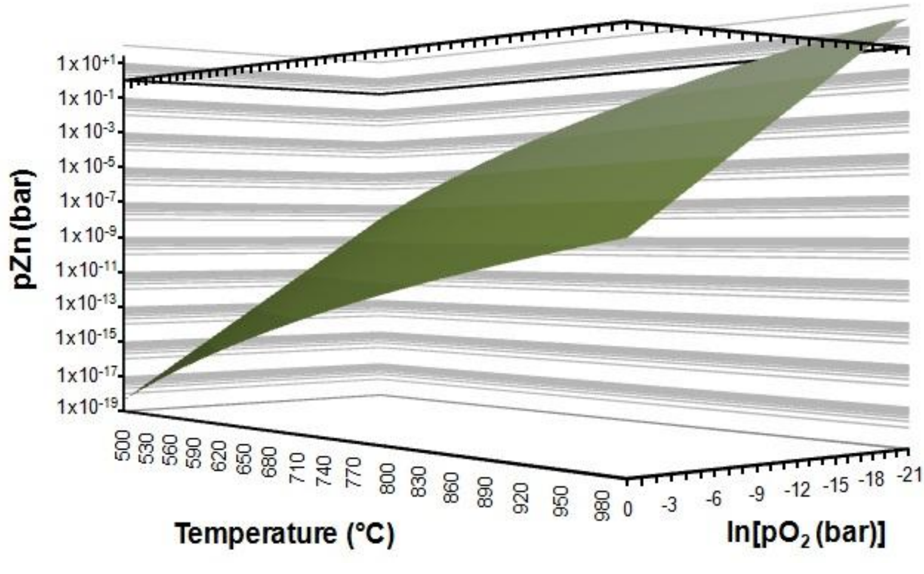

Fig. 4.24 – The dependence of the zinc partial pressure on temperature and oxygen pressure (adapted from [47]).

Indeed, results cycling from oxidizing to reducing then back to oxidizing conditions at high temperatures (900ºC) show permanent impairment of conductivity for these materials. In order to understand this phenomenon scanning electron microscopy has been performed on reduced samples (fig. 4.25).

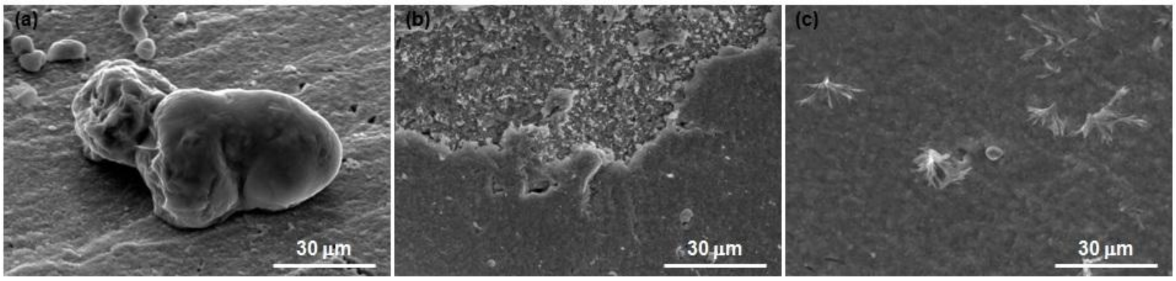

Fig. 4.25 - SEM surface micrograph of reduced (900ºC, 5 hours, flowing 10%H_2 : 90%N_2) Zn modified $BaZr_{0.85}Y_{0.15}O_{3-\delta}$ as a function of substitution mechanism: a) $BaZr_{0.812}Zn_{0.04}Y_{0.148}O_{3-\delta}$, b) $0.96BaZr_{0.852}Y_{0.148}O_{3-\delta}$+0.04ZnO and c) $BaZr_{0.852}Y_{0.108}Zn_{0.04}O_{3-\delta}$.

The resultant microstructures show some interesting differences: mechanisms a) and c) are shown to retain the dense ceramic but clear segregation phases are detected on the surface of these materials, figures 4.25 a) and 4.25 b). According to EDS (chemical analysis) measurements, the composition of the segregated phases are mainly constituted by barium and zinc (the amount of Zr and Y is reduced in these parts), while the underlying dense bulk sample is mainly composed by Ba, Zr, and Y (fig. 4.26 and 4.27).

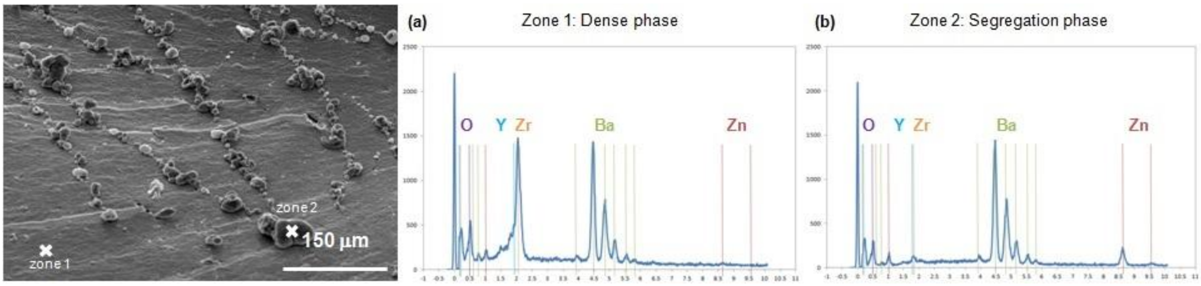

Fig. 4.26 - (a) SEM surface micrograph of reduced $BaZr_{0.812}Zn_{0.04}Y_{0.148}O_{3-\delta}$ (900ºC, 5 hours, flowing 10%H_2 : 90%N_2) and the correspondent energy spectra of (b) dense and (c) segregated phases – mechanism a).

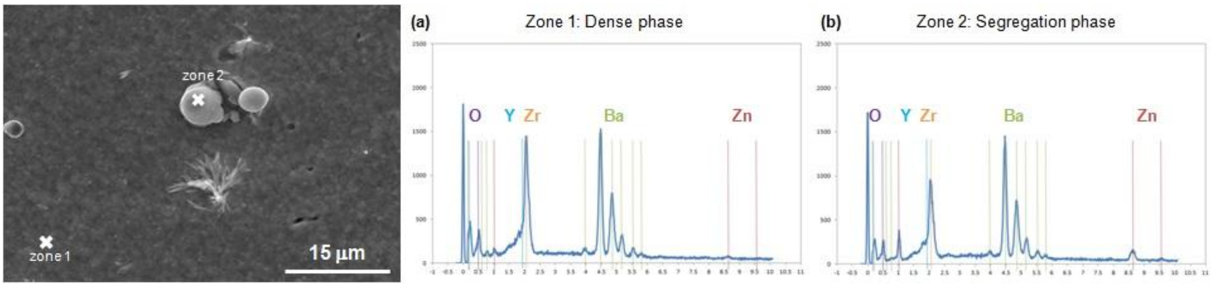

Fig. 4.27 - (a) SEM surface micrograph of reduced $BaZr_{0.852}Y_{0.108}Zn_{0.04}O_{3-\delta}$ (900ºC, 5 hours, flowing 10%H_2 : 90%N_2) and the correspondent energy spectra of (b) dense and (c) segregated phases – mechanism c).

On the contrary, the microstructure of samples in mechanism b) shows two distinct zones: a uniform part showing high densification levels and a newly formed “rough” zone with some pores and large glassy phases (fig 4.28). Nonetheless, chemical analysis measurements show homogeneous distribution of all the elements (Ba, Zr, Y and Zn) in both zones (fig. 4.29). Unfortunately, variation in the composition of the bulk ceramic and the glassy phase was unable to be ascertained under the resolution of the current EDS technique, due to interference with the composition of the underlying material. Further work is, therefore, necessary to fully understand this segregation.

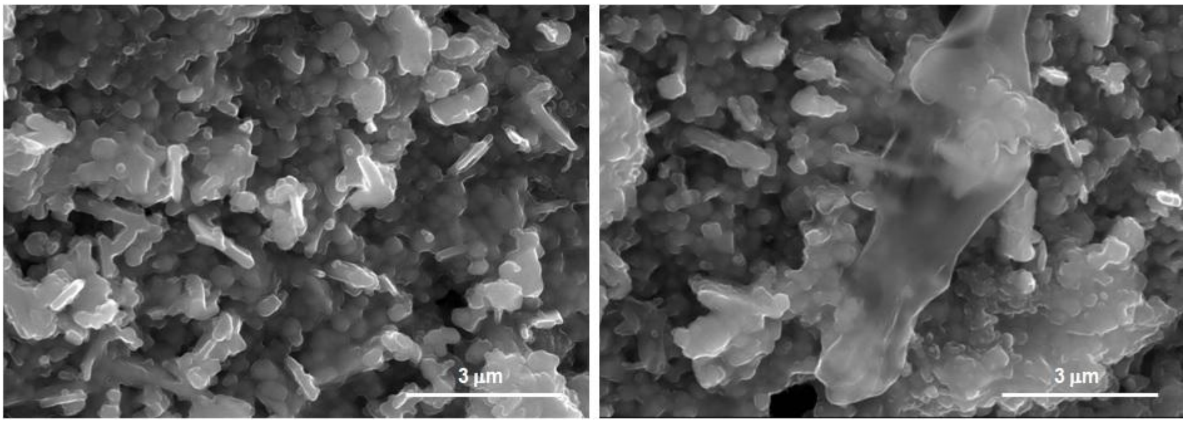

Fig. 4.28 - (a) SEM surface micrographs of (a) the “rough” zone of the reduced $0.96BaZr_{0.852}Y_{0.148}O_{3-\delta}+0.04ZnO$ (900ºC, 5 hours, flowing 10%H_2 : 90%N_2) and (b) its glassy phases.

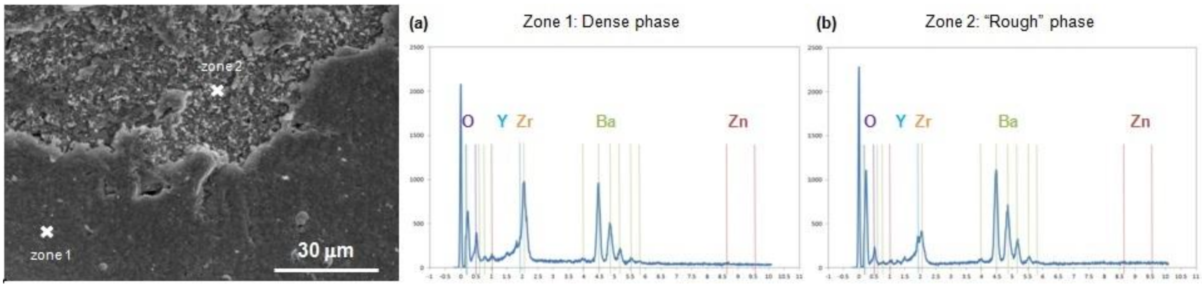

Fig. 4.29 - (a) SEM surface micrograph of reduced $0.96BaZr_{0.852}Y_{0.148}O_{3-\delta}+0.04ZnO$ (900ºC, 5 hours, flowing 10%H_2 : 90%N_2) and the correspondent energy spectra of the (b) dense and the (c) “rough” zones – mechanism b).

The microscopy results suggest that the high vapour pressure of Zn, expected at high temperatures and/or low pO_2, leads to segregation of Zn from the material and damaged ceramic microstructures. The protonics community should, therefore, be alert to such permanent damage under operation in these conditions and subsequent impairments in conductivity. These results concur with Babilo’s work [10] where microstructural degradation was reported under sintering temperatures higher than 1300ºC where, equation 4.22 is driven to the right and metallic zinc readily vaporizes.

$$ZnO(s) \leftrightarrow Zn(g) + \frac{1}{2}O_2(g) \tag{4.22}$$

4.1.4 CONCLUSIONS

In conclusion, introduction of ZnO into the lattice of barium zirconates promotes densification to ~ 35% comparing to the un-doped material, lowering the sintering temperature (from 1600ºC to 1300ºC). Different Zn-addition mechanisms do not show differences in terms of crystallographic phase forming a single cubic perovskite structure, which is similar to the un-doped $BaZr_{0.852}Y_{0.148}O_{3-\delta}$. However, the lattice parameters changes between Zn-addition mechanisms suggest that the structure of the perovskite oxides is very sensitive to their composition and promotes the formation of oxygen vacancies: when zinc goes into the B-site (mechanisms a and c), the vacancy concentration on Ba and O sites increase leading to a decrease in the lattice parameter. On the other hand, Ba deficiency (mechanism b) is responsible for the decrease in the lattice parameter due to the the perovskite phase changes (the composition would move from the single phase cubic perovskite phase field, to a two phase perovskite + Y_2O_3-based field, to a three phase perovskite + fluorite + Y_2O_3-based field and then finally to a two-phase perovskite + fluorite field).

The mechanism of ZnO addition has an impact on resultant microstructure. The different mechanisms lead to different grain growth: the formation of Ba-deficiency by mechanism b) has a negative impact on grain size, depleting grain growth. Chemical analysis by TEM and STEM-XEDS confirms the accumulation of Zn at the grain boundaries in these doped samples, which is suggested to be responsible for higher specific grain boundary conductivities and associated activation energies than in un-doped BZY.

Conversely, the bulk conductivity of Zn-modified yttrium-doped barium zirconate samples is somewhat lower than the un-modified counterpart at intermediate temperatures. At high temperatures, > 600ºC, the total conductivity of these materials is shown to be predominantly protonic in nitrogen atmospheres, whilst being predominately p-type electronic under oxygen. The total conductivity is shown to be the lowest for mechanism b). Nevertheless, the significant reduction in sintering temperature (from ~ 1600º to 1300ºC) and the high levels of densification render Zn-doped BZY samples a good candidate as an electrolyte in sensors, electrolyzers, catalytic membranes and fuel cells, especially at intermediate temperatures due to similar total conductivities.

4.2 EFFECT OF PHOSPHORUS ADDITIONS ON THE SINTERING AND TRANSPORT PROPERTIES OF PROTON CONDUCTING $BaZr_{0.85}Y_{0.15}O_{3-\delta}$

4.2.1 INTRODUCTION

The dispersion of nano-sized powder suspensions is essential for the preparation of stabilised solid suspensions required for thin ceramic applications. Phosphate esters represent one of the most commonly used dispersants to prevent nano-sized powder agglomeration, and are regularly applied for the stabilisation of analogous $BaTiO_3$ nano-powders [48-50]. Such phosphorous additions have also been shown to decrease the sintering temperature of $BaTiO_3$ through the formation of P- and Ba-containing phases that improve porosity coalescence and removal [19,51]. Analogously, the addition of phosphorous has recently been shown to slightly lower the sintering temperature required for attaining high density in barium zirconate ceramics while also improving mechanical properties [52]. Furthermore, the stability of a P-based sintering additive towards reduction is expected to be higher than that of common transition metal oxide sintering additives, such as NiO or CoO, thus avoiding the subsequent appearance of electronic conductivity in the reducing conditions of operation [12-14]. Nonetheless, studies of phosphate ester additions to $BaTiO_3$ materials have highlighted the presence of residual phosphorous after burn-out of the organic chain [19,33] with the formation of barium phosphate secondary phases. In $BaTiO_3$, the impact of these secondary phases on conductivity was shown to be dependent on sintering temperature. Although conductivities were impaired at sintering temperatures below 1275ºC, higher sintering temperatures lead to slight enhancement over the P-free base composition [19].

The motivation for this study is, therefore, to acquire knowledge of the effect of P_2O_5 additions in BZY in order to assess both the feasibility of the use of phosphate esters in BZY thin film preparation and the potential of phosphorus as a sintering additive.

4.2.2 PROCESSING METHODOLOGY

The specific composition selected in this study was $BaZr_{0.85}Y_{0.15}O_{3-\delta}$ (BZY) produced from BaO_2 (Sigma-Aldrich, 95% purity) and $(ZrO_2)_{0.92}(Y_2O_3)_{0.08}$ (TZ-8Y, TOSOH Co.). Stoichiometric amounts of P_2O_5 were added to $BaZr_{0.852}Y_{0.148}O_{3-\delta}$ by a solid state reaction. The mixtures were milled for a further 2 hours at a rotation speed of 150 rpm.

Green pellets were obtained after being pressed isostatically at 300 MPa for 15 minutes and two sintering conditions were tested; 1400ºC for 24 hours and 1500ºC for 5 hours. In both cases the sintering process was performed in air.

Densification studies were performed using a dilatometer, while phase analysis and the subsequent determination of lattice parameters were performed by X-ray diffraction (XRD) coupled with Rietveld refinement, respectively. Microstructural detail was investigated by scanning electron microscopy (SEM) on polished and thermally etched samples.

Electrical-conductivity measurements were performed on bars and data were collected on cooling in flowing wet and dry 10% H_2:90% N_2.

4.2.3 RESULTS AND DISCUSSION

4.2.3.1 DENSIFICATION

The densification behaviour of BZY as a function of P_2O_5 content is shown in Fig. 4.30.

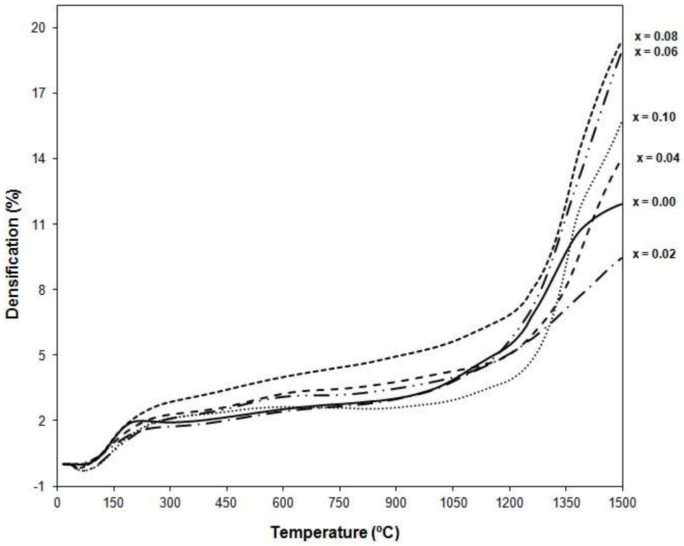

Fig. 4.30 - Densification behaviour of (1-x)$BaZr_{0.85}Y_{0.15}O_{3-\delta} \cdot xP_2O_5$ in the range x= 0 – 0.10.

The P_2O_5 additions are shown to have a significant effect on densification, monotonously promoting densification with increasing P_2O_5-content in the intermediate compositional range $0.04 \leq x \leq 0.08$. In contrast, the effect is slightly depleted at higher P_2O_5 contents (x = 0.10), while at low P_2O_5 contents (x = 0.02) densification is hindered in comparison to that of pure BZY. Figure 4.31 compares the temperature dependence of the linear shrinkage rate as a function of P_2O_5 content.

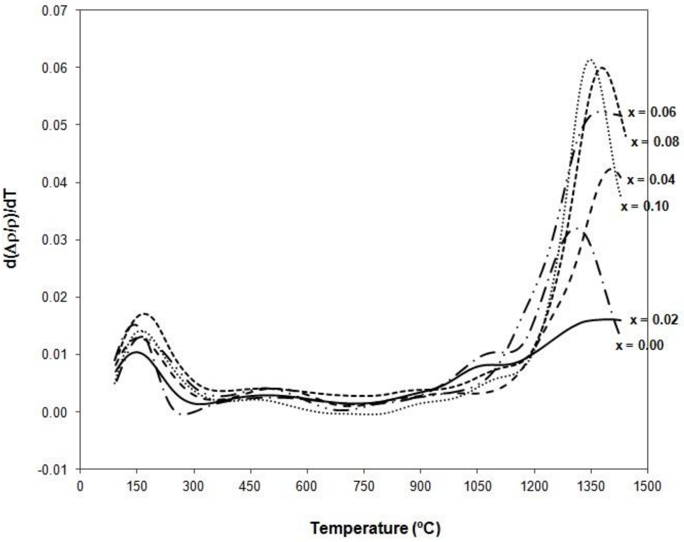

Fig. 4.31- Temperature dependence of the linear shrinkage rate of (1-x)$BaZr_{0.85}Y_{0.15}O_{3-\delta} \cdot xP_2O_5$ in the range x= 0 – 0.10.

P_2O_5 additions produce an increase in the maximum shrinkage rate and shift the temperature of maximum shrinkage rate to lower temperatures. The width of the shrinkage temperature range is also observed to narrow with increasing additive concentration. The presence of such sharp peaks in curves of linear shrinkage rate is characteristic of liquid-phase assisted sintering [53]. A similar phenomenon was noted for P-doped $BaTiO_3$ analogues, where improvements in densification were related to the presence of a P-based coating on the particle surface that improved porosity coalescence and removal of pores at lower sintering temperatures at the first stage of sintering [48,49]. In agreement with the dynamic measurements, sintering experiments performed at 1500ºC for 5 hours and 1400ºC for 24 hours show improvements in densification with increasing P_2O_5 content in the intermediate compositional range, fig. 4.32. Peak densities are achieved for the compositions x = 0.06 and 0.08, with densities in excess of 90% for both sintering conditions. A maximum density of 98% of the theoretical value is exhibited by composition x = 0.08 sintered at 1500ºC for 5 hours.

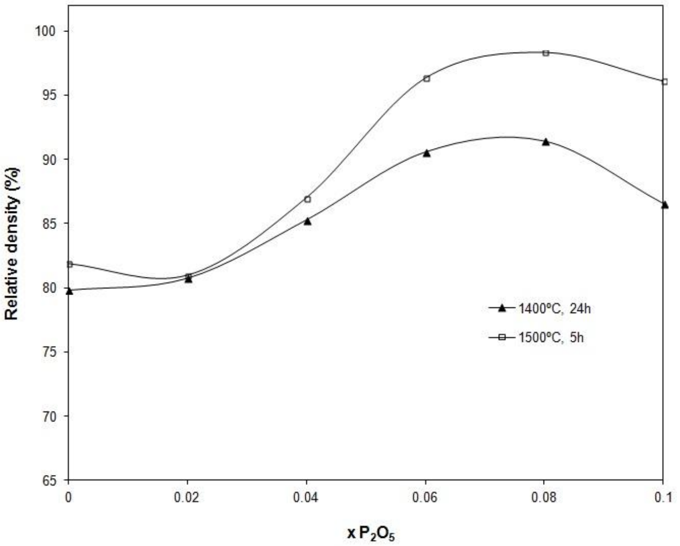

Fig. 4.32 - Sintering experiments performed at 1500ºC for 5 hours and at 1400ºC for 24 hours of (1-x)$BaZr_{0.85}Y_{0.15}O_{3-\delta} \cdot xP_2O_5$ in the range x= 0 – 0.10.

4.2.3.2 PHASE ANALYSIS AND MICROSTRUCTURE

The possible presence of liquid phases was assessed by SEM. A representative scanning electron micrographs of bulk samples of composition x = 0.04, 0.06 and 0.08 sintered at 1400°C are shown in fig. 4.33. A phase of glassy appearance is observed in all the samples. Unfortunately, analysis of the glass composition by X-Ray Energy Dispersive Spectroscopy (XEDS) proved to be inconclusive due to the overlapping of P, Y and Zr peaks in the spectra. Nonetheless, such glassy phases are absent from the microstructure of pure BZY sintered even at higher temperatures (1600ºC for 5 hours), suggesting that these glassy structures result from the P-additions (fig. 4.34).

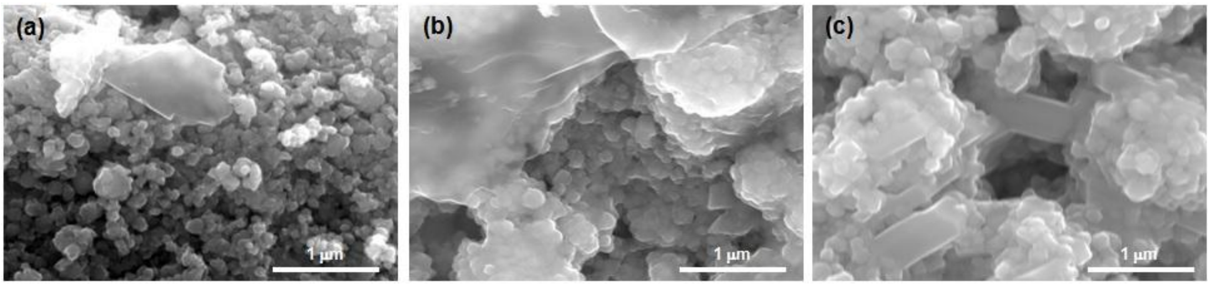

Fig. 4.33 - Scanning electron micrographs of a bulk sample of compositions (1-x)$BaZr_{0.85}Y_{0.15}O_{3-\delta} \cdot xP_2O_5$, (a) x = 0.04, (b) x = 0.06 and (c) x = 0.08, sintered at 1400°C for 24 hours.

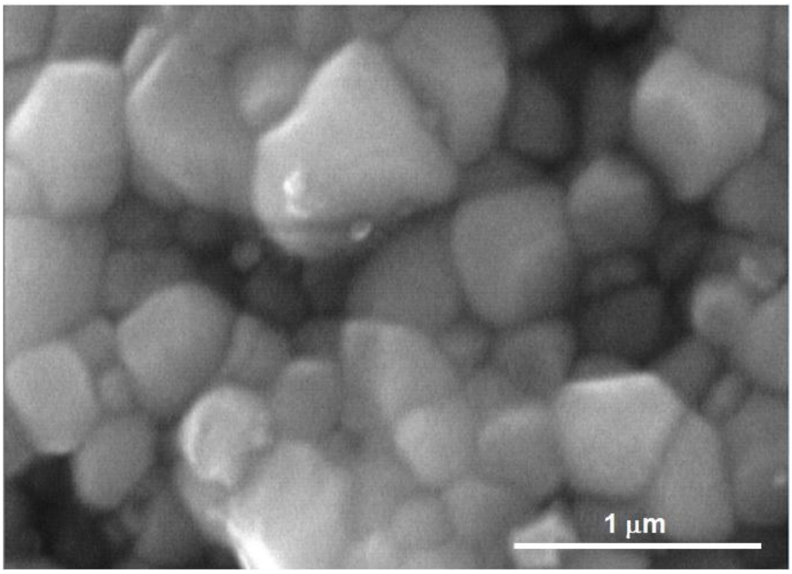

Fig. 4.34 - Scanning electron micrograph of a bulk sample of pure $BaZr_{0.85}Y_{0.15}O_3$, sintered at 1600°C for 5 hours.

A single-phase BZY perovskite is formed after mechanosynthesis, in agreement with a previous study [52]. On addition of the P_2O_5-additives and further light milling, impurity phases cannot be seen at the resolution of XRD for the concentrations studied. Nonetheless, fig. 4.35 shows the XRD patterns of a sample of composition $x = 0.10$ with posterior thermal treatment in the temperature range 600 – 1500°C. On heating, the formation of $Ba_3(PO_4)_2$ is revealed at temperatures greater than 600ºC, which persists up to the highest temperatures studied, reflecting the high thermodynamic stability of this phase [54]. The development of the $Ba_3(PO_4)_2$ phase is accompanied by the segregation of Y_2O_3 for temperatures ≤ 900ºC and additional traces of a fluorite $Zr_{1-x}Y_xO_{2-\delta}$ cubic solid solution at higher temperatures. Such progression of $Ba_3(PO_4)_2$ phase formation and secondary phase segregation can also be observed as a function of P_2O_5 content in fig. 4.36. As the value of x increases, one first observes the presence of the Y_2O_3 impurity phase, which is accompanied at $x \geq 0.06$ by the presence of a fluorite $Zr_{1-x}Y_xO_{2-\delta}$ cubic solid solution and the $Ba_3(PO_4)_2$ phase. These observations will be discussed further by monitoring lattice-parameter variations.

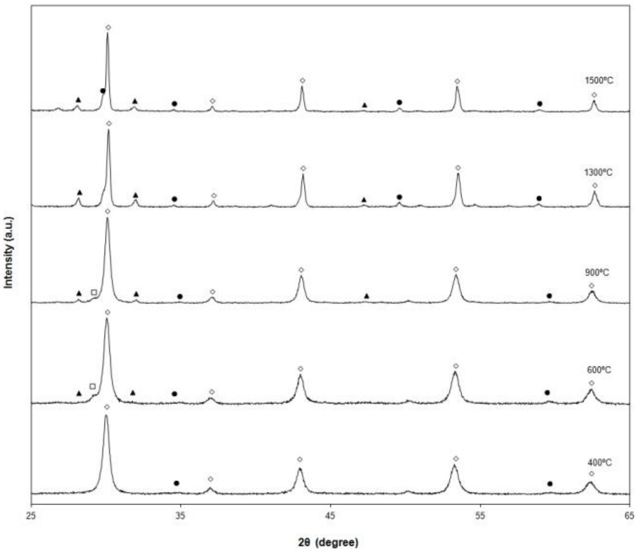

Fig. 4.35 - Evolution of powder XRD patterns with temperature for (1-x)$BaZr_{0.85}Y_{0.15}O_{3-\delta} \cdot xP_2O_5$, x = 0.10. The markers identify: (◊) the $BaZrO_3$- based phase, (•) a $Zr_{1-x}Y_xO_{2-\delta}$- based solid solution, (▲) $Ba_3(PO_4)_2$ and (□) Y_2O_3.

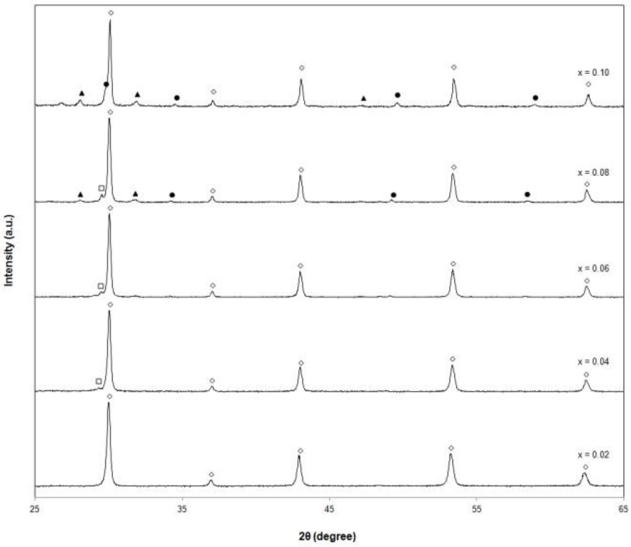

Fig. 4.36 - Powder XRD patterns of (1-x)$BaZr_{0.85}Y_{0.15}O_{3-\delta} \cdot xP_2O_5$, x = 0.02 – 0.10 as a function of composition x after sintering at 1500ºC for 5 hours. The markers identify: (◊) the $BaZrO_3$- based phase, (•) a $Zr_{1-x}Y_xO_{2-\delta}$- based solid solution, (▲) $Ba_3(PO_4)_2$ and (□) Y_2O_3.

The lattice parameters of (1-x)$BaZr_{0.85}Y_{0.15}O_{3-\delta} \cdot xP_2O_5$ as a function of x are shown in fig. 4.37 compared to the lattice parameter progression of join $Ba_{1-y}Zr_{0.85}Y_{0.15}O_{3-\delta}$, where the value y represents barium loss. If one considers that x moles of $Ba_3(PO_4)_2$ would be produced for every x moles of P_2O_5 added, the required Ba-loss from the perovskite would be represented by the equation y = 3x. This analogy appears to be strongly supported when these two joins are plotted together using this ratio, fig. 4.38. The decrease in perovskite lattice constant with increasing P_2O_5 additions parallels the general trend expected for the BZY lattice on Ba-loss. Yamazaki *et al.* [7] recently re-plotted the phase diagram of Imashuku *et al.* [16] based on information obtained from the study of join $Ba_{1-y}Zr_{0.8}Y_{0.2}O_{3-\delta}$ to highlight this factor. This phase diagram is reproduced in fig. 4.38 to show the location of the current join, $Ba_{1-3x}Zr_{0.85}Y_{0.15}O_{3-\delta}$, formed on addition of xP_2O_5 to BZY. One can observe that, as one removes barium from the perovskite phase, the composition would move from the single phase cubic perovskite phase field, to a two phase perovskite + Y_2O_3-based field, to a three phase perovskite + fluorite + Y_2O_3-based field and then finally to a two-phase perovskite + fluorite field. This phase progression corresponds well with the observed phase progressions noted by XRD in figs. 4.35 and 4.36 for P_2O_5 additions upon formation of $Ba_3(PO_4)_2$. Hence, this observation reinforces a suggested mechanism of Ba-loss from BZY upon addition of P_2O_5. Indeed, the lattice parameters of the perovskite phase shown in fig. 4.37 tend towards that of un-doped $BaZrO_3$ with increasing P_2O_5 addition, in agreement with the behaviour predicted from the phase diagram for BZY upon extensive Ba-loss, fig. 4.38.

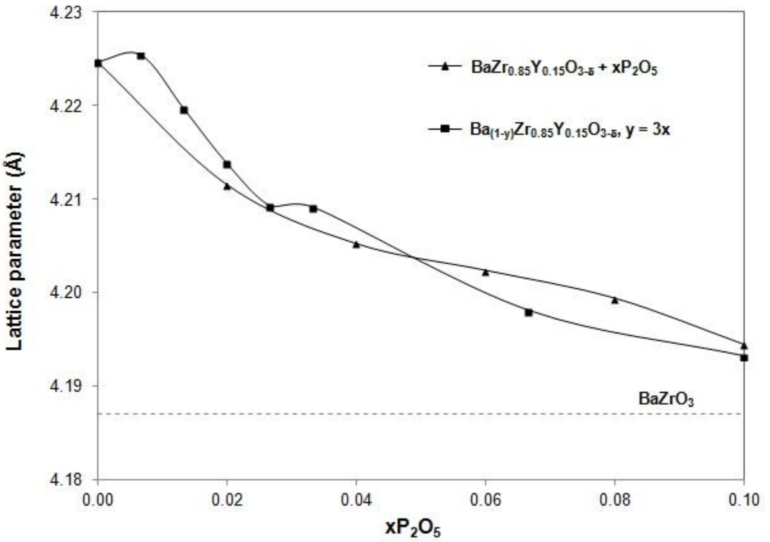

Fig. 4.37 - Evolution of lattice parameters of $BaZr_{0.85}Y_{0.15}O_{3-\delta}$ with P_2O_5 fractions in the range 0 - 0.10 sintered at 1500°C.

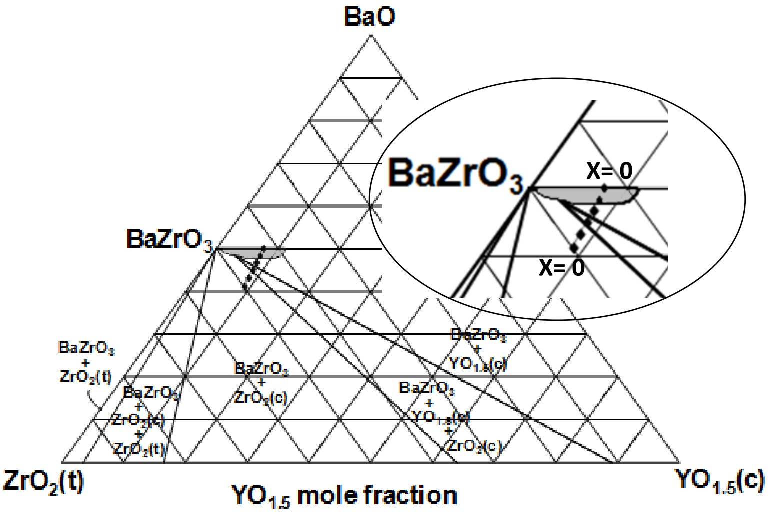

Fig. 4.38 - Phase diagram of BaO-$YO_{1.5}$-ZrO_2 from reference [7] showing the location of the barium deficient join, $Ba_{1-y}Zr_{0.85}Y_{0.15}O_{3-\delta}$.Formation of this join is expected on P-addition $(1-x)BaZr_{0.85}Y_{0.15}O_{3-\delta} \cdot xP_2O_5$, due to the formation of $Ba_3(PO_4)_2$ using the relationship 3x = y.

The grain size of P_2O_5-doped BZY on sintering at 1400 and 1500°C is shown in fig. 4.39 as a function of added P_2O_5. For small amounts of P_2O_5, up to 4 mol%, there is a significant decrease in grain size with increasing P_2O_5 content. Interestingly, Yamazaki *et al.* [7] noted a similar impairment of grain growth as a result of Ba-loss in the series $Ba_{1-y}Zr_{0.8}Y_{0.2}O_{3-\delta}$. Figure 4.38 highlights the restriction in grain growth with expected Ba-loss for the series $Ba_{1-y}Zr_{0.85}Y_{0.15}O_{3-\delta}$ in comparison to that of the P_2O_5-containing samples. Using the ratio 3x = y, as previously discussed, a close match of impairment of grain size between the P_2O_5-added system and the Ba-deficient system, can be observed. Caballero *et al.* [19,51] reported that grain growth of $BaTiO_3$ was inhibited by phosphorous ester additions and related this phenomenon to solute drag. Nonetheless, the close match of grain growth inhibition caused by Ba-deficiency and P_2O_5 addition in the current work, fig. 4.39, suggests that further analogies need to be presented. Yamazaki *et al.* [7] suggest that the grain sizes of BZY sintered samples clearly decrease with Ba-loss, suggesting that this phenomenon happens due to the precipitation of secondary phases, such as Y_2O_3, and its own limitations, as it was described in the previous chapters (section 4.1.3.2). Although, since Y_2O_3 could not be detected from the XRD, it suggests that the amount was quite low, less than the detectable limit of the instrument. Note that the latter analogy has also been widely proposed to explain grain-growth inhibition in doped $BaTiO_3$ materials [55]. At higher amounts of P_2O_5 (> 4 mol%), the trend is reversed and grain size is slightly increased. This may indicate progression into new phase fields upon extensive Ba-loss, fig. 4.38, with compositional shift of the perovskite phase towards that of un-doped $BaZrO_3$. In agreement with this analogy, Antunes *et al.* [6] have documented that un-doped $BaZrO_3$ offers improved grain growth over that of BZY.

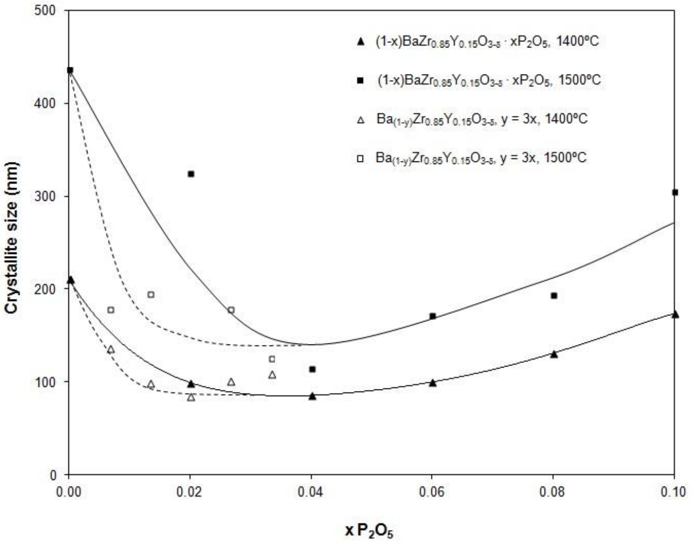

Fig. 4.39 - Comparison of the composition dependence of grain size of systems $Ba_{1-y}Zr_{0.85}Y_{0.15}O_{3-\delta}$ and $(1-x)BaZr_{0.85}Y_{0.15}O_{3-\delta} \cdot xP_2O_5$, using the ratio 3x = y. Samples sintered at 1400°C for 24 hours and 1500°C for 5 hours.

4.2.3.3 ELECTRICAL MEASUREMENTS

The temperature dependencies of the total conductivities for BZY and BZY $\cdot xP_2O_5$ are shown in fig. 4.40 in wet and dry 10% H_2/N_2. For the lightly doped compositions, the conductivity in wet conditions is higher than that of dry, suggesting proton conduction. The addition of P_2O_5 is shown to be highly detrimental to the total conductivity. Even lightly doped compositions, such as that containing only 2 mol% P_2O_5, show conductivity impairments of up to an order of magnitude at the highest temperatures. This effect is even more severe with increasing P_2O_5 content leading to a uniformly low conductivity that is approximately two orders of magnitude below that of the un-doped composition.

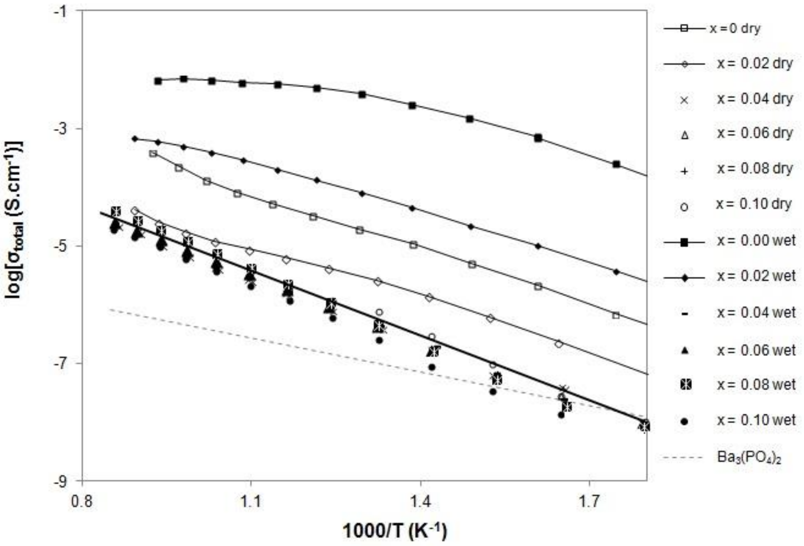

Fig. 4.40 - Temperature dependence of the total conductivity of system (1-x)$BaZr_{0.85}Y_{0.15}O_{3-\delta} \cdot xP_2O_5$ (x = 0 – 0.10) in wet and dry 10%H_2/N_2. Results of $Ba_3(PO_4)_2$ from reference [49].

In order to investigate this behaviour further, bulk and grain-boundary responses have been deconvoluted for samples x = 0 and 0.02. The bulk behaviour is shown in fig. 4.41. One can observe that bulk conductivity is slightly decreased with increasing P_2O_5 content. Further study of the grain-boundary response was undertaken on plotting $\sigma_{gb}* = \sigma_{gb}/D$ against temperature in Arrhenius form (fig. 4.42), where D is the mean grain size. This is a similar approach to that adopted by Yamakazi *et al.* [7] to provide an estimation of the inherent grain-boundary properties independent of microstructure, on the assumption that the proportionality factor of the grain-boundary thickness (d) remains effectively constant. The data in fig. 4.42 reveal a drop in $\sigma_{gb}*$ of well over an order of magnitude with P_2O_5 doping. Depletions of bulk and inherent grain-boundary transport properties have also previously been observed in the case of introducing Ba-loss to BZY [7]. Hence, the fall in the bulk conductivity in the present case, can be suggested to arise from a similar phenomenon that results from the extraction of Ba from the BZY lattice to form $Ba_3(PO_4)_2$. Nonetheless, the drop in $\sigma_{gb}*$ in the present materials is significantly larger than that which would be predicted from solely Ba loss from the BZY perovskite [7]. In the present case, the presence of P-based glassy phases coating the BZY particles, as seen in fig. 4.33, may also be significantly detrimental to the intergranular proton conductivity. Such large increases in grain-boundary resistivity lead to impedance spectra that are completely dominated by large grain-boundary responses in compositions of higher P_2O_5 content, leading to the low total conductivities observed in fig. 4.42.

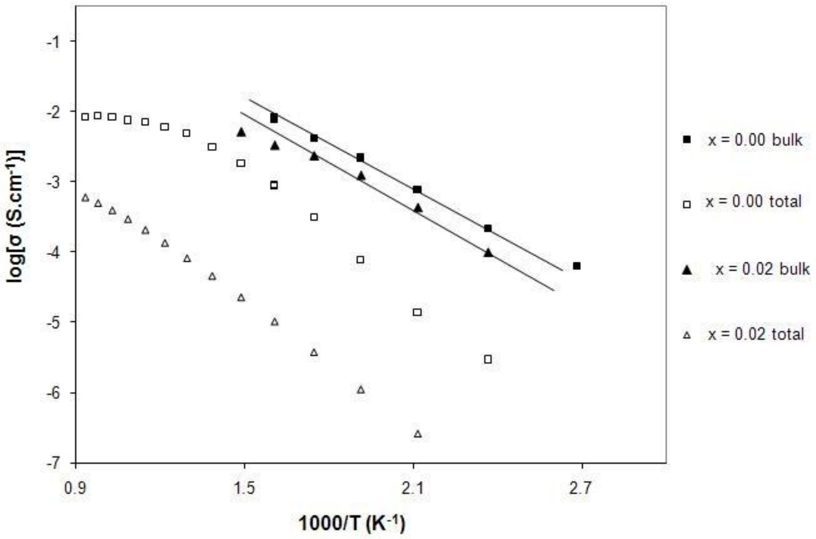

Fig. 4.41 - Temperature dependence of the bulk and total conductivities of the (1-x)$BaZr_{0.85}Y_{0.15}O_{3-\delta}$ · xP_2O_5 system, in wet 10%H_2/N_2.

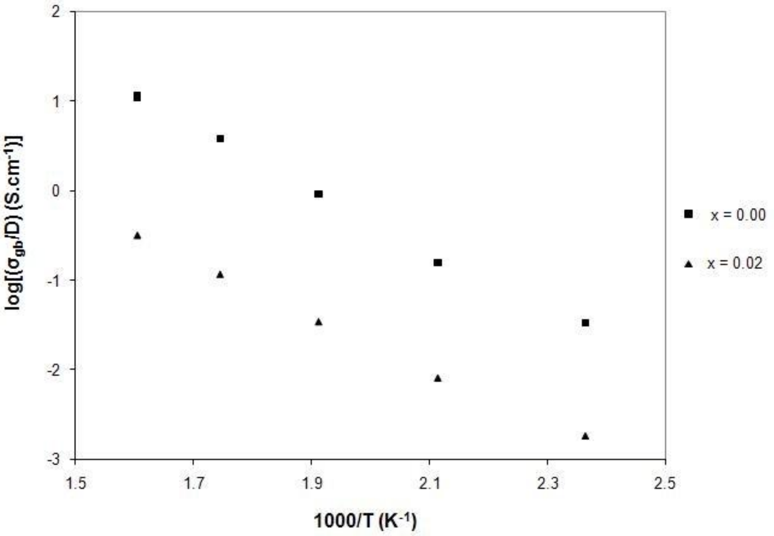

Fig. 4.42 - Temperature dependence of the grain-boundary conductivities of the (1-x)$BaZr_{0.85}Y_{0.15}O_{3-\delta}$ · xP_2O_5 system, in wet 10%H_2/N_2.

4.2.4 CONCLUSIONS

The effects of P additions on the sintering and electrical transport properties of the well-known, proton-conducting perovskite $BaZr_{0.85}Y_{0.15}O_{3-\delta}$ have been studied.

BZY reacts with P forming the highly stable $Ba_3(PO_4)_2$ phase at temperatures as low as 600°C. Correspondingly, the perovskite lattice parameter decreases with increasing P_2O_5 additions, as a result of removal of Ba from the perovskite lattice. P_2O_5 additions are further shown to impair grain growth. Parallels have been drawn with the expected behaviour of BZY materials as a function of

Ba-loss. For intermediate concentrations of P_2O_5, in the range $0.04 \leq x \leq 0.08$, densification of BZY is monotonously improved by the P-additions and the temperature of maximum densification rate is lowered. Nonetheless, reaction with P has a highly detrimental effect on the electrical transport properties of BZY decreasing both bulk and grain boundary conductivities. The biggest depletion is for the grain–boundary behaviour, as is the case for Ba-loss from BZY, and this appears to be additionally impaired in the current results due to the formation of isolating glassy phases that coat the BZY grains.

To put these results into perspective, one should realize that the dopant level of phosphate esters used as dispersants to prevent nano-sized powder agglomeration and stabilization in analogous $BaTiO_3$ powders have typically been in the range 0.13 - 5 wt% P_2O_5 (~0.002 to 0.05 mol fraction of P_2O_5) [40-44]. The current results show that even low levels of phosphorous cannot be used for BZY materials without serious negative consequences for proton conductivity. Hence, it is vital that the current results are taken into account by the PCFC community when attempting to prepare stabilized solid suspensions of BZY nanopowders required for thin ceramic applications. It is highly preferable that alternatives to phosphate esters should be found.

4.3 THE POTENTIAL OF BORON AS A SINTERING ADDITIVE FOR Ba(Zr,Y)$O_{3-\delta}$ MATERIALS

4.3.1 INTRODUCTION

Studies involving the search for redox stable sintering additives with ionic sizes much smaller than the average B-site ionic radius are still in focus [13,20,21]. Phosphorus was presented in the previous section as a potential sintering aid of this type for BZY. Although densification was noted to be improved, the last study highlighted that phosphorous additions rapidly impair proton conductivity. In this section, another potential choice will be investigated, that of boron addition. It is expected that the small ionic size of boron would prevent its substitution in the perovskite material, leading to potentially improved densification whilst maintaining the conductivity of $BaZrO_3$-based materials.

Lee *et al.* [20] showed that the densification temperature of $Ba_{0.997}Y_{0.003}TiO_{3-\delta}$ decreased by approximately 200ºC with respect to the additive free composition on addition of 4 mol% BN or 4 mol% BaB_2O_4. It was supposed that a B_2O_3-rich liquid phase was produced on decomposition of the BN component at around 1000ºC, with subsequent reaction with barium to form BaB_2O_4. According to the phase diagram (fig. 4.43), BaB_2O_4 is predicted to melt at 942ºC, and this phenomenon was suggested to lower the sintering starting temperature by liquid phase assisted sintering, increasing grain mobility and densification. Moreover, for small additive levels, improvements in conductivity over the base material were also noted. Similar improvements of densification have been observed for boron additions to $BaTiO_3$ under microwave sintering [21].

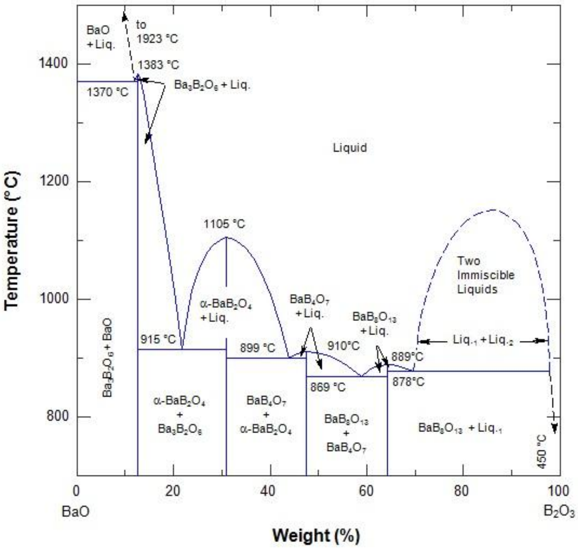

Fig. 4.43 - Phase diagram of system BaO-B_2O_3 (adapted from [57]).

Thus, in this work, the densification of un-doped and Y-doped $BaZrO_3$ (BZO and BZY, respectively) with boron additions will be investigated, using the boron source, H_3BO_3.

Additionally, a new doping approach will be under focus, which uses solvents to introduce the additives - solution doping method. More homogeneous doping is expected by the addition of the additives in the form of solution than can be obtained by simple milling with sintering additives in powder form.

According to that described in Chapter 1, perovskite-type proton conductors have been studied as new electrolyte materials for intermediate temperature operating SOFC (IT-SOFC). In line with this goal, a large body of research has been performed in order to develop thin electrolyte films based on these materials [58]. The most common techniques used to obtain this type of electrolyte film have been based on powder suspensions and/or slurries, where the ceramic powders are in contact with a liquid solvent, for example, dip coating [59-61], spin coating [8,59-72], tape casting [73-75] or settlement methods [76]. The selection of solvents for this aim, therefore, can be considered a critical step; moreover water-based solutions would be desirable, not only for environmental reasons, but also to reduce cost [75].

This work aimed to investigate the densification of $BaZrO_3$-based materials (BZO and BZY) with boron additions and to determine which solvent would be the most appropriate for dispersion of this sintering aid in these mechanosynthesized ceramic powders; additional information that will also be critical to produce thin electrolyte films.

4.3.2 PROCESSING METHODOLOGY

Powders of $BaZrO_3$ (BZO) and $BaZr_{0.85}Y_{0.15}O_{3-\delta}$ (BZY) were synthesized by the mechanosynthesis method previously described in section 4.2.1. For BZO, stoichiometric quantities of precursors BaO_2 (Sigma-Aldrich, 95% purity) and zirconium (IV) oxide - ZrO_2 (TZ-0Y, TOSOH Co.), were used, while the preparation of BZY used BaO_2 with the yttrium containing precursor, $(ZrO_2)_{0.92}(Y_2O_3)_{0.08}$ (TZ-8Y, TOSOH Co.) The addition of the boron additive was performed by the solution doping method. Stoichiometric quantities of the additive solution (H_3BO_3 in water, ethanol or methanol) were added to the BZO or BZY powder (1 g). The solvents (water, methanol and ethanol) were disposed and subsequently evaporated by means of oscillating and heating, respectively, in an ultrasonic bath, thus leaving the additives distributed evenly throughout the BZO and BZY powders (40°C, Ultrasonic bath (Ultrasons-H, J.P. Selecta, S.A.). The resultant powders were then placed into an oven at constant temperature of 60°C and dried thoroughly for 12 hours, followed by light dry-milling in an agate mortar and pestle.

Densification studies were assessed dynamically by dilatometer measurements, using rectangular compacts ($1.4 \times 0.5 \times 0.3$ cm^3) obtained by isostatic pressing at 300 MPa for 15 minutes. Sintered pellets were obtained after firing similar green compacts at 1250ºC for 5 hours in air.

Thermogravimetric analysis (TGA) was performed using a Netzsch STA 449F3. TGA measurements were performed in flowing N_2, and weight loss was recorded in steps upon heating. Data were collected every 300ºC from room temperature to 1200ºC with 24 hours stabilization time at each temperature.

In order to better understand the different mechanisms of B-addition, complementary tests were performed, such as X-ray diffraction, Raman and FT-IR spectroscopy. Phase analysis and determination of lattice parameters were performed by X-ray diffraction (XRD) in the range $10 \leq 2\theta \leq 115°$ with Cu $K\alpha$ radiation. Additional phase analysis was provided by Raman spectroscopy performed in the range 200 - 1400 cm^{-1} using a Renishaw 2000 instrument and room temperature infrared absorption spectra measured in the range of 300 - 1800 cm^{-1} were collected using a Spectrum-1000 Fourier transform infrared (FT-IR) instrument (Perkin-Elmer) and KBr pellet.

4.3.3 RESULTS AND DISCUSSION

4.3.3.1 CHOICE OF SOLVENT: THE BENEFIT OF NON-AQUEOUS *VS* AQUEOUS SOLVENTS ON DENSIFICATION OF $Ba(Zr,Y)O_{3-\delta}$ MATERIALS

Since the main method used in this work to introduce the additives was the solution doping method, the selection of solvent was considered to be a crucial step. Hence, the impact of three types of solvents, water, methanol, and ethanol, on the densification of pure $BaZr_{0.85}Y_{0.15}O_{3-\delta}$ (BZY) has been investigated.

4.3.3.1.1 DENSIFICATION

Figure 4.44 shows the densification behaviour of BZY as a function of solvent type: non-aqueous (ethanol and methanol) and aqueous (water).

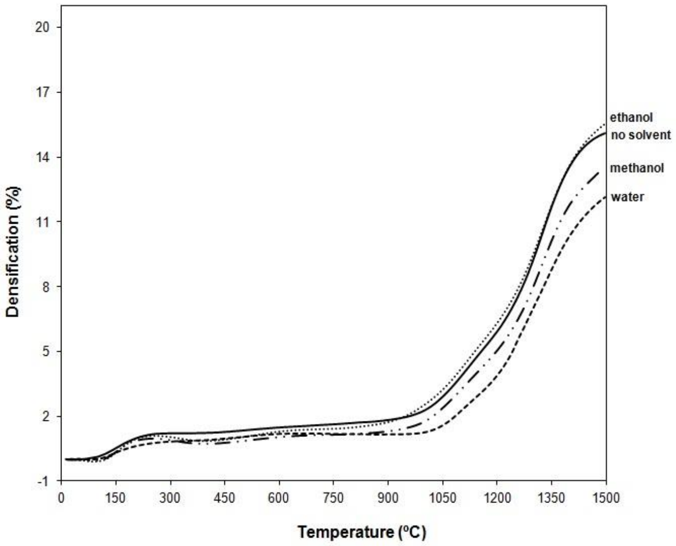

Fig. 4.44 – Sintering curves of $BaZr_{0.85}Y_{0.15}O_{3-\delta}$ after exposure to water, methanol and ethanol solutions.

While the densification behaviour of ethanol is shown to be similar to that of as-prepared BZY, both water and methanol are shown to be poor choices of solvent for the introduction of additives due to the impairment of densification. Furthermore, figure 4.45 concludes that the addition of water to BZY lowers the green and final densities of BZY, even though all powders have been dried under identical conditions at 60ºC for 12 hours before pressing.

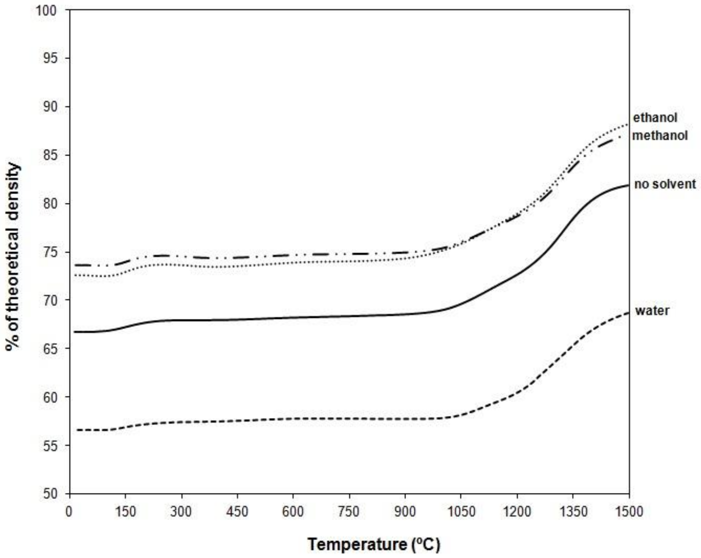

Fig. 4.45 - Influence of solvents (water, methanol and ethanol) in densification of $BaZr_{0.85}Y_{0.15}O_{3-\delta}$.

Figure 4.46 compares the temperature dependence of the linear shrinkage rate of $BaZr_{0.85}Y_{0.15}O_{3-\delta}$ as a function of the type of solvent. While alcohol solvents do not produce a notable variation in the maximum shrinkage rate, water is shown to significantly impair the shrinkage rate when compared with the solvent free sample.

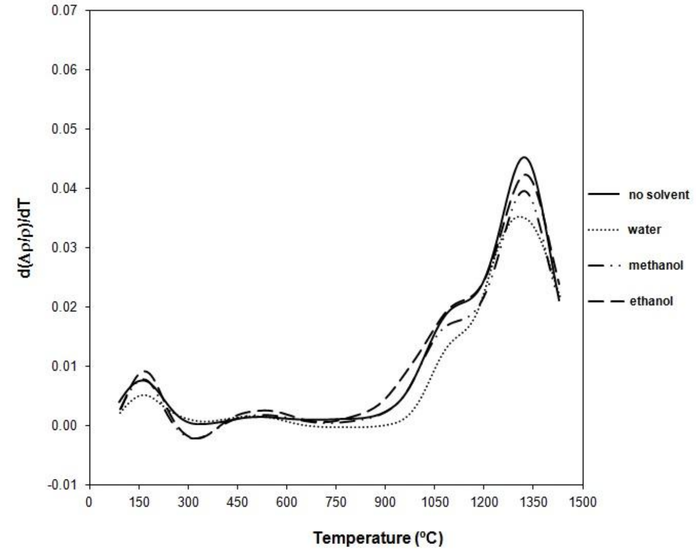

Fig. 4.46 - Temperature dependence of the linear shrinkage rate of $BaZr_{0.85}Y_{0.15}O_{3-\delta}$ after exposure to water, methanol and ethanol solutions.

The impairment of densification observed upon the addition of water is an important observation as it precludes the use of aqueous solvents for preparation of suspensions involving BZY, e.g., when producing thin films. Some possible reasons for this phenomenon can be suggested, such as: i) the formation of hydroxyl groups on hydration that persist to high temperature (~ 1000ºC) [77] or ii) possible elemental dissolution from BZY in the solvents. In the first case, the formation of hydroxyl groups may impair densification due to the elimination of oxygen vacancies that are required for densification (as described previously – section 1.3.1, by equation 1.8) or may affect the surface charge, leading to particle agglomeration that hinders the achievement of high green density [78]:

$$H_2O + O_O^x + V_O^{\bullet\bullet} \xrightarrow{K_H} 2OH_O^{\bullet} \tag{1.8}$$

In order to examine the possibility of the existence of hydroxide groups which could be responsible for the problems in the densification, thermogravimetric analysis (TGA) was performed (fig. 4.47).

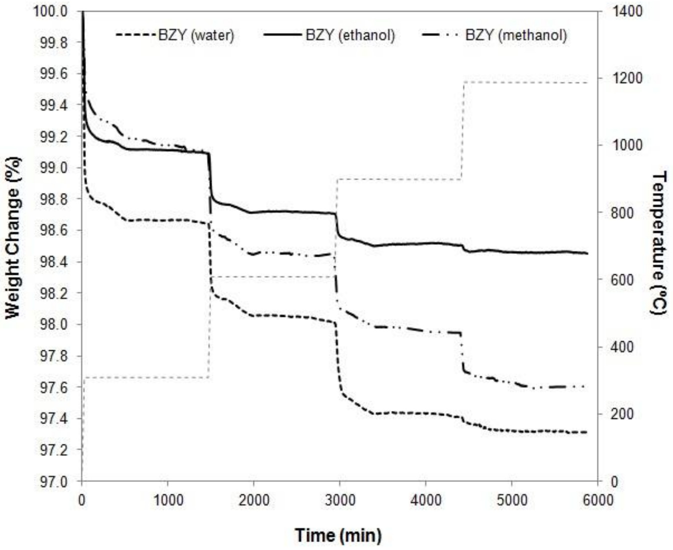

Fig. 4.47 – Weight change of $BaZr_{0.85}Y_{0.15}O_{3-\delta}$ sintered at 1300ºC for 5 hours after exposure to water, methanol and ethanol solutions, and temperature as a function of time under flowing N_2.

For all samples, the persistence of –OH groups to high temperatures is confirmed by the TGA results due to the observance of significant mass losses upon heating, with the largest losses occurring in the intermediate temperature range. This behaviour is typical for the hydration of BZY, as noted previously in the literature [77].The highest levels of weight change (larger mass loss) on increasing the temperature are noted for the sample exposed to water as a solvent. For the alcohol solvents, it is possible to conclude that the hydration reaction between BZY and methanol is stronger than that with ethanol, due to higher amounts of mass loss in the methanol case. Therefore, the recorded levels of hydration, ethanol < methanol < water, concur fully with the trend for densifications, where the levels of densification were noted in fig. 4.44 to decrease in the same sequence water < methanol < ethanol. These coincident results suggest that hydration is undesirable for the densification process, while being a phenomenon that is able to be minimised by solvent selection.

The second alternative to discuss is that the poor densification levels promoted by the addition of water could occur by the possible elemental dissolution from BZY in the solvents. In this respect, Ba-removal from perovskite materials has previously been documented to be a function of solvent acidity [75], while the presence of barium deficiency in these materials has been reported to deplete grain growth [7]. The acidity of the current solvents decreases with their increasing molecular length, water > methanol > ethanol, hence, it would be expected that water as a solvent would lead to the large elemental dissolution. Thus, to examine this hypothesis, the lattice parameter of BZY treated with these solvents was assessed after calcination at 1300ºC. Note lattice parameter variations are a very sensitive way to assess compositional variations in this type of material and would be expected to decrease with increasing Ba-removal [77]. However, all samples show similar lattice parameters (fig. 4.48), negating the analogy of elemental dissolution as the source of the different densification behaviour.

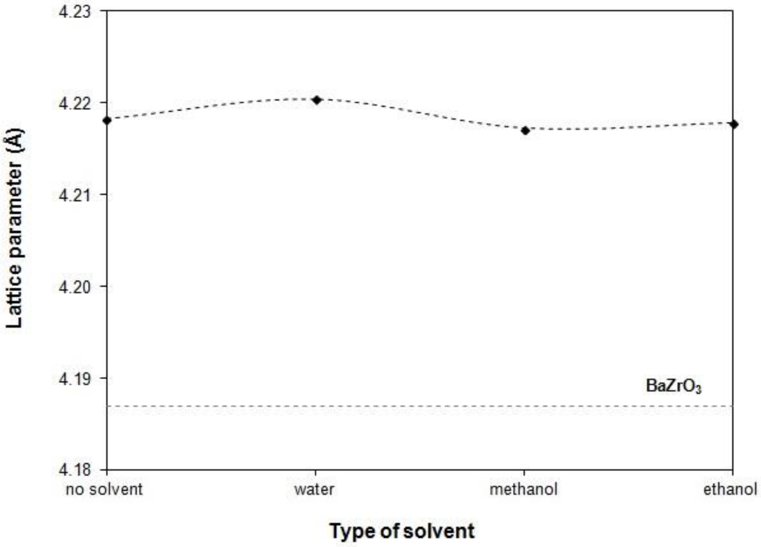

Fig. 4.48 – Evolution of lattice parameters of $BaZr_{0.85}Y_{0.15}O_{3-\delta}$ sintered at 1300ºC for 5 hours, before and after exposure to water, methanol and ethanol solutions.

4.3.3.2 ADDITION OF BORON TO $BaZrO_3$ (BZO)

4.3.3.2.1 DENSIFICATION

The temperature dependence of densification behaviour of BZO as a function of H_3BO_3 content is shown in fig. 4.49, using ethanol as the solvent. The results highlight that H_3BO_3 is a very efficient sintering aid for BZO, allowing densities approaching 100% that of the theoretical to be achieved at 1500ºC. In contrast, pure BZO only achieves a density of 80% that of the theoretical under the same conditions.

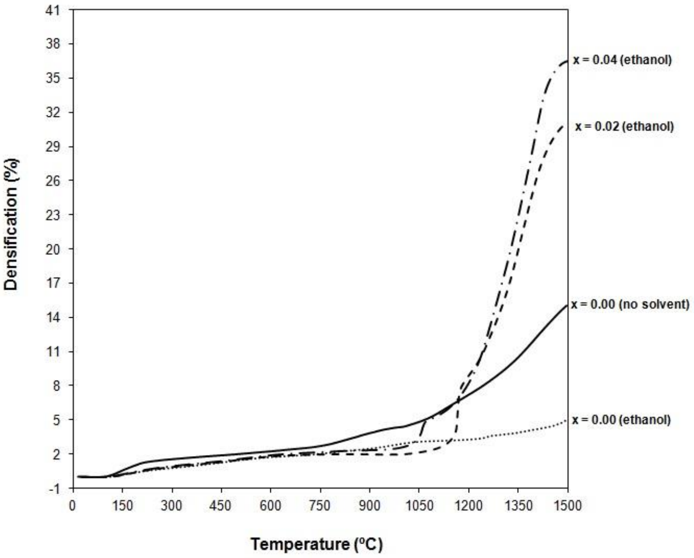

Fig. 4.49 - Densification behaviour of $(1\text{-}x)BaZrO_3 \cdot xH_3BO_3$ in the range x= 0 – 0.04, in ethanol.

The densification behaviour of the B-containing BZO is shown to occur in two steps: the first occurring in the temperature range 1050-1200ºC, and the second commencing at higher temperatures, fig. 4.50. Decomposition of the H_3BO_3 component would be expected to occur at low temperatures around 180ºC and may lead to subsequent reaction with the bulk $BaZrO_3$ phase at particle surfaces. In such a scenario, it is supposed that any resultant boron-containing reaction product may melt at elevated temperatures to produce the observed liquid assisting shrinkage behaviour. Lee *et al.* [20] reported a similar densification enhancement in barium titanate perovskite, $Ba_{0.997}Y_{0.003}TiO_{3-\delta}$ as a function of BN and BaB_2O_4 additives, commencing in a comparable temperature range 1050-1200ºC. Lee and co-workers [20] associated this behaviour with liquid phase assisted sintering that arises due to the presence of BaB_2O_4, a phase with a melting temperature of 942ºC [57]. Contrary to the titanium analogue, however, the densification behaviour of the current BZO-H_3BO_3 systems is shown to involve an additional higher temperature densification step.

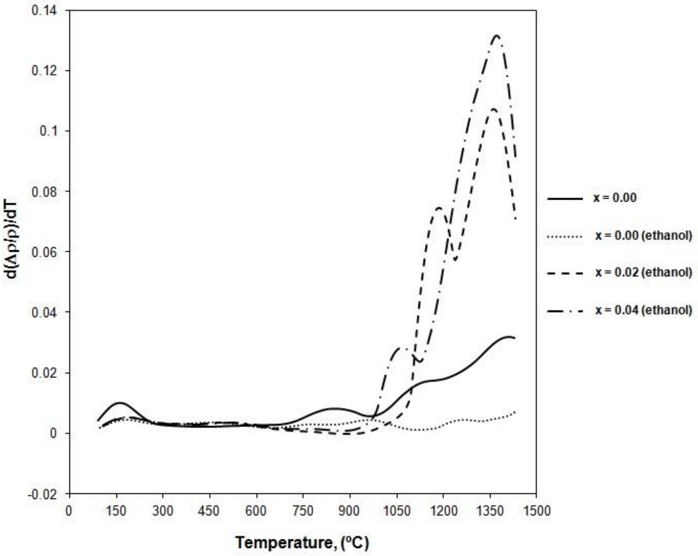

Fig. 4.50 - Temperature dependence of the linear shrinkage rate of (1-x)$BaZrO_3 \cdot xH_3BO_3$ in the range x= 0 – 0.04, in ethanol.

4.3.3.2.2 PHASE ANALYSIS

To try to understand the two step sintering behaviour shown in the current results, X-ray diffraction data have been taken of the compositions 0, 4, 6, 8, and 10 mol% H_3BO_3 added $BaZrO_3$, after annealing at 1250ºC for 5 hours. The XRD pattern of the 10 mol% H_3BO_3-containing $BaZrO_3$ phase is shown in figure 4.51. Minor amounts of the impurity phase $BaZr(BO_3)_2$ are detected as well as the expected impurity phase BaB_2O_4. It is, therefore, suggested that the observed two step densification profile arises due to the preliminary formation of BaB_2O_4, which melts at 942ºC to generate the first densification enhancement, in agreement to that suggested by Lee *et al.* [20] for $BaTiO_3$. This mechanism was followed by the formation of $BaZr(BO_3)_2$ at higher temperature, which shows an elevated melting temperature of 1320ºC [57,79].

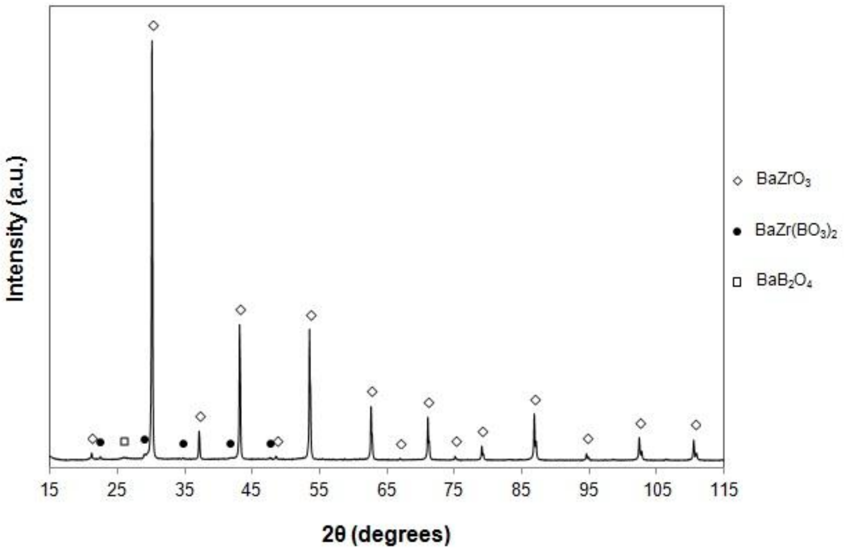

Fig. 4.51 - XRD pattern of 10 mol% of H_3BO_3 ethanol solution added $BaZrO_3$ powders after annealing at 1250ºC for 5 hours. The markers identify the main phase - (◊) the $BaZrO_3$- based phase, and the secondary phases - (•) $BaZr(BO_3)_2$, and (□) BaB_2O_4.

Haile *et al.* [78] pointed out that un-doped $BaZrO_3$ has a very low tolerance to A-site deficiency in contrast to aliovalent doped compositions [3]. Hence, any Ba-loss associated with the formation of binary boron-containing liquid phases, such as BaB_2O_4 [20], would be accompanied with the segregation of ZrO_2 as an impurity phase, as described by equation 4.23. In contrast, the formation of the ternary composition $BaZr(BO_3)_2$ would remove an equal amount of Ba and Zr from the perovskite lattice (equation 4.24):

$$BaZrO_3 + x\,H_3BO_3 \rightarrow (1-x)\,BaZrO_3 + x\,ZrO_2 + \frac{1}{2}x\,BaB_2O_4 + \frac{3}{2}x\,H_2O \tag{4.23}$$

$$BaZrO_3 + x\,H_3BO_3 \rightarrow (1-x)\,BaZrO_3 + x\,BaZr(BO_3)_2 + \frac{3}{2}x\,H_2O \tag{4.24}$$

The absence of a ZrO_2 impurity in the XRD pattern of fig.4.51 appears to disagree with mechanism equation 4.23 for the formation of BaB_2O_4. Thus, the validity of the suggested mechanisms is assessed by observation of the lattice parameter variation of the perovskite phase as function of B-content, fig. 4.52. Both mechanisms (equations 4.23 and 4.24) predict an unchanged perovskite lattice stoichiometry with B-addition. This hypothesis is reinforced by the experimental results, which show a constant lattice parameter on B-addition. The absence of a ZrO_2 impurity in the XRD pattern may, thus, occur solely due to a low quantity, which could be below the limit of resolution of the equipment.

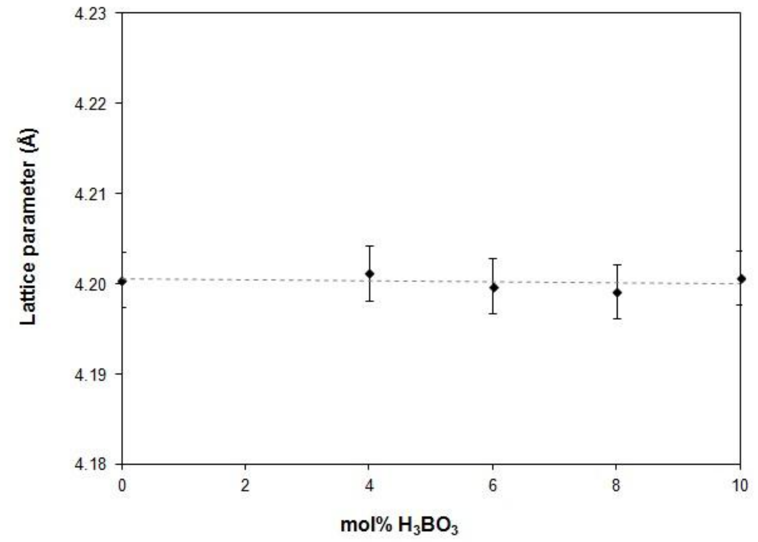

Fig. 4.52 - Evolution of lattice parameters of (1-x)$BaZrO_3 \cdot xH_3BO_3$ in the range x= 0 – 0.10 in ethanol, after annealing at 1250ºC for 5 hours.

4.3.3.3 ADDITION OF BORON TO $BaZr_{0.85}Y_{0.15}O_{3-\delta}$ (BZY)

4.3.3.3.1 DENSIFICATION

Figure 4.53 shows the linear shrinkage $BaZr_{0.85}Y_{0.15}O_{3-\delta}$ specimen with addition of H_3BO_3 (0, 2 and 4 mol%, water and ethanol solution).

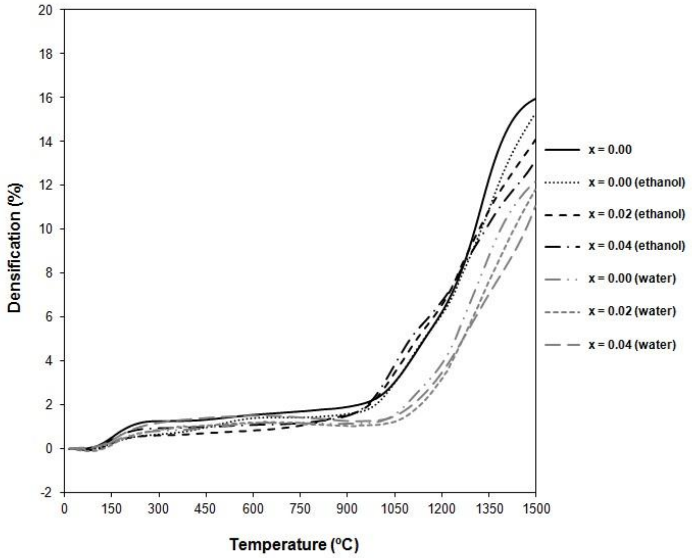

Fig. 4.53 - Densification behaviour of (1-x)$BaZr_{0.85}Y_{0.15}O_{3-\delta} \cdot xH_3BO_3$ in the range x= 0 – 0.04, in water and ethanol.

The boron additive was doped with H_3BO_3 in water and ethanol solutions. Samples based in water solution showed a later densification starting temperature than B-free BZY, and the maximum linear shrinkage was as low as 6%. The final densities of these specimens formed using water solutions were below 80% that of the theoretical; values that can be considered low (fig. 4.54). These results indicate that, by adding boron in the way of H_3BO_3 water solution, the densification was impaired in comparison to the additive free composition. .

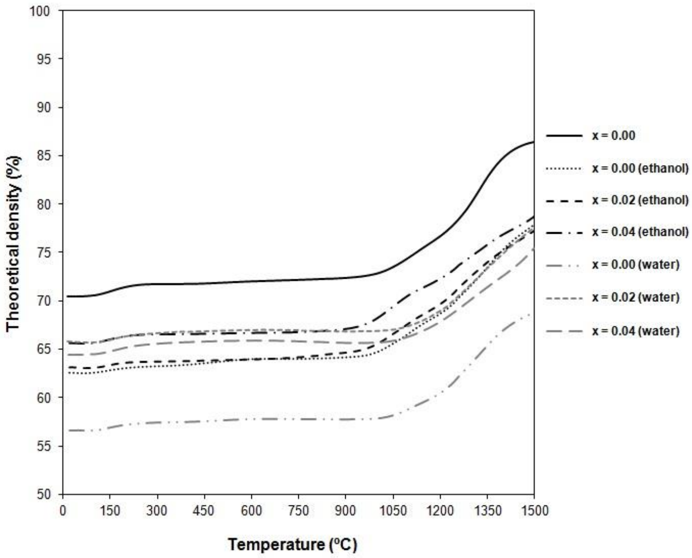

Fig. 4.54 - Influence of the amount of H_3BO_3 (0, 2 and 4 mol%) and the solvent (water and ethanol) in densification of $BaZr_{0.85}Y_{0.15}O_{3-\delta}$.

For comparison, the linear shrinkage curves of boron added $BaZr_{0.85}Y_{0.15}O_{3-\delta}$ specimens using an ethanol solution, are also presented in figure 4.53. In the case of 4 mol% boron added BZY (ethanol solution) the densification starting temperature similar to the plain BZY (950ºC), with a maximum linear shrinkage of 5.7%, and sintered density of 84% that of the theoretical. Compared with 4 mol% boron added BZY water solution samples, the corresponding samples prepared with an ethanol solution, showed relatively better densification in agreement with the results of section 4.3.3.1.

Nonetheless, in contrast to the positive effect of H_3BO_3 on densification behaviour in $BaZrO_3$, shown in section 4.3.3.2, the H_3BO_3 additive is shown to be an ineffective sintering aid for $BaZr_{0.85}Y_{0.15}O_{3-\delta}$. The synthesis route of the $BaZrO_3$ and $BaZr_{0.85}Y_{0.15}O_{3-\delta}$ powders and the doping methods of B-addition were identical in both cases, as were the morphologies of the mechanosynthesized powders. Hence, the difference in the effectiveness of boron as a sintering additive for each material is puzzling. A detailed investigation is, therefore, presented, involving a barrage of experimental techniques to understand this dramatic change in the mechanism of B-additions in the two cases.

4.3.3.3.2 PHASE ANALYSIS AND MICROSTRUCTURE

XRD data have been taken of the compositions of 0, 2, 4, 6, 8, and 10 mol% H_3BO_3 added $BaZr_{0.85}Zr_{0.15}O_{3-\delta}$ after annealing at 1250ºC for 5 hours. The XRD pattern of the 10 mol% H_3BO_3-containing BZY phase is shown in figure 4.55.

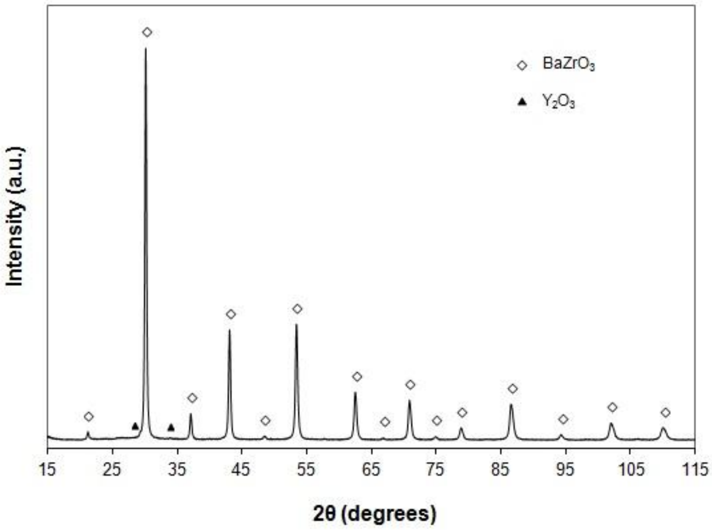

Fig. 4.55 - XRD pattern of 10 mol% of H_3BO_3 ethanol solution added $BaZr_{0.85}Y_{0.15}O_{3-\delta}$ powders after annealing at 1250ºC for 5 hours. The markers identify the main phase - (◊) the $BaZrO_3$- based phase, and the secondary phase - (▲) Y_2O_3.

From figure 4.55, it is possible to conclude that B-additions to BZY lead to the formation of a different secondary phase than in the BZO case (fig. 4.51), with slight traces of Y_2O_3 being detected at the highest H_3BO_3 contents.

Comparison of the lattice parameter variation of the perovskite phase in the BZO and BZY compositions as a function of B-content is shown in figure 4.56. In contrast to the BZO case, the BZY compositions show a decrease in lattice parameter with increasing B-content. Note that the annealing temperature of 1250ºC is below that where Ba-loss would be expected by volatilization [72]. Therefore, the noted decrease in lattice parameter with addition of H_3BO_3 can only be explained by reaction with the bulk BZY material and a subsequent change in stoichiometry of the base perovskite phase.

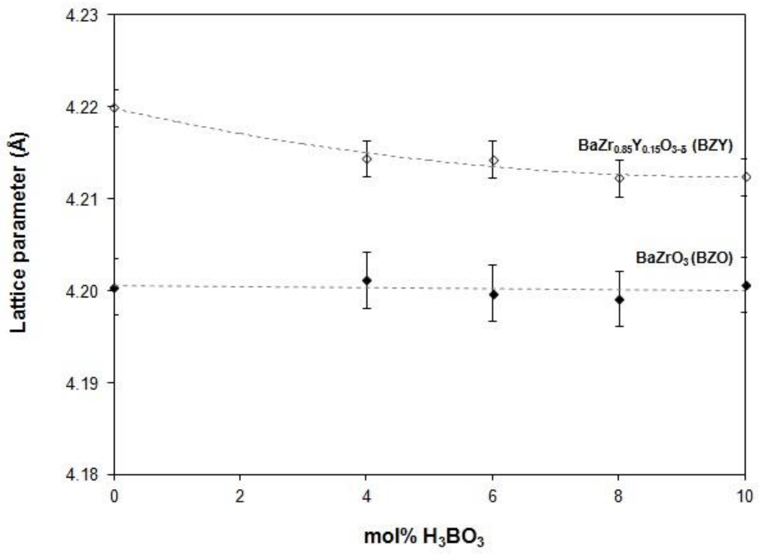

Fig. 4.56 - Evolution of lattice parameters of (1-x)$BaZrO_3 \cdot xH_3BO_3$ (BZO), and (1-x)$BaZr_{0.85}Y_{0.15}O_{3-\delta} \cdot xH_3BO_3$ (BZY) in the range x= 0 – 0.10 in ethanol, after annealing at 1250ºC for 5 hours.

As mentioned in section 4.3.3.2.2, Haile *et al.* [78] demonstrated that B-free $BaZrO_3$ has a very low tolerance to A-site deficiency in contrast to the aliovalent doped compositions. Hence, while the formation of BaB_2O_4 in the BZO case can be described by equation 4.23 (creating ZrO_2 impurity), conversely, reaction of boron with barium in BZY may process by the formation of a Ba-deficient perovskite phase. This possibility is discussed in equation 4.25. Note that equation 4.25 is written in a general form to express any composition between BaO and H_3BO_3 (see phase diagram, figure 4.43):

$$BaZr_{0.85}Y_{0.15}O_{3-\delta} + x\,H_3BO_3 \rightarrow Ba_{1-\frac{x(1-y)}{y}}Zr_{0.85}Y_{0.15}O_{3-\delta} + \frac{x}{y}\,Ba_{1-y}B_yO_{1+0.5y} + \frac{3}{2}x\,H_2O \qquad (4.25)$$

In the literature one can find the dependence of lattice parameter on Ba-deficiency for the composition $Ba_{(1-x)}Zr_{0.85}Y_{0.15}O_{3-\delta}$ [7]. This is reproduced in figure 4.57.

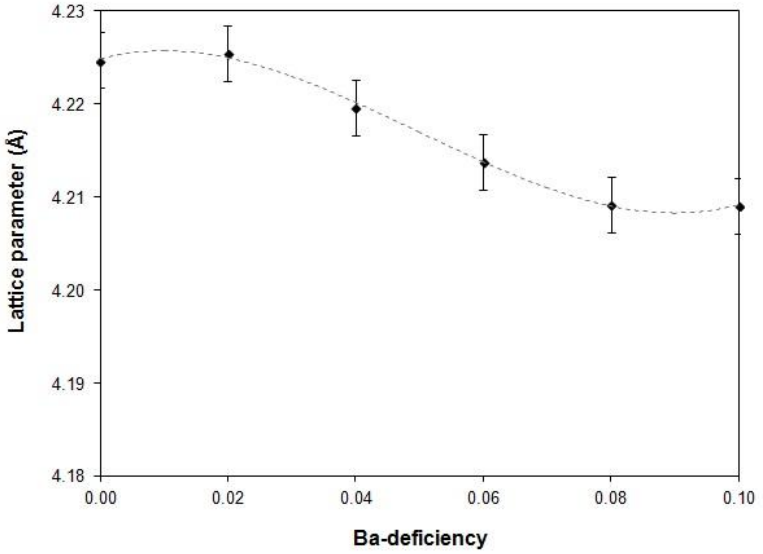

Fig. 4.57 – Reproduction of the evolution of lattice constants in sintered $Ba_{(1-x)}Zr_{0.85}Y_{0.15}O_{3-\delta}$ as a function of nominal Ba-deficiency [7].

From equation 4.25 one can see that in the case of B-additions, the resultant perovskite Ba-deficiency will be given by $\frac{x\,(1-y)}{y}$, where x is the fraction of H_3BO_3 added and y represents the binary join $Ba_{1-y}B_yO_{1+1.5y}$. The phase diagram shown in figure 4.43 suggests the existence of the following binary phases $Ba_3B_2O_6$, BaB_2O_4, BaB_4O_7, and BaB_8O_{13}. Assuming the reaction mechanism stated in equation 4.25 one can calculate the expected Ba-deficiency associated with the fraction of H_3BO_3 added for formation each possible binary phase.

From this calculated Ba-deficiency and the experimental dependence shown in figure 4.57 one can calculate the expected resultant lattice parameter. This is performed and demonstrated in figure 4.58. The figure suggests that Ba-loss and the formation of binary compositions $Ba_{1-y}B_yO_{1+1.5y}$ with values of $y \geq 0.66$ cannot account for the experimental lattice parameter variation. Interestingly the Ba-rich composition (a) $Ba_3B_2O_6$ shows the best agreement with the experimental lattice parameters at low H_3BO_3 contents, passing to (b) BaB_2O_4 at higher contents. It should be noticed that the composition $Ba_3B_2O_6$ is shown to have an elevated melting point of 1383ºC, from the phase diagram (fig. 4.43) [57]. The formation of this composition would, therefore, not be expected to lead to liquid phase sintering due to its high melting temperature.

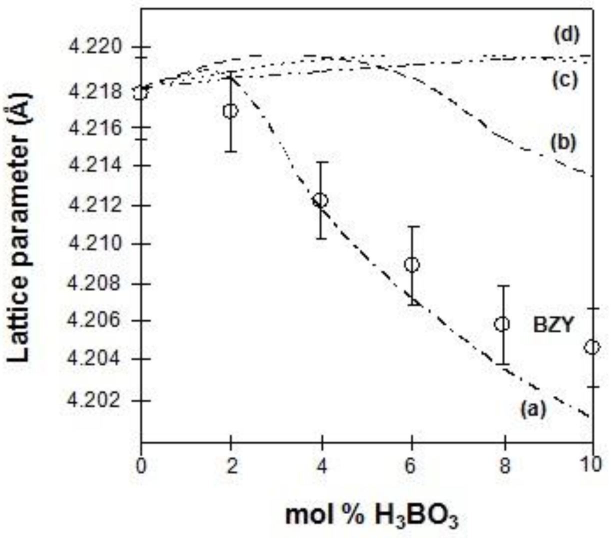

Fig. 4.58 – Calculated lattice parameters of (1-x)$BaZr_{0.85}Y_{0.15}O_{3-\delta}\cdot xH_3BO_3$ (BZY) in the range x= 0 – 0.10 in ethanol, as a function of H_3BO_3 addition for formation of the phases: (a) $Ba_3B_2O_6$, (b) BaB_2O_4, (c) BaB_4O_7 and (d) BaB_8O_{13}.

Due to the more facile removal of Ba in the Y-doped composition (in comparison to destruction of the perovskite phase in $BaZrO_3$), one possible analogy is that at low H_3BO_3 doping levels the Ba-rich, $Ba_3B_2O_6$ phase easily forms, leading to a high melting temperature. On further H_3BO_3 doping a mixture of $Ba_3B_2O_6$ and BaB_2O_4 would result, as can be predicted from the barium borate phase diagram in figure 4.43. Note that for a mixture of these two phases a molten phase and $Ba_3B_2O_4$ will form at temperatures above 915ºC. It is possible that in such a case only a limited quantity of molten phase would be available to wet the BZY grains and produce liquid phase assisted sintering.

The formation of these barium borate phases implies the depletion of Ba from the perovskite matrix with boron additions and associated reduction in the lattice constants of BZY. Upon sufficient Ba-loss Y_2O_3 can also be predicted as a secondary phase (see phase diagram in fig. 4.43) together with the formed barium borate phases BaB_2O_4 and/or $Ba_3B_2O_6$. Reaction of the expelled Y_2O_3 with boron may also result in formation of the phase YBO_3. It is expected that these boron containing phases, namely YBO_3 and $Ba_3B_2O_6$, would not improve sintering behaviour due to their high melting temperatures (1650ºC and 1383ºC, respectively) [57]. Thus, to search for the existence of additional phases, FT-IR (figs. 4.59, 4.60, 4.61 and 4.62) and Raman (fig. 4.63) spectroscopy were performed. These techniques are useful to detect minor amounts of additional phases that cannot be seen under the resolution of X-ray diffraction.

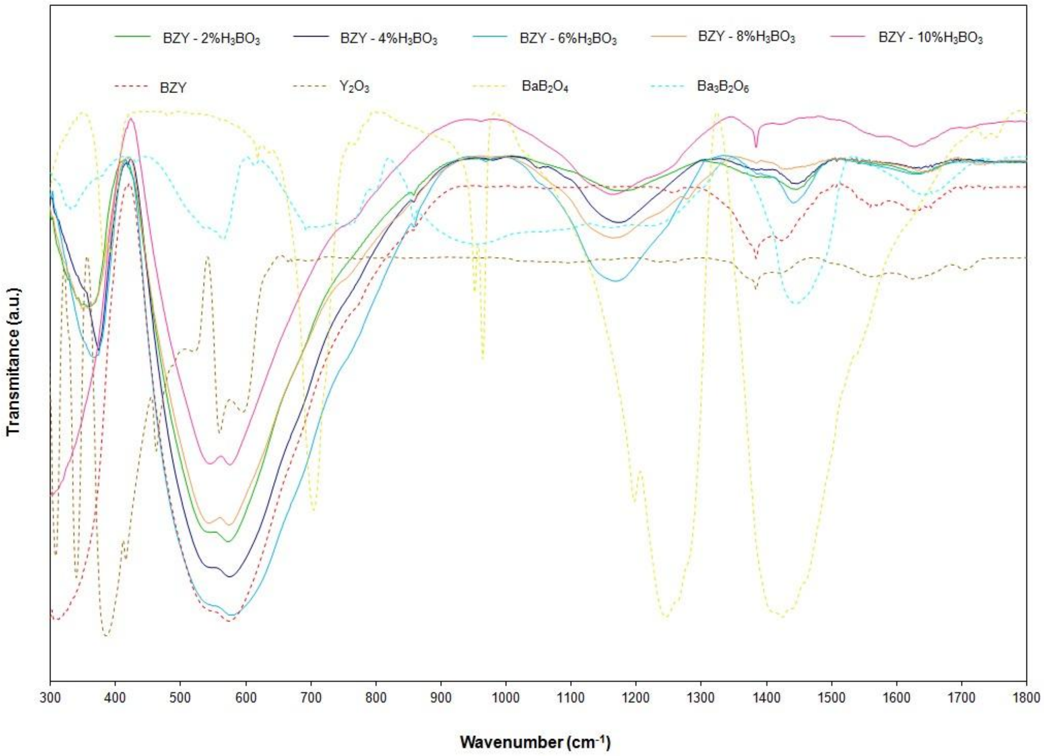

Fig. 4.59 - FT-IR transmission (300 – 1800 cm^{-1}) spectra of BaZr$_{0.85}$Y$_{0.15}$O$_{3-\delta}$ doped with 2, 4, 6, 8 and 10 mol% of H_3BO_3 and the precursors and segregation phases.

The FT-IR transmission spectra (fig. 4.59) can be divided in three different zones. From the wavenumber range 300 to 1000 cm^{-1} (zone 1 – fig. 4.60), it can be stated that the addition of H_3BO_3 does not show any notable influence on the main BZY phase when compared with the B-free BZY. In zone 2, corresponding to the wavenumber range of 950 to 1350 cm^{-1}, the secondary BaB_2O_4 phase can be detected (fig. 4.61) with its concentration increasing with increasing additions of H_3BO_3. Lastly, in zone 3, from 1300 to 1800cm^{-1} the segregated phases of Y_2O_3 and $Ba_3B_2O_6$ can be seen.

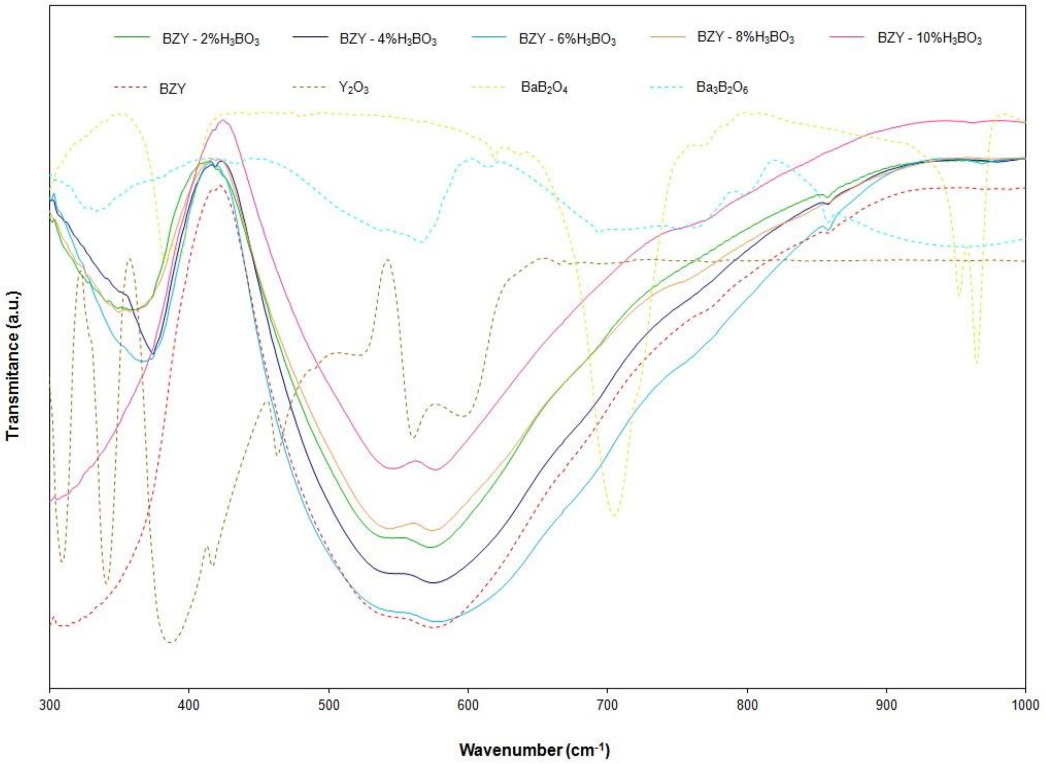

Fig. 4.60 - FT-IR transmission spectra corresponding to zone 1 (300 – 1000 cm^{-1}) of $BaZr_{0.85}Y_{0.15}O_{3-\delta}$ doped with 2, 4, 6, 8 and 10 mol% of H_3BO_3 and the precursors and segregation phases.

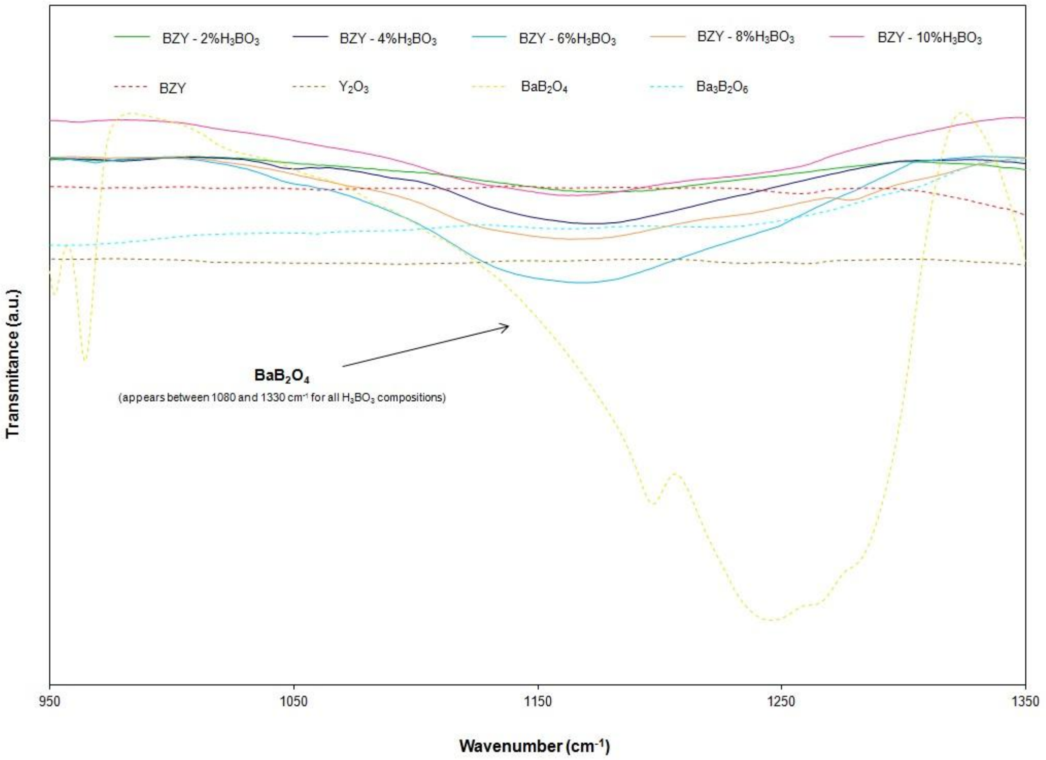

Fig. 4.61 - FT-IR transmission (950 – 1350 cm^{-1}) spectra of $BaZr_{0.85}Y_{0.15}O_{3-\delta}$ doped with 2, 4, 6, 8 and 10 mol% of H_3BO_3 and the precursors and segregation phases.

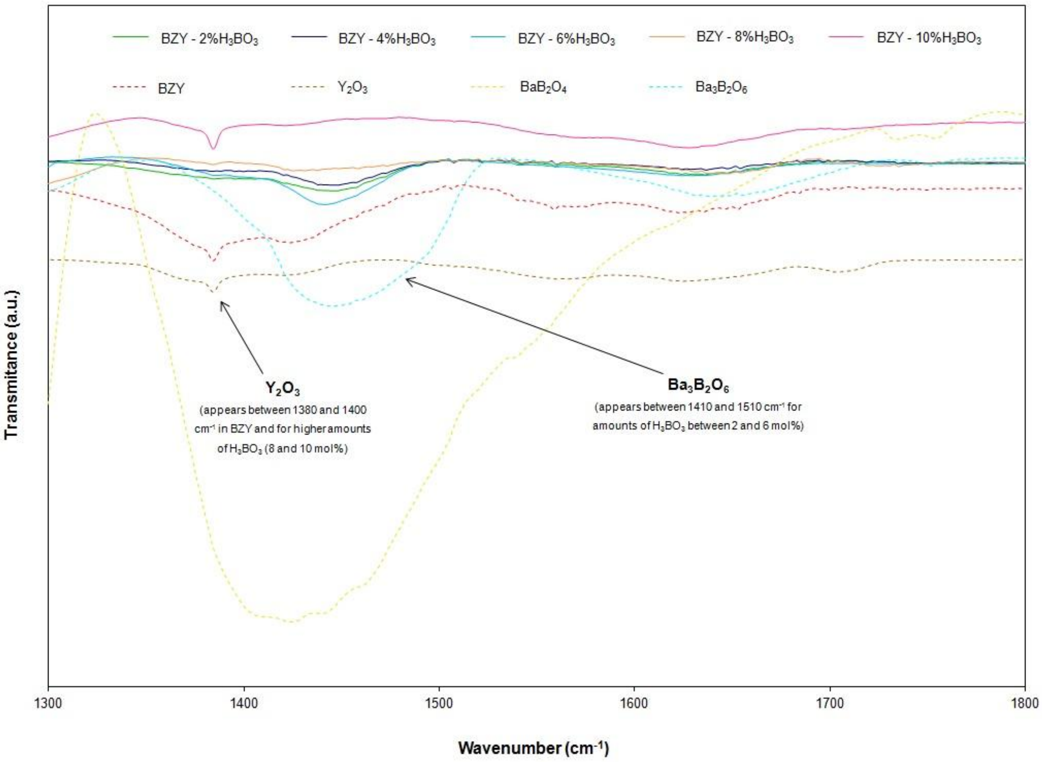

Fig. 4.62 - FT-IR transmission (1300 – 1800 cm^{-1}) spectra of $BaZr_{0.85}Y_{0.15}O_{3-\delta}$ doped with 2, 4, 6, 8 and 10 mol% of H_3BO_3 and the precursors and segregation phases.

Moreover, from fig. 4.62 it is also possible to conclude that the $Ba_3B_2O_6$ secondary phase is only clearly detected for concentrations lower than 6 mol% of H_3BO_3. Conversely, for higher H_3BO_3 concentrations, the amount of $Ba_3B_2O_6$ tends to disappear. These results are in agreement with phase diagram (fig. 4.43) and the previous, lower wavenumber, FT-IR region where the increasing boron content leads to the formation of a phase region containing two barium borate phases, that of $Ba_3B_2O_6$ and BaB_2O_4, where the BaB_2O_4/$Ba_3B_2O_6$ ratio increases with increasing amounts of H_3BO_3 (figs. 4.61 and 4.62). For the highest concentrations of H_3BO_3 the presence of the impurity Y_2O_3 is also observed (fig.4.62) in agreement with that expected upon extensive barium depletion from the perovskite phase (fig. 4.38, section 4.2.3.2). Raman spectroscopy analysis (fig. 4.63) also highlights the formation of Y_2O_3 at high H_3BO_3 levels in yttrium-doped $BaZrO_3$ annealed at 1250ºC, in agreement with the FT-IR results. Nonetheless, the Raman technique is shown to be less effective to separate the barium borate reaction products, such as BaB_2O_4 or $Ba_3B_2O_6$.

The undesirable presence of $Ba_3B_2O_6$ noted by the FT-IR technique explains the ineffective nature of the H_3BO_3 sintering additive for densification of BZY materials due to the high melting point of this phase (1383ºC) [57].

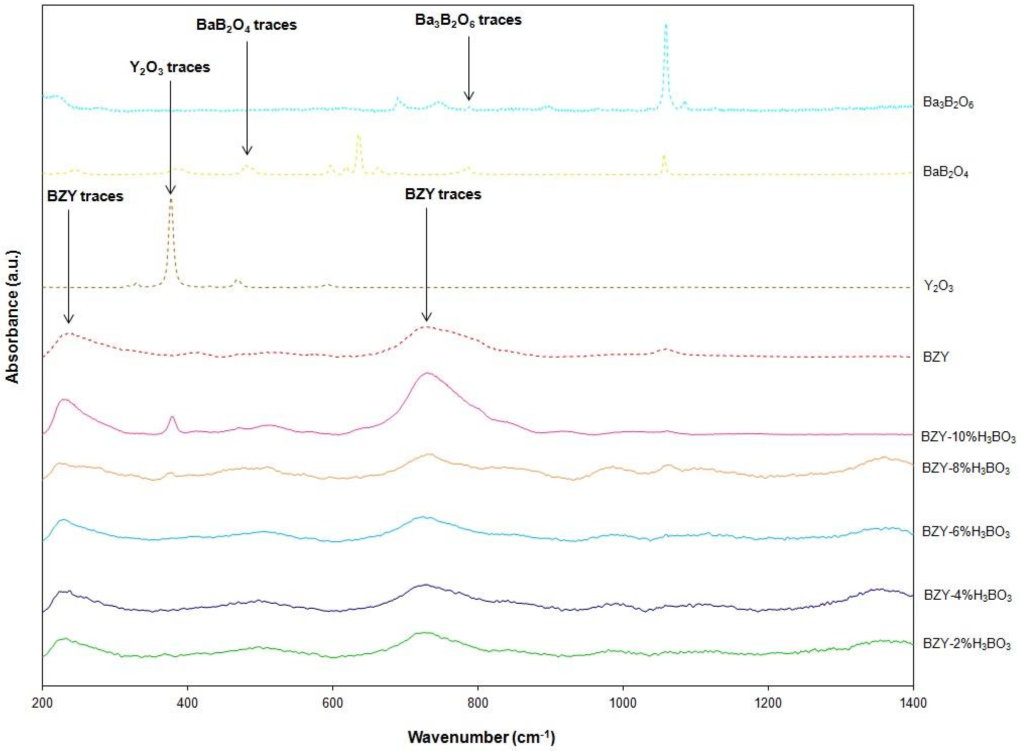

Fig. 4.63 – Raman spectroscopy spectra of $BaZr_{0.85}Y_{0.15}O_{3-\delta}$ doped with 2, 4, 6, 8 and 10 mol% of H_3BO_3 and the precursors (BZY and Y_2O_3) and segregation phases (YBO_3, BaB_2O_4 and $Ba_3B_2O_6$).

The H_3BO_3 additions also have a strong impact on the resultant microstructures, with the presence of secondary phases in BZO and BZY leading to widely different grain growth in each case. Representative scanning electron micrographs of bulk samples of composition (1-x)$BaZrO_3 \cdot xH_3BO_3$ and (1-x)$BaZr_{0.85}Y_{0.15}O_{3-\delta} \cdot xH_3BO_3$ when x = 0.04 and 0.10, sintered at 1250°C for 5 hours are shown in fig. 4.64.

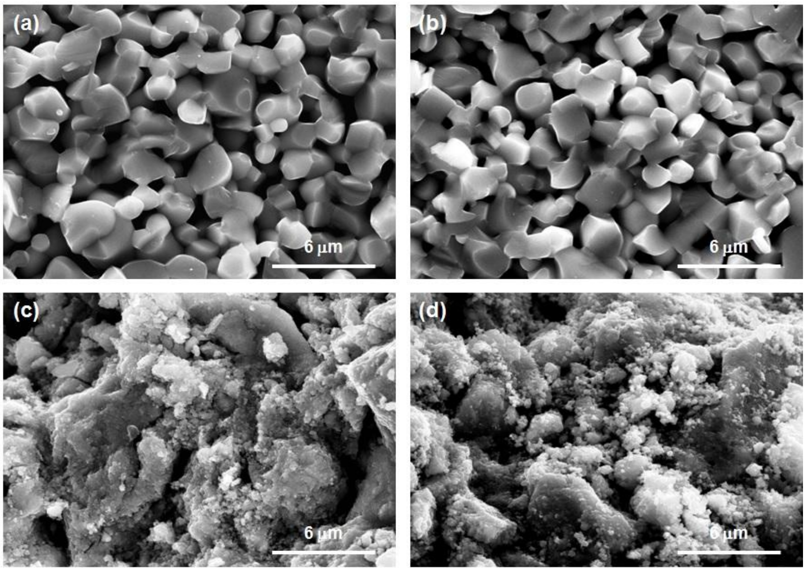

Fig. 4.64 - Scanning electron micrographs of a bulk sample of compositions (1-x)$BaZrO_3 \cdot xH_3BO_5$, (a) x = 0.04, (b) x = 0.10, and (1-x)$BaZr_{0.85}Y_{0.15}O_{3-\delta} \cdot xH_3BO_5$ (c) x = 0.04 and (d) x = 0.10, sintered at 1250°C for 5 hours.

From the perspective average grain sizes, table 4.11, it is possible to conclude that the secondary phases formed by an excess of B-addition to BZY, such as BaB_2O_4, Y_2O_3 and $Ba_3B_2O_6$, affect grain growth, with much higher grain sizes recorded for BZO doped with 4 and 10 mol% H_3BO_3 when compared to BZY for the same additive concentrations. This can be explained by literature data for the BZY material that shows a decreased grain growth on increasing barium deficiency [7]. Moreover, the existence of slight traces of Y_2O_3 at high barium deficiencies can also be responsible for depleted grain growth due to the pinning of the grains by yttria at the grain boundary. In 1996, Chen and co-workers [80] have reported a similar effect on the grain growth in fluorite ceria materials.

The current results, therefore, highlight that impaired densification is followed by not only a substantial decrease in perovskite lattice parameter (fig. 4.56) but by poor grain growth (table 4.11) and these factors can be linked to the presence of barium loss and related formation of Y_2O_3 and $Ba_3B_2O_6$ impurity phases.

Table 4.11 – Average grain sizes of B-modified BZO and BZY (4 and 10 mol% of H_3BO_3) sintered samples (1250ºC, 5 hours), calculated from SEM images.

Sample	Grain size (μm)
$(1-x)BaZrO_3 \cdot xH_3BO_3$, x = 0.04	1.614 ± 0.058
$(1-x)BaZrO_3 \cdot xH_3BO_3$, x = 0.10	1.504 ± 0.049
$(1-x)BaZr_{0.85}Y_{0.15}O_3 \cdot xH_3BO_3$, x = 0.04	0.882 ± 0.025
$(1-x)BaZr_{0.85}Y_{0.15}O_3 \cdot xH_3BO_3$, x = 0.10	0.926 ± 0.030

4.3.4 CONCLUSIONS

The effects of B-additions on the sintering behaviour of un-doped and Y-doped $BaZrO_3$ have been studied, including a new doping approach that uses solvents to introduce the additives. This method permits a highly homogeneous distribution of the boron based sintering additive in the powder samples. Solvent selection is shown to be critical. Although the use of water-based solvent would be desirable for environmental reasons and cost, the use of such solvent is shown to drastically impair densification and this has been related to a higher level of hydration of the perovskite proton conducting materials. In contrast, ethanol shows the best sintering results of the solvents studied with effectively no negative impacts on the densification of BZY. This solvent was, therefore, adopted for the introduction of sintering additives by the solution doping method.

The densification behaviour of H_3BO_3 (0 - 10 mol%) added $BaZrO_3$ (BZO) shows boron to be a very effective sintering aid, whereas, in contrast, for the acceptor doped composition BZY no improvement in densification can be obtained. Densification commences at lower temperature compared with additive-free BZO, with a higher final density of ~ 97%. Additionally, $BaZrO_3$ doped with H_3BO_3 leads to a two step sintering performance: the first step occurs before ~ 1110ºC and the second step appears for higher temperatures. The higher levels of densification are attributed to the formation of secondary phases, namely BaB_2O_4 (melting temperature phase of 942ºC) and subsequently $BaZr(BO_3)_2$ (melting point of 1320ºC), leading to the observed assisted sintering behaviour.

Nevertheless, the densification behaviour of $BaZr_{0.85}Y_{0.15}O_{3-\delta}$ (BZY) with the same H_3BO_3 additive shows unenhanced levels of densification compared with the plain BZY. Comparing with BZO lattice constants, a substantial decrease in perovskite lattice parameter is shown with increasing H_3BO_3 addition to BZY due to depletion of barium in the perovskite phase and the formation of additional barium borate phases, such as $Ba_3B_2O_6$, BaB_2O_4. At high H_3BO_3 levels this Ba-depletion is accompanied by Y_2O_3 segregation from the perovskite phase. For lower concentrations than 6 mol% of H_3BO_3, $Ba_3B_2O_6$ is detected. However, increasing the amount of H_3BO_3 (> 6 mol%), the amount of $Ba_3B_2O_6$ tends to disappear, while the concentration of the BaB_2O_4 phase increases.

Low levels of B-modified BZY densification can be explained by the high melting temperature of the $Ba_3B_2O_6$ segregated product. The depletion of Ba from the perovskite phase and segregation of Y_2O_3 upon formation of the barium borate phases is also shown to hinder grain growth.

Thus, despite being a good sintering additive for BZO, the addition of H_3BO_3 is ineffective as a sintering additive for BZY.

4.4 REFERENCES

[1] Bohn, H.G. and Schober, T. (2000). “Electrical Conductivity of the High-Temperature Proton Conductor $BaZr_{0.9}Y_{0.1}O_{2.95}$.” Journal of the American Ceramic Society **83(4):** 768-772.

[2] Kreuer, K.D. (2003). “Proton-Conducting Oxides.” Annual Reviews Materials Research **33:** 333-359.

[3] Iguchi, F., Tsurui, T., Sata, N., Nagao Y. and Yugami, H. (2009). “The relationship between chemical composition distributions and specific grain boundary conductivity in Y-doped $BaZrO_3$ proton conductors.” Solid State Ionics **180:** 563-568.

[4] Giannici, F., Shirpour, M., Longo, A., Martorana, A., Merkle, R. and Maier, J. (2011). “Long-Range and Short-Range Structure of Proton-Conducting Y:$BaZrO_3$.” Chemistry of Materials **23(11):** 2994-3002.

[5] Han, D., Nose, Y., Shinoda, K. and Uda, T. (2012). “Site selectivity of dopants in $BaZr_{1-y}M_yO_{3-\delta}$ (M = Sc, Y, Sm, Eu, Dy) and measurement of their water contents and conductivities.” Solid State Ionics **213:** 2-7.

[6] Antunes, I., Brandão, A., Figueiredo, F.M., Frade, J.R., Grácio, J. and Fagg, D.P. (2009). “Mechanosynthesis of nanopowders of the proton-conducting electrolyte material $Ba(Zr,Y)O_{3-\delta}$.” Journal of Solid State Chemistry **182(8):** 2149-2156.

[7] Yamazaki, Y., Hernandez-Sanchez, R. and Haile, S.M. (2010). “Cation non-stoichiometry in yttrium-doped barium zirconate: phase behaviour, microstructure, and proton conductivity.” Journal of Materials Chemistry **20:** 8158-8166.

[8] Peng, C., Melnik, J., Jinxia, L., Luo, J., Sanger, A.R. and Chuang, K.T. (2009). “ZnO-doped $BaZr_{0.85}Y_{0.15}O_{3-\delta}$ proton conducting electrolytes: Characterization and fabrication of thin films.” Journal of Power Sources **190(2):** 447-452.

[9] Yamazaki, Y., Hernandez-Sanchez, R. and Haile, S.M. (2009). “High Total Proton Conductivity in Large-Grained Yttrium-Doped Barium Zirconate.” Chemistry of Materials **21(13):** 2755-2762.

[10] Babilo, P. and Haile, S.M. (2005). “Enhanced Sintering of Yttrium-Doped Barium Zirconate by Addition of ZnO.” Journal of the American Ceramic Society **88(9):** 2362-2368.

[11] Tao, S. and Irvine, J.T.S. (2006). “A Stable, Easily Sintered Proton-Conducting Oxide Electrolyte for Moderate-Temperature Fuel Cells and Electrolyzers.” Advanced Materials **18(12):** 1581-1584.

[12] Ricote, S. and Bonanos, N. (2010). “Enhanced sintering and conductivity of cobalt or nickel doped solid solution of barium cerate and zirconate.” Solid State Ionics **181:** 694-700.

[13] Tong, J.H., Clark, D., Bernau, L., Sanders, M. and O’Hayre, R. (2010). “Solid-state reactive sintering mechanism for large-grained yttrium-doped barium zirconate proton conducting ceramics.” Journal of Materials Chemistry **20:** 6333-6341.

[14] Park, J.-S., Lee, J.-H., Lee, H.-W. and Kim, B.-K. (2010). “Low temperature sintering of $BaZrO_3$-based proton conductors for intermediate temperature solid oxide fuel cells.” Solid State Ionics **181:** 163-167.

[15] Ito, N., Matsumoto, H., Kawasaki, Y., Okada, S. and Ishihara, T. (2008). “Introduction of In or Ga as second dopant to $BaZr_{0.9}Y_{0.1}O_{3-\delta}$ to achieve better sinterability.” Solid State Ionics **179:** 324-329.

[16] Imashuku, S., Uda, T., Nose, Y. and Awakura, Y. (2010). “To Journal of Phase Equilibria and Diffusion Phase Relationship of the BaO-ZrO_2-$YO_{1.5}$ System at 1500 and 1600ºC.” Journal of Phase Equilibria and Diffusion **31:** 348-356.

[17] Ryu, K.H. and Haile, S.M. (1999). “Chemical stability and proton conductivity of doped $BaCeO_3$-$BaZrO_3$ solid solutions.” Solid State Ionics **125:** 355-367.

[18] Tao, S. and Irvine, J.T.S. (2007). “Conductivity studies of dense yttrium-doped $BaZrO_3$ sintered at 1325ºC.” Journal of Solid State Chemistry **180(12):** 3493-3503.

[19] Caballero, A.C., Fernández, J.F., Moure, C. and Durán, P. (1997). “Effect of residual phosphorus left by phosphate ester on $BaTiO_3$ ceramics.” Materials Research Bulletin **32(2):** 221-229.

[20] Lee, J.-H., Heo, Y.-W., Lee, J.-A., Ryoo, Y.-D., Kim, J.-J. and Cho, S.-H. (1997). “Grain boundary and its related properties of boron added Y-doped $BaTiO_3$ ceramics.” Solid State Ionics **101/103:** 787-791.

[21] Fabbri, E., Pergolesi, D. and Traversa, E. (2010). “Materials challenges toward proton-conducting oxide fuel cells: a critical review.” Chemical Society Review **39:** 4355-4369.

[22] Luisetto, I., Licoccia, S., D’Epifanio, A., Sanson, A., Mercadelli, E., Bartolomeo, E.D. (2012). “Electrochemical performance of spin coated dense $BaZr_{0.80}Y_{0.16}Zn_{0.04}O_{3-\delta}$ membranes.” Journal of Power Sources **220:** 280-285.

[23] Zhang, C., Zhao, H., Xu, N., Li, X. and Chen, N. (2009). “Influence of ZnO addition on the properties of high temperature proton conductor $Ba_{1.03}Ce_{0.5}Zr_{0.4}Y_{0.1}O_{3-\delta}$ synthesized via citrate-nitrate method.” International Journal of Hydrogen Energy **34(6):** 2739-2746.

[24] Wang, Y., Chesnaud, A., Bevillon, E., Yang, J. and Dezanneau, G. (2011). “Influence of ZnO additive on the properties of Y-doped $BaSnO_3$ proton conductor.” Materials Science and Engineering B **176(15):** 1178-1183.

[25] Yokokawa, H., Sakai, N., Kawada, T. and Dokiya, M. (1991). “Thermodynamic stability of perovskites and related compounds in some alkaline earth-transition metal-oxygen systems.” Journal of Solid State Chemistry **94(1):** 106-120.

[26] Mogensen, M., Lybye, D., Bonanos, N., Hendriksen, P.V. and Poulsen, F.W. (2004). “Factors controlling the oxide ion conductivity of fluorite and perovskite structured oxides.” Solid State Ionics **174:** 279-286.

[27] Kronmuller, H., Parkin, S. (2007). “Handbook of Magnetism and Advanced Magnetic Materials.”, Volume 5, John Wiley and Sons, Inc.

[28] Babilo, P., Uda, T. and Haile, S.M. (2007). “Processing of yttrium-doped barium zirconate for high-proton conductivity.” Journal of Materials Research **22(5):** 1322-1330.

[29] Chatzichristodoulou, C., Norby, P., Hendriksen, P.V. and Mogensen, M.B. (2015). “Size of oxide vacancies in fluorite and perovskite oxides.” Journal of Electroceramics **34:** 100-107.

[30] Chen, P.-L. and Chen, I.-W. (1994). “Role of Defect Interaction in Boundary Mobility and Cation Diffusivity of CeO_2.” Journal of the American Ceramic Society **77(9):** 2289-2297.

[31] Routbort, J.L., Rothman, S.J., Chen, N., Mundy, J.N. and Baker, J.E. (1991). “Site selectivity and cation diffusion in $YBa_2Cu_3O_{7-\delta}$.” Physical Review B: Condensed Matter and Materials Physics **43:** 5489-5497.

[32] Mather, G.C., García-Martín, S., Benne, D., Ritter, C. and Amador, U. (2011). “A-site cation deficiency in the $SrCe_{0.9}Yb_{0.1}O_{3-\delta}$ perovskite: effects of charge-compensation mechanism on structure and proton conductivity.” Journal of Materials Chemistry **21:** 5764-5773.

[33] Caballero, A.C., Fernández, J.F., Moure, C. and Durán, P. (1998). “Phase formation in phosphorus doped $BaTiO_3$.” Materials Letters **35:** 72-77.

[34] Kreuer, K.D., Adams, St., Münch, W., Fuchs, A., Klock, U. and Maier, J. (2001). “Proton conducting alkaline earth zirconates and titanates for high drain electrochemical applications.” Solid State Ionics **145:** 295-306.

[35] Wu, J., Cao, J., Han, W.-Q., Janotti, A. and Kim, H.-C. (2011). “Functional Metal Oxide Nanostructures.” Springer Science+Business Media, LLC, New York.

[36] Song, S.-J., Wachsman, E.D., Dorris, E. and Balachandran, U. (2002). “Defect chemistry modelling of high-temperature proton-conducting cerates.” Solid State Ionics **149:** 1-10.

[37] Lim, D.-K., Park, C.-J., Choi, M.-B., Park, C.-N. and Song, S.-J.(2010). “Partial conductivities of mixed conducting $BaCe_{0.65}Zr_{0.2}Y_{0.15}O_{3-\delta}$.” International Journal of Hydrogen Energy **35:** 10624-10629.

[38] Baek, H.-D. (1998). “Modeling of electrical conductivity in high-temperature proton-conducting oxides.” Solid State Ionics **110:** 255-262.

[39] Brandão, A.D., Antunes, I., Frade, J.R., Torre, J., Mikhalev, S.M. and Fagg, D.P. (2012). “Mechanochemical preparation, sintering aids and hybrid microwave sintering in the proton conductor $Sr_{0.02}La_{0.98}Nb_{1-x}V_xO_{4-\delta}$, x = 0.015.” International Journal of Hydrogen Energy **37(8):** 7252-7261.

[40] Frade, J.R. (1995). “Theoretical behaviour of concentration cells based on ABO_3 perovskite materials with protonic and oxygen ion conduction.” Solid State Ionics **78:** 87-97.

[41] Nowotny, J. and Sorrel, C.C. (1997). “Electrical Properties of Oxide Materials.” Trans Tech Publication, Ltd.

[42] Kobayashi, T., Abe, K., Ukyo, Y. and Matsumoto, H. (2001). “Study on current efficiency of steam electrolysis using a partial protonic conductos $SrZr_{0.9}Yb_{0.1}O_{3-\alpha}$.” Solid State Ionics **138(3-4):** 243-251.

[43] Sherafat, Z., Paydar, M.H., Antunes, I., Nasani, N., Brandão, A.D. and Fagg, D.P. (2015). “Modeling of electrical conductivity in the proton conductor $Ba_{0.85}K_{0.15}ZrO_{3-\delta}$.” Electrochimica Acta **165:** 443-449.

[44] Yamazaki, Y., Yang, C.-K. and Haile, S.M. (2011). “Unraveling the defect chemistry and proton uptake of yttrium-doped barium zirconate.” Scripta Materialia **65:** 102-107.

[45] Patnaik, A.S. and Virkar, A.V. (2006). “Transport Properties of Potassium-Doped $BaZrO_3$ in Oxygen- and Water-Vapor-Containing Atmospheres.” Journal of The Electrhochemical Society **153(7):** A1397-A1405.

[46] http://www.doitpoms.ac.uk/tlplib/ellingham_diagrams/ellingham.php accessed on June 29, 2014; activity of the University of Cambridge; created in 2004.

[47] Krestovnikov, A.N., Vladimirov, L.P., Gulyanitskii, B.S. and Ya, A. (1963). “Handbook for Calculation of Equilibria in Metallurgical Reactions (in Russian).” Metallurgizdat, Moskow.

[48] Hsiue, G.H., Chu, L.W. and Lin, I.N. (2007). “Optimized phosphate ester structure for the dispersion of nano-sized barium titanate in proper non-aqueous media.” Colloids and Surfaces A: Physicochemical and Engineering Aspects **294:** 212-220.

[49] Chartier, T. and Jorge, E. (1993). “Dispersion properties of $BaTiO_3$ tape-casting slurries.” Journal of the European Ceramic Society **11(5):** 387-393.

[50] Mikeska, K.R. and Cannon, W.R. (1988). “Non-aqueous dispersion properties of pure barium titanate tape casting.” Colloids and Surfaces **29(3):** 305-321.

[51] Caballero, A.C., Villegas, M., Fernández, J.F., Moure, C., Durán, P., Florian, P. and Coutures, J.-P. (1999). “Reactive sintering of phosphorous coated $BaTiO_3$.” Journal of the European Ceramic Society **19:** 979-983.

[52] Gao, D.Y. and Guo, R.S. (2010). “Densification and properties of barium zirconate ceramics by addition of P_2O_5.” Materials Letters **64(5):** 573-575.

[53] Barsoum, M.W. (1997). “Fundamentals of ceramics.” McGraw-Hill Companies, New York.

[54] Min, D.J. and Sano, N. (1989). “Determination of the Standard Gibbs Energies of Formation of Ba_3P_2 and $Ba_3(PO_4)_2$.” Metallurgical and Materials Transactions B **20:** 871-877.

[55] Xue, L.A., Chen, Y. And Brook, R.J. (1988). “The influence of ionic radii on the incorporation of trivalent dopants into $BaTiO_3$.” Materials Science and Engineering B **1(2):** 193-201.

[56] Chisholm, C.R.I., Toberer, E.S., Louie, M.W. and Haile, S.M. (2010). “Engineering the Next Generation of Solid State Proton Conductors: Synthesis and Properties of $Ba_{3-x}K_xH_x(PO_4)_2$.” Chemistry of Materials **22(3):** 1186-1194.

[57] Levin E.M. and McMurdie, H.F. (1949). “The System BaO-B_2O_3.” Journal of Research of the National Bureau Standards **42:** 131-138.

[58] Srinivasan, S. (2006). “Fuel Cells: From Fundamentals to Applications.” Springer Science + Business Media, LLC, New York.

[59] Hong, L., Chen, X.F. and Cao, Z.D. (2001). “Preparation of a perovskite $La_{0.2}Sr_{0.8}CoO_{3-x}$ membrane on a porous MgO substrate.” Journal of the European Ceramic Society 21(12): 2207-2215.

[60] Savaniu, C. and Irvine, J.T.S. (2002). “Sol-gel preparation and characterization of dense proton conducting $Sr_3CaZr_{0.5}Ta_{1.5}O_{8.75}$ thin films.” Solid State Ionics **150:** 295-308.

[61] Van Gestel, T., Sebold, D., Meulenberg, W.A. and Buchkremer, H.P. (2008). “Development of thin-film nano-structured electrolyte layers for application in anode-supported solid oxide fuel cells.” Solid State Ionics **179:** 428-437.

[62] Wang, W.B., Cao, X.B., Gao, W.J., Zhang, F., Wang, H.T. and Ma, G.L. (2010). “Ammonia synthesis at atmospheric pressure using a reactor with thin solid electrolyte $BaCe_{0.85}Y_{0.15}O_{3-\alpha}$ membrane.” Journal of Membrane Science **360:** 397-403.

[63] Jasinski, P., Molin, S., Gazda, M., Petrovsky, V. and Anderson, H.V. (2009). “Applications of spin coating of a polymer precursor and slurry suspensions for Solid Oxide Fuel Cells fabrication.” Journal of Power Sources **194(1):** 10-15.

[64] Zhang, L., Chen, F. and Xia, C. (2010). “Spin-coating derived solid oxide fuel cells operated at temperatures of 500ºC and below.” International Journal of Hydrogen Energy **35(24):** 13262-13270.

[65] Yang, Z., Wang, W., Xiao, J., Zhang, H., Zhang, F., Ma, G. and Zhou, Z. (2012). “A novel cobalt-free $Ba_{0.5}Sr_{0.5}Fe_{0.9}Mo_{0.1}O_{3-\delta}$ – $BaZr_{0.1}Ce_{0.7}Y_{0.2}O_{3-\alpha}$ composite cathode for solid oxide fuel cells.” Journal of Power Sources **204:** 89-93.

[66] Xu, X., Xia, C., Huang, S. and Peng, D. (2005). “YSZ thin films deposited by spin-coating for IT-SOFCs.” Ceramics International **31(8):** 1061-1064.

[67] Chen, K., Tian, Y., Lü, Z., Ai, N., Huang, X. and Su, W. (2009). “Behavior of 3 mol% yttria-stabilized tetragonal zirconia polycrystal film prepared by slurry spin coating.” Journal of Power Sources **186(1):** 128-132.

[68] Yang, R.-J., Lee, M.-C., Chang, J.-C., Lin, T.-N., Chang, Y.-C., Kao, W.-X., Lee, L.-S. and Cheng, S.-W. (2012). “Fabrication and characterization of a $Sm_{0.2}Ce_{0.8}O_{1.9}$ electrolyte film by the spin-coating method for a low temperature anode-supported solid oxide fuel cells.” Journal of Power Sources **206:** 111-118.

[69] Fontaine, M.L., Larring, Y., Haugsrud, R., Norby, T., Wiik, K. and Bredesen, R. (2009). “Novel high temperature proton conducting fuel cells: Production of $La_{0.995}Sr_{0.005}NbO_{4-\delta}$ electrolyte thin films and compatible cathode architectures.” Journal of Power Sources **188(1):** 106-113.

[70] Hamakawa, S., Li, L., Li, A. and Iglesia, E. (2002). “Synthesis and hydrogen permeation properties of membranes based on dense $SrCe_{0.95}Yb_{0.05}O_{3-\alpha}$ thin films.” Solid State Ionics **148:** 71-81.

[71] Fontaine, M.L., Larring, Y., Smith, J.B., Raeder, H., Andersen, Ø.S., Einarsrud, M.-A., Wiik, K. and Bredesen, R. (2009). “Shaping of advanced asymmetric structures of proton conducting ceramic materials for SOFC and membrane-based process applications.” Journal of the European Ceramic Society **29(5):** 931-935.

[72] Peng, C., Melnik, J., Luo, J.L., Sanger, A.R. and Chuang, K.T. (2010). “$BaZr_{0.8}Y_{0.2}O_{3-\delta}$ electrolyte with and without ZnO sintering aid: Preparation and characterization.” Solid State Ionics **181:** 1372-1377.

[73] Costa, R., Hafsaoui, J., de Oliveira, A.P.A., Grosjean, A., Carnel, M., Chesnaud, A. And Thorel, A. (2009). “Tape Casting of Proton Conducting Ceramic Material.” Journal of Applied Electrochemistry **39(4):** 485-495.

[74] Song, J.-H., Park, S.-I., Lee, J.-H. and Kim, H.-S. (2008). “Fabrication characteristics of an anode-supported thin-film electrolyte fabricated by the tape casting method for IT-SOFC.” Journal of Materials Processing Technology **198:** 414-418.

[75] Negra, M.D., Zhang, W., Bonanos, N. and Ricote, S. (2014). “Behavior of $BaCe_{0.9-x}Zr_xY_{0.1}O_{3-\delta}$ in water and ethanol suspensions.” Journal of Materials Science **49(6):** 2588-2595.

[76] Matsuka, M., Agranovski, I.E. and Braddock, R.D. (2010). “Preparation of asymmetric perovskite-type membranes by a settlement method.” Ceramics International **36(2):** 643-651.

[77] Yamazaki, Y., Babilo, P. and Haile, S.M. (2008). “Defect Chemistry of Yttrium-Doped Barium Zirconate: A Thermodynamic Analysis of Water Uptake.” Chemistry of Materials **20(20):** 6352-6357.

[78] Haile, S.M., Staneff, G. and Ryu, K.H. (2001). “Non-stroichiometry, grain boundary transport and chemical stability of proton conducting perovskites.” Journal of Materials Science **36(5):** 1149-1160.

[79] Hornebecq, V., Gravereau, P., Chaminade, J.P. and Lebraud, E. (2002). “$BaZr(BO_3)_2$: a non-centrosymmetric dolomite-type superstructure.” Materials Research Bulletin **37(13):** 2165-2178.

[80] Chen, P.-L. and Chen, I.-W. (1996). “Grain Growth in CeO_2: Dopant Effects, Defect Mechanism, and Solute Drag.” Journal of the American Ceramic Society **79(7)**: 1793-1800.

CHAPTER 5. EMERGING MATERIALS: (Ba,Sr)GeO_3-BASED ION CONDUCTORS

Research efforts dedicated to the improvement of material properties for solid oxide fuel cells (SOFCs) are extremely active. One of the major challenges in this area is in lowering the operating temperature to the intermediate temperature regime, 500-700ºC, while maintaining good electrochemical performances [1,2].

The electrolyte, which transports oxide-ions from the cathode to anode, plays a key role in cell performance since its ionic conductivity determines the operating temperature range to minimise internal ohmic resistance losses. Thus, there is therefore considerable interest in developing alternative electrolytes with oxide-ion conductivity achieving or exceeding 10^{-2} $S.cm^{-1}$ at intermediate temperatures. Materials showing high oxide-ion conductivity and displaying new combinations of charge carrier and structural prototypes are particularly attractive, such as innovative tetrahedral structures displaying high oxygen interstitial or vacancy mobility without necessary constraint of the high lattice symmetries [2,3].

Recently, Goodenough *et al.* [4,5] reported a superior oxide-ion electrolyte family of monoclinic doped $SrMO_3$-based oxide ion conductors (M = Si, Ge) as promising candidates for intermediate temperature-solid oxide fuel cells (IT-SOFC), which shows good ionic conductivity values ($\sigma \geq 10^{-2}$ $S.cm^{-1}$), at intermediate temperatures (625ºC).

The introduction of a cation at the Sr-site of $SrMO_3$, such as K^+ or Na+, was suggested to lead to the introduction of terminal-oxygen vacancies on tetrahedral anion complexes that provide elevated oxide-ion conductivity [6]. Nonetheless, the exact mechanism for conduction remains under debate, with alternative proposals being offered such as the presence of interstitial oxygen atoms provided by distortions of the M_3O_9 unit to allow corner sharing [4]. In this respect, substitution of K^+ for Sr^{2+} was shown to be highly hygroscopic at room temperature, adding further to the discussion of whether the oxygen conductivity could be explained by oxygen vacancies or oxygen interstitial atoms [4]. According to Singh *et al.* [8], the hygroscopic behaviour of K-substituted oxides would necessitate water absorption into oxygen vacancies that, if located at a terminal position of a M_3O_9 complex, would stabilize the steric hindrance of the large Sr^{2+} and K^+ ions. In contrast, the presence of interstitial oxygen caused by corner sharing of these units would suggest an alternative case where hydration would be considered unlikely [8].

The use of steric hindrance to stabilize a terminal-oxygen vacancy on a tetrahedral anion complex is a novel design principle that has led these novel oxide-ion conductors to attract much attention of late [1,4,5,7,8]. Singh *et al.* [4] have concluded that Ge analogue generally provides higher oxide-ion conductivity in comparison with Si analogues.

The higher volume of Ba^{2+} ions than that of Sr^{2+} may lead to an increase of the steric hindrance resulting in structural distortions that can have a positive impact in the conduction of O^{2-} ions [9]. In addition, the hygroscopic nature of these materials may well offer a route to proton conductivity that would be enhanced due to the basicity of Ba^{2+} and K^+ ions. According to these assumptions, the current work also aims to investigate the type of conduction of these materials: ionic, protonic and electronic.

Thus, the current chapter is constituted by three sections focused on acceptor doping of $BaGeO_3$ and $SrGeO_3$ in order to determine whether oxygen vacancies, formed as charge compensating defects, could give competitive ionic conductivity in the intermediate operating temperature range. In addition, the current work studies the applicability of mechanochemical preparation methods to produce these materials.

The first section is based on the study of the ability of mechanosynthesis to produce pure $BaGeO_3$. It is known that $BaGeO_3$ exists in at least two polymorphic forms: a low-temperature α form and a high-temperature β form with an orthorhombic pyroxene-type structure [10-13]. The current study was based on the use of a wide range of techniques in order to understand the impact of mechanosynthesis as a synthesis method. Produced powders were observed by transmission electron microscopy (TEM) and analysed by FT-IR (Fourier transform infrared spectroscopy) measurements. Phase compositions and temperature dependent transitions were analysed by Rietveld refinement high-temperature X-ray diffraction data (HT-XRD), complimented by thermogravimetric analyses (TGA/DSC).

The second section concerns the effect of K-addition to $BaGeO_3$ materials. $Ba_{1-x}K_xGeO_{3-0.5x}$ materials were studied in order to assess the effect of K^+ on the oxide-ion conductivity and to compare the impact of the lattice distortions promoted by Ba in comparison with the known $Sr_{1-x}K_xGeO_{3-0.5x}$ material presented in the literature. The study was based on high-temperature X-ray diffraction (HT-XRD), scanning electron microscopy (SEM), thermogravimetric analyses (TGA), Raman spectroscopy and impedance measurements.

Lastly, the third section presents the effect of mechanosynthesis to produce the novel $SrGeO_3$-based materials containing potassium that show improved oxide-ion conductivity compared to un-doped $SrGeO_3$. $Sr_{1-x}K_xGeO_{3-0.5x}$ (x = 0 and 0.20) materials were studied using the following techniques: XRD, SEM, TGA as well as Raman and impedance spectroscopy.

5.1 LOW-TEMPERATURE MECHANOSYNTHESIS OF β-$BaGeO_3$

5.1.1 INTRODUCTION

Germanates are of wide interest in material science and technology for displaying a rich range of conductive, dielectric, optical and acoustic-optical properties. $M^{II}GeO_3$ ceramics with divalent metal ions (Ba^{2+}, Sr^{2+}, Ca^{2+}, Ni^{2+} or Cu^{2+}) are used on an industrial scale to produce heterophasic ceramic bodies, such as dielectric ceramic materials for multi-layer capacitors [14]. Their high dielectric strength, low dissipation factor and relatively low firing temperatures permits use of inexpensive, non-noble metals and alloys thereof as electrodes in the fabrication of these devices [14-17].

Additionally, these materials have also noted a particular interest as alternative SOFC electrolytes due to the ability to produce oxide-ion defects, such oxygen vacancies, promoting oxide-ion transport by the vacancy-hopping mechanism. Recently, Goodenough and co-workers [4,5,7] reported a new family of oxide-ion conductors based on Ge oxides, the $Sr_{3-x}A_xGe_3O_{9-0.5x}$ (A = Na, K).

Germanates are very interesting materials due to their complex polymorphism [13]. $BaGeO_3$ exists in at least two polymorphic forms, a low-temperature α form, reported as having a monoclinic (hexagonal) structure by Liebau [18], and a high-temperature β form with an orthorhombic pyroxene-type structure composed of [Ge_2O_6]-*zweier* single chains, first reported by Hilmer [19]. The polymorphism has been the source of conflicting information in the literature as regards phase formation, transformation temperatures and accepted crystallographic structure [10-13]. The low-temperature form is closely related to pseudo-wallastonite, consisting of alternate layers of Ba cations and $[GeO_3]_3$ rings. A recent study indicates that the X-ray structure is better refined in the monoclinic *C2/c* space group rather than a hexagonal crystal system. The non-random stacking of the rings is rather complex giving rise to diffuse scattering observed by selected area electron diffraction [13].

The phase diagram of the BaO-GeO_2 system (fig. 5.1) was first described by Grebenshchikov *et al.* [20] then revised by Guha [11]. It was reported in a study of the polymorphism of $BaGeO_3$ [10] that the low-temperature polymorph transforms to the high-temperature phase at 1200°C via an intermediate phase change at 1100°C. In 1983, Yamaguchi *et al*. [12] reported the metastable formation of the high-temperature polymorph of $BaGeO_3$ at 660ºC from an amorphous starting material prepared by the hydrolysis of barium and germanium alkoxides. The same authors report the transformation of the β to α phase at 780 - 840°C followed by a transition to the β phase at 1180 - 1200°C, with melting taking place at 1270°C.

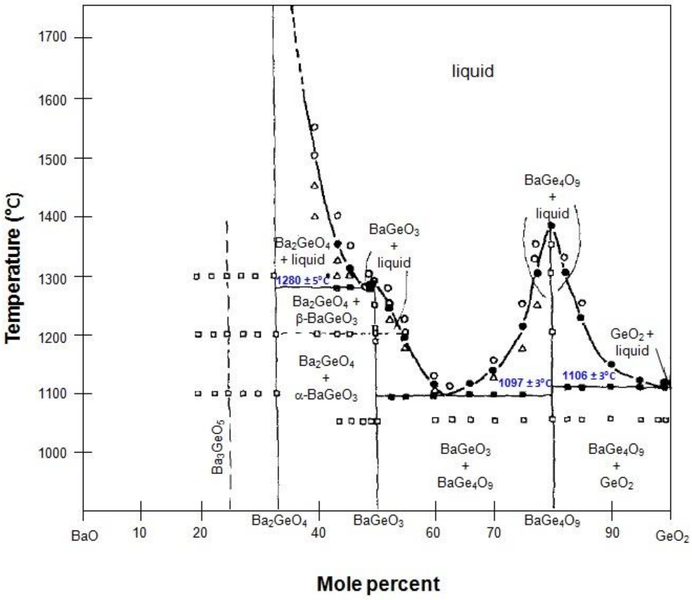

Fig. 5.1 - Phase diagram of BaO-GeO$_2$ showing the location of the phase transitions of BaGeO$_3$ polymorphs (adapted from [11]).

The current work reports the novel result of the preparation of the high-temperature orthorhombic polymorph of BaGeO$_3$ (β form) by room-temperature mechanosynthesis from a reactant powder mixture of BaO$_2$ and GeO$_2$.

5.1.2 PROCESSING METHODOLOGY

Powders of BaGeO$_3$ were prepared by mechanosynthesis from stoichiometric quantities of BaO$_2$ (Sigma-Aldrich, 95% purity), and GeO$_2$ (Sigma-Aldrich, ≥99.99% trace metal basis). The commercial powder of barium peroxide is a mixture of approximately 95 mol% BaO$_2$ and 5 mol% BaCO$_3$. Thus, in order to calculate the exact quantities of each component, thermogravimetric analysis (TGA) in flowing CO$_2$ were performed, using a Netzsch STA 449F3 (fig. 3.5) with a 1600°C rod by complete carbonation of a sample in flowing CO$_2$.

The nature of the phase transition and its temperature dependence as a function of temperature was studied by Rietveld refinement of high-temperature X-ray diffraction (HT-XRD) data, collected with a Bruker D8 Advance over the range 10° ≤ 2θ ≤ 80° with a step size of 0.015° and measurement time of 1s/step. Diffractograms were registered from room temperature to 1200ºC in 100ºC intervals, then again at room temperature after cooling. Phase composition at each temperature was estimated by quantitative Rietveld refinement with the Fullprof program using interpolation of points to model the background and amorphous contribution.

Thermogravimetric analysis and differential scanning calorimetry (TGA/DSC) were carried out in an Ar atmosphere at a rate of 10ºC/min to 1100ºC using a NETZSCH STA 449F3 instrument in a High Temperature Platform 400; alumina was employed as standard for DSC.

Room temperature infrared absorption spectra were recorded using a Spectrum-1000 Fourier transform infrared (FT-IR) instrument (Perkin-Elmer). The spectra were collected in the range 300 - 1800 cm^{-1} using a KBr pellet.

Microstructure was investigated by transmission electron microscopy (TEM) coupled with energy dispersive X-ray spectroscopy (EDS) in a 300kV Hitachi H-9000 microscope equipped with a Röntec EDS detector. Samples were prepared by dispersing fresh powders in ethanol on perforated copper grids.

5.1.3 RESULTS AND DISCUSSION

5.1.3.1 PHASE FORMATION AND CRYSTAL STRUCTURE

XRD powder patterns showing the formation of the β polymorph of $BaGeO_3$ as a function of milling time are shown in fig. 5.2. The onset of phase formation can be observed after 60 min and the pure orthorhombic β phase appears after 300 min.

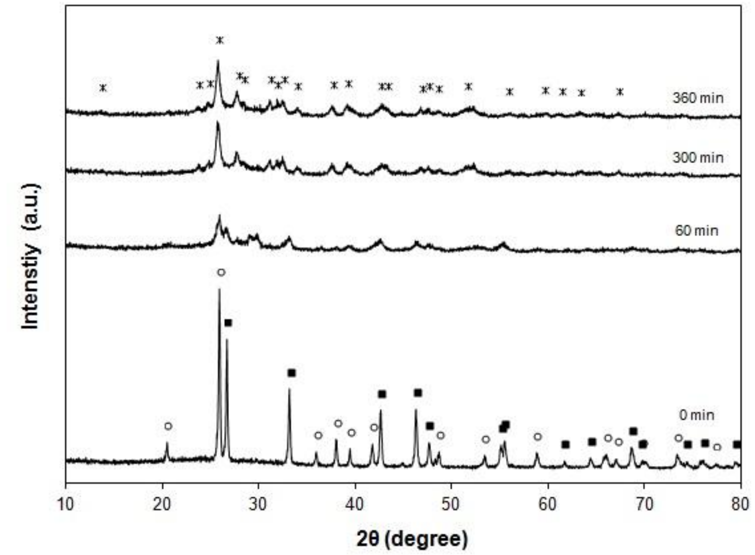

Fig. 5.2 - Evolution of powder X-Ray diffraction patterns with milling time (0, 60, 300 and 360 min) for the $BaO_2 + GeO_2$ mixture. The markers identify the precursors (■) BaO_2, (○) GeO_2 and (*) β-$BaGeO_3$.

Further milling leads to a notable increase in intensity of the reflections indicating that crystallinity is improved with greater milling time (fig. 5.3).

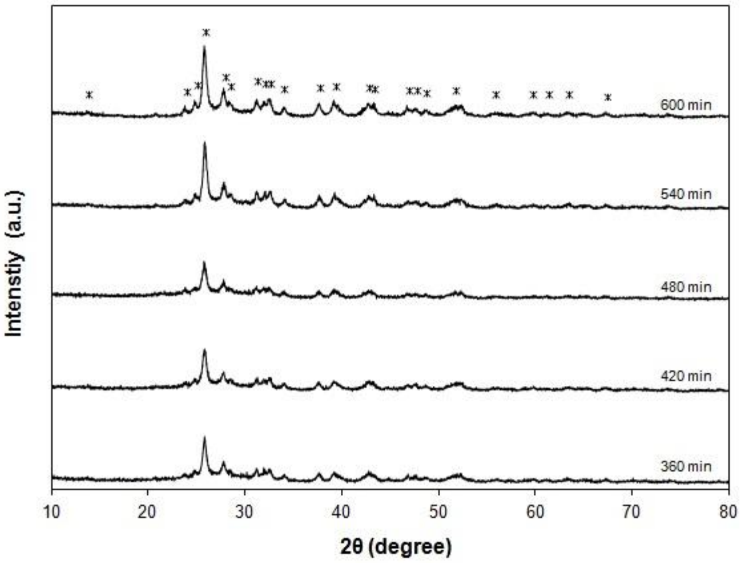

Fig. 5.3 - Evolution of powder X-Ray diffraction patterns with milling time (360, 420, 480, 540 and 600 min) for the BaO_2 + GeO_2 mixture, showing a substantial increase in intensity of the reflections representing that crystallinity is improved with larger milling time. The markers identify (*) the orthorhombic β-$BaGeO_3$ phase.

Rietveld refinement of XRD data of material subjected to 600 minutes of milling was performed in space group $P2_12_12_1$ according to published structural data of the high-temperature polymorph [19]. The thermal vibration factors (TVFs) of the cations were rather high and so the TVFs of all ions were constrained to a constant value in the final refinement. As the TVFs tend to correlate with other parameters, such as the background [21], the significant amorphous contribution to the XRD pattern in the present case could contribute to correlation effects during refinement leading to the high TVFs of the cations. Final structural parameters with constrained TVFs and reliability factors indicating the quality of the refinement are listed in table 5.1. The observed diffraction pattern and the difference pattern between observed and calculated data on convergence of the refinement are shown in fig. 5.4.

Table 5.1 – Structure refinement data for mechanosynthesized β-BaGeO$_3$: space group *P2$_1$2$_1$2$_1$*; lattice parameters: a = 4.51766(5) Å, b = 5.6315(6) Å and c = 12.614(1) Å; Rp = 2.83; Rwp = 3.76; χ^2 = 1.15.

Atom	**x/a**	**y/b**	**z/c**	**Occupancy**
Ba (1)	0.226(1)	0.1858(4)	0.3573(2)	1.0
Ge (1)	0.673(1)	0.700(1)	0.4220(4)	1.0
O (1)	0.318(5)	0.702(4)	0.441(1)	1.0
O (2)	0.78(1)	0.893(4)	0.335(2)	1.0
O (3)	0.707(7)	0.424(3)	0.402(2)	1.0

* Thermal vibration factors were constrained to B_{iso} = 0.8

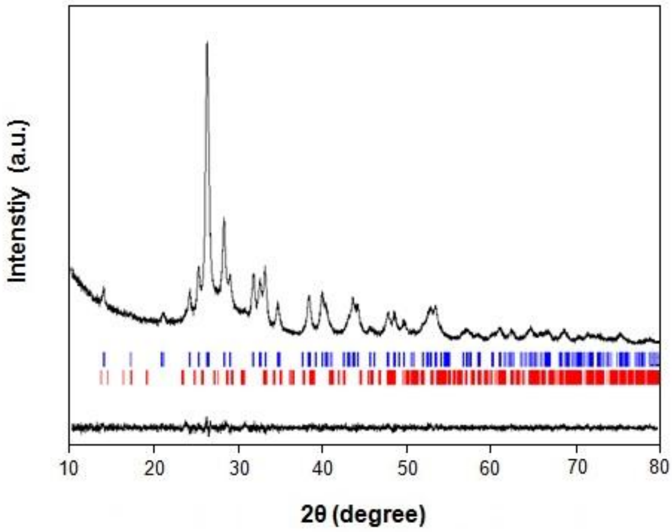

Fig. 5.4 - Observed and difference X-ray powder diffraction profiles of mechanosynthesized BaGeO$_3$ after 600 minutes of milling. The Bragg peaks of β- and α-phases are indicated by vertical blue and red bars, respectively.

Inspection of table 5.2 reveals a decrease in the cell parameters with increasing milling time from 300 to 600 minutes. On the other hand, the amount of crystallised fraction increases.

Table 5.2 – Lattice parameters obtained from Rietveld refinement of XRD and crystallised faction of orthorhombic polymorph of $BaGeO_3$ for different milling times (300 and 600 minutes), determined from quantitative Rietveld refinement.

Milling time	**a (Å)**	**b (Å)**	**c (Å)**	**Crystallised fraction**
300 min	4.59785(4)	5.73389(3)	12.83389(3)	42.7 %
600 min	4.51766(5)	5.6315(6)	12.614(1)	71.5 %

5.1.3.2 MICROSTRUCTURE

The grains of $BaGeO_3$ fresh powders produced by mechanosynthesis at room temperature are essentially spherical in shape, a geometry which may favour ceramic processing [22], in the form of loose agglomerates, as shown in fig. 5.5.

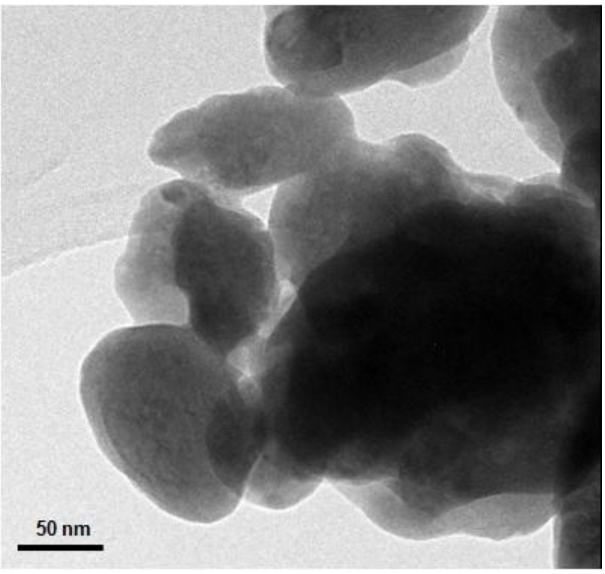

Fig. 5.5 - Transmission electron micrograph of $BaGeO_3$ fresh powder prepared in a one-step process by mechanosynthesis at room: milled for 600 minutes at 650rpm.

An amorphous component was also readily observed by TEM, fig. 5.6 a) surrounding the crystalline grains. A second micrograph, fig. 5.6 b), shows that the bulk grain consists of nanopolycrystalline domain structure, where the large number of bright spots in the inset of fig. 5.6 b) corresponds to numerous crystallites of different orientations within a single grain.

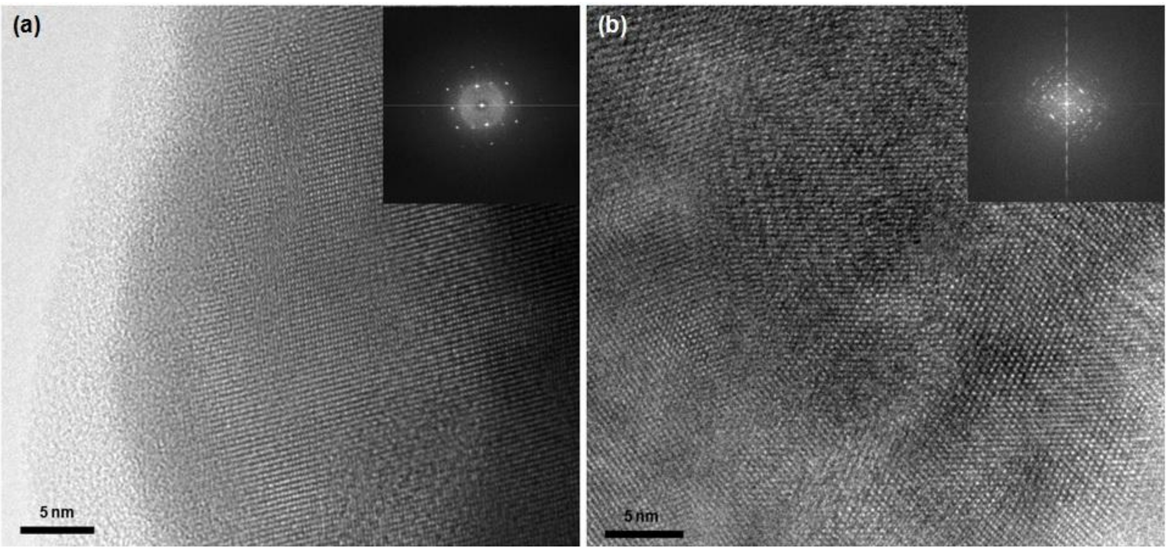

Fig. 5.6 - Transmission electron micrograph of $BaGeO_3$ fresh powder prepared in a one-step process by mechanosynthesis at room: milled for 600 minutes at 650rpm, showing (a) a crystalline domain within an amorphous matrix, and (b) a grain composed of randomly oriented nanodomains.

5.1.3.3 YIELD

Figure 5.7 shows the evolution of the amount of crystallised fraction from 300 minutes (5 hours) to 600 minutes (10 hours) of milling time.

According to the figure, the amount of crystallised phase increases monotonously with increasing milling time: there is an increase from about 40% at 5 hours to 70% after 10 hours of milling. These results suggest that a considerable amount of non-reacted precursors still remain after extended milling times that are responsible for the amount of non-crystallised phase (about 30% at 10 hours).

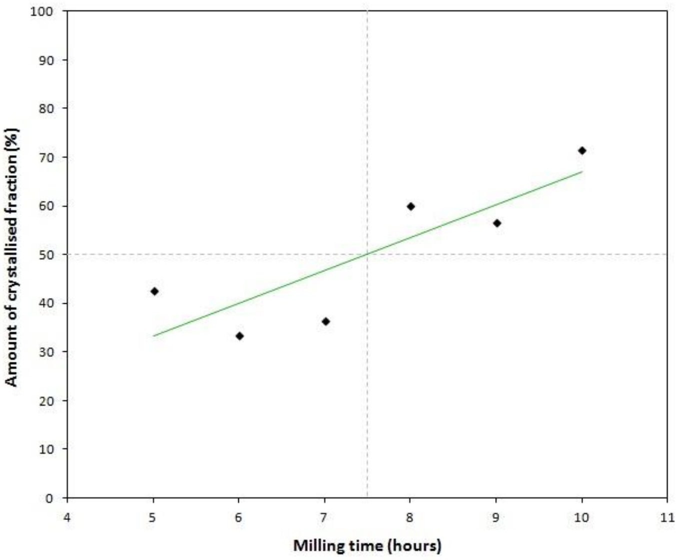

Fig. 5.7 – Evolution of the amount of crystallised fraction of $BaGeO_3$ powders milled for different times between 300 and 600 minutes (5 and 10 hours), determined from quantitative Rietveld refinement.

The existence of residual reactants is confirmed by FT-IR (fig. 5.8) of the fresh powder after 600 minutes of milling time, showing bands associated with the precursors BaO_2, GeO_2 and $BaCO_3$. The presence of carbonate can be explained by both the BaO_2 fresh precursor powder, which contains some $BaCO_3$ impurities, as well as possible carbonation of the highly reactive mechanosynthesized powder on exposure to air that is especially likely for extremely fine powders of high surface areas formed after extended milling times.

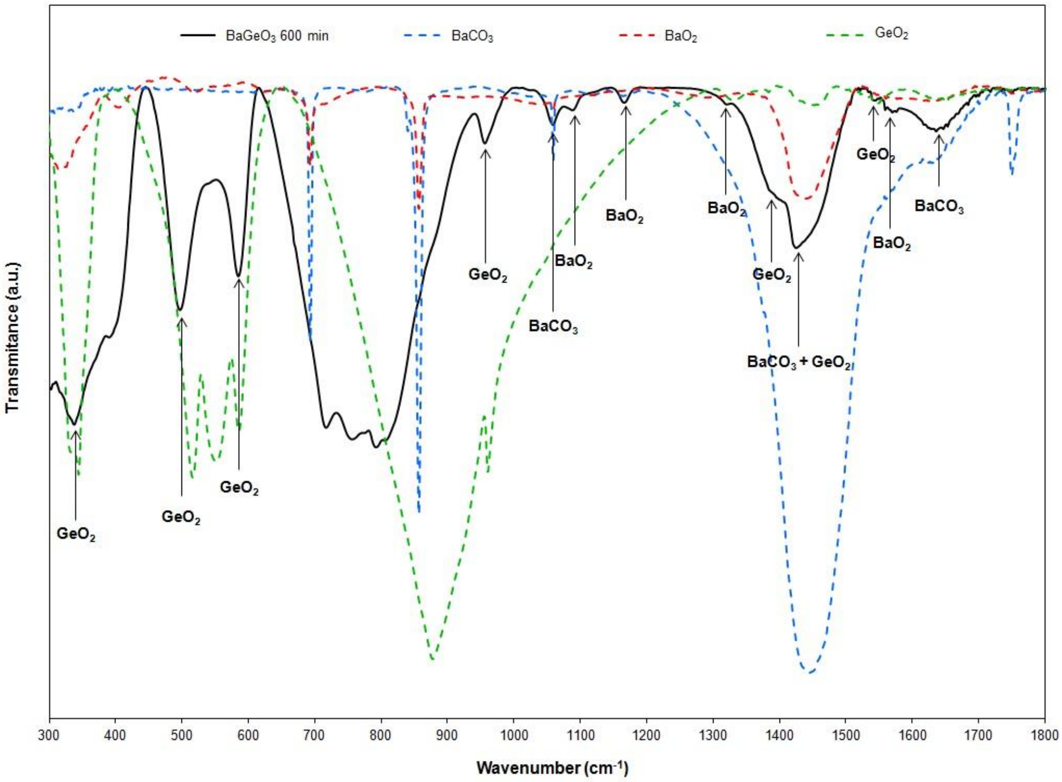

Fig. 5.8 – FT-IR spectra of $BaGeO_3$ fresh powders after 600 minutes of milling showing bands associated with the precursors: BaO_2, GeO_2 and $BaCO_3$.

The progression of the reaction between BaO_2 and GeO_2 yields oxygen as follows:

$$BaO_2 + GeO_2 \Leftrightarrow BaGeO_3 + \frac{1}{2}O_2 \uparrow \tag{5.1}$$

Thermograms of the material after 300 minutes of milling time, fig. 5.9, shows mass losses that are, therefore, likely to be related to such residual reactants. The overall mass losses appear to occur in several stages, with initial weight losses shown at low temperatures <500ºC that are accompanied by broad endotherms. These low temperature features are likely to be associated with the removal of adsorbed moisture, as previously documented in the literature for these materials [12]. A second weight loss is noted above 700ºC, following minor endothermic (~630ºC) and exothermic (~650ºC) events. Finally a substantial endothermic event is observed at approximately 950ºC without notable weight change. To understand the origin of these events, XRD diffraction was performed as a function of temperature and is discussed in the next section.

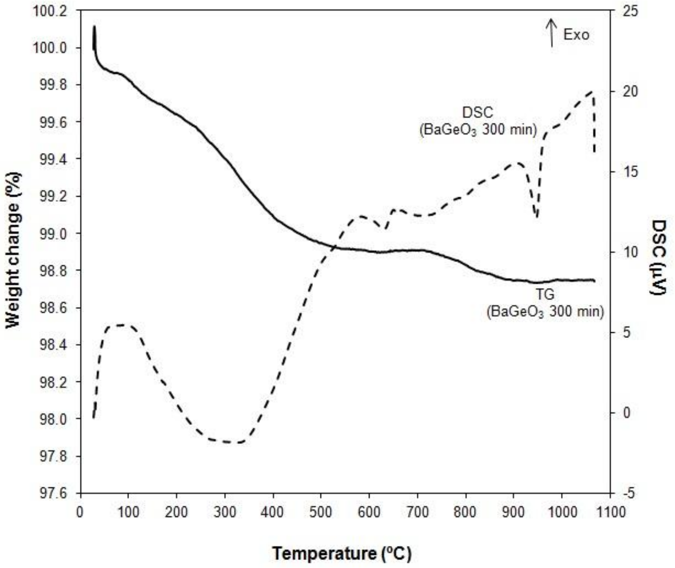

Fig. 5.9 - Thermogravimetry of mechanically activated powders obtained from an initial powder mixture of BaO_2+GeO_2 after milling for 300 minutes at 650rpm.

5.1.3.4 PHASE TRANSITIONS

XRD patterns of the sample milled for 300 minutes registered as a function of temperature in the range 25 - 1000°C are shown in fig. 5.10, plus the corresponding phase compositions calculated by quantitative Rietveld refinement of the HT-XRD data presented in fig. 5.11.

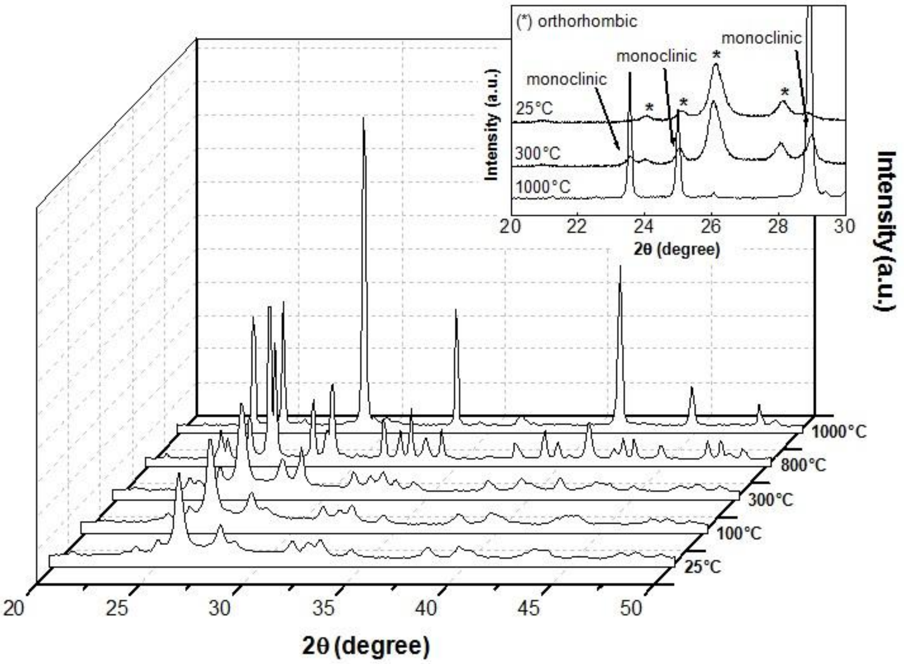

Fig. 5.10 - Evolution of high-temperature X-ray diffraction patterns of 300 minutes $BaGeO_3$ fresh powders at 25ºC, 100ºC, 300ºC, 800ºC and 1000ºC. The markers identify the (*) orthorhombic polymorph – β-$BaGeO_3$.

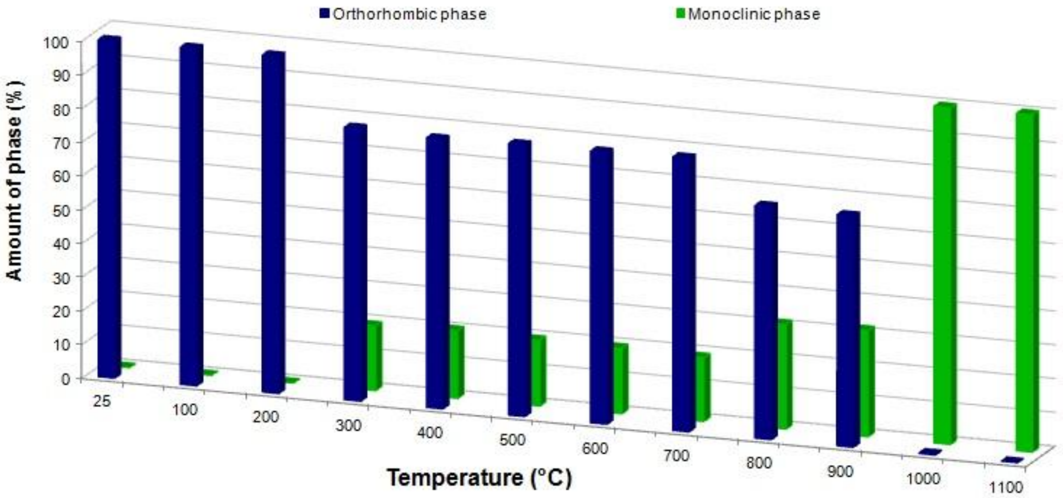

Fig. 5.11 - Evolution of the quantities of $BaGeO_3$ polymorphs (monoclinic α-$BaGeO_3$ and orthorhombic β-$BaGeO_3$ in blue and black plots, respectively) of the powder milled for 300 minutes as a function of temperature as determined by quantitative Rietveld refinement of powder X-ray diffraction data.

From fig. 5.11 it is possible to conclude that, in addition to the orthorhombic β polymorph, the α polymorph (monoclinic) becomes apparent at 300°C. The apparent absence of any thermal event in this region, in the results of fig. 5.9, suggests that the formation of the α polymorph may be due to increasing crystallinity of this phase with increasing temperature, rather than that of a phase transformation or phase formation. From 300ºC to 700ºC, the weight content of the α phase does not alter significantly, whereupon it increases to ~ 31 wt.% at 800ºC. The increase in the amount of the $BaGeO_3$ phase at 800ºC can be attributed to the second weight loss in the thermogravimetric experiment of fig.5.7 due to the presence of residual reactants. In this respect, note that the reduction of BaO_2 to BaO has previously been documented to occur in the temperature range 523ºC-877ºC, with the principal endothermic event centred at ~630ºC [23]; a temperature in close agreement with the minor endothermic event noted in the thermogravimetric results. The immediately following exothermic event (~650ºC) and subsequent weight loss in fig 5.9, likely coincide with the formation of $BaGeO_3$ from the residual reactants, as supported by the increase in the relative amount of this phase shown in fig. 5.11. At still higher temperatures, complete transition of the β polymorph to the α phase is shown to be essentially complete at 1000 °C. Nonetheless, this cannot be related to the endothermic event shown between 900ºC and 1000ºC in the thermogravimetric results of fig. 5.9 as this phase transformation has previously been reported to be exothermic in nature [10,12]. Hence, an alternative suggestion is that this endothermic event corresponds to the crystallographic change of the $BaCO_3$ impurity from hexagonal to cubic-type structure, as noted in the literature [23]. In this respect, note that this structural change of $BaCO_3$ occurs before its decomposition.

The corresponding variations in unit-cell volume for the two polymorphs on heating from 25 to 1100°C are shown in fig 5.12. The cell volume of the orthorhombic form changes linearly with temperature (fig. 5.12a) despite the fact that the phase quantity changes in a stepwise fashion. In general, the volume of the monoclinic form also follows a linear dependency; nonetheless the discontinuity in the plot (fig. 5.12b) at the highest temperatures may signify some more structural complexity or, alternatively, is an artifact of the poor high-temperature refinements.

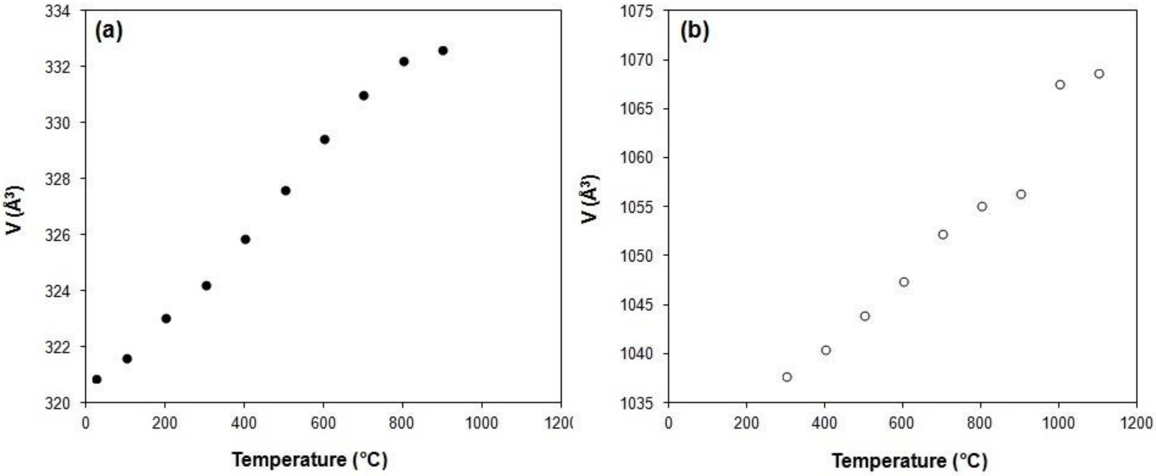

Fig. 5.12 - Evolution of the unit-cell volume with temperature for: a) orthorhombic and b) monoclinic polymorphs of $BaGeO_3$.

5.1.4 CONCLUSION

The high-temperature β form of barium metagermanate was prepared under ambient conditions (air, no external heat source) by mechanosynthesis of BaO_2 and GeO_2. The metastable phase forms agglomerates of spherical grains that are composed of randomly oriented nanocrystals within an amorphous matrix. The combination of FT-IR, thermogravimetric experiements and XRD suggest that the amorphous content is likely to result from unreacted starting product (BaO_2, $BaCO_3$).

On heating, the β-form is joined by the presence of the monoclinic α phase, with the transition being complete upon heating at 1100ºC. Both polymorphs exhibit linear expansion of the lattice parameter on heating in the range 25-1100°C.

5.2 MECHANICAL PREPARATION OF $Ba_{0.8}K_{0.2}GeO_{3-\delta}$ NANOPOWDERS: A NEW OXIDE-ION CONDUCTOR

5.2.1 INTRODUCTION

Recently, a new family of superior solid oxide-ion conductors have been studied by Goodenough and co-workers [4,5]. These materials are based on the monoclinic doped $SrMO_3$-based oxides (M = Si, Ge) and are potential candidates for intermediate temperature-solid oxide fuel cells (IT-SOFC), showing good ionic conductivity (higher than 10^{-2} S.cm^{-1}), at 625ºC (considered an intermediate operation temperature for SOFC).

The introduction of an alkali metal cation at the Sr-site of $SrGeO_3$ causes the introduction of terminal-oxygen vacancies on tetrahedral anion complexes ions, which has been reported to improve the oxide-ion conductivity [4-6]. Introducing a large K^+ (1.51 Å) ion on the Sr^{2+} (1.26 Å) site was found to be responsible for the formation of oxygen vacancies in a specific plane at the in-plane O3 and O5 sites [9]. This phenomenon may occur due to steric hindrance by the large Sr^{2+} and K^+ ions. As a result, a terminal-oxygen vacancy would jump between clusters in a double-well potential much like a proton in an asymmetric hydrogen bond of an alkaline solution. Furthermore, no oxygen interstitials were evident, although debate about the exact conduction mechanism still continues [1,4,5,7,8].

Substitution of Sr^{2+} for the higher radii Ba^{2+} ions may lead to considerable structural distortions as well as providing an increase of the steric hindrance, and, thus, may potential have a considerable impact on the oxide-ion conduction.

In the current work, the effect of K-addition to $BaGeO_3$ materials was studied. $Ba_{1-x}K_xGeO_{3-0.5x}$ materials were analysed in detail in terms of their structural and transport properties in order to assess the effect of K^+ substitution on the oxide-ion conductivity and to compare the impact of the expected larger lattice distortions promoted by Ba in comparison with the known $Sr_{1-x}K_xGeO_{3-0.5x}$ presented in the literature. Moreover, as both Ba and K are basic elements raising the probability for hydration of oxygen vacancies (eq.1.8), the current work also aimed to assess for potential proton conductivity in these materials.

$$H_2O + O_O^x + V_O^{\bullet\bullet} \rightarrow 2OH_O^{\bullet} \qquad (1.8)$$

The study was based on the characterization of the material by different techniques: high-temperature X-ray diffraction (HT-XRD), scanning electron microscopy (SEM) as well as impedance spectroscopy. Based on the literature for the Sr-analogue, the solubility limit for K-additions was found to be 25 mol%. However, Singh *et al.* [4] highlighted an optimal composition between 15 and 20 mol% which shows the best oxide-ion conductivity results (higher than 10^{-2} $S.cm^{-1}$ by 700ºC). Thus, the performance of these systems in the current work is preliminarily investigated using the fixed composition x = 0.20

5.2.2 PROCESSING METHODOLOGY

The specific composition selected in this study was $Ba_{0.8}K_{0.2}GeO_{2.9}$ and was attempted to be produced by mechanosynthesis for 5 hours. Stoichiometric amounts of BaO_2 (Sigma-Aldrich, 95% purity), KO_2 (Sigma-Aldrich) and high purity GeO_2 (Sigma-Aldrich, ≥99.99% trace metal basis) were mixed at 650 rpm.

Green samples were isostatically pressed at 200 MPa for 30 minutes and heated at 1100ºC for 5 hours in air.

The conductivity measurements were performed on sintered pellets using platinum electrodes and data was collected on cooling in different flowing dry and wet atmospheres: N_2 and O_2. The electrical properties were also studied as a function of dry oxygen partial pressure (pO_2), obtained by mixing O_2 and N_2 gases controlled by digital mass flow controllers.

The nature of phase transitions and their temperature dependence was studied by high-temperature X-ray diffraction (HT-XRD), collected with a Bruker D8 Advance DaVinci over the range $10° \leq 2\theta \leq 110°$ with a step size of 0.05° and measurement time of 1s/step. Diffractograms were registered from room temperature to 1200ºC in intervals of 100ºC to 500ºC and intervals of 50ºC for temperatures between 550 and 1200ºC.

The microstructure of the surface of polished and thermally etched sintered samples was investigated by scanning electron microscopy (SEM) using a Hitachi 4100S instrument.

5.2.3 RESULTS AND DISCUSSION

5.2.3.1 PHASE FORMATION AND CRYSTAL STRUCTURE

The powder XRD patterns (fig. 5.13) show that $Ba_{0.8}K_{0.2}GeO_{2.9}$ is not single phase after typical mechanosynthesis conditions, contrary to that obtained for the K-free $BaGeO_3$ in the previous section.

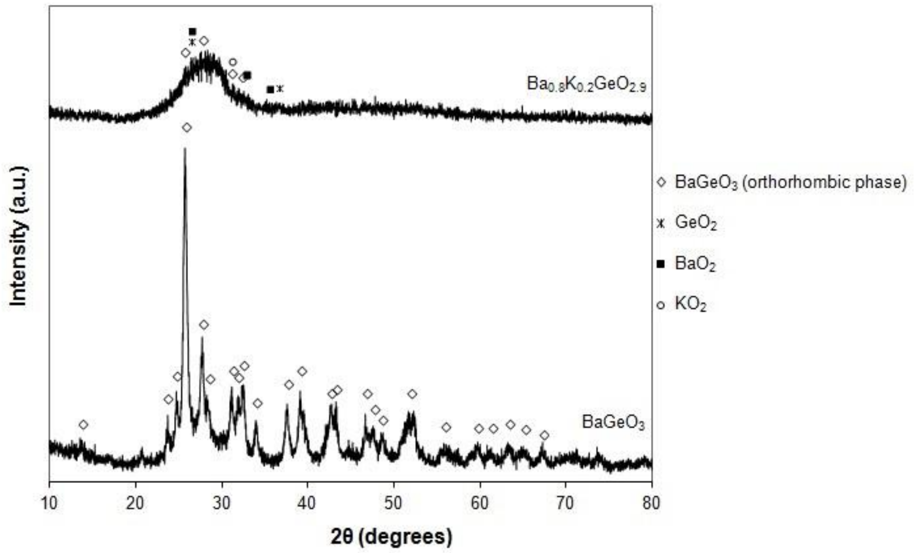

Fig. 5.13 – Powder XRD patterns of K-free and K-doped BaGeO$_3$ (BaGeO$_3$ and Ba$_{0.8}$K$_{0.2}$GeO$_{2.9}$, respectively) after mechanosynthesis. The markers identify the (◊) BaGeO$_3$ orthorhombic phase, as well as the precursors: (*) GeO$_2$, (■) BaO$_2$ and (○) KO$_2$.

Chapter 5.1 showed that high energy milling of BaO$_2$ and GeO$_2$ powders can lead to the mechanochemical formation of the high-temperature β-phase (orthorhombic phase) of BaGeO$_3$. In contrast, the introduction of KO$_2$ to this precursor mixture leads to amorphization of the precursors, without any clear mechanochemical reaction, fig. 5.14.

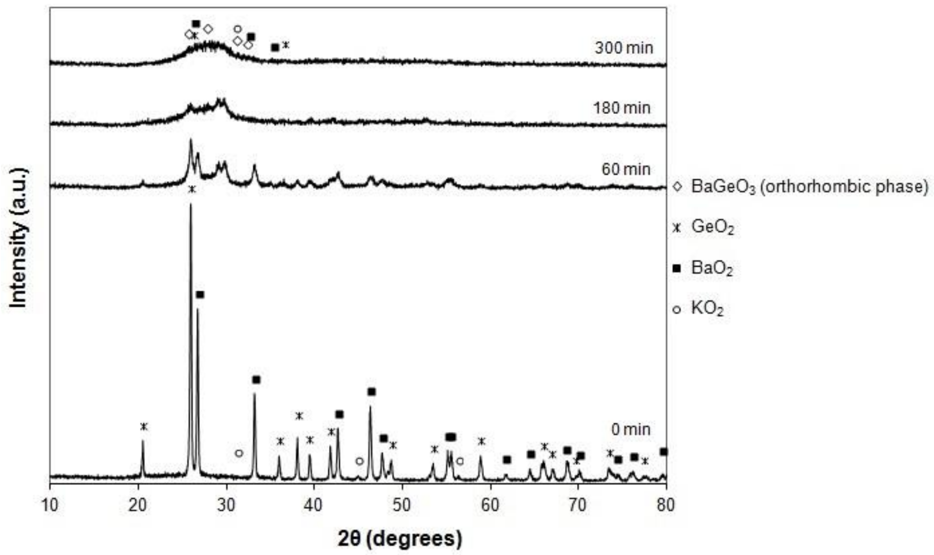

Fig. 5.14 - Evolution of powder X-Ray diffraction patterns with milling time (0, 60, 180 and 300 min) for the BaO$_2$ + KO$_2$ + GeO$_2$ mixture. The markers identify the precursors: (*) GeO$_2$, (■) BaO$_2$ and (○) KO$_2$, as well as the potential (◊) BaGeO$_3$ orthorhombic phase.

Contrary to that noted for $BaGeO_3$ in section 5.1.3.1, further milling times, up to 300 minutes, also could not improve on the crystallinity of the XRD reflections or convert the precursor powders to a single phase. The final powder is an almost amorphous mixture between the precursors (BaO_2, GeO_2 and KO_2) and possibly also the high-temperature β-form of $BaGeO_3$ (as shown before, in figure 5.13).

Thus, in order to achieve a pure single phase, a subsequent calcination step was shown to be required (fig. 5.15).

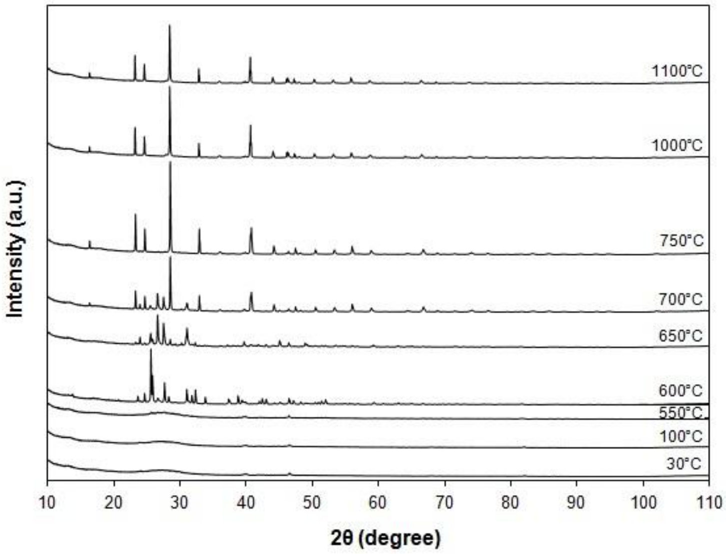

Fig. 5.15 – Powder high-temperature XRD patterns of $Ba_{0.8}K_{0.2}GeO_{2.9}$ during the heating, at different temperatures (30, 100, 550, 600, 650, 700, 750, 1000 and 1100ºC).

Increasing the temperature leads to the formation of different phases: at 600ºC there is an increase in the peaks intensity, appearing a considerable amount of β-form $BaGeO_3$ (orthorhombic unit cell) – fig. 5.16.

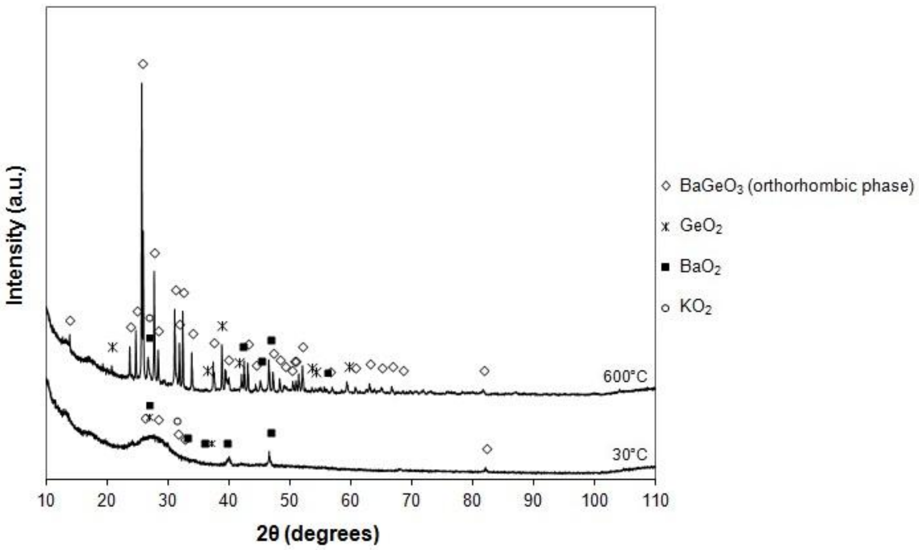

Fig. 5.16 – Evolution of powder high-temperature XRD patterns of $Ba_{0.8}K_{0.2}GeO_{2.9}$ in the heating, at 30ºC and 600ºC. The markers identify the precursors: (*) GeO$_2$, (■) BaO$_2$ and (○) KO$_2$, as well as the (◊) BaGeO$_3$ orthorhombic phase.

However, increasing the temperature to 700ºC, the low-temperature α-form of BaGeO$_3$ (monoclinic phase) starts appearing at the same time as the β-form (orthorhombic phase). Both phases co-exist until 750ºC, where the orthorhombic phase disappears – fig. 5.17.

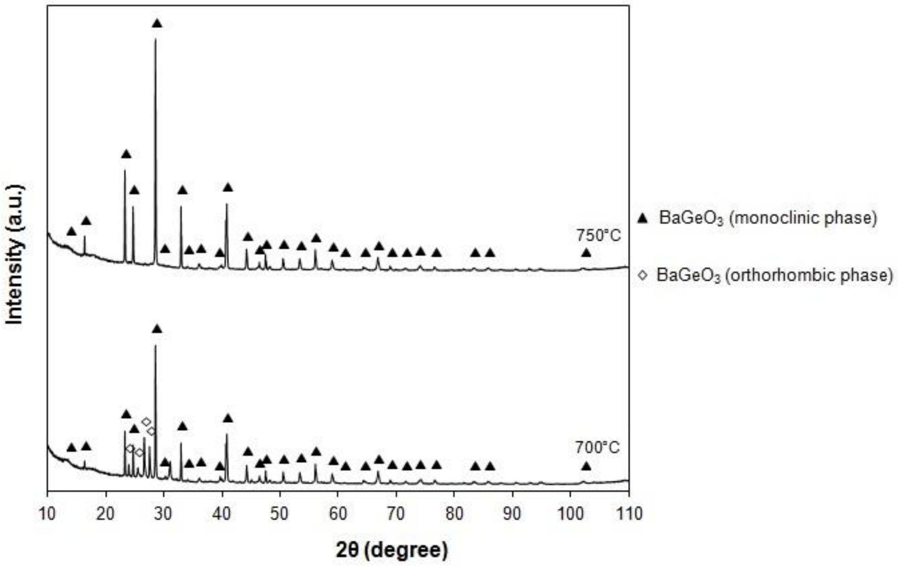

Fig. 5.17 – Evolution of powder high-temperature XRD patterns of $Ba_{0.8}K_{0.2}GeO_{2.9}$ in the heating, at 700ºC, 750ºC. The markers identify the precursors: (*) GeO$_2$, (■) BaO$_2$ and (○) KO$_2$, as well as the BaGeO$_3$ (◊) orthorhombic and (▲) monoclinic phases.

Figure 5.18 presents the XRD pattern of $Ba_{0.8}K_{0.2}GeO_{2.9}$ sintered at 1100ºC for 5 hours, showing a single phase based on the α polymorph of $BaGeO_3$ with monoclinic unit cell.

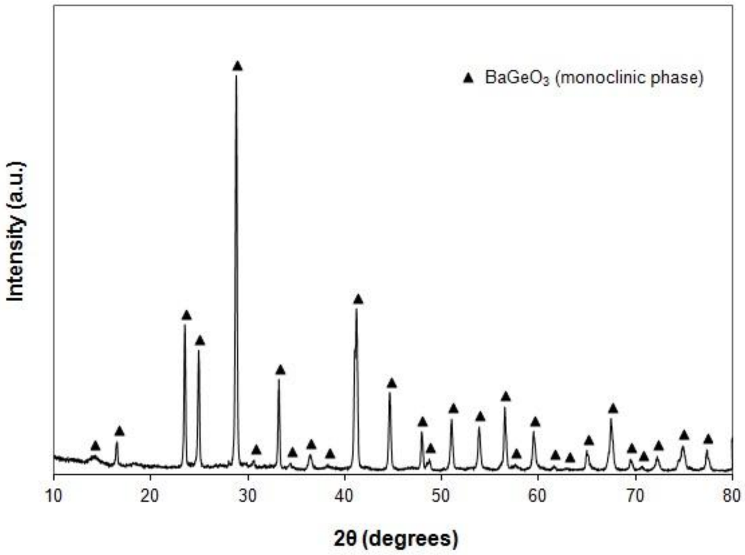

Fig. 5.18 – XRD patterns of $Ba_{0.8}K_{0.2}GeO_{2.9}$ sintered at 1100ºC for 5 hours. The markers identify (▲) the $BaGeO_3$ monoclinic phase.

Rietveld refinement was performed using the FullProf software and the obtained structural parameters are shown in table 5.3.

Table 5.3 – Structural parameters of monoclinic K-free and K-doped $BaGeO_3$.

Compound	Lattice parameters				Cell volume	Reference
	a (Å)	b (Å)	c (Å)	β	V (Å^3)	
$BaGeO_3$	13.1260	7.5750	11.6200	112.350	1068.70	This work (last section - 5.1.3.4)
$Ba_{0.8}K_{0.2}GeO_{2.9}$	13.1026	7.6190	11.7007	112.154	1081.84	This work
$Sr_{0.8}K_{0.2}GeO_{2.9}$	12.5691(2)	7.2731(1)	11.2803(3)	111.32(1)	960.64	[4]

Comparing the unit cell values between K-free and K-doped $BaGeO_3$, an increase in lattice volume was obtained, as expected from the substitution of potassium for barium due to the larger ionic radii of K^+ (1.51 Å) compared to Ba^{2+} (1.42 Å) [9].

On comparison with the reported $Sr_{0.8}K_{0.2}GeO_{2.9}$ material [4], $Ba_{0.8}K_{0.2}GeO_{2.9}$ shows higher unit cell parameters due to the larger ionic radius of Ba^{2+} compared to Sr^{2+} (1.42 and 1.26 Å, respectively) [9].

5.2.3.2 MICROSTRUCTURE

The SEM micrograph of the sintered $Ba_{0.8}K_{0.2}GeO_{2.9}$ pellet is given in figure 5.19. According to the micrograph, the pellet reveals high levels of densification with grains that appear bar-shaped.

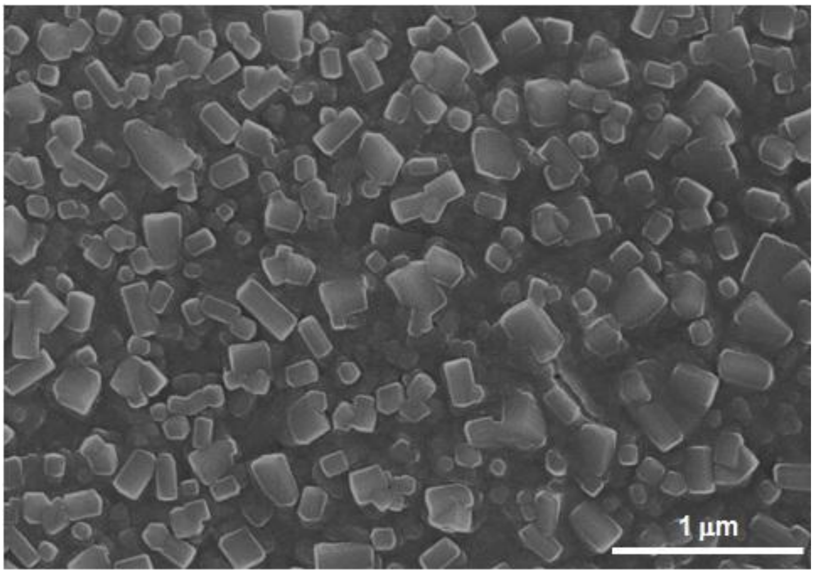

Fig. 5.19 – SEM micrograph of the surface of $Ba_{0.8}K_{0.2}GeO_{2.9}$, sintered at 1100°C for 5 hours.

The observed dense microstructure is in agreement with the calculated geometrical density of the samples, which was ~ 88% of the theoretical density of the material.

5.2.3.3 ELECTRICAL MEASUREMENTS

The conductivity behaviour of the K-doped $BaGeO_3$ samples was assessed by A.C. impedance spectroscopy under dry and wet N_2 and O_2 atmospheres. Such impedance spectra were fitted by a series combination of distributed RQ elements, where the fitting parameters extracted for each distributed arc are the resistance value, R, the pseudo-capacitance, Q, of the constant phase element and the parameter n. These parameters can be related to the true capacitance by the equation 5.2 [24]:

$$C = R^{\frac{1-n}{n}} Q^{\frac{1}{n}} \tag{5.2}$$

Figure 5.20 shows an example of impedance spectra measured at low temperatures (300ºC) in dry oxygen atmospheres, confirming the presence of the dominant bulk response at high frequency with capacitance values in the 10^{-12} - 10^{-11} F/cm^2 range. The grain boundary response was shown to offer a negligible contribution to the impedance spectra for the whole temperature range. The impedance responses were, thus, modelled by the respective equivalent circuit presented in figure 5.20 across the temperature range, where the total resistance is predominately given by the dominant bulk response.

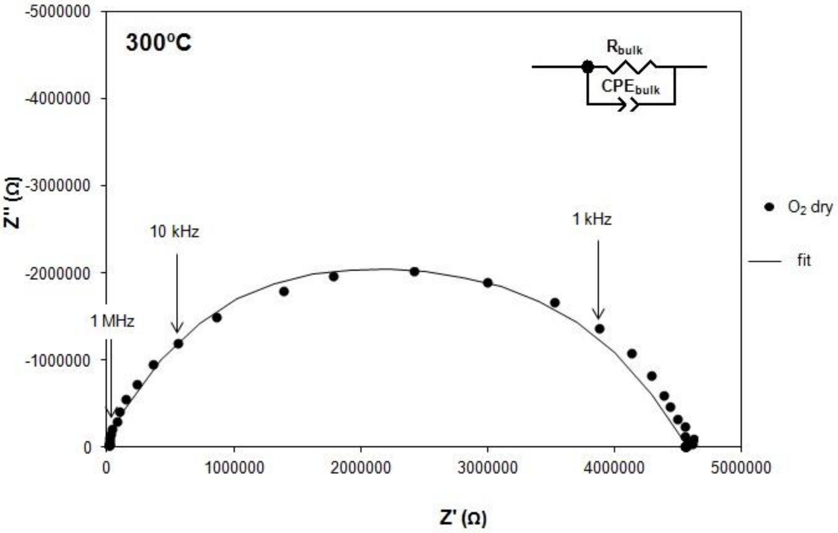

Fig. 5.20 - Typical impedance spectra and respective equivalent circuit measured at 300°C in dry oxygen atmosphere of $Ba_{0.8}K_{0.2}GeO_{2.9}$, showing the bulk response at higher Z' frequencies.

The temperature dependencies of the total conductivities for $Ba_{0.8}K_{0.2}GeO_{2.9}$ are shown in fig. 5.21 in wet and dry N_2 and O_2.

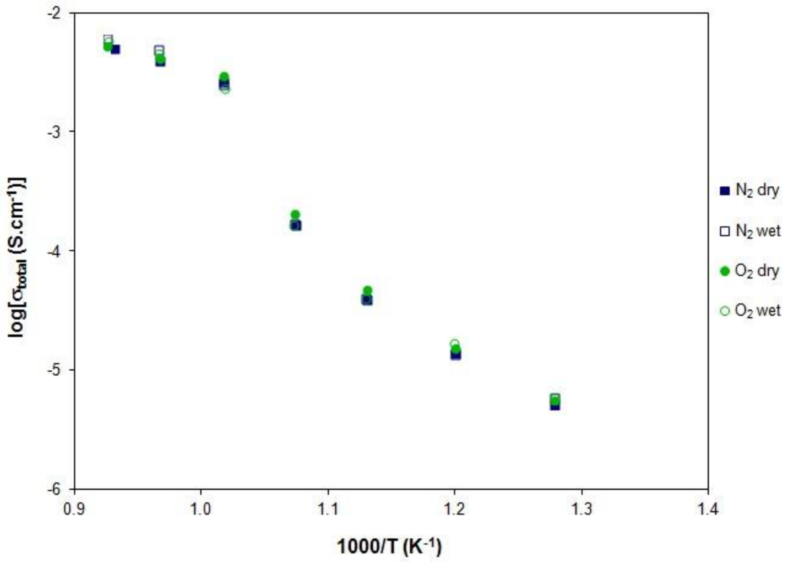

Fig. 5.21 - Temperature dependence of the total conductivity of system $BaK_{0.2}GeO_{2.9}$ in wet ($pH_2O = 3.30x10^{-2}$ atm) and dry N_2 and O_2.

The total conductivity (fig. 5.21) shows a significant “jump” between 700 and 650ºC that will be discussed in the later section 5.2.3.4. In addition, the existences of two distinct activation energies for conduction are noted, corresponding to the temperature regime above 700ºC (~ 0.82 eV) and to temperatures below 650ºC (~ 1.49 eV), either side of the conductivity jump. Moreover, the total conductivities are effectively equal and independent by the atmosphere that is used (N_2 or O_2 in dry or wet conditions). The lack of a pH_2O dependence of conductivity negates proton conduction in these materials.

Meanwhile, the independence of conductivity on partial pressure of oxygen (pO_2) is a key indicator of typical oxide-ion conductors. Figure 5.22 shows the dependence of pO_2 in a temperature range of 700 to 500ºC.

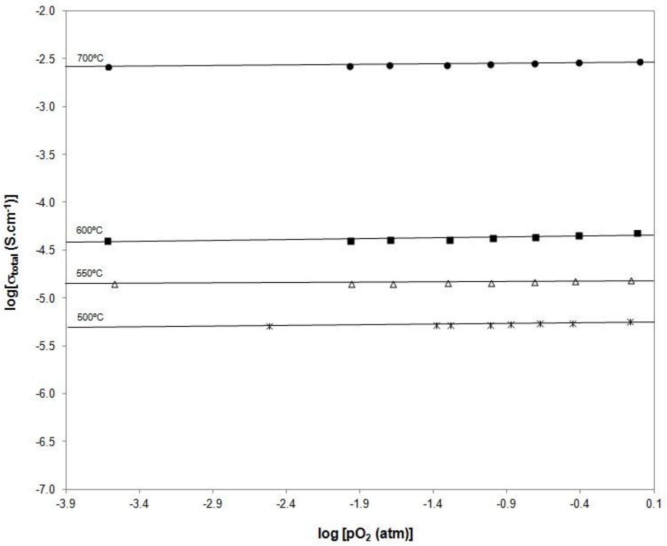

Fig. 5.22 - Temperature dependence of $B_{0.8}K_{0.2}GeO_{2.9}$ *vs* pO_2 under dry condition at various temperatures (700ºC to 500ºC).

The total conductivity of $Ba_{0.8}K_{0.2}GeO_{2.9}$ is shown not to depend on the partial pressure of oxygen (pO_2) – fig. 5.22, reinforcing the suggestion that this material may be a pure oxide-ion conductor, in agreement with that previously reported for the Sr-analogue [1,4,5].

Figure 5.23 compares the conductivity values for $Ba_{0.8}K_{0.2}GeO_{2.9}$ and that reported for $Sr_{0.8}K_{0.2}GeO_{2.9}$ [4].

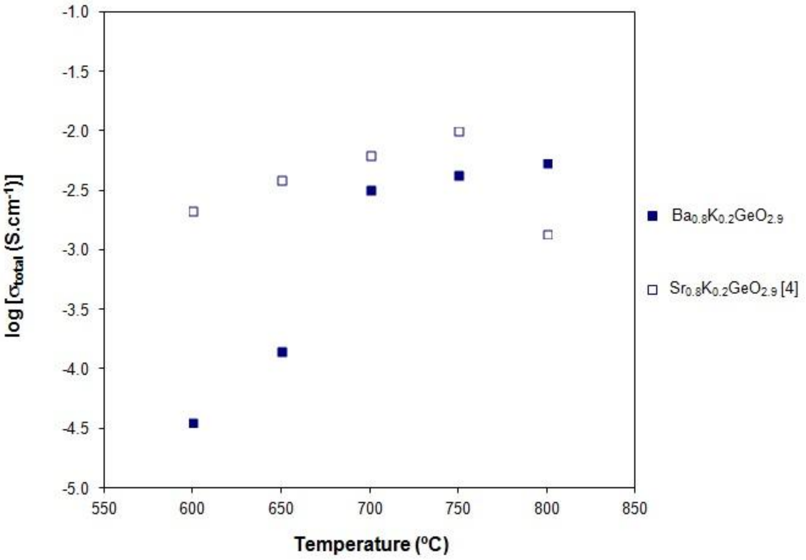

Fig. 5.23 – Comparison between O^{2-} conductivity of $Ba_{0.8}K_{0.2}GeO_{2.9}$ and reported of $Sr_{0.8}K_{0.2}GeO_{2.9}$ [4], at different temperatures (650, 700, 750 and 800ºC).

From figure 5.23 it is possible to conclude that, in the higher temperature range 700ºC ≤ T ≤ 800ºC, $Ba_{0.8}K_{0.2}GeO_{2.9}$ system shows similar conductivity values as the reported $Sr_{0.8}K_{0.2}GeO_{2.9}$ system, offering a competitive oxide-ion conductivities as an alternative candidate electrolytes for an IT-SOFC. At lower temperatures the conductivity of the Ba-composition is shown to be inferior to the reported conductivities of the Sr-analogue, due to the observed conductivity "jump" for the Ba-composition between high and low temperature regimes, fig 5.21.

5.2.3.4 PHASE TRANSITIONS AND STRUCTURAL CHANGES

Structural changes may justify the "jump" in the total conductivity (denoted on figure 5.21). Thus, in order to understand possible phase transitions, high-temperature X-ray diffraction was performed as a function of temperature, upon cooling (fig. 5.24).

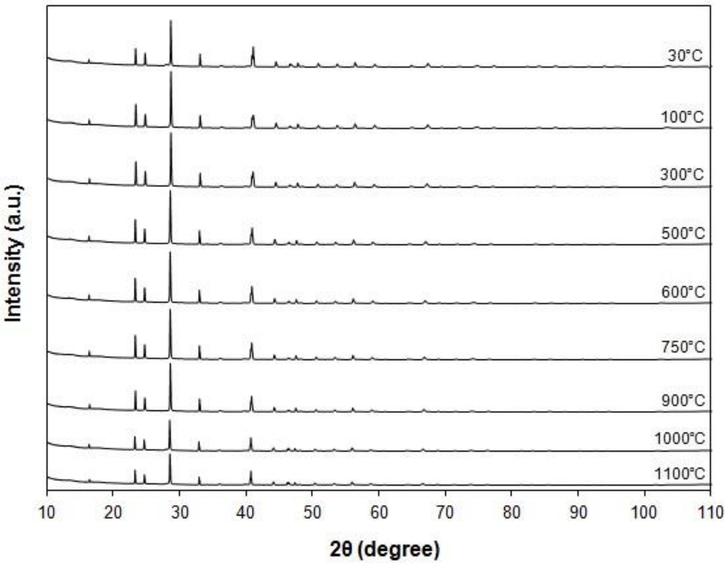

Fig. 5.24 – Powder high-temperature XRD patterns of $Ba_{0.8}K_{0.2}GeO_{2.9}$ during the cooling, at different temperatures (1100, 1000, 900, 750, 600, 500, 300, 100 and 30ºC).

Nonetheless, the XRD patterns recorded during cooling do not show any observable phase transformations. To emphasise this point the XRD patterns bridging the conductivity "jump" are replotted in figure 5.25 at a larger scale. The absence of notable structural changes on heating (previously presented on section 5.2.3.1 – fig. 5.15), measured by XRD, suggests that changes in the cation lattice cannot explain the observed jump in conductivity. On the other hand, a recent study of the Sr-analogue by neutron diffraction showed a variation in the oxygen vacancy distribution as the temperature increased [5]. It is, therefore, plausible that a structural change in the anion lattice may occur on heating that is not characterised by XRD. Thus, alternative experimental techniques must be suggested to characterise the conductivity jump that are sensitive to the lighter atoms, such as neutron diffraction or Raman spectroscopy.

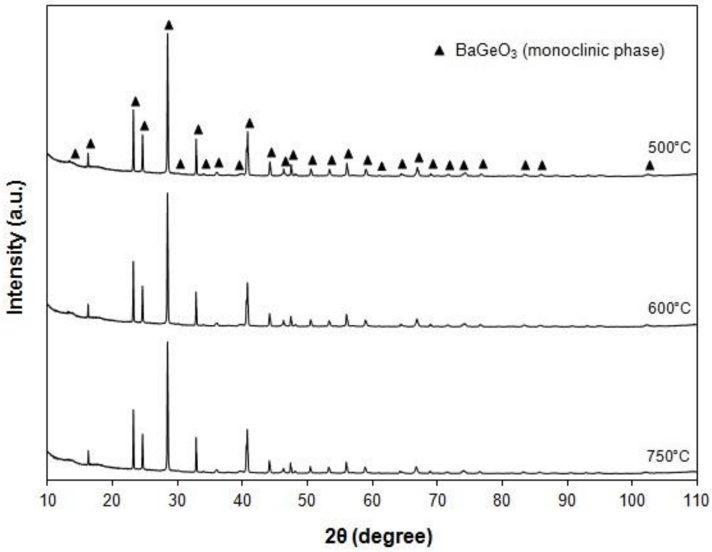

Fig. 5.25 – Evolution of powder high-temperature XRD patterns of Ba$_{0.8}$K$_{0.2}$GeO$_{2.9}$ in the cooling, at 750ºC, 700ºC and 500ºC. The markers identify (▲) the BaGeO$_3$ monoclinic phases.

In the future, additional tests should be done in order to confirm this assumption. As a preliminary investigation, thermogravimetric analysis has been performed (fig. 5.26).

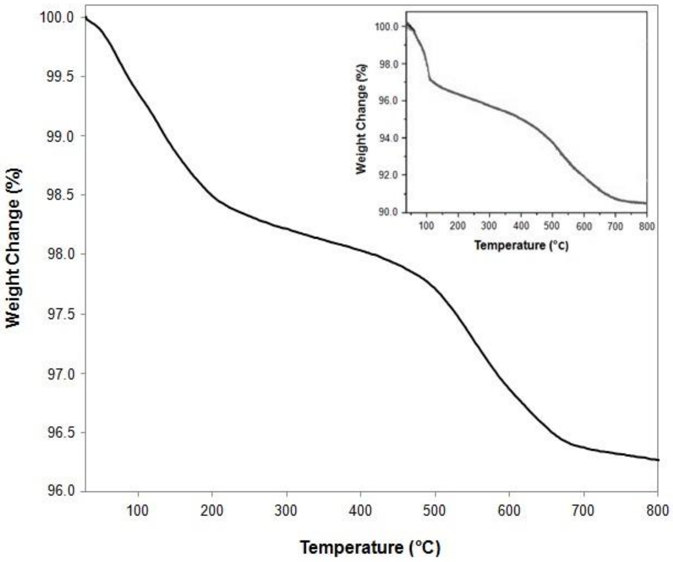

Fig. 5.26 – TGA plot for Ba$_{0.8}$K$_{0.2}$GeO$_{2.9}$ obtained in oxygen with a heating rate of 2ºC/min. Inset image shows the TGA plot reported by Martinez-Coronado *et al.* [5] for Sr$_{0.8}$K$_{0.2}$Ge$_{2.9}$ obtained in air with a heating rate of 2ºC/min.

Figure 5.26 shows the thermogravimetric behaviour of $Ba_{0.8}K_{0.2}GeO_{2.9}$ powders formed in the current work upon heating in O_2 atmosphere. According to Martinez-Coronado *et al.* [5] the pronounced weight change presented during heating to 150 - 200ºC can be attributed to the loss of water, while, the further weight loss of ~ 2% above 200ºC suggests the loss of oxygen. The loss of water is in agreement with the hydration of similar materials noted by Singh *et al.* [8], who suggested that presence of oxide ion vacancies in the lattice act as centers for water absorption. Similar thermogravimetric behaviour was detected by Martinez-Coronado and his group [5] for the Sr based analogue, as shown in the inset image of figure 5.26.

As no structural changes were noted on the cation lattice on heating by XRD (figures 5.24 and 5.25), the observed loss of oxygen may impact only the anion lattice. This concept would agree with the variation in the oxygen vacancy distribution noted in these materials as a function of temperature by neutron diffraction [5]. This change in oxygen content and possible vacancy order on the oxygen sublattice, possibly could explain the noted conductivity “jumps”.

5.2.4 CONCLUSIONS

In conclusion, K-doped $BaGeO_3$ materials offer competitive oxide-ion conductivities in the intermediate temperature range 700ºC ≤ T ≤ 800ºC that makes them a promising new electrolyte material.

In comparison with more well-known O^{2-} conductors, such as YSZ, $Ba_{0.8}K_{0.2}GeO_{2.9}$ shows a decrease in the densification temperature (from temperatures higher than 1350ºC to 1100ºC) that can be an important attraction for the market due to reducing production costs.

The chemical stability and independence of conductivity on pO_2 was confirmed under a wide range of oxygen partial pressures between N_2 and O_2 atmospheres. This behaviour suggests predominant ionic conduction that, due to its independence on pH_2O, is likely to be oxide-ion conducting in nature.

5.3 MECHANICAL PREPARTION OF NANOPOWDERS OF OXIDE-ION ELECTROLYTES WITH $SrGeO_3$ STRUCTURE

5.3.1 INTRODUCTION

Singh *et al.* [4] reported a new family of oxide-ion conductors which shows the structure $Sr_{3-x}A_xM_3O_{9-0.5x}$, A = Na or K and M = Si or Ge. The Ge analogue showed better performance in terms of O^{2-} conductivity in comparison with the Si analogues. The presence of the acceptor dopants (Na or K) was reported to be responsible for the introduction of charge compensating oxygen vacancies that are important to promote oxide-ion conductivity [1,4,5,7,8]

K-additions to $SrGeO_3$-based materials were reported to be possible between 0 and 40 mol%. Nonetheless, oxide-ion conductivity higher than 10^{-2} $S.cm^{-1}$ by 700ºC was reached only in the range 0 to 25 mol%. Two different activation energies for oxide-ion conduction were observed in low- and high-temperature regions [4]. In order to understand this behaviour and to compare results with the previous $Ba_{0.8}K_{0.2}GeO_{3-\delta}$ composition, $Sr_{1-x}K_xGeO_{3-0.5x}$ materials, where x = 0.20, will form the basis of the present work, where the structural and conductivity properties of this material will be reported. Again, preparation of powders will be attempted by mechanochemical reaction (mechanosynthesis) of stoichiometric quantities of SrO_2, K_2CO_3 and GeO_2. Note all previous work on this new family of oxide-ion conductors has been performed on materials prepared by standard solid state reaction routes [4,5,7]. A wide range of techniques were used for a complete characterization of $Sr_{0.8}K_{0.2}GeO_{2.9}$ (x = 0 and 0.20) materials, such as: X-ray diffraction, scanning electron microscopy, thermogravimetric analysis as well as Raman and impedance spectroscopies.

5.3.2 PROCESSING METHODOLOGY

Powders of $Sr_{0.8}K_{0.2}GeO_{2.9}$ were produced by the mixing of stoichiometric quantities of SrO_2 (Sigma-Aldrich, 98% purity) and high purity GeO_2 (Sigma-Aldrich, ≥99.99% trace metal basis). The synthesis was attempted based on a mechanochemical reaction (mechanosynthesis) for 5 hours at 650 rpm.

The green pellet samples were obtained after pressing isostatically at 200 MPa for 30 minutes, while sintered pellets were obtained from these green composites by firing at 1100ºC for 5 hours in air.

The progression of the reaction was monitored by X-ray diffraction (XRD) analysis of powder samples collected at regular time periods.

To characterize the electrical properties, measurements were performed on sintered pellets with platinum electrodes and data were collected on cooling in flowing N_2 and O_2 atmospheres in dry and wet conditions. Additionally, these properties were also studied as a function of dry oxygen partial pressure (pO_2), obtained by mixing O_2 and N_2 gases.

Structural analysis was performed by scanning electron microscopy (SEM) on the surface of polished and thermally etched sintered samples, using a Hitachi 4100S instrument.

5.3.3 RESULTS AND DISCUSSION

5.3.3.1 PHASE FORMATION AND CRYSTAL STRUCTURE

The powder XRD patterns (fig. 5.27) show that $Sr_{0.8}K_{0.2}GeO_{2.9}$ is not single phase after mechanical milling, contrary to what observed for the K-free $SrGeO_3$ material.

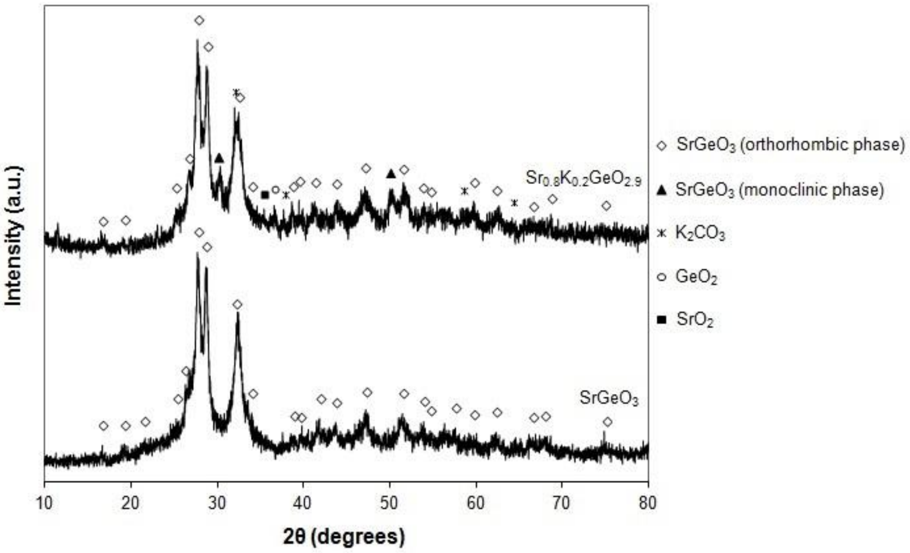

Fig. 5.27 – Powder XRD patterns of K-free $SrGeO_3$ and $Sr_{0.8}K_{0.2}GeO_{2.9}$ after mechanosynthesis. The markers identify: (◊) $SrGeO_3$ orthorhombic phase, (▲) $SrGeO_3$ monoclinic phase, (*) K_2CO_3, (●) GeO_2 and (■) SrO_2.

The substitution of K^+ on the Sr^{2+} site of $SrGeO_3$ leads to traces of the low-temperature monoclinic $SrGeO_3$ phase in addition to that of the high-temperature orthorhombic form, fig. 5.27. On contrary, K-free $SrGeO_3$ powders produced by mechanosynthesis shows a single phase based on the high-temperature orthorhombic form. Nonetheless, the background of the XRD patterns of fig. 5.27 is non-linear, suggesting that room temperature mechanosynthesis may not have achieved complete conversion, with quantities of reactants (as SrO_2, GeO_2 and K_2CO_3) possibly present as amorphous impurities.

Figure 5.28 presents the XRD pattern of $Sr_{0.8}K_{0.2}GeO_{2.9}$ sintered at 110ºC from the mechanosynthesized powders. A highly crystalline single phase of $Sr_{0.8}K_{0.2}GeO_{2.9}$ can be observed with monoclinic unit cell, space group C12/c1 (space group number 15), in agreement with the literature [4].

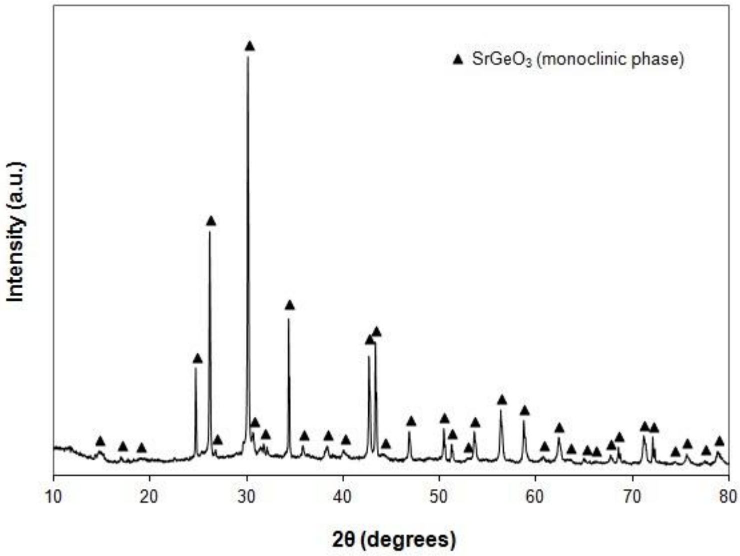

Fig. 5.28 – XRD patterns of sintered $Sr_{0.8}K_{0.2}GeO_{2.9}$ at 1100ºC for 5 hours. The markers identify the $SrGeO_3$ monoclinic phase (▲).

Rietveld refinement was performed using the FullProf software. Table 5.4 shows the comparison of structural parameters obtained from the Rietveld refinement of the XRD measurements at room temperature of (Ba,Sr)GeO_3-based materials. In agreement with the larger ionic radius of Ba^{2+} (1.42 Å) compared to Sr^{2+} (1.26 Å), the unit cell parameters are shown to decrease by the change of Ba^{2+} to Sr^{2+} in the preparation of these materials. The current cell parameters are shown to be consistent with that of the literature [4].

Table 5.4 – Structural parameters of K-doped (Ba,Sr)GeO_3.

Compound	**Lattice parameters**				**Cell volume**	**Reference**
	a (Å)	**b (Å)**	**c (Å)**	**β**	**V (Å^3)**	
$Ba_{0.8}K_{0.2}GeO_{2.9}$	13.1026	7.6190	11.7007	112.154	1081.84	This work (last section – 5.2.3.1)
$Sr_{0.8}K_{0.2}GeO_{2.9}$	12.4319(2)	7.2313(0)	11.2801(0)	111.19(3)	945.49	This work
$Sr_{0.8}K_{0.2}GeO_{2.9}$	12.5691(2)	7.2731(1)	11.2803(3)	111.32(1)	960.64	[4]

5.3.3.2 MICROSTRUCTURE

The scanning electron microscopy (SEM) study reveals that the pellets are well-sintered and that the grains are in intimate contact with each other (fig. 5.29).

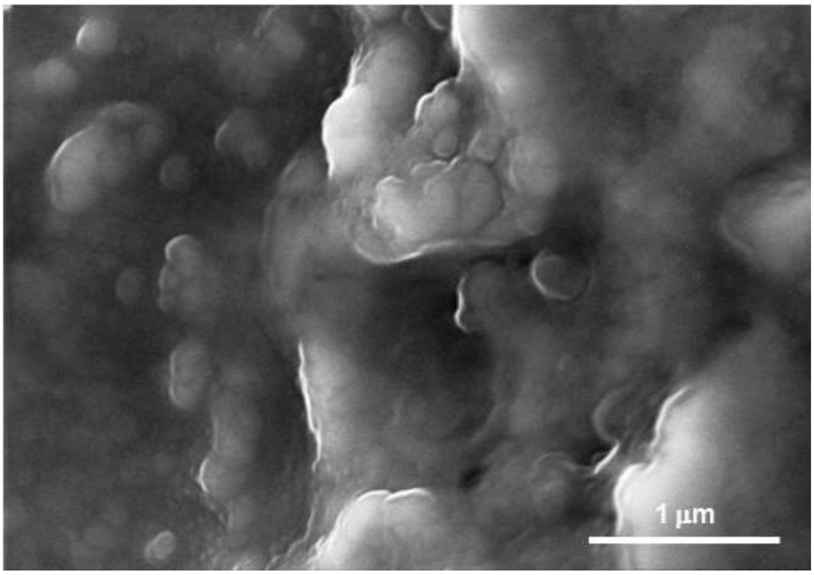

Fig. 5.29 - Scanning electron micrograph (SEM) from the surface of a dense bulk sample of $Sr_{0.8}K_{0.2}GeO_{2.9}$, sintered at 1100°C for 5 hours.

The density of the pellets measured by geometrical analysis was about 90% of the theoretical density of the material.

5.3.3.3 ELECTRICAL MEASUREMENTS

Figure 5.30 shows an example of A.C. impedance spectra measured at 400ºC in dry oxygen atmosphere. Similar to that described previously for the Ba analogue (section 5.2.3.3), the grain boundary response is unresolvable and the bulk response is shown to be dominant across the temperature range. This type of impedance response was, thus, modelled by the equivalent circuit presented in the figure. The total conductivity was taken to be effectively equal to the dominant bulk response.

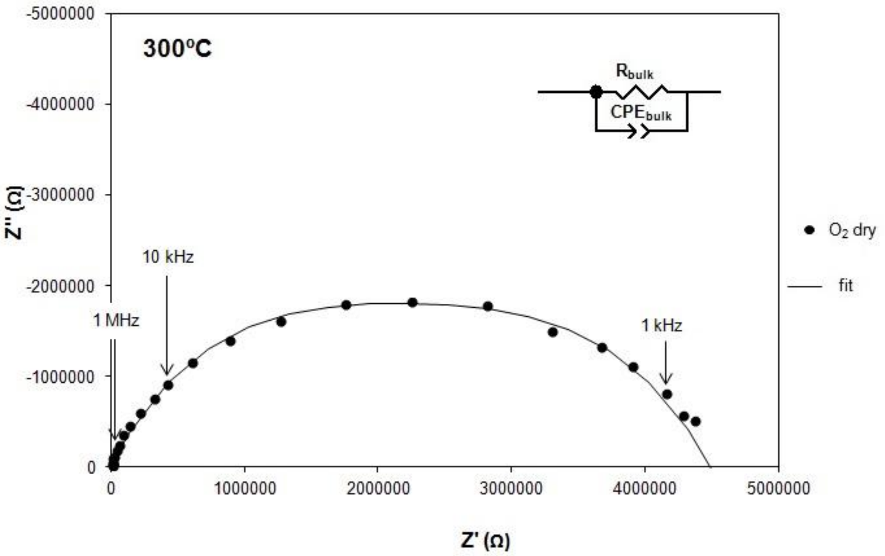

Fig. 5.30 - Typical impedance spectra and respective equivalent circuit measured at 300°C in dry oxygen atmosphere of $Sr_{0.8}K_{0.2}GeO_{2.9}$, showing the bulk response at higher Z' frequencies.

An Arrhenius plot (log σ_{total} vs 1000/T) for $Sr_{0.8}K_{0.2}GeO_{2.9}$ is shown in fig. 5.31. Two different activation energies can be clearly seen for the low-temperature, *i.e.* ≤ 600ºC, and high-temperature regions, *i.e.* ≥ 650ºC: 1.09 and 0.85 eV, respectively. As noted in the Ba-analogue, the total conductivities are similar and independent by the atmosphere that is used (N_2 or O_2 in dry or wet conditions) and a "jump" in the conductivity can also be observed, occurring between 600ºC and 650ºC. Note that this jump is at a slightly lower temperature than recorded for the Ba-analogue in fig 5.21 (between 650ºC and 700ºC). These results suggest that these materials do not offer protonic conduction in these conditions and that the conductivity is likely to be oxide-ion conducting in nature, in agreement to that described by Wei *et al.* [1].

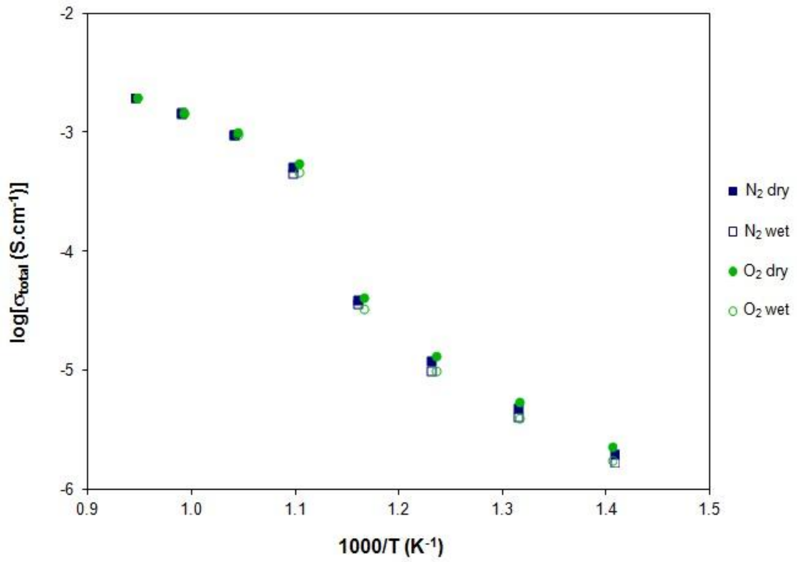

Fig. 5.31 - Temperature dependence of the total conductivity of $Sr_{0.8}K_{0.2}GeO_{2.9}$, under dry and wet (pH_2O = $3.30x10^{-2}$ atm) N_2 and O_2 atmospheres.

The presence of oxide-ion conduction is reinforced by the independence of conductivity over a wide range of pO_2, shown by Figure 5.32 in the temperature range of 700 to 500ºC.

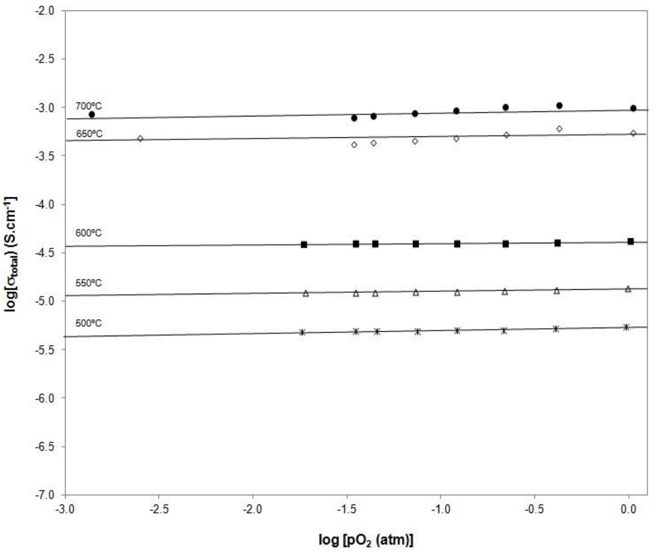

Fig. 5.32 - Temperature dependence of $Sr_{0.8}K_{0.2}GeO_{2.9}$ *vs* pO_2 under dry condition at various temperatures (700 to 500ºC).

Figure 5.33 shows the oxide-ion conductivities values for $Sr_{0.8}K_{0.2}GeO_{2.9}$ prepared by two different routes: mechanosynthesis followed by a sintered step at 1100ºC for 5 hours (current work) and the reported work by Singh *et al.* [4] where the sample was prepared by a solid state reaction followed by a densification at 1100ºC for 15 hours.

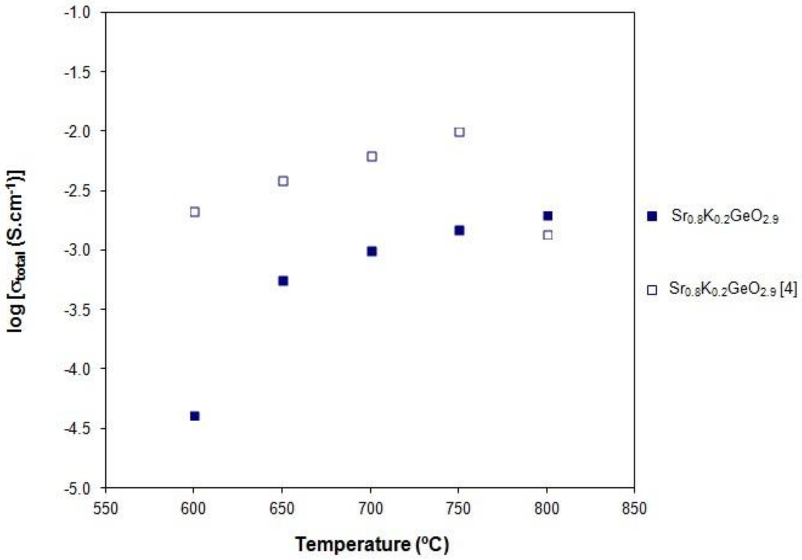

Fig. 5.33 – O^{2-} conductivity (σ_{total}) of $Sr_{0.8}K_{0.2}GeO_{2.9,}$ and reported of $Sr_{0.8}K_{0.2}GeO_{2.9}$ [4], at different temperatures (650, 700, 750 and 800ºC).

From figure 5.33 it is possible to conclude that, at intermediate temperatures, both systems shows similar activation energies: K-doped $SrGeO_3$ material prepared by mechanosynthesis is 0.80 eVin the (temperature range of 650ºC - 800ºC; in the case of $Sr_{0.8}K_{0.2}GeO_{2.9}$ powder prepared by solid state reaction [4] E_a = 0.86 eV between 600ºC and 750ºC. Additionally, it can be concluded that at high temperatures, *i.e.* 800ºC, the total conductivity is in agreement with the literature. However, at temperatures lower than 750ºC a significantly difference in conductivity is shown between the current date and that of the literature. Moreover, in the literature data a jump in conductivity is not observed. In the previous section 5.2.3.4, for the Ba-analogue, it was suggested that the “jump” in conductivity may be due to structural variations on the anion sublattice. In this respect a recent article by Martinez-Coronado *et al.* [5] performed thermogravimetric analysis on the composition $Sr_{0.8}K_{0.2}GeO_{2.9}$ (inset image of figure 5.34) revealed considerable weight loss in heating above 200ºC. The authors attributed this weight loss to the loss of oxygen. Figure 5.34 shows the thermogravimetric behaviour of $Sr_{0.8}K_{0.2}GeO_{2.9}$ powders formed in the current work upon heating in O_2 atmosphere. The figure reveals that, similar to the work of Singh *et al.* [8], the continuous weight loss above 200ºC suggests the loss of oxygen. As no structural changes were noted on the cation lattice on heating for the isostructural material $Ba_{0.8}K_{0.2}GeO_{2.9}$ by XRD (section 5.2.3.4), the observed loss of oxygen may again be suggested to impact only the anion lattice in the current case. This concept would agree with the variation in the oxygen vacancy distribution noted in these materials as a function of temperature by neutron diffraction [5]. This change in oxygen content and possible vacancy order on the oxygen sublattice, possibly could explain the noted conductivity “jumps” in the current work.

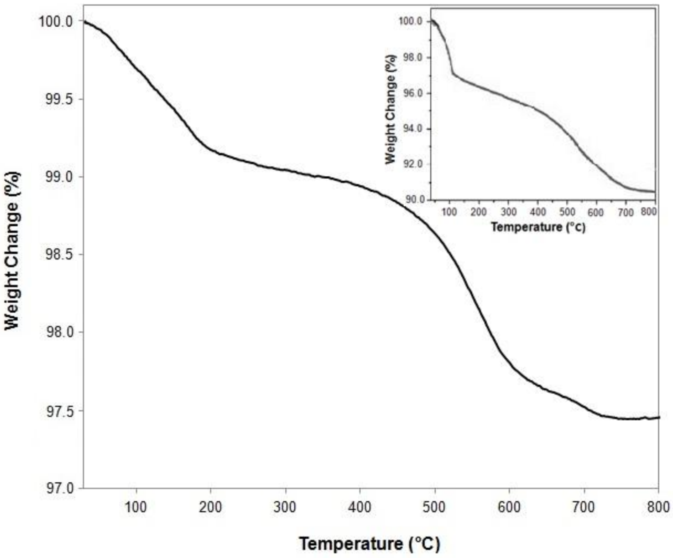

Fig. 5.34 – TGA plot for $Sr_{0.8}K_{0.2}GeO_{2.9}$ obtained in oxygen with a heating rate of 2ºC/min. Inset image shows the TGA plot reported by Martinez-Coronado *et al.* [5] for $Sr_{0.8}K_{0.2}Ge_{2.9}$.

On reference to the work of Singh *et al.* [4] their conductivity measurements were performed on samples pressed at a very high pressure (5 GPa) in comparison to the current measurements that were performed on samples pressed at only 200 MPa. The density of the ceramics tested may, therefore, be substantially higher than 90% in the work of Singh *et al.* [4] although this data, unfortunately, is not provided. Moreover, very high pressures have also been reported to cause phase changes in $SrGeO_3$ materials, even being reported to yield the cubic perovskite structure upon pressurized sintering at 5 GPa [25]. Thus, the reason that the jumps are not observed in the work by Singh *et al.* [4] may be kinetic in nature, with oxygen exchange being slow in their highly dense samples pressed at 5 GPa or that the very high pressure used has led to residual stresses preventing or altering structural changes on the oxygen sublattice. In the current work each impedance measurement at any temperature is recorded after a dwell time of 3 hours with a second impedance measurement performed to ensure the attainment of equilibrium after a further 1 hour. Moreover, these data are measured on pellets with levels of density reaching only ~90% that of the theoretical. It is unclear from the available literature if the conductivity results of Singh and co-workers [4] measured on potentially denser samples were obtained under conditions of equilibrium with respect to the oxygen sublattice. This feature must, therefore, be studied further.

Finally, it is important to conclude that $Sr_{0.8}K_{0.2}GeO_{2.9}$ system produced by mechanosynthesis offer competitive oxide-ion conductivities in the temperature range 700ºC to 800ºC making it an alternative candidate electrolytes for an IT-SOFC.

5.3.4 CONCLUSIONS

In summary, it is concluded that $Sr_{0.8}K_{0.2}GeO_{2.9}$ is a superior oxide-ion conductor well suited for IT-SOFCs. It has shown high levels of O^{2-} conductivity in the temperature range between 700 and 800ºC as well as high chemical stability and purity oxide-ion conduction, which was confirmed by the dependence of ionic conductivity on pO_2.

Moreover, the combination of mechanical activation and calcination was shown to be a competitive synthesis technique to produce nanopowders of $Sr_{1-x}K_xGeO_{3-0.5x}$ materials with relatively high densification levels ~ 90%).

Considering its competitive costs in synthesis due to the lower required sintering temperatures (1100ºC) $Sr_{1-x}K_xGeO_{3-0.5x}$ has great potential to become a new class of technologically and strategically important electrolytes for commercial IT-SOFCs.

To conclude there is a new family of oxide-ion conductors based on K-doped $SrGeO_3$ materials whose low densification temperatures and the attractive oxide-ion conductivity in the operation range between 700 and 800ºC, make to these materials attractive candidate electrolytes for intermediate temperature solid oxide fuel cells (IT-SOFC). Nonetheless, further work is necessary to assess the presence of a conductivity jump around 650ºC, requiring analytical technique that will reveal possible structural changes on the anion sublattice, for example, Raman Spectroscopy, or Neutron diffraction amongst others.

5.4 REFERENCES

[1] Wei, T., Singh, P., Gong, Y., Goodenough, J.B., Huang, Y. and Huang, K. (2014). "$Sr_{3-3x}Na_{3x}Si_3O_{9-1.5x}$ (x = 0.45) as a superior oxide-ion electrolyte for intermediate temperature-solid oxide fuel cells." Energy & Environmental Science **7:** 1680-1684.

[2] Tealdi, C., Malavasi, L., Uda, I., Ferrara, C., Berbenni, V. and Mustarelli, P. (2014). "Nature of conductivity in $SrSiO_3$-based fast ion conductors." Chemical Communications **50:** 14732-14735.

[3] Xu, J., Wang, X., Fu, H., Brown, C.M., Jing, X., Liao, F., Lu, F., Li, X., Kuang, X. and Mingmei, W. (2014). "Solid-State ^{29}Si NMR and Neutron-Diffraction Studies of $Sr_{0.7}K_{0.3}SiO_{2.85}$ Oxide Ion Conductors." Inorganic Chemistry **53:** 6962-6968.

[4] Singh, P. and Goodenough, J.B. (2012). "$Sr_{1-x}K_xSi_{1-y}Ge_yO_{3-0.5x}$: a new family of superior oxide-ion conductors." Energy & Environmental Science **5:** 9626-9631.

[5] Martinez-Coronado, R., Singh, P., Alonso-Alonso, J. and Goodenough, J.B. (2014). "Structural investigation of the oxide-ion electrolyte with SrMO3 (M = Si/Ge) structure." Journal of the Materials Chemistry A **2:** 4355-4360.

[6] Nishi, F. (1997). "Strontium Metagermanate, $SrGeO_3$." Acta Crystallographica Section C **53:** 399-401.

[7] Goodenough, J.B. and Singh, P. "Monoclinic Sr1-xAxSi1-yGeyO3-0.5x, wherein A is K or Na, oxide ion conductor." Patent US 2014/0080019 A1 (2014).

[8] Singh, P. and Goodenough, J.B. (2013). "Monoclinic $Sr_{1-x}Na_xSiO_{3-0.5x}$: New Superior Oxide Ion Electrolytes." Journal of the American Chemical Society **135:** 10149-10154.

[9] Shannon, R.D. (1976). "Revised Effective Ionic Radii and Systematic Studies of Interatomic Distances in Halides and Chalcogenides." Acta Crystallographica Section A **32:** 751-767.

[10] Guha, J.P., Kolar, D. and Porenta, A. (1976). "Polymorphic Modifications of Barium Metagermanate." Journal of Thermal Analysis **9:** 37-41.

[11] Guha, J.P. (1979). "Phase equilibria in the system BaO-GeO_2." Journal of Materials Science **14:** 1744-1748.

[12] Yamaguchi, O., Niimi, T. and Shimizu, K. (1983). "Formation and Transformation of $BaGeO_3$." Materials Letters **2(2):** 119-121.

[13] Többens, D.M., Kahlenberg, V., Gspan, C. and Kothleitner, G. (2006). "Atomic and domain structure of the low-temperature phase of barium metagermanate ($BaGeO_3$)." Acta Crystallographica Section B **62:** 1002-1009.

[14] Payne, D.A. and Park, S.M. "Heterophasic ceramic composition." Patent US 4,218,723 (1980).

[15] Köferstein, R., Jäger, L., Zenkner, M. and Abicht, H.-P. (2007). "A barium germanium 1,2-ethanediolato complex as precursor for barium metagermanate." Thermochimica Acta **457:** 55-63.

[16] Köferstein, R., Jäger, L., Zenkner, M. and Abicht, H.-P. (2008). "Preparation and sintering behaviour of a fine grain $BaTiO_3$ powder containing 10 mol% $BaGeO_3$." Joural of the Materials Science **43:** 832-838.

[17] Chu, M.S.H., Bultitude, J., Hood, C., Nimmo, K.L. and Rand, M. "Temperature stable dielectric." Patent US 5,858,901 (1999).

[18] Liebau, F. (1960). "Zür Kristallchemie der silikate, germanate, fluoberyllate des formeltyps ABX_3." Neues Jahrbuch Mineralogie Abhandlungen **94:** 1209–1222.

[19] Hilmer, W. (1962), "Die struktur der hochtemperaturform des bariumgermanates BaGeO3(h)." Acta Crystallographica **15:** 1101–1105.

[20] Grebenshchikov, R.G., Toropov, N.A. and Shitova, V.I. (1965). *Izv. Akad. Nauk SSSR.* Neorgan. Materialy **1:** 1130.

[21] McCusker, L.B., von Dreele, R.B., Cox, D.E., Louër, D., Scardi, P. (1999). "Rietveld refinement guidelines." Journal of Applied Crystallography **32:** 36-50.

[22] Guillaume, B., Boschini, F., Garcia-Cano, I., Rulmont, A., Cloots, R. and Ausloos, M. (2005). "Optimization of $BaZrO_3$ sintering by control of the initial powder size distribution; a factorial design statistical analysis." Journal of the European Ceramic Society **25(16):** 3593-3604.

[23] Jorda, J.L. and Jondo, T.K. (2001). "Barium oxides: equilibrium and decomposition of BaO_2." Journal of Alloys and Compounds **327:** 167-177.

[24] Sherafar, Z., Paydar, M.H., Antunes, I., Nasani, N., Brandão, A.D. and Fagg, D.P. (2015). "Modeling of electrical conductivity in the proton conductor $Ba_{0.85}K_{0.15}ZrO_{3-\delta}$." Electrochimica Acta **165:** 443-449.

[25] Nakatsuka, A., Arima, H., Ohtaka, O., Fujiwara, K. and Yoshiasa, A. (2015). "Crystal structure of $SrGeO_3$ in the high-pressure perovskite-type phase." Acta Crystallographica Section E **71:** 502-504.

CHAPTER 6. FINAL CONSIDERATIONS AND FUTURE WORK

6.1 FINAL CONSIDERATIONS

The main objective of this dissertation was the development of novel ionic conducting ceramic materials to use in the electrolyte for either proton ceramic or solid oxide fuel cells (PCFCs and SOFCs, respectively). The research aimed to develop new materials with superior properties, namely on transport characteristics and chemical stability, by manipulation of processing.

The main challenges in the development of a solid electrolyte for PCFC are high proton conductivity and good chemical stability as shown by perovskite-type oxides. $BaZrO_3$ doped with 15 mol% of Y (BZY) has been presented as being one of the most attractive materials, filling both requirements: superior stabilities in steam or CO_2 containing atmospheres as well as competitive proton conduction. Nevertheless, challenges surrounding the use of barium zirconate materials centre on: (i) decreasing the sintering temperature in order to achieve full density and (ii) improving the grain boundary conductivity. In order to improve the sinterability of these materials, various co-dopants and sintering aids were studied, such as zinc, phosphorous and boron.

Introduction of ZnO into the lattice of barium zirconates promotes densification to ~ 35%, producing highly dense materials compared to the un-doped material, lowering the sintering temperature (from 1600ºC to 1300ºC). Different Zn-addition mechanisms do not show differences in terms of crystallographic phase, forming a single cubic perovskite structure for all compositions. However, their resultant microstructure is noted to show significant alterations. The different mechanisms lead to different grain growth, since the potential formation of Ba-deficiency in mechanism b) is shown to have a seriously negative impact on grain size. For all mechanisms, chemical analysis suggests an accumulation of Zn at the grain boundaries that is suggested to be responsible for higher specific grain boundary conductivities and associated activation energies than in Zn-free BZY. At high temperatures, >600ºC, the conductivity of these materials is shown to be predominantly protonic in nitrogen atmospheres, whilst is p-type electronic under oxygen and is lowest for mechanism b). The significant reduction in sintering temperature (from ~ 1600ºC to 1300ºC) and the high levels of densification render Zn-doped BZY samples good candidates as proton conductors for sensors, catalytic membranes and fuel cells. However, mechanisms a) and c) can be suggested to be the preferential mechanisms for Zn addition, when working at elevated temperatures.

BZY is shown to react with P_2O_5 additions forming the highly stable $Ba_3(PO_4)_2$ phase at temperatures as low as 600°C. As a result of removal of Ba from the perovskite lattice, the perovskite lattice parameter decreases with increasing P_2O_5 additions and grain growth is noted to be seriously impaired. For intermediate concentrations of P_2O_5 (4 - 8 mol%), densification of BZY is improved and the temperature of maximum densification rate is lowered. However, reaction with P dramatically decreases both bulk and grain boundary conductivities. The biggest depletion is for the grain–boundary behaviour, which is found to occur due to the formation of isolating glassy phases that coat the BZY grains.

The effects of B-additions on the sintering behaviour of un-doped and Y-doped $BaZrO_3$ were reported in chapter 4. A new doping approach, which uses solvents to introduce the additives, was studied. This method allows highly homogeneous levels of boron to be obtained in the samples. Solvent selection is critical once water-based solutions would be desirable not only for environmental reasons, but also to reduce cost. Despite this interest in aqueous solvents, ethanol is shown to offer the best sintering results for BZY, while water was shown to impede densification. The choice of ethanol, therefore, enables the introduction of additives by the solution doping method.

The densification behaviour of H_3BO_3 added $BaZrO_3$ (BZO) shows boron to be a very effective sintering aid (~ 97% of the theoretical density at 1250ºC), whereas, in contrast, the densification behaviour of $BaZr_{0.85}Y_{0.15}O_{3-\delta}$ (BZY) shows low levels of densification compared with un-doped BZY. The higher levels of densification of BZO are found to occur at 1500ºC due to the formation of secondary phases, namely BaB_2O_4 (melting temperature phase of 942ºC) and subsequently $BaZr(BO_3)_2$ (melting point of 1320ºC). Conversely, the low levels of B-modified BZY densification can be explained by the high melting temperature phases of segregated products ($Ba_3B_2O_6$, m.p. = 1383ºC) which are also responsible for a substantial decrease not only in perovskite lattice parameter but also in the grain growth. The associated segregation of Y_2O_3 may also hinder densification due to a reduction in the number of oxygen vacancies.

The emerging materials $(Ba,Sr)GeO_3$ doped with K were studied for a detailed characterization of the role of the ionic radius in divalent cations on crystallographic structure, compositional homogeneity and oxide-ion transport.

Room temperature mechanosynthesis is shown to be an effective synthesis method for the preparation of the high-temperature β form of barium metagermanate. Although, on heating, the β-form partially transforms to the monoclinic α phase, with the transition being complete at 1000ºC. Both polymorphs exhibit linear lattice parameter expansion on heating in the range 25-1000 °C. The β polymorph is once more reformed on heating above 1100 °C.

Despite the ability to form Ba and Sr germanates by mechanosynthesis, K-doped $BaGeO_3$ and $SrGeO_3$ are unable to be produced by this route, with high energy milling only producing amorphization of precursors. However, pure powders of these materials could be formed upon calcination of these mechanically activated powders above 700ºC. These materials offer high chemical stability and purity for oxide-ion conduction as well competitive O^{2-} conductivities in the intermediate temperature range 700ºC ≤ T ≤ 800ºC, which makes them a potential new material for O^{2-} conductivity applications. Compared with the well-known electrolytes used in SOFCs, such as YSZ, $(Ba,Sr)_{1-x}K_xGeO_{3-0.5x}$ (x = 0.20) materials could be densified at much lower temperatures (1100ºC), potentially reducing production costs and being attractive for the market. The chemical stability and independence of conductivity on pO_2 is confirmed for these materials under a wide range of oxygen partial pressures between N_2 and O_2 atmospheres. This behaviour suggests predominant ionic conduction that, due to its independence on pH_2O, is likely to be oxide-ion conducting in nature. Nonetheless, a conductivity jump is shown in these materials upon increasing temperature around 600ºC-700ºC. This jump is shown to not be related to the cation sublattice, while thermogravimetric measurements alternatively suggest that this feature is due to loss of oxygen upon heating and alterations to the anion lattice.

6.2 FUTURE WORK

This section outlines strategies and future work that may provide several improvements in sinterability and proton conductivity of perovskite-type proton conductors, focusing on the principal work of the thesis, that of $BaZrO_3$-based materials.

The influence of ZnO on the chemical stability of yttrium-doped barium zirconate was investigated in this work. According to the electrical conductivity measurements, Zn-modified samples show a stable behaviour under oxidizing conditions under the operation temperatures. However, the stability of zinc in reducing operating conditions was brought under question with distinct microstructural damage produced under reducing conditions.

On consultation of suitable thermodynamic tables (Ellingham diagram), it was concluded that the most common transition metal element sintering additives (Cu, Co, Ni and Zn) can be susceptible to reduction under normal conditions of operation. According to this hypothesis, the stability of many of these additives under reducing operating conditions remains to be tested and more stable alternatives to promote densification are still needed. In this respect, there are many studies on the proton conductivity of barium zirconate-based materials in which the B-site is modified. However, studies on the modification of the A-site are rather limited.

Ba-loss is a common problem when one tries to densify $BaZr_{1-x}Y_xO_{3-\delta}$ materials due to the requirement of very high sintering temperatures. As discussed in this thesis, some authors have attempted to link such Ba-loss with poor total conductivity values in these materials, while alternative explanations have been based on poor homogeneity and separation of the perovskite into two distinct phases. One should note that these two concepts may be linked.

Yamazaki *et al.* [1] reported the impact of a precisely controlled level of barium deficiency in 20 mol% yttrium-doped barium zirconate ($Ba_{1-x}Zr_{0.8}Y_{0.2}O_{3-\delta}$), on the proton conductivity and phase purity. It was demonstrated that the perovskite phase is tolerant to Ba-deficiency up to $x = 0.06$ and it was suggested that this non-stoichiometry was accommodated by cationic crossover and incorporation of yttrium on the A-site, although no concrete proof was provided. At higher values of x, a two phase system was observed with the appearance of yttria as a secondary phase.

On the other hand, studies of Ba-deficiency in 15 mol% yttrium-doped $BaZrO_3$ ($Ba_{1-x}Zr_{0.85}Y_{0.15}O_{3-\delta}$) performed in our group, have highlighted a more complex behaviour with anomalous evolutions of lattice parameter and conductivity with increasing x in the single phase region, with inflections at the composition 0.02. With respect to the conductivity, this feature can be noted for both bulk and total conductivities which are shown to decrease after the point of inflection. Grain size measurements also have indicated anomalous progression with Ba-deficiency. Rapid decreases in grain size are noted until composition x = 0.02, followed by a small and relatively constant grain size for further Ba-deficiencies.

Our analogy is that the single phase perovskite region may actually be very limited, *i.e.* only up to x = 0.02. Immediately, beyond this region one enters the perovskite + Y_2O_3 two phase region, which only becomes observable under the resolution of XRD at x > 0.06. At values of 0.02 < x < 0.08 this two phase region manifests itself either as an enrichment of the grain boundary with Y_2O_3 or as a non-uniform grain composition with Y_2O_3 segregation. Note in both of these cases the loss of the acceptor dopant yttrium would be predicted to impair oxygen vacancy concentration and, hence, proton conductivity. Thus, further more detailed analysis must be performed with more sensitive techniques such as TEM in order to confirm the above information. If our analogy is correct and Y_2O_3 is immediately expelled from the lattice on Ba-loss, its presence in the grain boundary may explain the limited grain growth and negative impacts on observed conductivity. This analogy would also correspond well with recent theoretical results of Han *et al.* [2] that suggest that yttrium is actually too small to crossover to the A-site in BZY (at least in any substantial concentration).

Dudek *et al.* [3] studied the system $(Ba_{1-y}Ca_y)(Zr_{0.9}Y_{0.1})O_3$, where calcium substitutes for barium. They showed a higher total conductivity for composition y = 0.05, although, no morphological information or attempts to separate the conductivity into bulk/grain boundary contributions were presented. A similar concept was offered by Bućko *et al.* [4] who studied the structural and electrical properties of $(Ba_{1-x}Sr_x)(Zr_{0.9}M_{0.1})O_3$, M = Y, La solid solutions. Interestingly, these authors also reported that the composition containing 5 mol% of strontium, offered the highest total conductivity and the lowest activation energy for the yttria system. Nonetheless, once again, only total conductivity values were reported, with no attempts to separate the conductivity into bulk/grain contributions.

In our opinion, the results of Dudek *et al.* [3] and Bućko *et al.* [4] can possibly be related to the reduced average A-site ionic radius, due to Ca or Sr doping, which would facilitate yttrium crossover to the A-site. Such enhancement of yttrium crossover would prevent Y_2O_3 segregation (caused by Ba-loss occurring during sintering) which would otherwise produce negative impacts on grain growth and conductivity.

In order to understand the described mechanisms, we have starting to study the impact of Ba-deficiency on grain growth and proton conductivity in a system containing 5mol% of Sr doped on the A-site, $Ba_{0.95-x}Sr_{0.05}Zr_{0.85}Y_{0.15}O_{3-\delta}$, where x = 0, 0.02, 0.04, 0.6, 0.08 and 0.10. Preliminary results suggest that this concept can offer positive effects on grain growth. Large grains are formed across the series, even for high Ba-deficiencies. Nonetheless, analysis of the XRD patterns highlights the following phase progression. Formation of a pure perovskite at x = 0, is followed immediately by a two phase region of the perovskite with slight traces of Y_2O_3, then a phase region of the perovskite with slightly misshapen main peaks (possibly due to a second perovskite phase of higher lattice parameter) then reversion back to a pure perovskite phase at x = 0.10. The corresponding lattice parameters firstly decrease and then increase with increasing x. This inflection has the opposite direction to that noted in the Sr-free system. Grain growth is also dramatically altered going through a minimum at intermediate values of x, and then reverting back to large at the highest Ba-deficiency x = 0.1.

The obtained results are very interesting. The radical changes in physical behaviour between Sr-free and Sr-containing systems can be expected to have significant impact on their electrical behaviour. To reinforce our analogy, more information must be gathered. It is important to analyse the uniformity of grain composition as well as to assess possible grain boundary enrichment by yttrium in these materials. A detailed TEM/EDS analysis could be a good started technique to achieve this goal. Additionally, a detailed structural analysis, performed by Rietveld refinements of XRD results, and conductivity measurements should also be done.

We hypothesise that the small Sr content may succeed to prevent Y_2O_3 expulsion and/or segregation at the grain boundaries, due to facilitating preferential crossover to the A-site. In this way grain growth and high levels of conductivity can be maintained, in compositions with high Ba-deficiency. Such a result would be highly beneficial for those aiming to use these materials as electrolytes in electrochemical devices, as the negative effects of Ba-loss during sintering could be avoided.

K-doped $(Ba,Sr)GeO_{3-\delta}$ materials was reported as a new family of oxide-ion conductors due to their improved chemical stability and purity for oxide-ion conduction as well competitive O^{2-} conductivities in the intermediate temperature range 700ºC ≤ T ≤ 800ºC. Additionally, comparing with the well-known electrolytes used in SOFCs, such as YSZ, these materials show a decrease in the densification temperature (from ≥ 1350ºC to 1100ºC) which will lead to a reduction in the production costs.

However, both Ba- and Sr-based materials have shown a significant “jump” in the the total conductivity between 700-650ºC and 650-600ºC, respectively, which was studied by high-temperature X-ray diffraction. According to the reported results, it is expected that this “jump” occurred due to possible structural changes and/or phase transitions between the monoclinic to the orthorhombic structures (low-temperature α-form ↔ high-temperature β-form of $AGeO_3$, A = Ba or Sr). Nevertheless additional work should be done in the future to confirm this assumption, such as: low speed scan high-temperature XRD, namely during the cooling between 750 and 450ºC, high-temperature Raman spectroscopy (heating and cooling) and/or thermogravimetric analysis with larger dwell times between 750 and 450ºC.

6.3 REFERENCES

[1] Yamazaki, Y., Hernandez-Sanchez, R. and Haile, S.M. (2010). “Cation non-stoichiometry in yttrium-doped barium zirconate: phase behaviour, microstructure, and proton conductivity.” Journal of Materials Chemistry **20:** 8158-8166.

[2] Han, D., Nose, Y., Shinoda, K. and Uda, T. (2011). “Site selectivity of dopants in $BaZr_{1-y}M_yO_{3-d}$ (M = Sc, Y, Sm, Eu, Dy) and measurement of their water contents and conductivities.” Solid State Ionics **213:** 2-7.

[3] Dudek, M. and Bućko, M.W. (2008). ”Ceramic electrolytes based on $(Ba_{1-x}Ca_x)(Zr_{0.9}Y_{0.1})O_3$ solid solution.” Journal of Solid State Electrochemistry **14(4):** 565-570.

[4] Bućko, M.M. and Dudek, M. (2009). ”Structural and electrical properties of $(Ba_{1-x}Sr_x)(Zr_{0.9}M_{0.1})O_3$, M = Y, La, solid solutions.” Journal of Power Sources **194:** 25-30.